

# Enabling Collective Operation of Indoor Flying Robots

THESIS SUBMITTED TO THE

SWISS FEDERAL INSTITUTE OF TECHNOLOGY LAUSANNE  
ÉCOLE POLYTECHNIQUE FÉDÉRALE DE LAUSANNE

FOR THE DEGREE OF

DOCTOR OF SCIENCE IN MANUFACTURING SYSTEMS AND ROBOTICS (EDPR)

BY

James F. Roberts

Thesis committee:

Prof. Max-Olivier Hongler, committee president

Prof. Dario Floreano, thesis director

Dr. Jean-Christophe Zufferey, thesis co-director

Prof. Panos Trahanias, external referee

Prof. Erol Sahin, external referee

Dr. Francesco Mondada, internal referee

Lausanne

April 2011



---

# Acknowledgements

---

First, I would like to thank my thesis directors Prof. Dario Floreano and Dr. Jean-Christophe Zufferey. I am grateful to Dario for inviting me to the LIS and for providing support throughout my time at EPFL. Since the beginning of my PhD studies, Jean-Christophe Zufferey has provided me with invaluable support for everything from strategic issues to technical details. His contribution has been critical to the completion and the success of this thesis.

I also thank my thesis referees Prof. Panos Trahanias, Prof. Erol Sahin, and Dr. Francesco Mondada, as well as my thesis committee president Prof. Max-Olivier Hongler. I am grateful to EPFL for providing a great studying and working environment, to the Swarmanoid Future Emerging Technologies Project (FET-IST-022888) and to the Swiss National Science Foundation for funding my research.

I owe special thanks to Timothy Stirling, for his significant contribution to this work and being a valuable friend and colleague throughout the Swarmanoid Project. I would like to thank the following people for helping with the Eye-bot fabrication and calibration: IRIDIA, Université Libre de Bruxelles; Prof. Marco Dorigo, Dr. Ali Emre Turgut, Arne Brutschy, Manuele Brambilla, Nithin Mathews. LIS, Ecole Polytechnique Fédérale de Lausanne (EPFL); Thomas Schaffter, Peter Dürr, Jürg Germann, Yannick Gasser, Michal Dobrzynski, Géraud L'Eplattenier, Adrien Briod and Adam Klaptocz. I would also like to thank Michael Bonani and Philippe Rétornaz for providing valuable feedback during the sensor design phase. Additionally, I would also like to thank the following people for providing the ABB robot, wheeled robot and mechanical interface: LRSO, EPFL; Lionel Flaction, Tarek Baaboura, Prof. Reymond Clavel, Dr. Francesco Mondada. Additionally, I would like to thank Julien Brahier from HEIG-VD who provided the Leica tracking system and assisted with the Eye-

bot tracking.

A special thanks to the all the workshop personal for all there help and willingness to do "special requests", especially André Badertscher, Philippe Vosseler, Manuel Leitos, José Luis Garciacano, Jean-Paul Brugger, Pierre-André Joly, Jean-Pierre Grobet, Peter Bruehlmeier and Mose Silvestri.

I would like to thank my past and current colleagues at the Laboratory of Intelligent Systems for making the lab such an amazing place to work, and especially Felix Stephan Schill, Antoine Beyeler, Andrea Maesani, Pawel Lichocki, Meysam Basiri, Trevis Alleyne, Pavan Ramdya, Pradeep Ruben Fernando, Ramón Pericet Camara, Simon Harding, Sabine Hauert, Julien Hubert, Walter Karlen, Mirko Kovac, Daniel Marbach, Sara Mitri, Severin Leven, Mototaka Suzuki, Danesh Tarapore, Yannick Weibe, Steffen Wischmann, Maja Varga and Markus Waibel.

Several students have contributed to this work. I wish to thank in particular Peter Oberhauser, Kasper Leuenberger, Philippe Bérard, Simon Fivat and Lucas Oehen for their contribution to this research. Also, not to be forgotten, the administrative assistants who are the ones that make it all work. Thanks to Michelle Wälti, Ioanna Paniara, Anouk Hein and Filomena Jacquier.

Thank you to Kev, my mentor who inspired me to "find out where I fit in". I am very grateful to my family, Kristine, Raymond, Amity and Josh, for their unconditional support during my studies and my thesis. Finally, I am very grateful to Inês, who is my inspiration and muse, and her family for being like a second family to me, while being so far away from home.



---

# Abstract

---

Collective flying robots show great potential in many diverse indoor applications. Their added robustness, parallel operation and redundancy has clear advantages over a single flying robot. However, flying within cluttered and unprepared indoor environments, even for a single flying robot, is extremely challenging.

The main reason why collective flying robots have not yet been successful within indoor environments, is due to a combination of several challenges related to the size constraints placed on an indoor hovering platform, which directly limits the available energy, embedded sensing and processing capabilities of a flying robot. The energetic cost of flying, places limits on the flight endurance and practicality of a swarm of flying robots. The current spatial-coordination approaches implement methods that are either too computationally expensive, or impractical for real-world operation, within unknown and unprepared indoor environments.

The goal of this thesis was to develop a practical methodology for enabling energy efficient, autonomous indoor flying robots capable of inter-robot spatial-coordination for unprepared indoor environments, without using external aids. In order to enable collective operation of indoor flying robots, several practical methodologies have been proposed and demonstrated.

A generalised design strategy has been proposed to dimension a hovering platform for a specific flight endurance, payload capability and robustness criteria. The developed method can be used as a practical design tool for anyone working with hovering platforms. The dimensioning strategy has created a design, which is highly suitable for carrying the necessary sensing and processing required to enable the collective operation of indoor flying robots.

A simple sensing and control strategy is proposed for enabling anti-drift control and obstacle avoidance behaviours on an indoor highly dynamic, hovering platform. The approach has enabled one of the first indoor hovering platforms that could achieve such

a capability without using any external aids.

For the collective operation of indoor flying robots to work in reality, the on-board energy needs to be managed efficiently and conserved in a way that allows a swarm of robots to be useful, extending beyond the individual 10-20 min flight time. A generalised energy model has been developed, allowing for the accurate estimation of the flight endurance and perching time of hovering platforms. The energy model can be used to optimise the battery selection process of a hovering platform, to obtain the highest possible endurance. This is the only model known that is able to predict any combination of flying endurance and perching times. Additionally, a method of attaching to the ceiling has been presented that allows a flying robot to conserve energy and have a stable birds-eye-view while performing static sensing tasks. By applying energy management techniques, through use of energy modelling and behaviours that reduce the flight time, the energetic cost of flying can be mitigated and the mission endurance can be extended over several hours, which is especially useful for collective operation.

A new infrared ranging technique has been developed that allows for a high sensing performance, including long range (12 m), high-speed (1 kHz / # robots) and high resolution (better than 1.1 cm up to 6 m). A practical on-board sensing method using this technique, has been developed that can provide spatial-coordination between multiple robots in three dimensions. The developed approach allows for easily adaptation, to suit other robots and applications, depending on a specific sensing speed and coverage requirement. The developed sensor is the worlds first embedded 3-D relative positioning sensor that has the ability to enable inter-robot spatial-coordination in three dimensions, which is necessary for achieving goal-directed flight on highly dynamic flying robots.

A practical autonomous flight control methodology has been demonstrated that can provide hovering platform stabilisation, 3-D obstacle avoidance and 3-D waypoint navigation, all using the 3-D relative positioning sensor. Goal-directed flight and collective deployment have been achieved using only the information from the 3-D relative positioning sensing. The developed methodologies within this thesis, has enabled for the first time, the collective operation of highly dynamic indoor flying robots, without using external aids.

**Keywords:** Indoor flight, collective operation, flying robot, autonomous, relative positioning sensor, hovering platform, ceiling attachment, 3-D waypoint, obstacle avoidance, control strategy, payload, endurance, perching.

---

# Résumé

---

Les groupes de robots volants ont un champ d'application très vaste dans les situations d'intérieur. D'une nature très robuste, leur capacité à effectuer des opérations en groupe leur donne un net avantage par rapport à un robot volant unique. Toutefois, voler dans des environnements intérieurs encombrés et non préparés est extrêmement compliqué, même pour un seul robot volant. La raison principale pour laquelle l'utilisation de groupes de robots volants dans des environnements intérieurs n'a pas été couronnée de succès est due à la corrélation de plusieurs défis relatifs aux contraintes de taille auxquelles est soumise une plateforme planante d'intérieur. Ces contraintes limitent directement l'énergie disponible, l'intégration de capteurs et la capacité de traitement d'un robot volant. Le coût énergétique nécessaire au vol pose des limites à l'endurance au vol et à la fonctionnalité d'un essaim de robots volants. Les approches de coordination spatiale actuelles mettent en place des méthodes qui sont soit trop coûteuses du point de vue informatique ou peu pratiques pour des opérations dans la vraie vie, qui comportent des environnements intérieurs inconnus et non préparés.

Le but de cette thèse est de développer une méthodologie pratique afin de permettre l'utilisation de robots d'intérieurs volants et autonomes, économes en énergie, capables de coordination spatiale inter robotique dans un environnement intérieur non préparé, sans recours à une aide extérieure. Afin de permettre une opération collective de robots d'intérieurs volants, plusieurs méthodologies pratiques ont été proposées et démontrées.

Une stratégie de conception généralisée a été proposée afin de constituer une plateforme planante avec une endurance de vol, une charge utile et un critère de robustesse spécifiques. La méthode développée peut être utilisée comme un outil de conception pratique pour toute personne travaillant avec des plateformes planantes. La stratégie de dimensionnement a permis une conception qui se prête particulièrement à l'exécution de la télédétection et du traitement nécessaire afin de permettre des opérations collectives de robots volants.

Une stratégie de télédétection et de contrôle simple est proposée pour permettre un contrôle anti-dérive et de comportement d'évitement d'obstacles sur une plateforme d'intérieur hautement dynamique et planante. L'approche a permis la création de l'une des premières plateformes planantes d'intérieur avec une capacité pareille sans aide extérieure.

Afin de permettre la réalisation d'une opération collective de robots volants d'intérieur, l'énergie utilisée par les robots doit être gérée de manière efficace et conservée dans une manière

permettant à un essaim de robots d'être utile pendant plus de 10-20 minutes de vol. Un modèle d'énergie généralisée a été développé, permettant une estimation correcte de l'endurance de vol et de la durée pendant laquelle la plateforme est maintenue dans les airs. Le modèle énergétique peut être employé afin d'optimiser le processus de sélection de batterie d'une plateforme planante, afin d'obtenir l'endurance la plus élevée possible, Ceci est le seul modèle connu capable de prédire une combinaison d'endurance de vol et de positionnement dans les airs (perching time). Par ailleurs, une méthode d'accrochage au plafond a été présentée, permettant à un robot volant de conserver de l'énergie et de posséder une vue aérienne stable tout en performant des tâches de télédétection statiques. Par l'application de techniques de gestion de l'énergie par le biais de modélisation énergétique et des comportements réduisant le temps de vol, le coût énergétique du vol peut être atténué et l'endurance de la mission peut être accrue de plusieurs heures, ce qui revêt une importance particulière pour une opération collective.

Une nouvelle technique de mesure de la portée aux moyen de rayons infra-rouges très sensible à été développé. Elle possède une grande sensibilité y compris pour la longue-distance (12 m), haute vitesse (1 kHz / # robots) et haute résolution (meilleur que 1.1 cm up to 6 m). Une approche pratique de l'on-board sensing method qui permet d'obtenir une coordination spatiale trois dimensions a été développé en utilisant cette nouvelle technique. L'approche développé permet une adaptation facile à d'autres robots ou applications. Le senseur développé est une première mondiale en ce qui concerne les embedded 3-D relative positioning sensor qui permette une coordination spatiale en trois dimensions entre des robots ce qui est nécessaire pour des tâches précises avec des robots dynamiques.

Une méthode pratique de contrôle de vols autonomes à été developpé qui permet d'obtenir une stabilisation des hovering platforms, un évitement d'obstacles 3-D, et une navigation 3-D waypoint tout ceci en utilisant le relative-positionning 3D sensor. Des vols à haute précision et avec objectifs ont été rendus possibles on utilisant uniquement les informations du senseur 3-D infra-rouge. La méthodologie développée dans cette thèse a permis pour la première fois une opération collective de vol indoors sans utilisation d'aides externes.

**Mots-clés:** Vol intérieur, collective opération, robot volant, autonomes, capteur de position relative, planant plate-forme, fixation au plafond, 3-D waypoint, l'évitement d'obstacles, stratégie de contrôle, charge utile, l'endurance, percher.

---

# Contents

---

<b>Acknowledgements</b>	<b>i</b>
<b>Abstract</b>	<b>iii</b>
<b>Résumé</b>	<b>v</b>
<b>Contents</b>	<b>vii</b>
<b>1 Introduction</b>	<b>1</b>
1.1 Background and motivation . . . . .	2
1.2 State of the art . . . . .	4
1.2.1 Commercial platform limitations . . . . .	4
1.2.2 Energy saving techniques . . . . .	11
1.2.3 Autonomous indoor flight . . . . .	13
1.2.4 Relative positioning sensing . . . . .	16
1.2.5 Summary of the main challenges . . . . .	20
1.3 Main contribution . . . . .	21
1.4 Objectives and thesis overview . . . . .	22
<b>2 Hovering platform design</b>	<b>25</b>
2.1 Introduction . . . . .	26
2.2 Materials and methods . . . . .	31
2.2.1 Platform dimensioning method . . . . .	31
2.2.2 Realistic propeller figure of merit . . . . .	35
2.3 Results . . . . .	37
2.3.1 Optimising for robustness . . . . .	37
2.3.2 Optimising for high-endurance . . . . .	39
2.3.3 Optimising for high-payload . . . . .	41

2.3.4	Robustness optimised hovering platform . . . . .	44
2.3.5	Endurance optimised hovering platform . . . . .	47
2.3.6	Payload optimised hovering platform . . . . .	49
2.3.7	Comparison against commercial platforms . . . . .	52
2.4	Conclusion . . . . .	54
<b>3</b>	<b>Autonomous indoor flight</b>	<b>57</b>
3.1	Introduction . . . . .	58
3.2	Materials and methods . . . . .	60
3.2.1	Embedded electronics . . . . .	60
3.2.2	Attitude sensing . . . . .	62
3.2.3	Autonomous flight sensing . . . . .	64
3.2.4	Control strategy . . . . .	66
3.3	Results . . . . .	68
3.3.1	Experiment room . . . . .	69
3.3.2	Altitude control . . . . .	70
3.3.3	Obstacle avoidance . . . . .	71
3.3.4	Anti-drift control . . . . .	71
3.4	Conclusion . . . . .	74
<b>4</b>	<b>Energy management</b>	<b>75</b>
4.1	Introduction . . . . .	76
4.2	Materials and methods . . . . .	79
4.2.1	Flight endurance model . . . . .	79
4.2.2	Perching endurance model . . . . .	82
4.2.3	Hovering platform preparation . . . . .	83
4.3	Results . . . . .	85
4.3.1	Static thrust characterisation . . . . .	85
4.3.2	Battery selection optimisation . . . . .	86
4.3.3	Endurance test . . . . .	88
4.3.4	Ceiling attachment test . . . . .	90
4.4	Conclusion . . . . .	92
<b>5</b>	<b>3-D relative positioning</b>	<b>93</b>
5.1	Introduction . . . . .	94
5.2	Materials and methods . . . . .	95

---

5.2.1	Functioning principle . . . . .	95
5.2.2	Coordination among multiple sensors . . . . .	98
5.2.3	Infrared transmission . . . . .	100
5.2.4	Infrared reception . . . . .	101
5.2.5	Physical constraints and possible layouts . . . . .	103
5.2.6	Integration on a flying robot . . . . .	105
5.3	Results . . . . .	108
5.3.1	Resolution and noise . . . . .	109
5.3.2	Relative positioning error . . . . .	111
5.3.3	Light immunity . . . . .	124
5.3.4	Proximity sensing . . . . .	126
5.3.5	Sensor limitations . . . . .	126
5.3.6	Comparison with other relative sensors . . . . .	127
5.4	Conclusion . . . . .	130
<b>6</b>	<b>Validation</b>	<b>131</b>
6.1	Introduction . . . . .	132
6.2	Optimising for high-payload and robustness . . . . .	135
6.3	Flight control strategy . . . . .	136
6.4	Results . . . . .	142
6.4.1	Eye-bot hovering platform . . . . .	142
6.4.2	Comparison against commercial platforms . . . . .	145
6.4.3	Energy efficient swarm search implementation . . . . .	147
6.4.4	Flight controller tuning . . . . .	147
6.4.5	Goal-directed flight . . . . .	148
6.4.6	Collective deployment . . . . .	150
6.5	Conclusion . . . . .	157
<b>7</b>	<b>Conclusion</b>	<b>159</b>
7.1	Motivation and challenges . . . . .	160
7.2	Accomplishments . . . . .	161
7.3	Limitations and future work . . . . .	163
7.4	Future applications . . . . .	165
7.5	Outlook . . . . .	168

<b>A Appendix</b>	<b>169</b>
A.1 Eye-bot structure . . . . .	170
A.2 Eye-bot electronics . . . . .	173
A.2.1 Flight critical avionics . . . . .	173
A.2.2 Additional optional sensors . . . . .	175
A.2.3 Swarmanoid specific electronics . . . . .	178
A.2.4 Relative positioning sensor support . . . . .	179
A.2.5 Fitting the relative positioning sensor . . . . .	180
<b>Bibliography</b>	<b>183</b>
<b>Curriculum Vitae</b>	<b>193</b>



---

# List of Figures

---

1.1	Commercially available hovering platforms ( $\leq 106$ cm) with autopilot, as shown in Table 1.1 . . . . .	7
1.2	Payload versus diameter comparison for commercially available platforms (see Table 1.1). The background shows a gradient of increasing risk of a collision as the platform size approaches the 100 cm doorway limitation. "-RP" indicates a platform with rotor protection. . . . .	8
1.3	Endurance versus diameter comparison for commercially available platforms (see Table 1.1). The background shows a gradient of increasing risk of a collision as the platform size approaches the 100 cm doorway limitation. "-RP" indicates a platform with rotor protection. . . . .	9
1.4	Relative positioning sensors as shown in Table 1.2, sorted by date .	18
2.1	Internal workings of a brushed ( <i>right</i> ) and brushless ( <i>right</i> ) dc motor	27
2.2	<i>Left</i> : Single brushless motor (Hyperion HP-2205/46). <i>Right</i> : Coaxial brushless motor (Himax CR2805) . . . . .	27
2.3	Different types of propeller varieties, from a high rigidity to high flexibility ( <i>left to right</i> ) . . . . .	29
2.4	Carbon-fibre rectangular bar ( <i>left</i> ) and fibre glass plating ( <i>right</i> ), showing the direction of the fibres . . . . .	31
2.5	Typical quad-rotor configuration ( <i>top-down</i> ) showing the platform diameter ( $d_1$ ), propeller diameter ( $d_2$ ) and centre diameter ( $d_3$ ), with a 5% propeller clearance . . . . .	34

2.6	Figure of merit determined from the calculated ideal power ( $P_i$ ) and the measured actual power ( $P_a$ ), for the three different propeller varieties . . . . .	36
2.7	Figure of merit determined from the calculated ideal power ( $P_i$ ) and the measured actual power ( $P_a$ ), for a single and coaxial propeller arrangement . . . . .	37
2.8	High-robustness design. <i>Left</i> : Estimated propeller-motor efficiency with respect to the platform diameter. <i>Right</i> : Estimated battery weight with respect to the platform diameter. The dotted line indicates the recommended platform size, which is selected using the desired battery loading ( $m_p = 100$ g, $FM = 0.24$ (flexible propellers), $L_p = 18\%$ , $L_b = 16\%$ ) . . . . .	39
2.9	High-endurance design. <i>Left</i> : Estimated propeller-motor efficiency with respect to the platform diameter. <i>Right</i> : Estimated battery weight with respect to the platform diameter. The dotted line indicates the recommended platform size, which is selected using the desired battery loading ( $m_p = 25$ g, $FM = 0.32$ (thin-electric propellers at $T = 125$ g), $L_p = 5\%$ , $L_b = 34\%$ ) . . . . .	41
2.10	High-payload design. <i>Left</i> : Estimated propeller-motor efficiency with respect to the platform diameter. <i>Right</i> : Estimated battery weight with respect to the platform diameter. The dotted line indicates the recommended platform size, which is selected using the desired battery loading ( $m_p = 1000$ g, $FM = 0.39$ (coaxial thin-electric propellers), $L_p = 50\%$ , $L_b = 22\%$ ) . . . . .	43
2.11	Hovering platform optimised for a high robustness against collisions	45
2.12	Thrust curve of the Hyperion <i>HP-2205/46</i> motor with a X-UFO 8 inch propeller. The dotted lines indicate the hover point thrust and power . . . . .	46
2.13	Hovering platform optimised for a high endurance capability . . .	48
2.14	Thrust curve of the Emotion 24G 2C motor with an APC 7x5 inch propeller. The dotted lines indicate the hover point thrust and power . . . . .	48
2.15	Hovering platform optimised for a high-payload capability . . . .	50

2.16	Thrust curve of the Himax CR2805 motor with twin APC 7x5 inch propellers. The dotted lines indicate the hover point thrust and power . . . . .	51
2.17	Payload versus diameter comparison against commercially available platforms (see chapter 1, table 1.1). The background shows a gradient of increasing risk of a collision as the platform size approaches the 100 cm doorway limitation. "-RP" indicates a platform with rotor protection. . . . .	53
2.18	Endurance versus diameter comparison against commercially available platforms (see chapter 1, table 1.1). The background shows a gradient of increasing risk of a collision as the platform size approaches the 100 cm doorway limitation. "-RP" indicates a platform with rotor protection. . . . .	53
3.1	High-speed brushless motor control board. <i>Left:</i> Top-view, <i>Right:</i> Bottom-view . . . . .	61
3.2	<i>Left:</i> Flight control board. <i>Right:</i> Xbee wireless module . . . . .	62
3.3	Quad-rotor hovering platform coordinate system . . . . .	63
3.4	<i>Left-top:</i> Four infrared sensors mounted on top of the hovering platform, used for obstacle detection. <i>Left-bottom:</i> Ultrasonic sensor used for altitude sensing. <i>Right:</i> Signal strength response of the infrared distance sensor. . . . .	65
3.5	Hovering platform fitted with embedded control boards and sensors	66
3.6	View of experiment room through the 180° field-of-view downward pointing dome camera, hovering platform visible in the center	69
3.7	<i>Left:</i> Altitude response during a single run - take-off, hover and landing. <i>Right:</i> Mean altitude response of ten independent runs - take-off and hover. . . . .	70
3.8	Obstacle avoidance trajectory plot. The dotted box defines the limits where the platform would collide with the wall at the hover height. The black circles represent the starting and ending positions	72
3.9	Anti-drift trajectory plot. The dotted box defines the limits where the platform would collide with the wall at the hover height. The black circles represent the starting and ending positions . . . . .	73

4.1	Comparison of the different battery technologies in terms of volumetric and gravimetric energy density (Tarascon and Armand, 2001) . . . . .	77
4.2	Discharge curve of a single cell LIPO battery. The dotted line represents the critical cell voltage. . . . .	81
4.3	Quad-rotor fitted with the propulsion system, control boards, sensors and ceiling attachment device . . . . .	83
4.4	<i>Left</i> : Ceiling attachment mechanism. <i>Right</i> : Functional diagram. . . . .	84
4.5	Thrust curve of the motor-propeller system showing the power required for a certain hover thrust (taken at a nominal voltage of 12.5 V) . . . . .	86
4.6	Flight time versus battery mass, showing the optimum battery mass for the quad-rotor without additional payload ( $m_s=0.431$ kg, $m_p=0$ kg, $p_a=2.44$ W, $p_p=0$ W, $e_d=164$ W.h/kg) . . . . .	87
4.7	List of battery packs sorted by flight endurance. Battery-A = TP-2100-3S1P, Battery-B = TP-1320-3S1P ( $m_s=0.431$ kg, $m_p=0$ kg, $p_a=2.44$ W, $p_p=0$ W) . . . . .	88
4.8	Estimated and measured endurance for variable payloads and active payload power consumptions. Error bars have been plotted on each sample point marked by a circle ( $m_s=0.431$ kg, $p_a=2.44$ W. Battery-A: $m_b=0.144$ kg, $e_d=172$ W.h/kg. Battery-B: $m_b=0.085$ kg, $e_d=164$ W.h/kg). . . . .	89
4.9	Altitude log during a single autonomous ceiling attachment and detachment cycle . . . . .	91
5.1	Example diagram showing the idealised 3-D geometry of one sensor receiving ( <i>left</i> ) and another transmitting sensor ( <i>right</i> ), where both are represented as spheres. The received signal strength ( $s$ ) is proportional to the inverse square of the sphere-to-sphere range ( $r$ ). The sensor with the strongest signal strength is defined as $s_0$ and the angular spacing ( $\beta$ ) of the sensors is $\frac{\pi}{4}$ . The bearing and elevation offset angles can be triangulated using the three sensor values ( $s_{-1,0,1}$ ) along the corresponding plane. In this example the emitting and receiving functionalities are represented separately, however during normal operation each sensor will implement both functions. . . . .	96

5.2	Sensor timing diagram. Each sensor takes a turn in transmitting (TX) while the others receive (RX) and calculate the range, bearing and elevation measurements. . . . .	99
5.3	Transmission block diagram showing the infrared transmission path of the emitter arrays . . . . .	100
5.4	Theoretical signal strength of the cascaded filtering output (solid line) with respect to the range. The four individual stage outputs of the cascaded filter before they are added together are shown as dashed-dotted lines where each represents 25 % of the total global signal. . . . .	102
5.5	Reception block diagram showing the infrared reception path of the cascaded filtering method . . . . .	103
5.6	2.5-D relative positioning sensor (2-D planar reception with 3-D transmission for a robustness to tilting) . . . . .	105
5.7	<i>Left</i> : Close-up of a transmitter array ( <i>top</i> ) and receiver array ( <i>bottom</i> ). <i>Middle-left</i> : A single sensor section with two receiver arrays and four transmitter arrays. <i>Right</i> : A complete sensor ring showing eight sensor sections connected together . . . . .	107
5.8	Calibration setup showing the transmitting sensor ( <i>left</i> ) and the receiving sensor ( <i>right</i> ). The ABB robot aligns each photodiode of the receiving sensor with the centre of the transmitting sensor, taking 25 samples at each step. After the data is collected the Wheeled robot moves the transmitting sensor along the guide rail to the next 10 cm position. . . . .	109
5.9	Resolution ( <i>top</i> ) and signal standard deviation ( <i>bottom</i> ) characteristics of the infrared photodiodes over the calibrated range, each item of the box-plot shows the variance across the sensors 48 photodiodes . . . . .	110
5.10	Characterisation setup showing the transmitting sensor ( <i>left</i> ) with respect to the receiving sensor ( <i>right</i> ), along a six by three two dimensional vertical grid with a 100 cm spacing. Three laser pointers, providing a straight edge, helped with the alignment of the distance ( <i>Laser-1</i> ) and angles ( <i>Laser-2,3</i> ) between the two sensors . . . . .	111

5.11	Range measurements over the 600 cm calibration range of the sensor at a fixed bearing ( $0^\circ$ ) and elevation ( $0^\circ$ ). Error bars show the standard deviation . . . . .	113
5.12	Box-plot of the range error over the distance, indicating the variance across the samples at a fixed bearing ( $0^\circ$ ) and elevation ( $0^\circ$ ) .	113
5.13	Box-plot of the range error over the distance, indicating the variance across all tested bearings at a fixed elevation ( $0^\circ$ ) . . . . .	114
5.14	Box-plot of the range error over the distance, indicating the variance across all tested elevations (see Table 5.1) at a fixed bearing ( $0^\circ$ ) . . . . .	115
5.15	Extended range measurements for the full range of the sensor at a fixed bearing ( $22.5^\circ$ ) and elevation ( $0^\circ$ ). Error bars show the standard deviation. The signal skew above 600 cm is because the sensor has not been calibrated at these ranges, due to the limited size of the calibration room . . . . .	117
5.16	Box-plot of the extended range error over the distance, indicating the variance across the samples at a fixed bearing ( $22.5^\circ$ ) and elevation ( $0^\circ$ ) . . . . .	117
5.17	Bearing measurements across the 6 tested bearings of the sensor, at a fixed distance (300 cm) and elevation ( $0^\circ$ ). Error bars show the standard deviation . . . . .	118
5.18	Box-plot of the bearing error across the 6 tested bearings, indicating the variance across the samples at a fixed distance (300 cm, middle data set) and elevation ( $0^\circ$ ) . . . . .	119
5.19	Box-plot of the bearing error with respect to the distance, indicating the variance across the 6 tested bearings at a fixed elevation ( $0^\circ$ ) . . . . .	119
5.20	Box-plot of the bearing error with respect to the elevation angle, indicating the variance across the 6 tested bearings . . . . .	120
5.21	Elevation measurements across the 13 tested elevation angles of the sensor (see Table 5.1). Error bars show the standard deviation. The measurements are not evenly distributed due to the vertical grid geometry . . . . .	121

5.22	Box-plot of the elevation error across the 13 tested elevation angles of the sensor, indicating the variance across the samples, which are spread over all distances and heights . . . . .	122
5.23	Box-plot of the elevation error with respect to the distance, indicating the variance across the elevation angles for each tested distance with a fixed bearing ( $0^\circ$ ) . . . . .	123
5.24	Box-plot of the elevation error with respect to the bearing angle, indicating the variance across the 13 tested elevation angles . . . .	124
5.25	Proximity sensing showing the range as a function of the reflected signal strength from a single sensing sector, for a white, glossy wall and a brown, dull wall . . . . .	127
6.1	"From Humanoid to Swarmanoid", a heterogeneous robotic swarm made up of several Foot-bots ( <i>wheeled</i> ), Hand-bots ( <i>climbing</i> ) and Eye-bots ( <i>flying</i> ) . . . . .	133
6.2	Simulation of search algorithm, showing Eye-bots building a chain	133
6.3	Eye-bot design. <i>Left</i> : Estimated propeller-motor efficiency with respect to the platform diameter. <i>Right</i> : Estimated battery weight with respect to the platform diameter. The dotted line indicates the recommended platform size, which is selected using the desired battery loading ( $m_p = 600$ g, $FM = 0.39$ (coaxial thin-electric propellers), $L_p = 30\%$ , $L_b = 22\%$ ) . . . . .	136
6.4	Eight propeller, hovering platform coordinate system . . . . .	138
6.5	Functional diagram of the autonomous flight control system . . . .	139
6.6	The Eye-bot - A flying robot custom designed for indoor collective operation, fitted with a 3-D relative positioning sensor ( <i>base perimeter</i> ) and ceiling attachment mechanism ( <i>top</i> ), having a diameter of 50 cm and a maximum take-off weight of 2 kg including a payload of 600 g . . . . .	144
6.7	Thrust curve of the Himax CR2805 motor with twin APC 7x5 inch propellers. The dotted lines indicate the hover point thrust and power . . . . .	145

6.8	Payload versus diameter comparison against commercially available platforms (see chapter 1, table 1.1). The background shows a gradient of increasing risk of a collision as the platform size approaches the 100 cm doorway limitation. "-RP" indicates a platform with rotor protection . . . . .	146
6.9	Endurance versus diameter comparison against commercially available platforms (see chapter 1, table 1.1). The background shows a gradient of increasing risk of a collision as the platform size approaches the 100 cm doorway limitation. "-RP" indicates a platform with rotor protection . . . . .	146
6.10	Goal-directed flight - Diagram of the experiment room showing the desired flight path of the flying Eye-bot with respect to the reference Eye-bot . . . . .	149
6.11	Goal-directed flight - The flight trajectory of the Eye-bot over 14 trials. <i>Top</i> : Trajectory plot of the room length ( $x$ ) versus the room height ( $z$ ). <i>Bottom</i> : Trajectory plot of the room length ( $x$ ) versus the room width ( $y$ ) . . . . .	151
6.12	Goal-directed flight - The final ceiling attachment locations, room length ( $x$ ) versus the room width ( $y$ ), for all 14 flights. The mean position is 827 cm for $x$ and 0.41 cm for $y$ . The dash-dotted circle represents the standard deviation of the 14 positions . . . . .	152
6.13	Collective deployment - Diagram of the experiment room showing the desired flight path of the flying Eye-bot with respect to the reference Eye-bots . . . . .	153
6.14	Collective deployment - The flight trajectory of the Eye-bot over 15 trials. <i>Top</i> : Trajectory plot of the room length ( $x$ ) versus the room height ( $z$ ). <i>Bottom</i> : Trajectory plot of the room length ( $x$ ) versus the room width ( $y$ ) . . . . .	155
6.15	Collective deployment - The final ceiling attachment locations, room length ( $x$ ) versus the room width ( $y$ ), for all 15 flights. The mean position is 907 cm for $x$ and $-1$ cm for $y$ . The dash-dotted circle represents the standard deviation of the 15 positions . . . . .	156
A.1	Structural pieces cut from quasi-isotropic carbon fibre plate . . . . .	170
A.2	Head ( <i>left-top</i> ), four motor arms ( <i>left-bottom</i> ) and main body ( <i>right</i> ) built from four, four and ten pieces of carbon fibre plate, respectively	171



---

A.3	<i>Left</i> : Carbon fibre leg and close-up of replaceable crash joint. <i>Right</i> : Arm fitted with coaxial motor and counter-rotating propellers	172
A.4	Ceiling attachment and detachment mechanism, designed to attach to ferrous ceilings . . . . .	173
A.5	Eye-bot fitted with coaxial motors, control boards and sensors . . .	174
A.6	Communications architecture . . . . .	175
A.7	Wireless computer interface ( <i>left</i> ) and main control board ( <i>right</i> ) . .	176
A.8	Flight computer ( <i>left</i> ) and four channel, high-speed brushless motor controller ( <i>right</i> ) . . . . .	176
A.9	Top sensor board ( <i>left</i> ) and bottom sensor board ( <i>right</i> ) . . . . .	177
A.10	Prototype distance scanner with rotating transformer . . . . .	178
A.11	i.MX31 embedded computer ( <i>left</i> ) and Pan-tilt video camera ( <i>right</i> )	179
A.12	Relative positioning processor ( <i>left</i> ) and communications hub ( <i>right</i> )	180
A.13	The Eye-bot, a flying robot custom designed for indoor collective operation, fitted with a 3-D relative positioning sensor ( <i>base perimeter</i> ) and ceiling attachment mechanism ( <i>top</i> ), having a diameter of 50 cm and a maximum take-off weight of 2 kg including a payload of 600 g. . . . .	181



---

# List of Tables

---

1.1	Review of commercially available hovering platforms ( $\leq 106$ cm) with autopilot, sorted by size . . . . .	6
1.2	Review of relative positioning sensors, sorted by date. Cells marked in <b>bold</b> and <i>italics</i> indicate either a major sensor benefit or limitation, respectively. . . . .	17
2.1	Comparison between the high-robustness dimensioning design and the real hovering platform performance . . . . .	46
2.2	Comparison between the high-endurance dimensioning design and the real hovering platform performance . . . . .	49
2.3	Comparison between the high-payload dimensioning design and the real hovering platform performance . . . . .	51
4.1	Mission endurance estimation for two test cases, each including three cycles of hovering and perching . . . . .	91
5.1	Elevation angles calculated from the geometry between the sensors	116
5.2	Summary of the specifications for the 3-D relative positioning sensor	125
5.3	State of the art comparison between top three relative positioning sensors and the developed 3-D sensor. Cells marked in <b>bold</b> indicate the best performing in that category . . . . .	129
6.1	Comparison between the design and the real platform performance	143



---

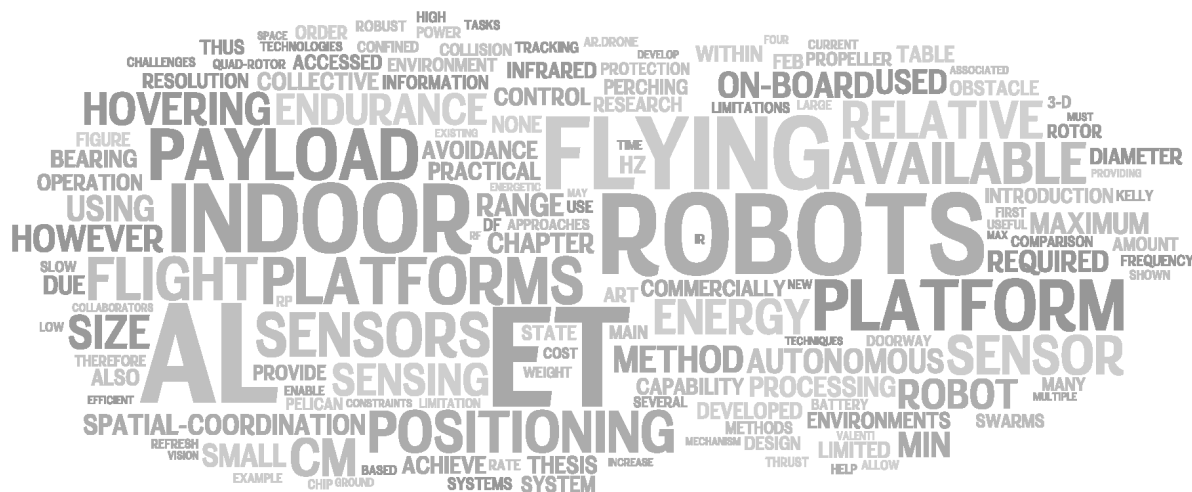
# 1

---

## Introduction

---

**T**HE goal of this thesis is to develop a practical methodology for enabling energy efficient, autonomous indoor flying robots capable of collective operation. This opening chapter introduces the background and motivation for using swarms of indoor flying robots and discusses the challenges associated with collective operation. The state of the art is then reviewed, including commercial hovering platforms, autonomous indoor flight research, energy saving techniques and spatial-coordination approaches pointing out their limitations. The approach of this thesis is then highlighted, which aims to solve these challenges. The chapter ends with an overview of the thesis and describes the main contributions of this work.



## 1.1 Background and motivation

Flying robots show great potential in many diverse indoor applications as they can rapidly travel over rough terrain, naturally overcome large obstacles and can provide powerful sensing with a bird's-eye view (Zufferey et al., 2011). Swarms of indoor flying robots are expected to be robust due to redundancy (Sahin, 2005), allow for parallel operation and provide an environment where individual robots can help each other, for example to achieve indoor navigation (Stirling et al., 2010) or to create mobile sensor networks (Ogren et al., 2004). Swarms of indoor flying robots can be deployed for searching tasks in disaster situations, such as earthquakes or terrorist attacks, to locate humans who may need help (Greer et al., 2002). They can also be used for exploration tasks in hazardous environments, for example in chemical and biotechnology buildings, to trace plumes of dangerous chemicals (Kovacina et al., 2002) or biological hazards. Furthermore, they can provide surveillance and monitoring capability (Min et al., 2009) for law enforcement to locate suspicious objects (Altshuler et al., 2008).

For tasks that employ several indoor flying robots, spatial-coordination between robots is essential in achieving collective operation. There are numerous multi-robot spatial-coordination algorithms that have been developed that assume absolute or relative positioning information between robots is available. Such algorithms range from simple inter-robot collision avoidance behaviours (Hoffmann and Tomlin, 2008) to more complex behaviours such as flocking (Pilz et al., 2009) or chain formation (Stirling et al., 2010). These algorithms are typically developed in simulation with the hope to then be ported to real-robots for practical validation. However, there are many challenges that have prevented the practical use of swarms of indoor flying robots within unprepared indoor environments. This thesis identifies the four main challenges as follows.

The first challenge associated with indoor flying robots is to achieve robust autonomous flight with an obstacle avoidance capability. Hovering platforms are useful indoors as slow translational velocities are desired due to the limited space available for flying. In order to keep the translational velocities low and to dampen the platform's dynamics, stability control based on attitude sensing from an Inertial Measurements Unit (IMU) is required. However, even with stability control a platform will have a tendency to drift away during hover. This platform drift is due to the imbalance of the inertial forces and moments act-

ing on the suspended system over time and the errors introduced by the IMU (Fowers et al., 2007; Grzonka et al., 2009). In order to control this drift, the robot needs to know its pose and/or ego-motion (Amidi et al., 1999; Rudol et al., 2008). When outdoors, this can be done using an absolute positioning sensor such as GPS (Hoffmann et al., 2004) which can additionally provide spatial-coordination and goal-directed flight. However, GPS cannot be used indoors, as reception is poor and the positioning is unreliable (Rudol et al., 2008). Additionally, within indoor environments, such as in office buildings, there are many obstacles to avoid such as walls, furniture and people. Therefore, it is a necessity that the robot is equipped with sensors that can detect these obstacles to prevent collisions and to aid in navigation.

The second challenge associated with indoor flying robots is the limited amount of payload available for sensors and embedded processing. The width of corridors and doorways ( $\approx 100$  cm) creates a strong platform size (in the order of  $< 70$  cm diameter) and weight limitation that leads to a limited payload capacity (Soundararaj et al., 2009; Grzonka et al., 2009) and short flight endurance (Roberts et al., 2008; Stirling et al., 2010; Valenti et al., 2007). Sensors that fit the payload constraints typically offer a reduced performance with short operating ranges, slow update rates and noisy signals. This payload limitation reduces the available possibilities for on-board sensing, processing and communication hardware.

The third challenge associated with indoor flying robots is the energetic cost of flying, which is orders of magnitude higher than that of terrestrial locomotion. The specific energy density of the current battery technology limits the available amount of energy that can be placed on a flying robot (Tarascon and Armand, 2001), as the battery weight must be suitable for the platforms size constraints. Currently, this amount of energy equates to only tens-of-minutes of useful flight endurance (Valenti et al., 2007; Roberts et al., 2008), thus severely limiting the practicality of a flying robot. The types of indoor tasks that these robots will be used for are often tasks that require sensor analysis over an extended period of time, for example mobile sensor networks (Ogren et al., 2004) or surveillance and monitoring (Min et al., 2009), thus if the robot is hovering in a static position while performing the task, then the valuable and limited energy resource is not efficiently managed.

The fourth challenge associated with swarms of indoor flying robots is the

lack of on-board sensing technologies available for spatial-coordination among the individual robots. In order for several robots to work together in an autonomous and collective manner, they must be fitted with sensors that allow them to perform inter-robot spatial-coordination and collective operation. In reality on-board sensors that are capable of sensing the 3-D trajectories required for spatial-coordination of small indoor flying robots, are non-existent.

To summarise, four main challenges have been identified that are blocking the practical use of swarms of flying robots for indoor applications. First, it is challenging to achieve robust autonomous flight with an obstacle avoidance capability. Second, there is a limited amount of payload available for sensors and embedded processing. Third, the energetic cost of flying limits the practicality of a flying robot. Finally, there is a lack of on-board sensing technologies available for spatial-coordination that can operate in real-world environments.

## 1.2 State of the art

This section discusses the limitations of commercially available platforms and some possible energy saving techniques for indoor flying robots. The latest research is then presented in autonomous indoor flight and the current techniques for relative positioning sensing.

### 1.2.1 Commercial platform limitations

In the last decade there has been a growing interest in flying robotics both commercially and for research. In the commercial sector there are numerous companies developing remote controlled hovering platforms that could be considered for indoor swarming systems each with their underlying benefits and limitations. When searching for a suitable indoor platform the most important features, as suggested in section 1.1, are to have a small platform size to allow for safe passage through confined spaces (e.g. doorways), and a high payload capability in order to carry useful onboard sensing and processing. However, these two features are in contradiction with each other making platform selection difficult.

Table 1.1 shows a list of the current, most commonly used hovering platforms that are commercially available (see figure 1.1). Commercial systems have been



chosen for comparison as they represent the last several years of development and are a good performance measure as they are often not bound by the tighter constraints of indoor autonomous flight. Additionally, most autonomous indoor flight research has been performed using one of these platforms, typically the smaller platforms. Companies such as Draganfly<sup>1</sup>, Microdrones<sup>2</sup>, and AirRobot<sup>3</sup> are targeting the professional photography and government markets, whereas companies such as Ascending technologies<sup>4</sup> and Skybotix<sup>5</sup> are targeting the research market. Recently (2010), a new market has been initiated by a company called Parrot<sup>6</sup> who are developing flying robots for augmented reality gaming with a remote interface to an iPhone/iPad. Most of these platforms can be purchased with GPS options that can provide fully autonomous waypoint control for outdoor operation. However, none offer a solution providing autonomous collision avoidance and collective operation within indoor environments.

For robust indoor operation, it is desirable for the rotors to be protected from small collisions that can be potentially damaging to the platform, the surrounding environment and to people. Without rotor protection even small collisions can be potentially fatal. Most of the platforms shown in Table 1.1 are shipped without any form of rotor protection with the exception of two platforms, the AR.Drone (removable) and AR100 - B (basic carbon fibre rods). At the same time adding protection further increases the size of the platform and reduces the available payload. For example, the Pelican has an optional rotor protection kit that adds  $\approx 5$  cm to the size and reduces the payload by 130 g, giving a new diameter of 80 cm and a payload of 370 g.

When flying within confined indoor spaces such as in offices with hallways and small rooms, typically the most confined space where the hovering platform would fly is limited by the size of a standard doorway (100 cm). These platforms have been selected as they have a maximum diameter that is equal to or less than the standard doorway limitation, with an exception of the DF-X8 which is slightly larger (106 cm). The DF-X8 is of particular interest as it's payload

---

<sup>1</sup><http://www.draganfly.com> (accessed Feb. 2011)

<sup>2</sup><http://www.microdrones.com> (accessed Feb. 2011)

<sup>3</sup><http://www.airrobot.de> (accessed Feb. 2011)

<sup>4</sup><http://www.asctec.de> (accessed Feb. 2011)

<sup>5</sup><http://www.skybotix.com> (accessed Feb. 2011)

<sup>6</sup><http://ardrone.parrot.com> (accessed Feb. 2011)

Table 1.1: Review of commercially available hovering platforms ( $\leq 106$  cm) with autopilot, sorted by size

Platform Name (Company Name)	Rotor Configuration	Take-off Weight Max.	Payload Max.	Payload Loading	Battery Loading	Endurance Max.	Diameter Max.	Rotor Protection
Hornet (Ascending Tech.)	Hex-rotor	350 g	50 g	14 %	38 %	15 min	29 cm	None
Coax (Skybotix)	Coaxial-Heli.	320 g	70 g	22 %	27 %	20 min	34 cm	None
Hummingbird (Ascending Tech.)	Quad-rotor	750 g	200 g	27 %	18 %	20 min	53 cm	None
AR.Drone (Parrot)	Quad-rotor	550 g 550 g	150 g 100 g	27 %	12 %	15 min 12 min	56 cm 64 cm	None Full
Pelican (Ascending Tech.)	Quad-rotor	1250 g 1250 g	500 g 370 g	40 %	30 %	20 min 18 min	75 cm 80 cm	None Full
DF-X4 (Draganfly)	Quad-rotor	980 g	250 g	26 %	16 %	20 min	79 cm	None
MD4-200 (Microdrones)	Quad-rotor	1000 g	200 g	20 %	20 %	30 min	92 cm	None
DF-X6 (Draganfly)	Hex-rotor	1500 g	500 g	33 %	16 %	20 min	99 cm	None
AR100-B (AirRobot)	Quad-rotor	1100 g	200 g	18 %	20 %	30 min	100 cm	Basic
DF-X8 (Draganfly)	Oct-rotor	2700 g	1000 g	37 %	16 %	20 min	106 cm	None



Figure 1.1: Commercially available hovering platforms ( $\leq 106$  cm) with autopilot, as shown in Table 1.1

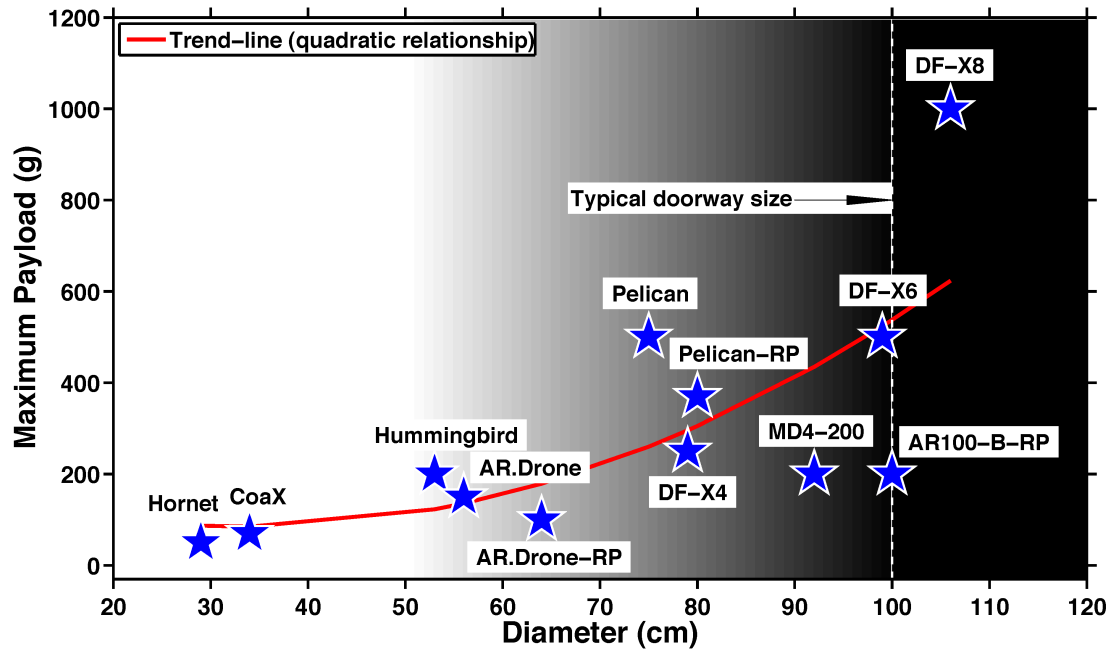


Figure 1.2: Payload versus diameter comparison for commercially available platforms (see Table 1.1). The background shows a gradient of increasing risk of a collision as the platform size approaches the 100 cm doorway limitation. "-RP" indicates a platform with rotor protection.

capability is two times greater than any other platform in this size class with a similar maximum endurance. The difference between this platform and the others is that it has four pairs of counter-rotating propellers (eight rotors in total). Counter-rotating propellers in a coaxial arrangement, allow for almost twice the thrust when compared to a single propeller with the same diameter, at the cost of approximately 22% increase in induced power for the same given thrust (Leishman, 2006). This suggests that there is a possibility to design a smaller platform ( $\approx 50$  cm diameter) that uses counter-rotating propellers to provide an improved payload capability over the existing platforms, while also reducing the risk of collisions, thus making it easier to fly through confined spaces. Most of the platforms shown in Table 1.1 have around 12 to 20 min maximum flight endurance (with no payload), with the exception of two platforms, the MD4 - 200 and AR100 - B, which are capable of a 30 min flight endurance.

A graphical comparison showing the maximum payload versus the diameter of the platforms from Table 1.1 can be seen in figure 1.2. Similarly, a graphical comparison showing the maximum endurance versus the diameter can be

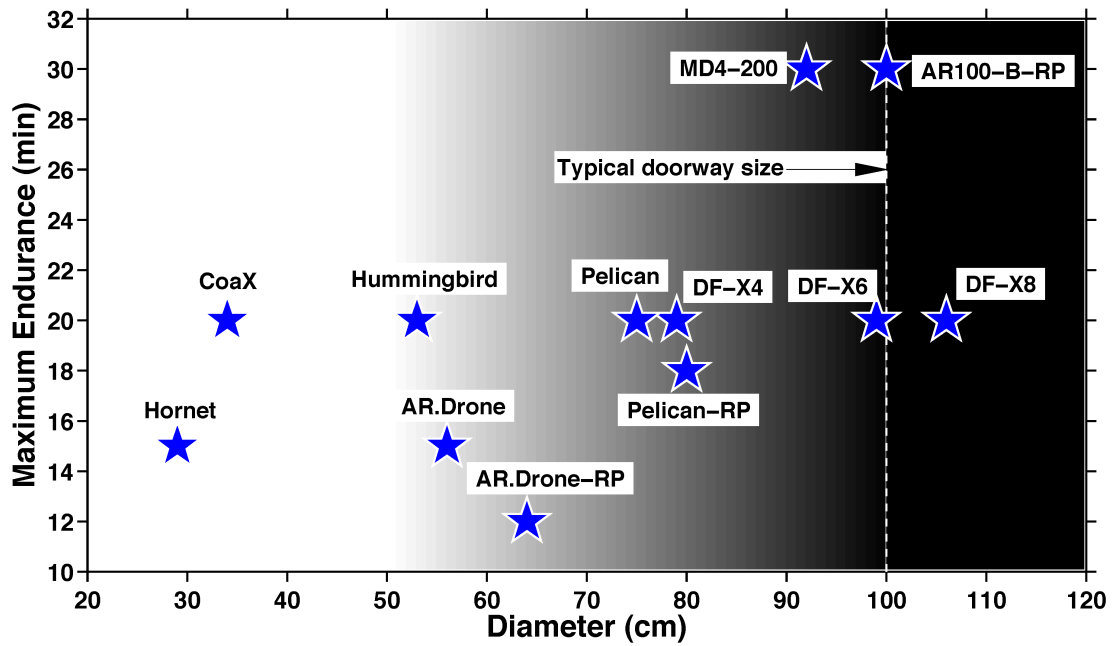


Figure 1.3: Endurance versus diameter comparison for commercially available platforms (see Table 1.1). The background shows a gradient of increasing risk of a collision as the platform size approaches the 100 cm doorway limitation. "-RP" indicates a platform with rotor protection.

seen in figure 1.3. The shaded gradient represents the increase in risk of a collision as the platform size approaches the 100 cm standard doorway limitation. Most companies only specify the maximum cases for payload and endurance separately, thus a direct comparison cannot be performed as the true flight endurance is a function of the added payload.

Momentum theory can be used to explain the relationship between propeller thrust ( $T$ ), the ideal power required to hover ( $P$ ) and the induced velocity ( $v_i$ ) at the propeller disk, using the following equations (Leishman, 2006):

$$T = 2\rho A v_i^2, \quad P = 2\rho A v_i^3$$

where  $\rho$  is the density of air at a given altitude and  $A$  is the propeller disk area. Note that the power required to hover will increase with the cube of the induced velocity, thus at a given thrust, a reduction in the induced velocity leads to an increased efficiency. Therefore, the air flow through the disk must be large, which implies that a larger propeller would have a lower induced velocity and thus be more efficient. The static thrust efficiency, also known as the figure of merit ( $FM$ ), is defined by the ratio of the ideal power and the actual power

required to hover. The literature states that a well-designed propeller can achieve a  $FM$  ranging from 0.50 to 0.8, corresponding to a small propeller (7.5 cm) to a full sized helicopter (several meters) respectively (Liu and Moschetta, 2009; Coleman, 1997; Leishman and Ananthan, 2006; Leishman, 2006).

Therefore, as the platform size increases both the available thrust and the rotor efficiency increase, which in turn also increases the amount of available payload. It is interesting to note that payload loading (ratio between the maximum payload and take-off weight) and battery loading (ratio between the battery and take-off weight) for the platforms in Table 1.1 is on average 26% and 21%, respectively.

By plotting the trend line of the data points, it is shown in figure 1.2 that the platforms having a similar maximum endurance (12 to 20 min) follow the quadratic relationship in regard to the propeller disk area (by doubling the radius of the propeller the available propeller disk area is quadrupled). However, the MD4-200 and AR100-B platforms that have a much higher endurance (30 min) have a much smaller (2.5 to 5 times less) payload than the other platforms of approximately the same size, with a payload loading of 18% and 20% respectively. This suggests that there is a compromise between payload capacity and flight endurance, where the ratio of payload and battery weight can be adjusted (within the hardware limitations) depending on the desired endurance.

The risk of a collision while flying is related to the maximum platform size and the minimum immediate confined space, where the platform size must be less than this confined space. Additionally, the performance of the position and obstacle detection controllers while flying thorough this confined space is also important as it determines how precise the platform must be controlled to prevent a collision.

Analysing the capabilities of these platforms shows that there is a compromise between platform size and payload capability. The maximum payload for this size class is defined by the Pelican, which is 370 g (with rotor protection). This size is only possible if the position and obstacle detection controller error is less than  $\pm 10$  cm, which is a challenging task in itself. Thus, there is a compromise between platform size and payload capability that also affects the sensing requirements. This can be generalised to say that the higher the performance of the position and obstacle detection controller, the smaller the clearance can be between the platform size and the minimum confined space.

## 1.2.2 Energy saving techniques

Due to the energetic cost of flying the current commercially available platforms that are suitable for indoor operation have a maximum flight endurance that is limited to  $\approx 20$  min without payload (section 1.2.1). Every bit of extra weight added to a hovering platform equates to a reduced flight endurance. Additionally, the flight endurance is directly related to the amount of energy that is stored in a platform's battery, where the major limiting factor is the specific energy density of the current battery technology (Tarascon and Armand, 2001). As the energy on a hovering platform is a limited and valuable resource, it must be managed efficiently. There are some methods that researchers have come up with to help to mitigate this problem in an attempt to increase the practicality of flying robots.

Valenti and collaborators have developed a health management system to aid online mission planning for swarms of flying robots (Valenti et al., 2007). They have found that it is possible to estimate the remaining flight endurance by comparing the platforms battery voltage and thrust command over time. The motivation for doing this was to acquire information about the health of the platform and possible detection of faults to help manage the energy constraints on flying robots. Their testing results show that the comparison between the predicted and actual remaining flight time varies in the order of two minutes.

Thomas and collaborators have investigated several energy scavenging techniques including Photonic (solar), kinetic-flow (wind), thermal, electromagnetic, and autophagous structure - power concepts that allow for energy generation through self-consumption of system structure, for small unmanned systems (Thomas et al., 2006). However, for most of these techniques the amount of energy that can be collected indoors is minimal and hence not practical for small flying robots.

Alternatively, perching mechanisms can help mitigate the energetic cost of flying while performing static sensing tasks. Currently, there is a lot of research in developing mechanisms for vertical perching, which has been inspired by climbing robots (Spenko et al., 2008). Kovač and collaborators have developed a simple and lightweight perching mechanism that can attach to and detach from trees and facades of buildings (Kovac et al., 2010). Their perching mechanism enables a small, fixed-wing plane (6 g) to perform repetitive head-first perching to vertical man-made and natural structures, while limiting the impact forces

acting on the plane. They also present a model that can be used to dimension the perching mechanism so that it can be used on different robots. Similarly, Desbiens and collaborators have developed an integrated system allowing a fixed-wing plane (375 g) to land and perch on vertical surfaces (Lussier Desbiens and Cutkosky, 2010). Their perching mechanism uses arrays of compliant micro-spines, which have been adapted from climbing robots. The motivations are to greatly increase mission life and provide the plane with a stable, secure location that is relatively free of debris. However, such designs require a specific angle and force in order to reliably attach to objects, thus introducing a difficult control problem for a hovering platform. Additionally, for indoor hovering platforms that can weigh up to several kilograms, the force acting on the attachment mechanism is very high. The sharp spikes that are used to attach to walls and furniture creates concerns regarding aesthetic damage when using such devices indoors.

Other approaches exist that can enable perching that is not damaging to the environment. Sitti and collaborators have developed a dry adhesive technology, which has been inspired by Geckos feet, using Van der Waals forces to attach to substrates (Sitti and Fearing, 2003; Murphy and Sitti, 2009). Dry adhesives can provide a large amount of adhesion force, however they reduce their effectiveness over time by attracting dust, and require power to overcome the adhesive forces in peeling away from the substrate. Prahlad and collaborators have developed electro-adhesion pads that can be turned on and off at will (Prahlad et al., 2008). The forces for a  $1 \text{ cm}^2$  area are between 0.2 and 1.4 N and requires 20 micro-watts per Newton of weight held. The technology is useful as it shows the ability to repeatably clamp to wall substrates that are heavily covered in dust or other debris. However, the adhesion force exerted by the robot on the flap is almost exclusively in shear and not in the peel direction, meaning that it is not suitable for adhesion to ceilings as it would easily peel off.

Even though none of these methods solve the energy problems involved with flying robots a combination of these methods may be useful to help mitigate the problem. For example to improve energy management by use of an accurate energy model, and to extend the mission endurance by utilising a perching mechanism.



### 1.2.3 Autonomous indoor flight

Due to the difficulty in developing small, light-weight and precise on-board sensing systems, many researchers are using off-board tracking sensors to achieve spatial-coordination and goal-directed flight. The external tracking method that is most commonly used for indoor flying robotics is a commercially available Vicon<sup>7</sup> tracking system. The Vicon system uses several infrared cameras and high powered infrared spotlights, which are designed to track reflective markers that have been placed on the hovering platform. Each robot needs to have geometrically unique markers in order for the system to differentiate between multiple platforms. The Vicon system provides accurate absolute positioning information (1 to 3 mm) at high update rates ( $\approx 300$  Hz) (Lupashin et al., 2010). This system is useful for the rapid development of highly dynamic controllers allowing for precise coordinated control of multiple robots (Valenti et al., 2007) or difficult manoeuvres such as multi-flip trajectories (Lupashin et al., 2010). However, it requires many tracking cameras to be pre-installed and carefully calibrated in the environment. If the robot flies outside of the sensor coverage area, the position tracking is lost and the robot will crash. There are other off-board sensors such as infrared trackers (Kirchner and Furukawa, 2005) and ultrasonic beacons (Eckert et al., 2011) that have been developed in research. However, these sensors provide absolute positioning only for a single platform. Vicon has been used in conjunction with other onboard sensors, such as the Kinect sensor by Microsoft<sup>8</sup>. The Kinect sensor has been placed on a Pelican quad-rotor, providing altitude and collision avoidance sensing<sup>9</sup>. Typically, with external tracking sensors, all the processing is done on a ground station and the control commands are sent to the flying robot using wireless communication. For practical reasons, external sensing systems like these are not viable methods for real-world applications in unknown and unprepared environments.

Other researchers are working with on-board vision systems that can extract motion information using feature tracking algorithms (Achtelik et al., 2009; Guevard et al., 2008; Courbon et al., 2009). This method can be beneficial, as cameras are often required in many applications for tasks like visual identification of tar-

---

<sup>7</sup>[www.vicon.com](http://www.vicon.com) (accessed Feb. 2011)

<sup>8</sup><http://www.xbox.com/en-US/kinect> (accessed Feb. 2011)

<sup>9</sup><http://hybrid.eecs.berkeley.edu> (accessed Feb. 2011)

gets. However, vision processing is computationally expensive (Achtelik et al., 2009; Soundararaj et al., 2009) and suitable image features are required for reliable motion detection (Guenard et al., 2008). Additionally, vision will not work in the dark or in poor lighting conditions without on-board illumination (Altug et al., 2005). This makes it difficult to fly within indoor environments, especially in disaster situations where unreliable illumination is common.

Alternatively, optic-flow can be used to extract motion information (Dahmen et al., 2009). This can be done either with a normal camera or with an optical computer mouse chip (Lange et al., 2009; Beyeler et al., 2009). Optical mice chips have the advantage of being small and light-weight. They have fast update rates for control and no additional processing is required. A disadvantage of all optic-flow based approaches is that highly textured environments are required with a good contrast. This means that they are also dependent on the available illumination, which is especially true for the mice sensors due to their poor sensitivity (Lange et al., 2009). Therefore, similarly to the standard vision systems, it is often necessary to have on-board illumination, which consumes more energy<sup>10</sup>. It is very challenging to use this method for goal-directed flight because integrating the noisy optic-flow signal is not reliable enough to perform odometry sensing (Iida, 2003).

Another method to use is a scanning laser range finder that can detect small movements in the robot's position by using scan matching algorithms (Angeletti et al., 2008; Grzonka et al., 2009). A benefit of this is that the scanner can also be used for obstacle avoidance. However, there are many problems associated with this approach. In large open areas or long parallel structures such as hallways with no doors, where there are no distinct features that can be detected, the motion of the robot cannot be calculated correctly (Achtelik et al., 2009). Additionally, erroneous readings can occur from many sources, including undetectable glass structures, such as windows, or rapid changes in the environment, e.g. people walking past. Changes in altitude can be another source of error, causing features to (dis)appear (Achtelik et al., 2009). Thus, subsequent scans may have large errors and the system may fail.

In order to achieve spatial-coordination between multiple robots using vision, optic-flow or laser scanners, details about the pose estimate with respect

---

<sup>10</sup><http://www.skybotix.com> (accessed Feb. 2011)

to the environment would need to be distributed among the robots. Therefore, a method such as Simultaneous Localisation and Mapping (SLAM) (Bachrach et al., 2009; Blösch et al., 2010) would be required to extract and compare each robots relative position information. This approach is computationally expensive and requires a high-bandwidth wireless link to a ground station for real-time processing (update rates  $>10$  Hz). For example, embedded visual SLAM has been used successfully on a robot vacuum cleaner (Jeong and Lee, 2005), with a Pentium III 1 GHz. Even with a fast processor (in embedded terms) the update rate of the system is only 2 Hz, which is not adequate for highly dynamic flying robots. As the processing power of small and light weight devices is increasing, such a method may be more viable in the future. However, this method is not efficient, if the task is to simply acquire relative positioning information.

Due to high computational requirements, many of these methods utilise off-board processing on a ground station (Soundararaj et al., 2009; Achtelik et al., 2009; Grzonka et al., 2009). Wireless data is transmitted to the ground station for processing and then control information is sent back to the robot. This often reduces feedback update-rates due to the reception, processing and retransmission loop (Altug et al., 2005; Fowers et al., 2007). The robustness of such a system is also limited by the fact that the ground station introduces a single point of failure. Furthermore, scalability to large swarm sizes is challenging due to available bandwidth limitations and computational requirements. Finally, the operating range of the robots is constrained by the effective communication range, which can be restrictive within indoor environments due to radio signal attenuation (Ladd et al., 2005). Therefore, new methods that utilise on-board processing that can operate in any unknown and unprepared environment are desirable.

Although off-board tracking sensors and SLAM approaches are questionable, when it comes to the practical application of swarms of indoor flying robots within unknown environments, relative positioning is possible, for example with an on-board relative positioning sensor that can detect the distance and angles between robots (see section 1.2.4). By having at least one robot stationary, used as a static reference point, flying robots could use the relative positioning information to achieve position control, mitigate platform-drift, enable goal-directed flight and swarming. Such an approach could be used in most situations, as it does not rely on feature extraction in the surrounding environment like laser scanners or vision systems.

### 1.2.4 Relative positioning sensing

The emerging field of collective robotics has created a need for research in relative positioning sensors that are capable of providing spatial coordination between individual robots. Various relative positioning technologies are available, each with their own limitations. For example, ultrasound can be used to achieve high accuracy range (8 mm) and bearing ( $3^\circ$ ) measurements using Time-of-Flight (TOF) (Shoval and Borenstein, 2001; Rivard et al., 2008). However, the refresh rate is relatively slow, up to 1.33 Hz for 10 robots, due to the slow propagation of the sound signal (Rivard et al., 2008). Many other systems exist that depend on complex processing with cameras (Nakamura et al., 2003) or other heavy hardware (Montesano et al., 2004) that are unsuitable for a small flying robot.

In contrast, using infrared (IR) signals as a medium for relative positioning has the benefits of higher update rates (the speed of light is 874 thousand times faster than the speed of sound) and small low cost hardware. A comparison between the existing relative positioning sensors can be seen in Table 1.2 and figure 1.4.

Early infrared based relative positioning sensors (Kelly and Keating, 1996) typically had a maximum range of 2.5 m (roughly half the infrared communication range (Kelly and Martinoli, 2004)) and a refresh rate of 10 Hz. The developed ranging method, using the Received Signal Strength Indicator (RSSI) pin from a Radio Frequency (RF) chip, became the standard technique for most of the sensors that followed. However, this sensor was frequency division multiplexed providing a unique carrier frequency for each robot. Such a method is not scalable to a large swarm, as there are a limited number of communication channels available within the defined frequency spectrum (220 to 400 kHz) (Kelly and Keating, 1996). To overcome this problem a new design (Kelly and Martinoli, 2004; Pugh and Martinoli, 2006) was developed that uses a single channel with a scalable communication protocol, where the refresh rate is inversely proportional to the number of robots to allow for signal dissipation. This new design increased the maximum range (3.0 m), however the refresh rate was much slower (2 Hz for 10 robots).

Alternatively, McLurkin and Smith (2004) are using a commercial infrared localisation sensor design by iRobot, called the ISIS<sup>TM</sup>, which has a small maximum range (2.5 m) and slow refresh rate (0.4 Hz for 10 robots). For all of the infrared relative positioning sensors mentioned thus far, the resolution of the

Table 1.2: Review of relative positioning sensors, sorted by date. Cells marked in **bold** and *italics* indicate either a major sensor benefit or limitation, respectively.

Author	Ranging Method	Coverage	Speed (10 robots)	Range Max.	Comments
Kelly and Keating (1996)	IR, RSSI RF chip	360° (4 sensors)	10 Hz	2.5 m	⊖ Low bearing resolution, ⊖ <i>frequency multiplexed</i>
Welsby and Melhuish (2001)	IR, RSSI RF chip	180° (3 sensors)	10 Hz	<b>20 m</b>	⊖ Low bearing & range resolution, ⊖ <i>frequency multiplexed</i>
McLurkin and Smith (2004)	IR, ISIS <sup>TM</sup>	360° (4 sensors)	0.4 Hz	2.5 m	Commercial sensor, ⊕ <b>obstacle avoidance</b> , ⊖ low bearing resolution
Pugh and Martinoli (2006)	IR, RSSI RF chip	360° (4 sensors)	2 Hz	3.1 m	⊖ Low bearing resolution
Kemppainen et al. (2006)	IR, variable gain	360° (1 sensor)	0.5 Hz	<b>10 m</b>	⊕ <b>Good bearing resolution</b> , ⊖ mechanical (reliability issues), ⊖ <i>frequency multiplexed</i>
Rivard et al. (2008)	Ultrasound, TOF	360° (3 sensors)	1.33 Hz	<b>6.7 m</b>	⊕ <b>Very good range &amp; bearing resolution</b> , ⊖ <i>speed of sound</i>
Pugh et al. (2009)	IR, RSSI RF chip	<b>360° (8 sensors)</b>	<b>25 Hz</b>	3.3 m	⊕ <b>Good range and bearing resolution</b>

bearing measurements is low, as only four sensors (or photodiodes) are used to cover a 360° 2-D plane (Kelly and Martinoli, 2004). To improve the bearing resolution, Kemppainen et al. (2006) have designed a long range (10 m) relative positioning sensor with a mechanically rotating single receiver. However, this method is not scalable due to the use of frequency division multiplexing, has a slow refresh rate (0.5 Hz) and may have reliability issues due to the rotating mechanics. Another method to improve the bearing resolution is to simply add more photodiodes. Pugh et al. (2009), using the RSSI RF chip ranging method,

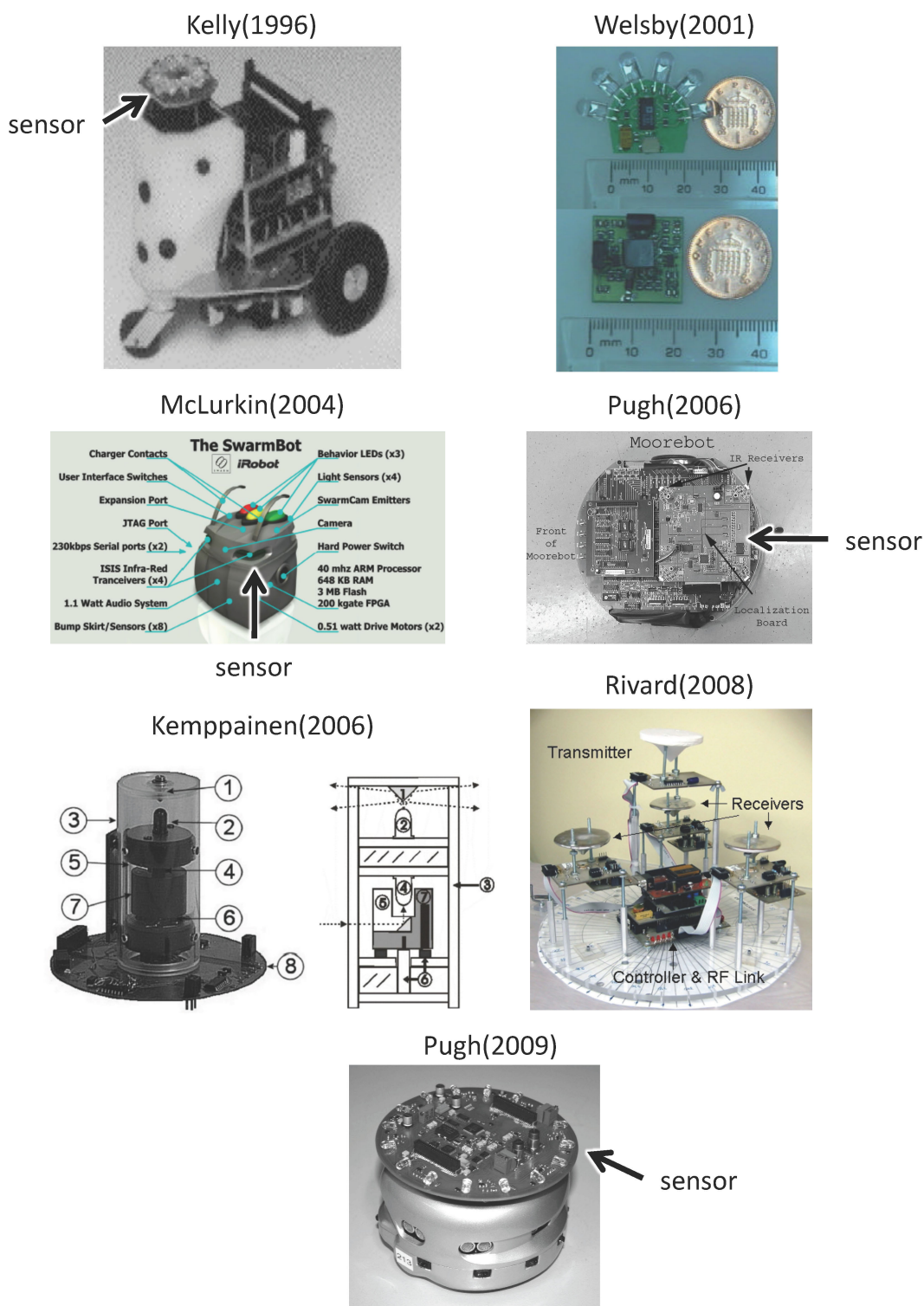


Figure 1.4: Relative positioning sensors as shown in Table 1.2, sorted by date

have designed an eight photodiode relative positioning sensor with an improved bearing resolution, a fast refresh rate (25 Hz for 10 robots) and a slightly improved maximum range of 3.3 m.

In addition to knowing the relative positions between robots it is also desirable to avoid collisions with walls or other obstacles. Typically, the only way to do this is by adding several distance sensors around the robots perimeter (Roberts et al., 2007) or by using a distance scanner (Angeletti et al., 2008; Grzonka et al., 2009). However, one of the advantages of using infrared as a medium for inter-robot spatial-coordination is that the transmitted infrared signal will reflect off nearby objects. Thus, if the sensor listens to its own infrared transmission, the signals on each of the receivers will hold information about the proximity to these objects (Payton et al., 2001; McLurkin and Smith, 2004). This means that additional sensors may not be required to achieve autonomous flight with obstacle avoidance.

To the best of our knowledge, the only on-board relative positioning system for an indoor flying robot is presented by Welsby and Melhuish (2001); Melhuish and Welsby (2002) for use on a swarm of Lighter Than Air Vehicles (LTAV). In their work, a long range (20 m) infrared relative positioning sensor, based on a cut down version of the design by Kelly and Keating (1996) (not scalable), is used to achieve a simple gradient ascent behaviour towards an emitting beacon. However, due to the small payload available on the LTAV and its very slow dynamics, their sensor was reduced to only 180° sensing.

All of these existing relative positioning sensors give only planar 2-D information. This 2-D information is useful for robots operating on the ground and for flying robots with slow dynamics that stay at the same height and do not tilt their body as they fly. However, for flying robots that have fast dynamics (e.g. helicopters and quad-rotors), fast and high accuracy sensing is required. During flight, these platforms can tilt as they translate and the difference in altitude can vary by several meters. Therefore, to achieve robust sensing for highly dynamic flying robots it is necessary to have a 3-D sensor coverage. Currently, there are no existing sensors, commercially available or in research that can provide on-board 3-D relative positioning.

### 1.2.5 Summary of the main challenges

To summarise, four problems have been identified that are blocking the practical use of swarms of flying robots for indoor applications.

First, none of the existing commercially available platforms offer a solution providing robust and autonomous indoor flight with an obstacle avoidance capability. This is mainly due to the difficulties involved in flying within the indoor size constraints. As the field is relatively new, there are no matured designs that are suitable for indoor applications. This has inspired a lot of research towards finding methods to achieve such a capability. The problem with current research methods is that they are either computationally expensive (laser scanner), requiring an external ground station, or will not work in dark or poor lighting conditions (vision, optic-flow). There is a need for simple sensing and control strategies to solve this challenge.

Second, the energetic cost of flying places strong limitations on the practicality of a flying robot. There is a limited amount of research in energy saving techniques for indoor flying robots. Further investigation is required to develop new methods to manage the energy and extend the mission endurance of indoor hovering platforms.

Third, the amount of available payload for on-board sensing and processing within the indoor size constraints, is limited to a maximum of  $\approx 370$  g including rotor protection (see table 1.1), with a platform size that leaves only  $\pm 10$  cm doorway clearance (based on a standard doorway size of 100 cm). Further investigation is required to develop smaller platforms with a higher payload capability to allow for better embedded sensing and processing.

Finally, there is a lack of on-board sensing technologies available that can enable spatial-coordination and collective operation in real-world environments. No existing sensors, commercially available or in research can provide on-board 3-D relative positioning and obstacle avoidance sensing within the payload capabilities of the current hovering platforms. Therefore, a new approach is required that does not rely on feature extraction in the surrounding environment like laser scanners or vision systems to enable practical and scalable swarming.

This thesis proposes that a combination of simple control strategies, energy modelling, ceiling attachment, high-efficiency contra-rotating propulsion and 3-D relative positioning sensing, is sufficient to overcome all of these challenges to enable autonomous and collective operation of indoor flying robots.



## 1.3 Main contribution

This thesis can be classified at the crossroad between indoor flying robotics and collective robotics (Melhuish and Welsby, 2002; Rudol et al., 2008; Valenti et al., 2007; Nardi et al., 2006; Pilz et al., 2009; Stirling et al., 2010). The aim is to identify the practical mechanisms required in terms of platform design, autonomous indoor flight, energy management and on-board sensing, to enable swarms of indoor flying robots for unprepared indoor environments, without using external aids, such as external tracking systems<sup>11</sup>.

The main contribution of this thesis includes:

- **a method for dimensioning indoor hovering platforms based on specific robustness, payload and flight endurance constraints**
- **a simple sensing and control method for achieving autonomous indoor flight with anti-drift control and obstacle avoidance**
- **an energy model for hovering platforms that allows for the prediction of flight and perching endurance**
- **a method of autonomously attaching to, and detaching from ferrous ceilings in order to conserve energy**
- **a practical on-board sensing and control method for achieving spatial-coordination between multiple robots in three dimensions.**

These main contributions have each been validated in experiments that have been performed on real flying robots.

---

<sup>11</sup>[www.vicon.com](http://www.vicon.com) (accessed Feb. 2011)

## 1.4 Objectives and thesis overview

The objectives of this thesis are closely tied to the four main challenges that have been identified in section 1.2.5, which also correlate with the thesis chapters. The organisation of this thesis follows the development of the proposed approaches and aims to accompany the reader through the refinement of our methodology.

- **Chapter 2: *Hovering platform design***

The first objective is to develop a design strategy for dimensioning a hovering platform, with an improved payload capability within the indoor size constraints. This chapter introduces a generalised design strategy for dimensioning a hovering platform for a specific flight endurance, payload capability and robustness criteria. The dimensioning strategy is then used to design three different hovering platforms optimised for each criteria. The chapter ends by showing a performance comparison between the three developed platforms against the commercially available platforms.

- **Chapter 3: *Autonomous indoor flight***

The second objective is to develop a simple sensing and control strategy, to achieve autonomous indoor flight with an obstacle avoidance capability. This chapter introduces an attitude estimation technique for stabilising a hovering platform using embedded inertial sensing. The robustness optimised hovering platform, from chapter 2, is then used to develop a simple sensing and control strategy for obstacle avoidance. The chapter ends by demonstrating the simple sensing and control strategy can enable anti-drift control and obstacle avoidance behaviours on an indoor hovering platform.

- **Chapter 4: *Energy management***

The third objective is to help mitigate the energetic cost of flying to improve the practicality of a flying robot. This chapter introduces the concept of using ceiling attachment to conserve energy, while providing a birds-eye-view of the environment. First, a proof of concept method is described, allowing a hovering platform to attach to, and detach from ferrous ceilings. Then an energy model is presented that allows for the estimation of flight endurance and perching time for hovering platforms. The chapter ends by demonstrating that the method can enable autonomous ceiling attachment and detachment on an indoor hovering platform.

- **Chapter 5: *3-D relative positioning***

The fourth objective is to develop a sensor that can enable spatial-coordination and collective operation between multiple flying robots, in real-world environments. This chapter introduces a practical on-board sensing method for achieving spatial-coordination between multiple robots in three dimensions. The design of a 3-D relative positioning sensor is first presented and shown how it can be constructed for a flying robot. Extensive characterisation is then performed on the sensor to determine the range, bearing and elevation performance. The chapter ends by comparing the developed 3-D relative positioning sensor with the best three 2-D relative positioning sensors from the literature.

- **Chapter 6: *Validation***

The last but not least objective, is to validate that the developed methodologies and technologies, are capable of enabling the collective operation of indoor flying robots. This chapter introduces an efficient swarm search scenario, based on the Swarmanoid<sup>12</sup> project application, which has been the driving motivation for this research. An autonomous flight control strategy is then presented. The dimensioning strategy, from chapter 2, is then used to design a suitable hovering platform for this application. A performance comparison between the developed platform and commercially available platforms is then shown. The chapter ends by demonstrating that the developed platform, when fitted with the 3-D relative positioning sensor, is capable of goal-directed autonomous indoor flight and collective deployment of highly dynamic flying robots.

- **Chapter 7: *Conclusion***

This thesis is concluded with a discussion of the main accomplishments and their significance, as well as the limitations of the proposed methods and the possibility for future work.

---

<sup>12</sup><http://www.swarmanoid.org> (accessed Feb. 2011)



---

# 2

---

## Hovering platform design

---

**I**N order to carry the additional sensing required for indoor collective operation, including relative positioning sensing and embedded processing, it is necessary first to understand how to fabricate an efficient indoor hovering platform. In the introduction, table 1.1 has indicated that there are a limited amount of commercially available platforms suitable for indoor operation. Out of this limited few, they are either too large to fly through doorways, or they have a payload limited to a maximum of  $\approx 370$  g including rotor protection (see table 1.1), with a platform size that leaves only  $\pm 10$  cm doorway clearance (based on a standard doorway size of 100 cm). However, the development of a hovering platform is a complex task requiring interdisciplinary skills in electronics, aerodynamics, control theory, mechanics and systems integration. This chapter introduces a generalised design strategy for dimensioning a hovering platform for a specific flight endurance, payload capability and robustness criteria. The dimensioning strategy is then used to design three different hovering platforms optimised for each criteria. Two of these platforms will later be used to develop stability controllers and suitable on-board sensing for indoor collective operation. The chapter ends by showing a performance comparison between the three developed platforms against the commercially available platforms.



## 2.1 Introduction

This chapter introduces a generalised design strategy for producing efficient hovering platforms tailored to a specific flight endurance, payload and robustness criteria, within the indoor size constraints (<100 cm). However, there is a compromise between these three criteria, which is strongly related to the physical aspects of the electric motors, propellers and structural design.

The first commutator-type Direct Current (DC) electric motor was invented by the British scientist William Sturgeon in 1832 (Cavendish, 2008). Commutator motors, as shown in figure 2.1<sup>1</sup> *left*, use spring loaded brushes (conductive pads) that carry the electrical current to a motors rotating armature. The commutator takes care of switching the electrical current at the exact timing required to produce a consistent rotational torque. This mechanical connection between the rotating and non-rotating parts of an electric motor introduces efficiency losses and mechanical wear. Thus, brushed motors typically have an efficiency, which can reduce as the brushes wear down. However, as the commutator takes care of the electrical switching, the speed of a brushed DC motor can be controlled using a simple transistor and a Pulse-Width-Modulated (PWM) signal. Due to this simple control and reduced cost, many devices today still operate using these motors.

The efficiency and mechanical wear limitations of a brushed motor have been overcome in 1962, by the invention of brushless motors (Wilson and Trickey, 1962). A brushless motor, shown in figure 2.1<sup>2</sup> *right*, as the name implies has no mechanical brushes, thus they are capable of reaching efficiencies of 80-90%. However, the increased efficiency of a brushless motor has come at a cost of more complex and expensive control electronics. The speed of a brushless DC motor must be controlled electrically by a three-phase controller. Therefore, for the highest possible propulsion efficiency, a brushless motor with a more complex controller is desirable.

The torque produced by a motor and propeller when operating, introduces a rotational force that needs to be canceled in order to stabilise the yaw component of the hovering platform (see section 3.2.4). Quad-rotor hovering platforms with four single brushless motors, like the one shown in figure 2.2 *left*, balance the

---

<sup>1</sup>[http://en.wikipedia.org/wiki/File:Electric\\_motor\\_cycle\\_1.png](http://en.wikipedia.org/wiki/File:Electric_motor_cycle_1.png) (accessed Feb. 2011)

<sup>2</sup><http://www.stevensaero.com> (accessed Feb. 2011)

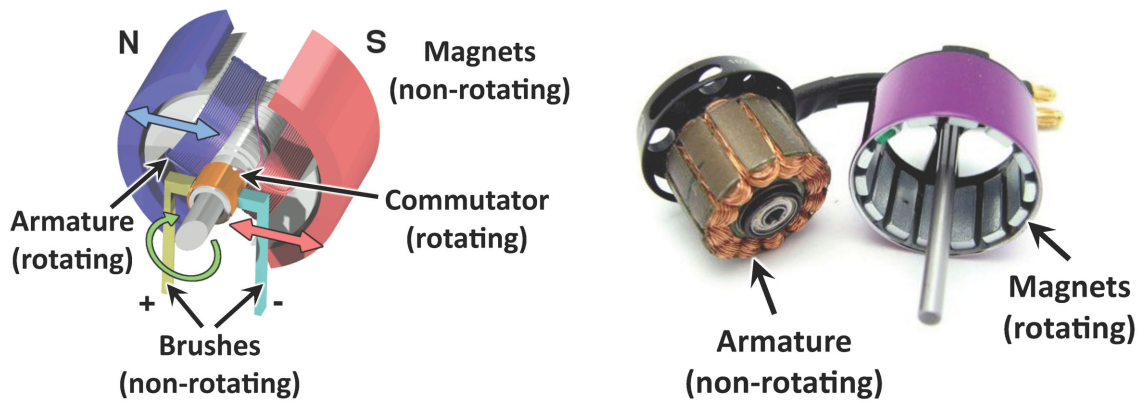


Figure 2.1: Internal workings of a brushed (*right*) and brushless (*right*) dc motor

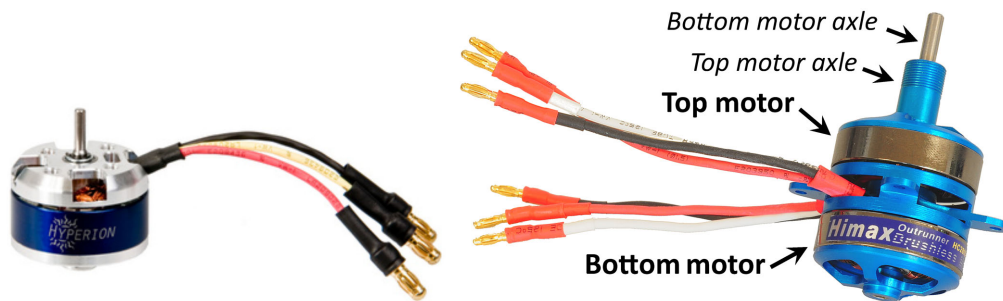


Figure 2.2: *Left*: Single brushless motor (Hyperion HP-2205/46). *Right*: Coaxial brushless motor (Himax CR2805)

four motor torques using two pairs of counter rotating propellers at alternate ends of the platform (see section 3.2.4). Recent developments with brushless motor design has produced a new breed of coaxial motor. A coaxial motor, as shown in figure 2.2 *right*, consists of two single motors that share a common axis. The two motors are mechanically coupled, where the bottom motor axle protrudes through the centre of the top motor. In the coaxial configuration, with two counter-rotating propellers, the torque produced from one motor and propeller can cancel the torque of the other. Therefore, creating a pure thrust force with minimal rotational components.

The literature states that counter-rotating propellers in a coaxial arrangement, allow for almost twice the thrust when compared to a single propeller with the same diameter, at the cost of approximately 22% increase in induced power for the same given thrust (Leishman, 2006). The power of each motor is related to the separation distance, when the torques between the two propellers are balanced. For a given thrust, altering the separation distance alters only the thrust

sharing ratios between the two propellers. The separation distance between the top and bottom propeller should be as small as possible in order to keep the power of the two motors equal (Coleman, 1997). However, the distance must be large enough to prevent the propellers from flexing and colliding with one another. Therefore, a brushless coaxial motor when compared to a single motor, can provide superior thrust performance with a small compromise in overall efficiency.

The performance of a propeller is influenced by both its shape and rigidity. There are several different types of propellers, shown in figure 2.3, designed for different applications, including the sport, thin-electric and slow-fly varieties made from composite material, and the static-thrust variety made from flexible nylon. Sport propellers are designed for a high rpm (max. rpm = 190K/diameter in inches<sup>3</sup>) and are optimised for fast flight speeds, thus they are not suitable for hovering platforms. Thin-electric propellers are designed for a medium rpm (max. rpm = 145K/diameter in inches) and are optimised for medium to slow flight speeds. Slow-fly propellers are designed for a low rpm (max. rpm = 65K/diameter in inches) and are optimised for slow to hovering flight speeds. Whereas, flexible static-thrust propellers are designed for a low rpm during hovering and are optimised for consumer safety. Generally, the width of the blade chord increases as the rpm specification decreases, in order to achieve optimal thrust generation at a lower rpm. Additionally, the blades tend to become thinner as the rpm specification decreases, thus reducing the propellers rigidity and weight. Therefore, the slow-fly and static-thrust propeller varieties should provide a higher thrust efficiency while hovering, where the induced velocity of the propeller is low.

A propeller when producing thrust will have a tendency to bend towards the direction of the produced force. This phenomena is called the propeller coning effect (Federal-Aviation-Administration, 2007). As the coning effect occurs, the pitch on the blades will reduce and produce less thrust. Therefore, flexible static-thrust propellers at a higher disk loading, will have a reduced performance when compared to rigid propellers. However, a flexible propeller will cone and twist to an equilibrium at a large range of speeds. This automatic equilibrium has a tendency of dampening the propellers dynamics and reducing vibration. A

---

<sup>3</sup>[http://www.apcprop.com/v/html/rpm\\_limits.html](http://www.apcprop.com/v/html/rpm_limits.html) (accessed Feb. 2011)



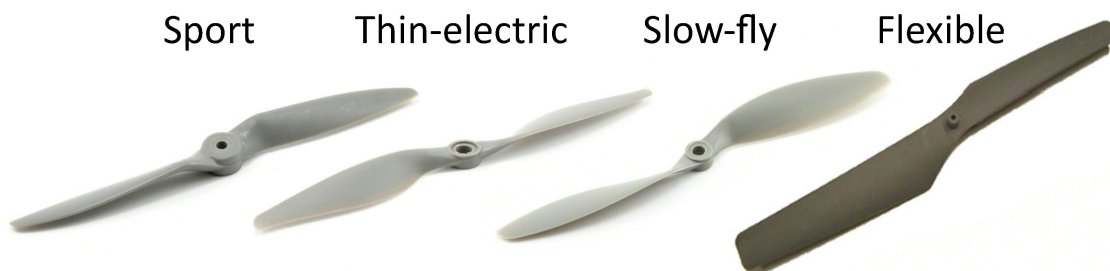


Figure 2.3: Different types of propeller varieties, from a high rigidity to high flexibility (*left to right*)

reduction in vibration is beneficial for the inertial sensors, in order to reduce attitude estimation noise while flying. A flexible propeller is also less dangerous for people, which is a preferred compromise for hovering platforms, such as the AR-Drone and Hummingbird (see chapter 1, figure 1.1). Therefore, a flexible static-thrust propeller is good for low payload and high safety requirements, whereas a rigid propeller is good for high payload requirements. However, with a rigid propeller, vibration isolation needs to be considered.

A coaxial counter-rotating propeller arrangement will have two mechanical resonant frequencies. Typically, the top and bottom propeller speeds will be different when the torque of each is balanced. This is due to the induced velocity being higher on the lower propeller, when inside the wake of the top propeller (Coleman, 1997). Meaning that as the speed changes, the harmonics of the propulsion system will vibrate over a large range of frequencies. Therefore, when using rigid propellers especially in a coaxial arrangement, vibration isolation is imperative for clean inertial sensing.

The only way to determine if a motor and propeller are a good combination is to perform static thrust tests. The thrust curve for different motor and propeller combinations can be performed using a thrust testing rig (see chapter 4, section 4.3.1). The thrust curve of each is a good comparative measure to find the best performing combination that matches the desired propeller-motor efficiency for the application. This propulsion system efficiency and the amount of battery capacity, will determine the flight endurance of the platform.

Now that a reasonable understanding about the propulsion system of an indoor hovering platform is in place, the next thing to consider is the structural design. The structural design of a hovering platform is also important. Every gram of extra weight added to the platform, which is not battery weight, equates

to a loss of endurance, thus the structure should be as light as possible. However, the structure must also be strong enough to support the propulsion system and robust enough to withstand small collisions and hard landings. The structure can be fabricated for a desired application. For example, if a highly robust platform is required, then the structure must be stronger. This implies that a highly robust platform will have a higher structural weight. A high level of mechanical design is required to create strong and light-weight structures that can withstand the high impact forces that a flying system typically encounters.

One of the lightest and strongest materials suitable for the platforms structure is carbon fibre. Carbon fibre material consists of thin fibres (5-10  $\mu\text{m}$ ) that are composed mostly of carbon atoms. The high strength of carbon fibre is due to the microscopic crystal structure formed by carbon bonded atoms, which are parallel to the fibre length. A high strength-to-weight ( $\text{MPa}: 1400, \text{Density}: 1.55 \text{ g/cm}^3$ )<sup>4</sup> ratio is achieved by combining several thousand fibres into a yarn, which is then woven into a fabric. The carbon fabric can be combined with plastic resin to form a composite material. However, carbon fibre is weak when compressed or exposed to high impact forces. For example, a carbon fibre square tube, as shown in figure 2.4 *left*, is extremely strong in the long axis because of the uni-directional fibres, but it will easily crack if hit with a hammer. Additionally, carbon fibre is expensive, thus it may not be suitable for a cheap and robust testing platform. Fibre-glass plating, as shown in figure 2.4 *right*, is a material with bi-directional fibres that is more resilient to cracking than carbon fibre. However, its strength-to-weight ( $\text{MPa}: 900, \text{Density}: 2 \text{ g/cm}^3$ )<sup>5</sup> ratio is not as good as carbon fibre. As fibre-glass (FR4) is used to fabricate Printed Circuit Boards, the material can be easily cut to any desired 2-D shape. Thus, fibre-glass can be used if a cheaper, more robust platform is desired, at the cost of an increased structural weight.

This section has shown that there is a compromise between the flight endurance, payload capability and robustness of a hovering platform. Which is strongly related to the physical aspects of the electric motors, propellers and structural design. The objective of the following section is to create a method of accurately dimensioning a hovering platform, based on a measured propeller efficiency (figure of merit) and modelling the interactions between these physical

---

<sup>4</sup><http://www.swiss-composite.ch> (accessed Feb. 2011)

<sup>5</sup><http://www.swiss-composite.ch> (accessed Feb. 2011)

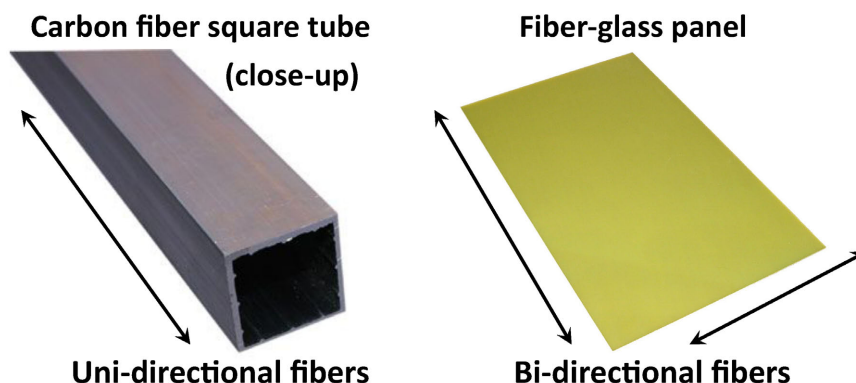


Figure 2.4: Carbon-fibre rectangular bar (*left*) and fibre glass plating (*right*), showing the direction of the fibres

aspects.

## 2.2 Materials and methods

This section describes a method to dimension a hovering platform for a specific payload, flight endurance and robustness criteria. As the method relies on a realistic figure of merit, the figure of merit has then been determined for the three different propeller varieties (flexible, slow-fly and thin-electric), which have been deemed useful for indoor hovering platforms.

### 2.2.1 Platform dimensioning method

This dimensioning method utilises Momentum theory and a quad-rotor dimensioning model in order to determine the relationship between platform size, battery weight and propeller-motor efficiency. The propeller-motor efficiency is determined by Momentum theory, which relies on a realistic figure of merit efficiency. This figure of merit efficiency relates directly to the type and size of propeller used. By adjusting the payload and battery weight, an estimated structural weight can be determined and the platform can be optimised for a specific payload, endurance and robustness criteria. As the the thrust generation model is incorporated within the Momentum theory, this simple method does not require detailed analysis of the propeller blades, in order to design a suitable hovering platform for a specific application.

The dimensioning method assumes that the design is constrained to a quad-rotor configuration. This has been chosen due to the high controllability of such a platform, which will later aid in achieving autonomous indoor flight. However, a coaxial helicopter arrangement would be more efficient in terms of thrust generation, due to the larger possible propellers within a given maximum diameter.

In order to estimate the platform size based on a specific payload, flight endurance and robustness<sup>6</sup> requirement, first the weight of the platform must be estimated. This can be achieved by using the information that has been gathered in chapter 1, table 1.1, about commercially available platforms. The typical payload loading ( $L_p$ : ratio between the maximum payload and take-off weight) ranges from 14% to 40%. These values can be used as a guide to determine a realistic goal for the take-off weight ( $m_t$ ) of a new platform given a desired payload requirement ( $m_p$ ):

$$m_t = \frac{m_p}{L_p} \quad (2.1)$$

Using a higher payload loading will enforce a compromise between a higher payload capability and a reduced flight endurance.

The next step is to find a realistic platform diameter ( $d_1$ ) to lift the given platform weight ( $m_t$ ) for a desired flight endurance ( $t_f$ ). For a coaxial helicopter, the platform diameter ( $d_1$ ) is directly related to the size of the rotors, thus the propeller disk area ( $A$ ) can be determined directly (Equation 2.4,  $d_1 = d_2$ ). However, for a quad-rotor configuration, shown in figure 2.5, the platform diameter ( $d_1$ ) does not define exactly the area used by the propellers. The propeller diameter ( $d_2$ ), leaving some clearance (5%) around the perimeter for rotor protection, based on simple geometry can be estimated by:

$$d_2 = d_1/2.8 \quad (2.2)$$

Similarly, the centre diameter ( $d_3$ ), which can be used for avionics and battery space, can then be estimated by:

$$d_3 = d_1/6.25 \quad (2.3)$$

---

<sup>6</sup>Robustness: additional weight and size of the platform structure, in order to increase strength and provide propeller protection

The propeller disk area ( $A$ ) can then be determined using the propeller diameter ( $d_2$ ) and the number of rotors ( $n_r$ ) :

$$A = n_r \pi \left( \frac{d_2}{2} \right)^2 \quad (2.4)$$

where,  $n_r$  is equal to 4 for a typical quad-rotor configuration. Note that as the propeller radius increases, the possible area that can be used for propulsion increases quadratically.

Momentum Theory can be used to explain the relationship between propeller thrust ( $T$ ), the ideal power required to hover ( $P_i$ ) and the induced velocity ( $v_i$ ) at the propeller disk, using the following equations (Leishman, 2006):

$$T = 2\rho A v_i^2, \quad V_i = \frac{P_i}{T} \quad (2.5)$$

where  $\rho$  is the density of air at a given altitude and  $A$  is the propeller disk area.

Assuming that the static thrust required to hover ( $T$ ) is equal to the weight of the platform ( $m_t$ ), the ideal power required to hover ( $P_i$ ) can then be estimated by rearranging equation 2.5 and replacing  $T$  by  $m_t$ :

$$P_i = m_t \sqrt{\frac{m_t}{2\rho A}} \quad (2.6)$$

The actual power required to hover ( $P_a$ ) for a single propeller is then determined using the figure of merit ( $FM$ ):

$$P_a = \frac{P_i}{FM} \quad (2.7)$$

There is a limited amount of data available in the literature, to accurately predict the figure of merit for the size and variety of propellers that are suitable for indoor hovering platforms. Therefore, a realistic figure of merit will be proposed in section 2.2.2.

The flight endurance is a function of the propeller-motor efficiency and battery capacity. The propeller-motor efficiency ( $\eta$ ), corresponds to the platform weight ( $m_t$ ) and the actual power required to hover ( $P_a$ ):

$$\eta = \frac{m_t}{P_a} \quad (2.8)$$

The battery capacity ( $c_b$ ) can be calculated using the actual power required to hover ( $P_a$ ) and the desired flight endurance ( $t_f$  in hours):

$$c_b = t_f P_a \quad (2.9)$$

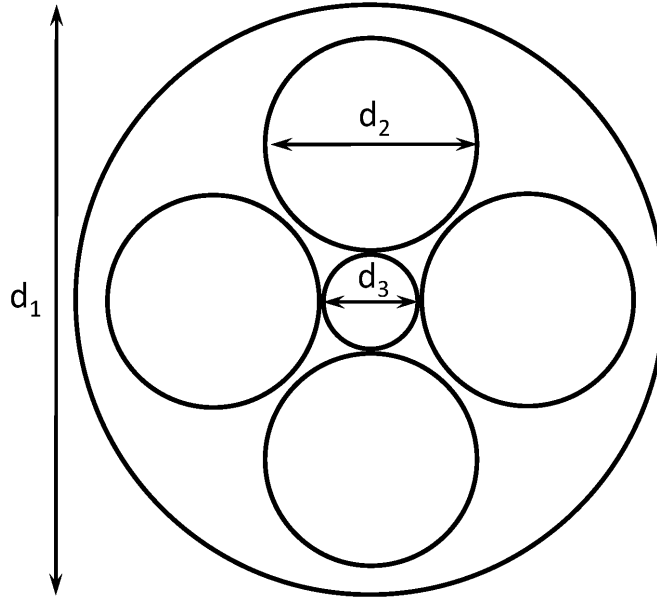


Figure 2.5: Typical quad-rotor configuration (*top-down*) showing the platform diameter ( $d_1$ ), propeller diameter ( $d_2$ ) and centre diameter ( $d_3$ ), with a 5% propeller clearance

This allows for the battery weight to be estimated using the specific energy density of the current Lithium Polymer battery technology:

$$m_b = \frac{c_b}{e_d} \quad (2.10)$$

where  $e_d$  is equal to 172 Wh/kg.

As both  $\eta$  and  $c_b$  change with respect to the platform diameter ( $d_1$ ), it is necessary to estimate the battery loading ( $L_b$ : ratio between the battery and take-off weight) to determine the platform size. The typical battery loading from chapter 1, table 1.1, ranges from 12% to 38%. This can be used as a guide to determine a realistic goal for the battery weight. In order to increase the robustness of the platform, the battery weight can be substituted for additional platform weight, thus reducing the battery loading ( $L_b$ ). The battery loading with respect to the platform weight ( $m_t$ ) is then indicated by:

$$L_b = \frac{m_b}{m_t - m_p} \quad (2.11)$$

The structure weight ( $m_s$ ) is then determined by the remaining weight left over after the payload ( $m_p$ ) and battery ( $m_b$ ) have been defined:

$$m_s = m_t - m_p - m_b \quad (2.12)$$

The relationship between the size of the platform, flight endurance, payload and robustness has been defined and formulated in a way that can be used directly as a design tool. This tool can be used to develop new hovering platforms for a specific criteria. However, before this is possible a realistic propeller figure of merit needs to be determined.

### 2.2.2 Realistic propeller figure of merit

The static thrust efficiency of a propeller, also known as the Figure of Merit ( $FM$ ), is defined by the ratio of the ideal power ( $P_i$ ) and the actual power ( $P_a$ ) required to hover (Leishman, 2006). The literature states that a well-designed propeller can achieve a  $FM$  ranging from 0.55 to 0.8, corresponding to a small propeller (7.5 cm diameter) to a full sized helicopter (several meters) respectively (Liu and Moschetta, 2009; Coleman, 1997; Leishman and Ananthan, 2006; Leishman, 2006). However, the information available for the propeller varieties that are suitable for indoor hovering platforms is limited.

In order to determine a realistic figure of merit ( $FM$ ), it is necessary to perform some static-thrust tests on real propellers. For the figure of merit to be a realistic representation of the actual propeller efficiency, the efficiency losses of the motor need to be minimised. Therefore, it is necessary to find the most efficient combination of motor and propeller, which minimises the power consumption introduced by the motor. The high-efficiency brushless motor ( $HP-2205/46$ ) that has been used was tested for a large range of propeller sizes and pitches, the best of these was used in the determining the figure of merit.

The figure of merit, shown in figure 2.6, has been determined using the calculated ideal power ( $P_i$  from equation 2.6) and the measured actual power ( $P_a$ ) for the thin-electric, slow-fly and flexible static-thrust propellers, over their full range of thrusts. Analysing the data shows that the  $FM$  is much lower than the literature states. Generally, for each propeller the  $FM$  slowly rises to until it reaches a maximum value, this value is used as the determined  $FM$ . For the flexible static-thrust propeller, the  $FM$  is equal to 0.23, which indicates that it is the lowest of the three varieties. The  $FM$  drops significantly above 175 g of thrust, this is due to the propellers high-flexibility and the coning effect as discussed in section 2.1. For the slow-fly and the thin-electric propellers, the  $FM$  is equal to 0.36 and 0.37 respectively, which is a significant increase when compared to the flexible propeller. The  $FM$  is very constant even for the higher thrust values,

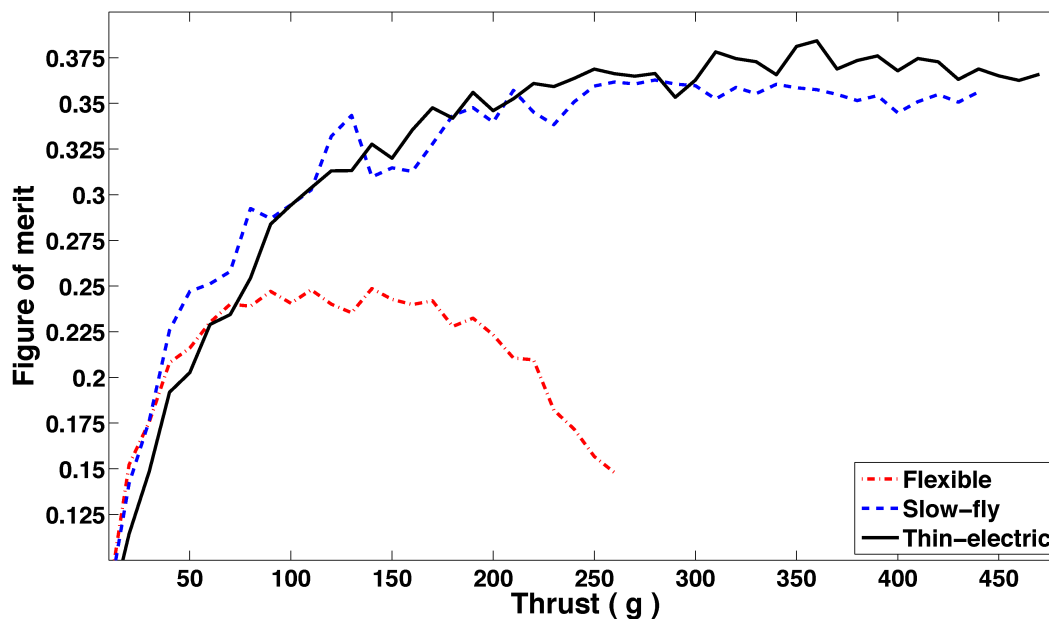


Figure 2.6: Figure of merit determined from the calculated ideal power ( $P_i$ ) and the measured actual power ( $P_a$ ), for the three different propeller varieties

therefore the coning effect does not appear to be apparent at these disk loadings.

Similarly, the figure of merit, shown in figure 2.6, has been determined for a single and coaxial propeller arrangement. The thin-electric propeller variety has been used in both cases, as this is more suitable for higher disk loadings as discussed in section 2.1. The chosen motor and propeller was the Himax CR2805 and APC 7x5 inch, respectively. In the case of the single propeller only the top motor is used. Analysing the data, shows that the  $FM$  for the single thin-electric propeller is the same as the previous test (0.37). This reinforces that the change in motor, propeller size and pitch have a smaller effect than changing the propeller shape and material. For the coaxial propeller arrangement, the  $FM$  is equal to 0.39, which is a slight improvement over the single propeller.

At the lower thrust levels (below 200 g), the  $FM$  for the coaxial propeller is 22% lower than that of the single propeller. This is exactly what the literature states about coaxial propellers as discussed in section 2.1. However, it is interesting that at higher thrust levels (above 280 g), the  $FM$  for both propeller types becomes fairly equal. Thus, at higher thrust loadings the 22% power increase of a coaxial propeller is no longer observable.

In conclusion a realistic figure of merit ( $FM$ ) has been determined for the three different propellers that are suitable for indoor hovering platforms. For



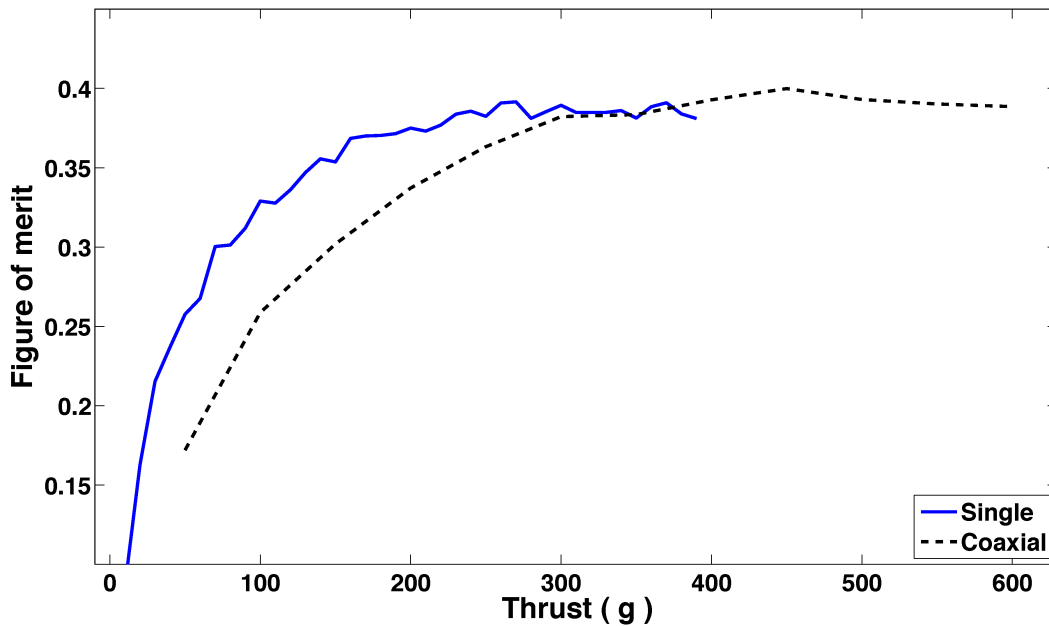


Figure 2.7: Figure of merit determined from the calculated ideal power ( $P_i$ ) and the measured actual power ( $P_a$ ), for a single and coaxial propeller arrangement

the flexible, slow-fly, thin-electric and coaxial (thin-electric), the  $FM$  is equal to 0.23, 0.36, 0.37 and 0.39, respectively. These  $FM$  values can now be implemented to determine a realistic platform design, using the developed dimensioning methodology.

## 2.3 Results

In order to demonstrate that the proposed dimensioning method can be used to construct real hovering platforms catered to a specific capability. Three example designs are implemented to show the difference between hovering platforms optimised for robustness, flight endurance and payload capability, respectively. Finally, a performance comparison between the fabricated platforms and the commercially available platforms is presented.

### 2.3.1 Optimising for robustness

On an indoor hovering platform, there is a high level of risk involved when developing new sensing and control strategies. Therefore, it is imperative that a hovering platform that has been developed for testing purposes, has a high-

degree of mechanical robustness, especially during the stability control development. This facilitates a rapid sensing and control development at a reduced risk and loss of time for repairs. The low number of moving parts of a quad-rotor, when compared to a conventional helicopter, creates an ideal platform for robust indoor operation.

In order to develop a robust hovering platform, the structure needs to be strong, which implies that a higher structural weight is required. A suitable material for this would be fibre-glass plating, as discussed in section 2.1. This will allow the platform to withstand higher impact forces, however the battery weight will have to be substituted for the additional structure weight. Flexible propellers would be a good choice for the propulsion system as they are more robust than the composite variety and are safe to operate. From chapter 1, table 1.1, the commercial platforms using flexible propellers, have a payload of approximately between 100 g-200 g, with a flight endurance of 15 min-20 min (with no payload). Therefore, given the additional weight required for a robust structure, a flight endurance of 10 min with a payload of 100 g has been chosen. This is enough payload to allow for some additional sensors that will be required for autonomous flight testing (see chapter 3). Note that this should be kept low as the flexible propellers are suitable only for a low thrust loading (see section 2.2.2).

The dimensioning method, presented in section 2.2.1, can now be used to determine the recommended size of the hovering platform. The platform weight can be estimated, using equation 2.1, based on the 100 g payload requirement and a 18% payload loading. A low payload loading is used to optimise for the flexible static-thrust propellers. This gives an estimated platform weight of 555 g. For a quad-rotor configuration this implies that each motor must be capable of producing a thrust of at least 139 g. As the platform will be optimised for robustness, the structure will have a higher weight, thus a small 16% battery loading has been chosen.

For this specific flight endurance and payload requirement, a realistic range of propeller-motor efficiencies, shown in figure 2.8 *left*, corresponding to various platform sizes can be determined using equation 2.2 through equation 2.8. This is based on the chosen 100 g payload and a FM of 0.24 for the flexible propellers (see section 2.2.2). Additionally, a realistic range of battery weights, shown in figure 2.8 *right*, corresponding to various platform sizes can be determined using

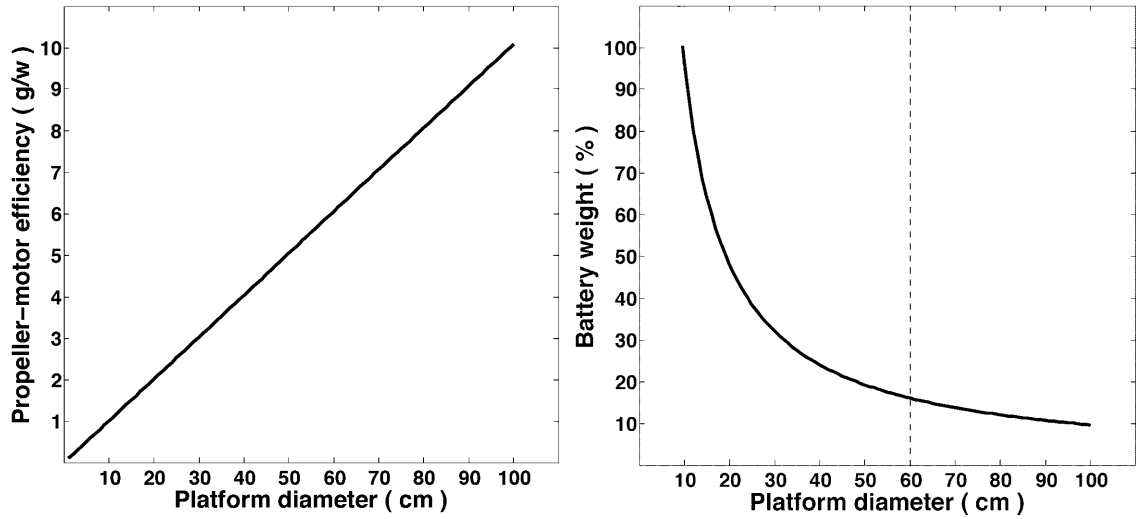


Figure 2.8: High-robustness design. *Left*: Estimated propeller-motor efficiency with respect to the platform diameter. *Right*: Estimated battery weight with respect to the platform diameter. The dotted line indicates the recommended platform size, which is selected using the desired battery loading ( $m_p = 100$  g,  $FM = 0.24$  (flexible propellers),  $L_p = 18\%$ ,  $L_b = 16\%$ )

equation 2.8 through equation 2.11.

Based on the desired 16% battery loading, an estimated platform size of 60 cm in diameter with a propeller diameter of 20 cm, would be suitable for a robust hovering platform. In order to implement this in reality, a motor that is capable of producing at least 139 g of thrust with a propeller-motor efficiency equal to  $\approx 6.0$  g/W would be required. The dimensioning method also indicates that the goal structure weight should be approximately 367 g and the goal battery weight should be approximately 89 g to achieve the desired 10 min flight endurance. The hovering platform weight distribution, shown in chart 2.1, indicates that some of the battery and payload is substituted to create a stronger structure.

### 2.3.2 Optimising for high-endurance

Naturally, an indoor hovering platform that is capable of a long flight endurance is desirable to improve the practicality of a flying robot. In order to develop a high endurance hovering platform, the structure needs to be as light as possible so that the size of the battery can be increased. A suitable material for this would be carbon fibre, as discussed in section 2.1. The maximum flight endurance of

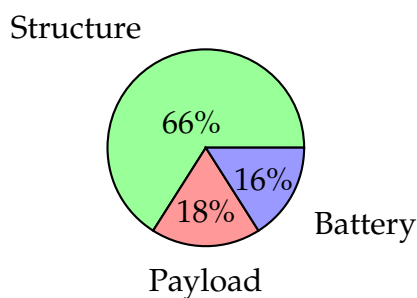


Chart 2.1: Weight distribution of the robustness optimised hovering platform

the commercial platforms is 30 min (see chapter 1, table 1.1) with no payload. Thus, a flight endurance of 30 min has been chosen as the goal flight endurance with a small payload of 25 g. Thin-electric propellers would be a good choice for the propulsion system as they produce the highest FM.

The dimensioning method, presented in section 2.2.1, can now be used to determine the recommended size of the hovering platform. The platform weight can be estimated, using equation 2.1, based on the 25 g payload requirement and a 5% payload loading. A very low payload loading is used to optimise for the flight time. This gives an estimated platform weight of 500 g. For a quad-rotor configuration this implies that each motor must be capable of producing a thrust of at least 125 g. As the platform will be optimised for endurance, the structure will need to be very light weight with a large battery, thus a 34% battery loading has been chosen.

For this specific flight endurance and payload requirement, a realistic range of propeller-motor efficiencies, shown in figure 2.9 *left*, corresponding to various platform sizes can be determined using equation 2.2 through equation 2.8. This is based on the chosen 25 g payload and a FM of 0.32 for the thin-electric propellers at the 125 g thrust (see section 2.2.2). Additionally, a realistic range of battery weights, shown in figure 2.9 *right*, corresponding to various platform sizes can be determined using equation 2.8 through equation 2.11.

Based on the desired 34% battery loading, an estimated platform size of 60 cm in diameter with a propeller diameter of 20 cm, would be suitable for a high-endurance hovering platform. In order to implement this in reality, a motor that is capable of producing at least 125 g of thrust with a propeller-motor efficiency equal to  $\approx 8.5$  g/W would be required. The dimensioning method also indicates that the goal structure weight should be approximately 300 g and the goal bat-

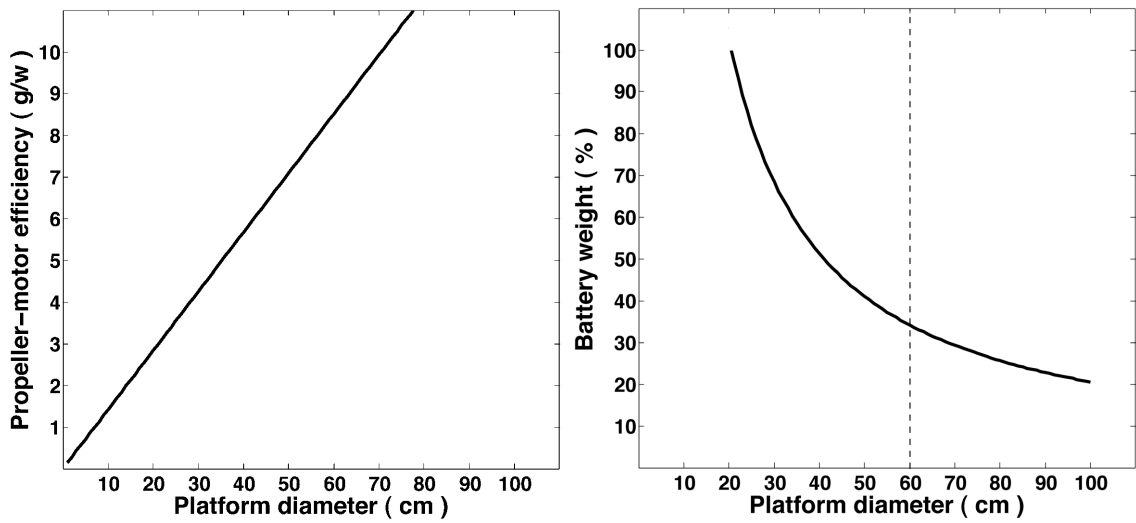


Figure 2.9: High-endurance design. *Left*: Estimated propeller-motor efficiency with respect to the platform diameter. *Right*: Estimated battery weight with respect to the platform diameter. The dotted line indicates the recommended platform size, which is selected using the desired battery loading ( $m_p = 25$  g,  $FM = 0.32$  (thin-electric propellers at  $T = 125$  g),  $L_p = 5\%$ ,  $L_b = 34\%$ )

tery weight should be approximately 170 g, to achieve the desired 30 min flight endurance. The hovering platform weight distribution, shown in chart 2.2, indicates that some of the structure and most of the payload is substituted for more battery to increase the endurance.

### 2.3.3 Optimising for high-payload

A high-payload capability is probably the most difficult and most desirable feature of an indoor hovering platform. A high-payload equates to an ability to

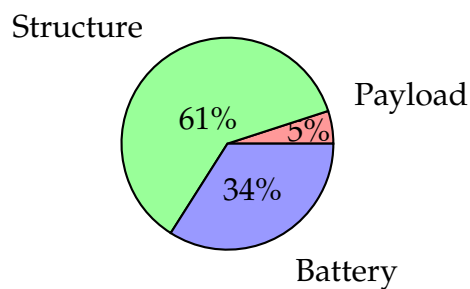


Chart 2.2: Weight distribution of the endurance optimised hovering platform

carry better sensing and processing power. For collective flying robots, this is a very important feature as they additionally need to carry the sensors for relative positioning sensing. In order to develop a high-payload capable indoor hovering platform, the propulsion system needs to have a high thrust capability within a small size. This implies that the structure needs to be strong enough to support the high thrust forces. A suitable material for this would be carbon fibre, as discussed in section 2.1. Additionally, to support the high power required by the high thrust propulsion system, a large battery must be used, thus the platform weight will be high. To keep the size of the platform small, a reasonable flight endurance for a high payload platform has been chosen as 10 min. A coaxial motor with counter-rotating thin-electric propellers would be a good choice for the propulsion system, as they can handle a high thrust and an increased thrust loading (see section 2.2.2). To allow for an envisioned relative-positioning sensor, additional sensors and processing capability, the platform payload capability can be defined as 1000 g.

The dimensioning method, presented in section 2.2.1, can now be used to determine the recommended size of the hovering platform. The platform weight can be estimated, using equation 2.1, based on the 1000 g payload requirement and a 50% payload loading. The high payload loading is used to optimise for the payload and the coaxial counter-rotating propellers. This gives an estimated platform weight of 2000 g. For a quad-rotor configuration this implies that each motor must be capable of producing a thrust of at least 500 g. As the platform will be optimised for a high-payload, the structure will need to be as light as possible yet strong, thus a medium 22% battery loading has been chosen.

For this specific flight endurance and payload requirement, a realistic range of propeller-motor efficiencies, shown in figure 2.10 *left*, corresponding to various platform sizes can be determined using equation 2.2 through equation 2.8. This is based on the chosen 1000 g payload and a FM of 0.39 for the coaxial counter-rotating thin-electric propellers (see section 2.2.2). Additionally, a realistic range of battery weights, shown in figure 2.10 *right*, corresponding to various platform sizes can be determined using equation 2.8 through equation 2.11.

Based on the desired 22% battery loading, an estimated platform size of 50 cm in diameter with a propeller diameter of 18 cm, would be suitable for a high-payload hovering platform. In order to implement this in reality, a coaxial motor that is capable of producing at least 500 g of thrust with a propeller-motor

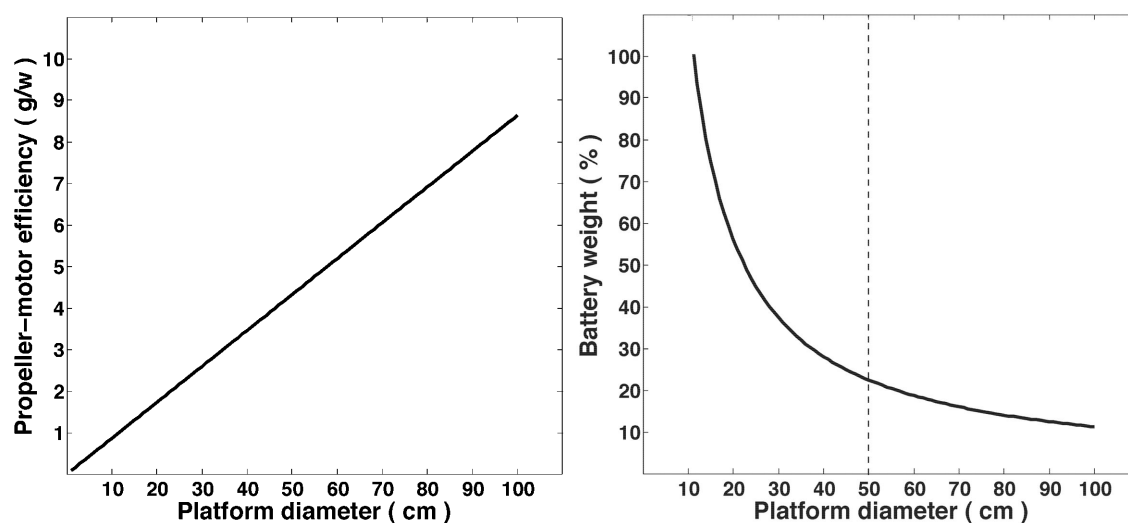


Figure 2.10: High-payload design. *Left*: Estimated propeller-motor efficiency with respect to the platform diameter. *Right*: Estimated battery weight with respect to the platform diameter. The dotted line indicates the recommended platform size, which is selected using the desired battery loading ( $m_p = 1000$  g,  $FM = 0.39$  (coaxial thin-electric propellers),  $L_p = 50\%$ ,  $L_b = 22\%$ )

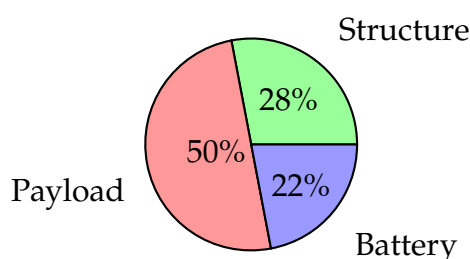


Chart 2.3: Weight distribution of the payload optimised hovering platform

efficiency equal to  $\approx 4.3$  g/W would be required. The dimensioning method also indicates that the goal structure weight should be approximately 552 g and the goal battery weight should be approximately 449 g, to achieve the desired 10 min flight endurance. The hovering platform weight distribution, shown in chart 2.3, indicates that the structure and battery are reduced to increase the payload capability.

### 2.3.4 Robustness optimised hovering platform

The robustness of the hovering platform has been increased by using materials that have a high impact strength and are able to flex slightly to absorb the impact. Flexible propellers are used so that they do not snap during a collision.

In order to minimise the effort and hardware skills required for hovering platform realisation, the use of Printed Circuit Board (PCB) fabrication techniques has been used to construct the robustness optimised hovering platform. The PCB rapid prototyping technique allows for a tight integration between the structure, electronics and sensors, in order to minimise wiring, reduce human labour and improve manufacturability.

Fibre-glass panels, as discussed in section 2.1, is a good choice of material for a robust indoor hovering platform. However, it is heavier when compared to carbon fibre. Fibre-glass, laminated with thin ( $\approx 35$   $\mu\text{m}$ ) copper layers (FR4), is the main material that is used to fabricate PCBs. This material allows for electrical connections to be routed directly onto a flat board. Traditionally, these boards are cut into unstructured rectangular shapes. However, the Computerised Numerically Controlled (CNC) machines that are used to cut these boards, are capable of cutting any 2-D shape with a high degree of precision ( $< 1$  mm). Using jigsaw-like construction and a bit of creativity in the computer design phase, a 3-D structure can be created from these 2-D laminated boards. This technique allows for sensors and electronics to be directly embedded into the structure of the flying robot, with minimal effort.

This technique has been used to rapidly construct the robustness optimised platform structure, shown in figure 2.11. The entire body is fabricated from 0.8 mm thick PCB with the motor connections directly routed into the four arms. The 2-D pieces tightly connect together and are fixed using epoxy glue. The holes for fixing the motors and other parts are pre-drilled during in the PCB fabrication process, so that all the pieces can be assembled easily. The structure already includes all the electrical connections, thus minimising the wiring. The quad-rotor arms are extended out to support a carbon fibre ring that allows the flying robot to survive small collisions with walls and other large objects including people. The platform is designed so that the avionics can be stacked in its centre with minimal effort. After receiving the boards from a PCB manufacture, the structure assembly process can be completed in a matter of minutes.

The chosen motor and propeller was the Hyperion *HP-2205/46* and X-UFO



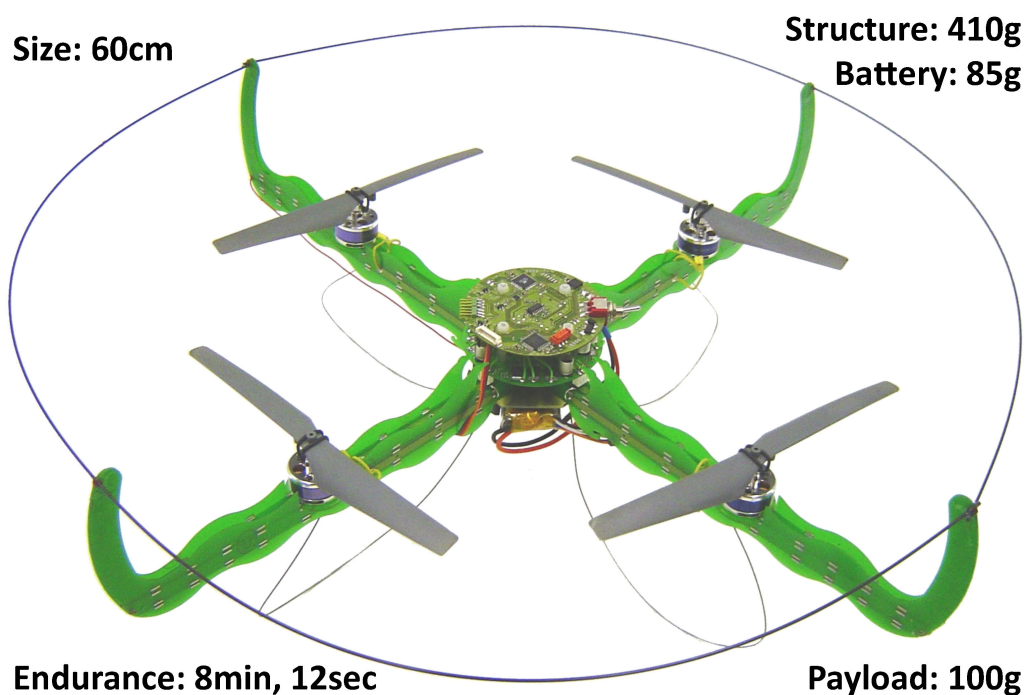


Figure 2.11: Hovering platform optimised for a high robustness against collisions

8 inch, respectively. The thrust curve for this motor and propeller combination is shown in figure 2.12. At the hover point thrust, which is defined as 1/4 of the platform weight (149 g), the motor-propeller efficiency can be determined. Notice that the hover point is in the middle of the thrust range, which is the optimal point for high reliability and a good compromise between payload and endurance capability.

Table 2.1 shows a comparison between the predicted dimensioning design and the real constructed, robustness optimised hovering platform. The design strategy is very similar to the real performance, with the diameter and payload matching exactly. The motor-propeller efficiency is 0.3 g/W lower, the structure weight is 43 g heavier and the battery that was used is 4 g lighter than the envisioned design. This is the main reason for the 1 min 48 sec reduction in the flight endurance. Additionally, the design strategy does not take into account the power consumption of the avionics, which would also contribute to a slight reduction in the flight endurance. For a comparative measure that will be used in section 2.3.7, the flight endurance without the 100 g payload is 11 min.

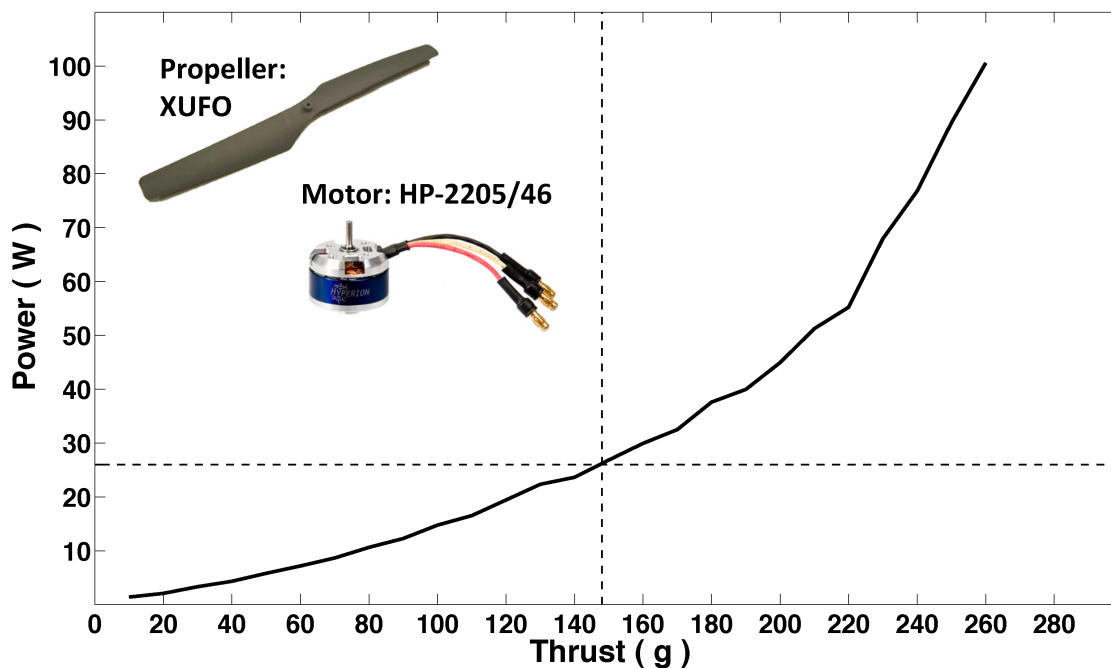


Figure 2.12: Thrust curve of the Hyperion *HP-2205/46* motor with a X-UFO 8 inch propeller. The dotted lines indicate the hover point thrust and power

Table 2.1: Comparison between the high-robustness dimensioning design and the real hovering platform performance

	Diameter	Endurance	Motor-propeller Efficiency	Payload	Structure Weight	Battery Weight
<b>Design:</b>	60 cm	10 min	6.0 g/W	100 g	367 g	89 g
<b>Real:</b>	60 cm	8 min, 12 sec	5.7 g/W	100 g	410 g	85 g

(endurance with no payload = 11 min)

### 2.3.5 Endurance optimised hovering platform

In order to keep the structural weight low, the endurance optimised hovering platform, shown in figure 2.13, has been constructed using only carbon fibre. This requires more manual fabrication skills and less computer design, however it is lighter than the Fibre-glass rapid prototyping method.

Two carbon fibre square tube bars are cut and joined in a cross, to create four support arms. To increase the strength of the cross section joint, two carbon plates are glued to each side of the joint. The avionics are installed in the centre on the bottom and the battery is installed in the centre on the top. The motors have a light-weight cylindrical attachment piece that fits tightly into a carbon tube. A hole is drilled into the four support arms, which is where the carbon tube for the motor mount is glued. Care must be taken when drilling to prevent the carbon fibre from splitting, due to the impact force of the drill bit. Once drilled the carbon piece has a high risk of post splitting, thus any hole that is made must be glued. This construction does not require any nuts or bolts, thus it is very light weight. The propellers have a protection ring built from carbon fibre rods. There are also carbon rods to support the platform while on the ground.

The chosen motor and propeller was the Emotion 24G 2C and APC 7x5 *inch*, respectively. This motor was chosen as it is 5 g lighter than the Hyperion motor, equating to a 20 g reduction in platform weight. The thrust curve for this motor and propeller combination is shown in figure 2.14. At the hover point thrust, which is defined as 1/4 of the platform weight (125 g), the motor-propeller efficiency can be determined. Notice that the hover point is in the lower thrust range, which is the optimal point for high-endurance capability, as the power slope is lower.

Table 2.2 shows a comparison between the predicted dimensioning design and the real constructed, endurance optimised hovering platform. The design strategy is very similar to the real performance, with the diameter, payload and battery matching exactly. The motor-propeller efficiency is 0.2 g/W worse and the structure weight is 5 g heavier than the envisioned design. This is the main reason for the 1 min 54 sec reduction in the flight endurance. Additionally, the design strategy does not take into account the power consumption of the avionics, which would also contribute to a slight reduction in the flight endurance. For a comparative measure that will be used in section 2.3.7, the flight endurance without the 25 g payload was 30 min.

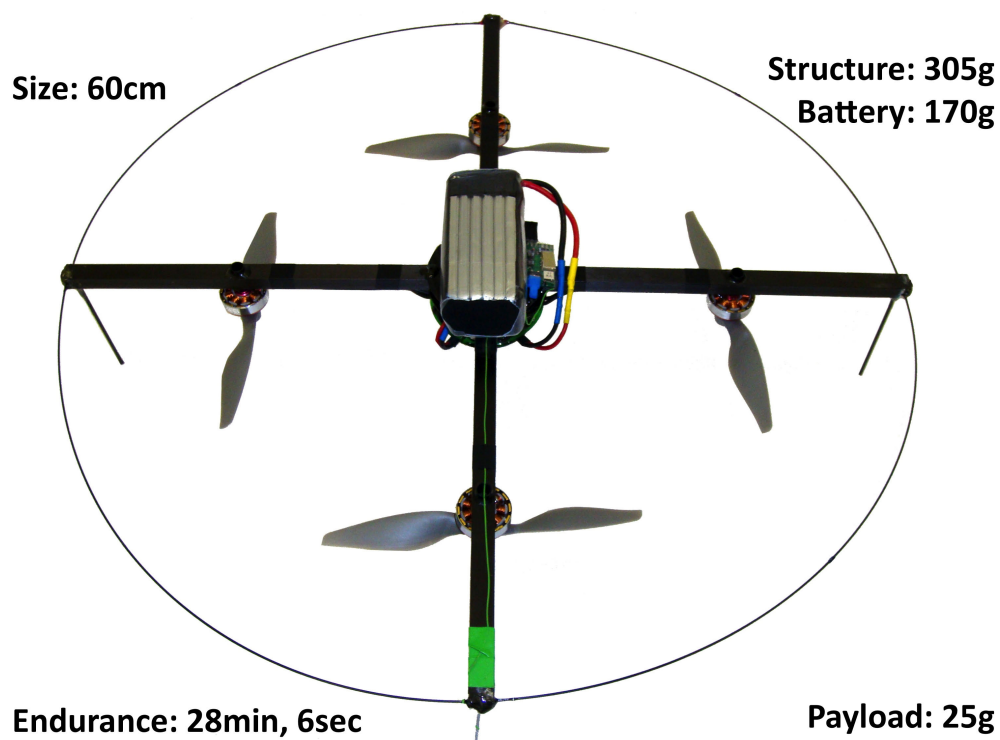


Figure 2.13: Hovering platform optimised for a high endurance capability

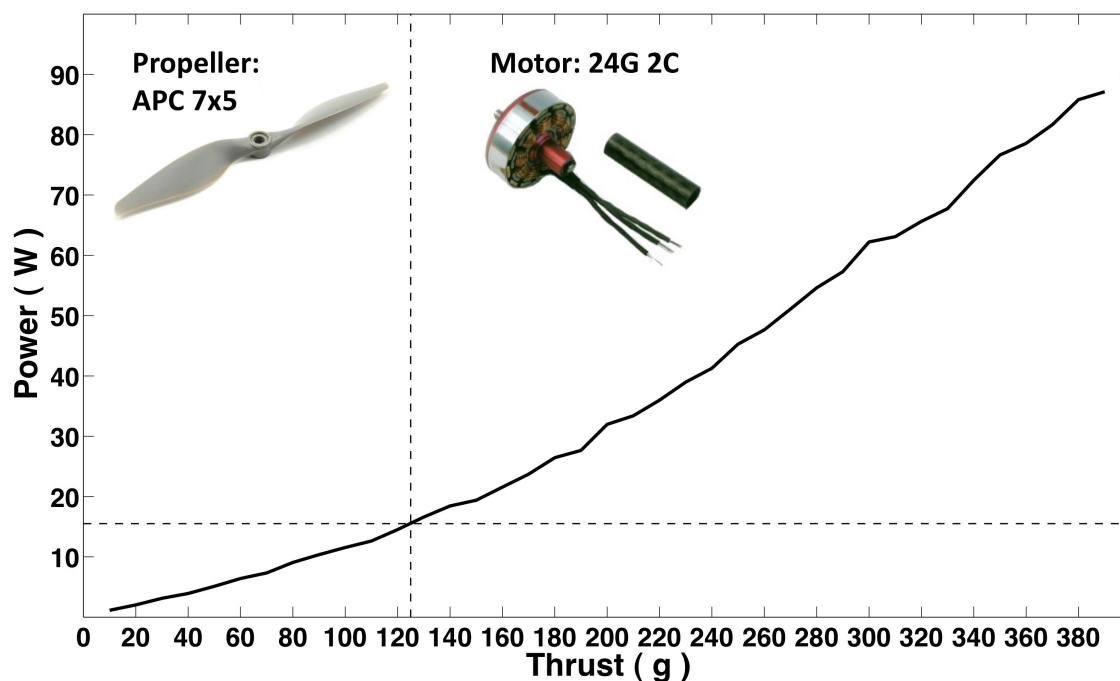


Figure 2.14: Thrust curve of the Emotion 24G 2C motor with an APC 7x5 inch propeller. The dotted lines indicate the hover point thrust and power

Table 2.2: Comparison between the high-endurance dimensioning design and the real hovering platform performance

	Diameter	Endurance	Motor-propeller Efficiency	Payload	Structure Weight	Battery Weight
<b>Design:</b>	60 cm	30 min	8.5 g/W	25 g	300 g	170 g
<b>Real:</b>	60 cm	28 min, 6 sec	8.3 g/W	25 g	305 g	170 g

(endurance with no payload = 30 min)

### 2.3.6 Payload optimised hovering platform

In order to construct the payload optimised hovering platform, shown in figure 2.15, a similar fabrication technique to the endurance optimised hovering platform is implemented. The structure weight needs to be low and very strong, thus it has been constructed using only carbon fibre with no drilled holes.

Similarly, two carbon fibre square tube bars are cut and joined in a cross, to create four support arms. To increase the strength of the cross section joint, two carbon plates are glued to each side of the joint. The avionics are installed in the centre on the top and the battery is installed in the centre on the bottom. In this case two motor control boards are used due to the coaxial motors. The motors are attached using carbon fibre spacers and plating fixed to both sides of the support arms. In this way the plating clamps the arm, thus eliminating the need for drilling holes in the arm and reducing its strength. This construction does require nuts and bolts, thus it is heavier than the previous method. The cables need to be thicker to carry the higher current required by the coaxial motors. Due to the additional weight of the platform, there are three carbon fibre rings added to the perimeter to protect the propellers. The base support is constructed using light-weight high-density foam, which is designed to absorb any impact forces during landing.

The chosen motor and propellers were the Himax CR2805 and twin counter-rotating APC 7x5E/EP *inch*, respectively. This motor was chosen as it is a coaxial motor with a thrust of up-to 600 g. The thrust curve for this motor and propeller combination is shown in figure 2.16. At the hover point thrust, which is defined as 1/4 of the platform weight (498 g), the motor-propeller efficiency can be de-

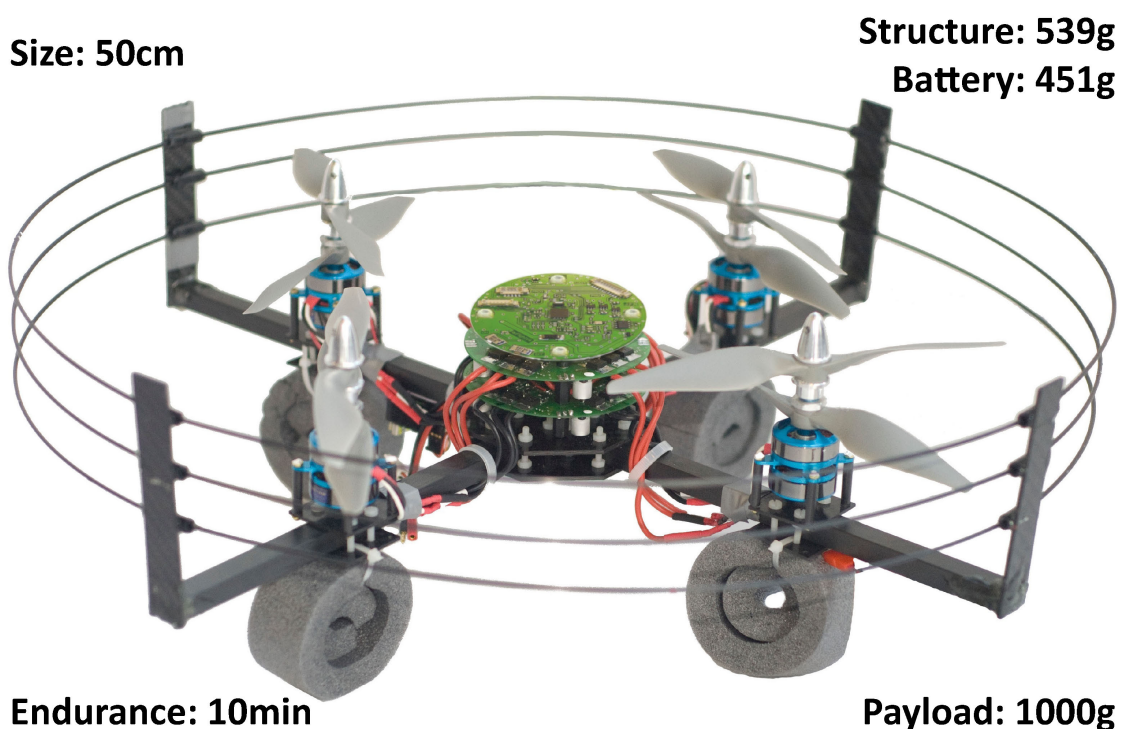


Figure 2.15: Hovering platform optimised for a high-payload capability

terminated. Notice that the hover point is in the upper thrust range, which is the optimal point for high-payload capability.

Table 2.3 shows a comparison between the predicted dimensioning design and the real constructed, payload optimised hovering platform. The design strategy is very similar to the real performance, with the diameter, endurance, motor-propeller efficiency and payload matching exactly. The structure weight is 7 g heavier and the battery that was used is 2 g heavier, which is very close to the envisioned design. Even though the design strategy does not take into account the power consumption of the avionics, the flight endurance is not affected due to the larger power of the coaxial motors dominating the overall power consumption. For a comparative measure that will be used in section 2.3.7, the flight endurance without the 1000 g payload was 26 min. This very good flight endurance is due to the payload being a substantial part (50%) of the overall weight of the platform and the figure of merit being higher for a coaxial rotor arrangement.

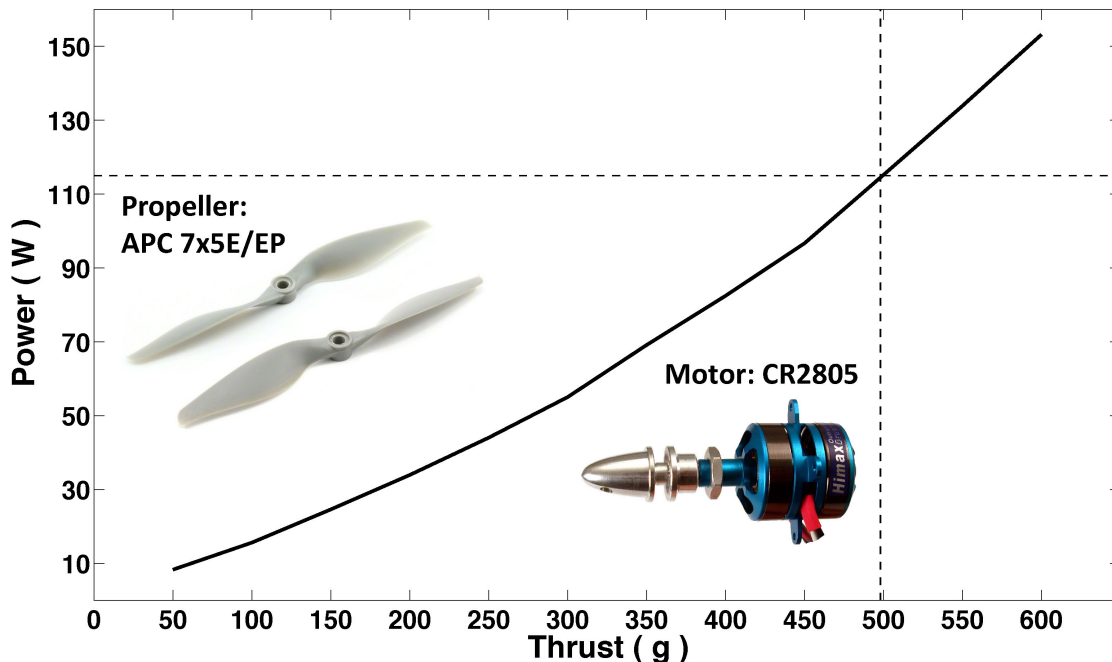


Figure 2.16: Thrust curve of the Himax CR2805 motor with twin APC 7x5 inch propellers. The dotted lines indicate the hover point thrust and power

Table 2.3: Comparison between the high-payload dimensioning design and the real hovering platform performance

	Diameter	Endurance	Motor-propeller Efficiency	Payload	Structure Weight	Battery Weight
<b>Design:</b>	50 cm	10 min	4.3 g/W	1000 g	552 g	449 g
<b>Real:</b>	50 cm	10 min	4.3 g/W	1000 g	539 g	451 g

(endurance with no payload = 26 min)

### 2.3.7 Comparison against commercial platforms

The three developed hovering platforms can now be compared against the commercially available platforms that have been presented in chapter 1, table 1.1. A graphical comparison showing the maximum payload versus the diameter can be seen in Figure 2.17. Similarly, a graphical comparison showing the maximum endurance versus the diameter can be seen in Figure 2.18. The shaded gradient represents the increase in risk of a collision as the platform size approaches the 100 cm standard doorway limitation. Most companies only specify the maximum cases for payload and endurance separately, thus a direct comparison cannot be performed as the true flight endurance is a function of the added payload. Thus, for a fair comparison they can only be compared in the maximum payload and flight endurance conditions, with a constant battery size.

The robustness optimised hovering platform ("Robust-RP") is the same size and has a very similar performance, in both payload and endurance, as the AR.Drone (with rotor protection) and Hummingbird (without rotor protection) commercial platforms. This is not surprising as they all use similar sized flexible propellers and have a platform weight that is almost equal. The AR.Drone and Hummingbird are also designed to be robust, thus they have been optimised for the same criteria.

The endurance optimised hovering platform ("Endurance-RP") is the same size and has a reduced payload performance when compared to the AR.Drone and Hummingbird commercial platforms. They both use similar sized propellers and have a platform weight that is almost equal. However, the endurance optimised hovering platform has 1.5 times longer flight endurance performance, when compared to any other commercial platform suitable for indoor operation (below 80 cm), and equal to the larger MD4-200 and AR100-B-RP.

The payload optimised hovering platform ("Payload-RP"), is the design that really stands out in comparison to the commercial platforms. The payload capability is 5 times higher than any other platform of the same size and equal to the DF-X8, which is more than 2 times larger in diameter. Additionally, the maximum flight endurance is 1.3 times longer, when compared to any other commercial platform suitable for indoor operation (below 80 cm). This platform is small (50 cm), has a high-payload capability (1000 g) and high flight endurance (10-26 min), therefore it is highly suitable for carrying the necessary sensing and processing required, to enable the collective operation of indoor flying robots.



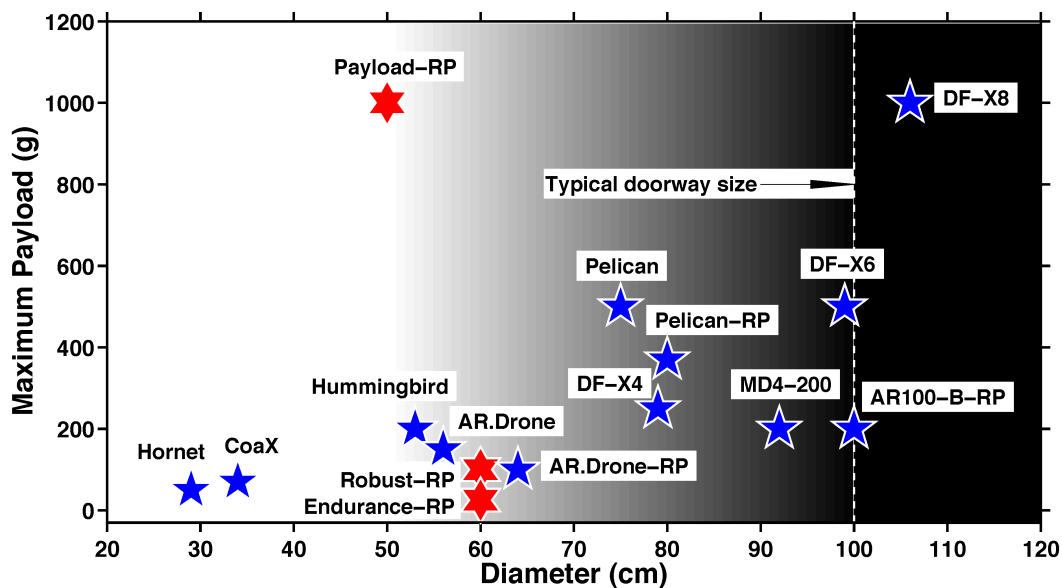


Figure 2.17: Payload versus diameter comparison against commercially available platforms (see chapter 1, table 1.1). The background shows a gradient of increasing risk of a collision as the platform size approaches the 100 cm doorway limitation. "-RP" indicates a platform with rotor protection.

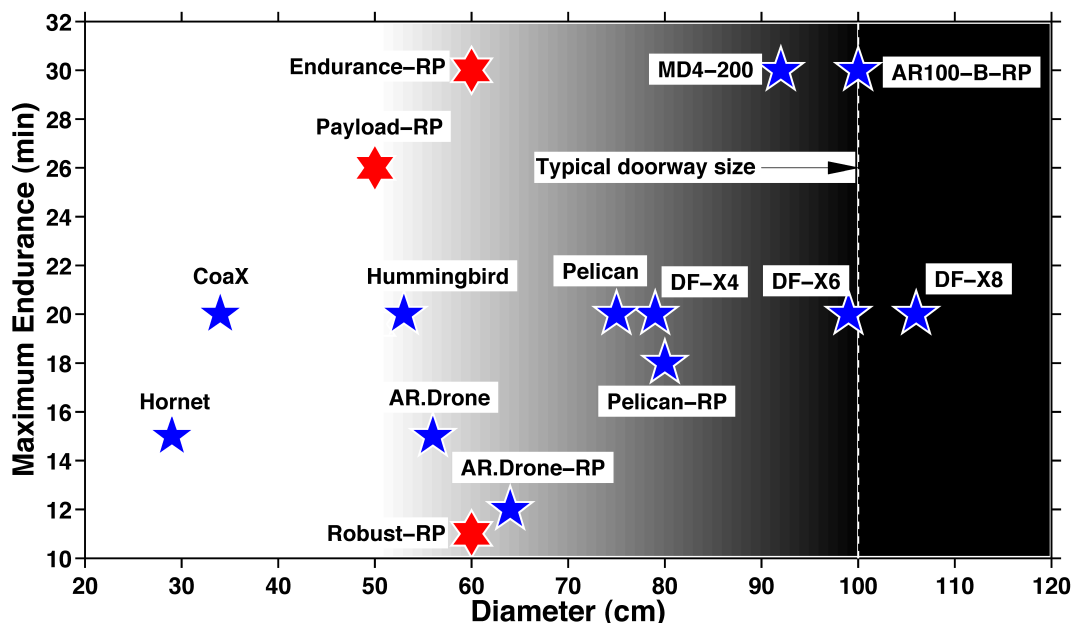


Figure 2.18: Endurance versus diameter comparison against commercially available platforms (see chapter 1, table 1.1). The background shows a gradient of increasing risk of a collision as the platform size approaches the 100 cm doorway limitation. "-RP" indicates a platform with rotor protection.

## 2.4 Conclusion

The existing commercially available hovering platforms are either too large to fly through doorways, or they are incapable of carrying a convincing amount of payload that would be suitable for indoor collective operation. In order to carry the on-board sensing and processing that is required for indoor collective operation, within the indoor size constraints, it was necessary to develop a method to create a new high-performance indoor hovering platform.

To accomplish this, a generalised design strategy has been introduced to dimension a hovering platform for a specific flight endurance, payload capability and robustness criteria. This design tool has shown that there is a relationship between the size, endurance, payload and robustness of a hovering platform. A platform optimised for robustness will allocate more of its weight to increase structural strength, while reducing endurance and payload. Whereas, a platform optimised for endurance will allocate more of its weight to the battery, while reducing the strength and payload. Additionally, a platform optimised for high-payload requires high thrust levels, which can improve the endurance capability.

Due to a lack of information within the literature, a realistic figure of merit has been determined for several propeller types that are suitable for indoor hovering platforms. The study has shown that a flexible propeller, when compared to a slow-fly and thin-electric propeller, has a reduced figure of merit and thrust, due to the coning effect. A coaxial (thin-electric) propeller has shown to have a greatly improved figure of merit and thrust capability over a single propeller.

The dimensioning strategy has allowed for three different hovering platforms to be optimised for robustness, endurance and payload, respectively. The robustness optimised hovering platform has proven to be highly reliable over the last few years of operation. It has provided countless flights and has been chosen to support the numerous experiments that will be presented in chapter 3 and chapter 4. The endurance optimised hovering platform has 1.5 times longer flight endurance, when compared to any other commercial platform suitable for indoor operation ( $\leq 80$  cm). The payload optimised hovering platform, with a diameter that is only half the size of a typical doorway opening, has a payload capability that is 5 times higher than any other platform the same size. Additionally, its maximum flight endurance is 1.3 times longer, when compared to any other commercial platform suitable for indoor operation ( $\leq 80$  cm).

The developed coaxial counter-rotating propulsion system, together with the dimensioning strategy, has produced an efficient hovering platform design, which is highly suitable for carrying the necessary sensing and processing required to enable the collective operation of indoor flying robots.



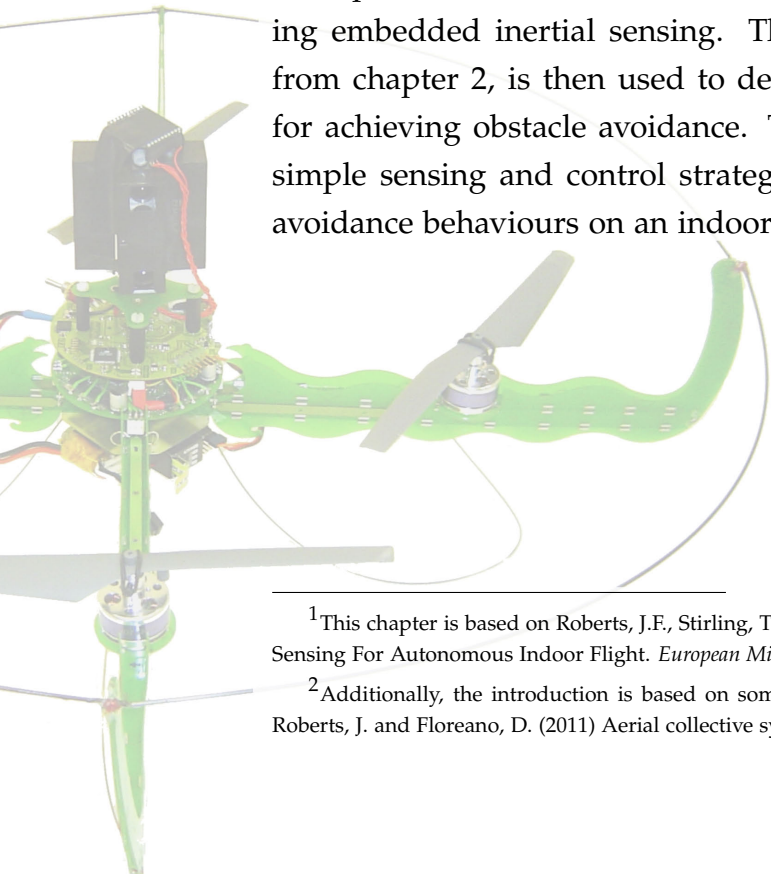
---

# 3

## Autonomous indoor flight

---

THE autonomous operation of a single indoor flying robot and the collective operation of several indoor flying robots, have a common initial goal. In order to achieve autonomous flight, they must both first achieve stable hovering and obstacle avoidance capabilities. None of the existing commercially available platforms offer a solution providing autonomous indoor flight with an obstacle avoidance capability (chapter 1). This is mainly due to the difficulties involved in flying within the indoor size constraints. The problem with current research methods is that they are either computationally expensive (laser scanner), requiring an external ground station, or will not work in the dark or poor lighting conditions (vision, optic-flow). Therefore, it is necessary to develop a simple sensing and control strategy to solve this challenge. This chapter<sup>1 2</sup> introduces a simple attitude estimation technique for stabilising a hovering platform using embedded inertial sensing. The robustness optimised hovering platform, from chapter 2, is then used to develop a simple sensing and control strategy for achieving obstacle avoidance. The chapter ends by demonstrating that the simple sensing and control strategy can enable anti-drift control and obstacle avoidance behaviours on an indoor highly dynamic, hovering platform.



---

<sup>1</sup>This chapter is based on Roberts, J.F., Stirling, T., Zufferey, J.-C. and Floreano, D. (2007). Quadrotor Using Minimal Sensing For Autonomous Indoor Flight. *European Micro Air Vehicle Conference and Flight Competition (EMAV2007)*.

<sup>2</sup>Additionally, the introduction is based on some material from Zufferey, J.-C., Hauert, S., Stirling, T., Leven, S., Roberts, J. and Floreano, D. (2011) Aerial collective systems. *In Handbook of Collective Robotics, Pan Stanford, 2011*.

### 3.1 Introduction

This chapter introduces a simple sensing and control strategy, to achieve autonomous indoor flight with an obstacle avoidance capability. This task alone introduces many difficult problems including attitude estimation, altitude sensing and obstacle sensing, all of which are important for successful autonomous indoor operation.

Flying robots are highly dynamic systems that operate in a three dimensional space, with 6 degrees of freedom. The amount of stability control required on a hovering platform can vary depending on the platforms intrinsic stability, and usually there is a trade-off between stability and controllability (Zufferey et al., 2011). Mechanically stabilised systems utilise the natural gyroscopic and/or aerodynamic effects created by a rotating mass or air-foil section, respectively (Wataru et al., 2003). The most common example of this is the contra-rotating helicopter with passive stabiliser bar (Matsue et al., 2005; Ohkura et al., 2005; Nardi et al., 2006; Holland et al., 2005), which can be found in almost every hobby/toy shop around the world. The top rotor is coupled to a weighted fly-bar and hinged in a way that controls the angle of attack of the rotor blades. The gyroscopic forces of this bar and the gravitational forces acting on it, allow it to act as both a 2-axis gyroscope for pitch and roll, and 3-D accelerometer for automatic levelling. Therefore, for complete stabilisation only a gyroscopic sensor for yaw rotational dampening is needed. This means that minimal sensors are required for stabilisation, but at the cost of more complicated hardware. The problem with this kind of stabilisation is that the forces acting to keep the system stable, also act against any control command that is given, thus limiting the amount of controllability. If the hinge on the rotor saturates due to a disturbance then stability is lost and the aircraft may find itself in an uncontrollable state. For systems not using mechanical stabilisation, electronic stability controllers are required. A real-time electronic controller stabilises the platform by closing the loop between the actuation system and the attitude sensing. The bandwidth of the platforms dynamics,  $f_d$  (Hz), is related to the speed at which the feedback system should track the sensor input and be able to stabilise the platform. As a rule of thumb, the controllers sampling period ( $\tau$ ) should be between (Levine, 1996):

$$\frac{1}{30 \cdot f_d} < \tau < \frac{1}{5 \cdot f_d}$$

The gyroscopes used for sensing the critical rotational dynamics of the platform, have a first-order bandwidth filter (to reduce phase delay) typically limited to 50 Hz. This is to attenuate the high frequency noise produced by the gyroscopes internal vibratory resonant frequency, which should be as low as possible in order to increase the sensitivity of the sensor (Apostolyuk, 2006). If the minimum recommended sampling rate of 5 times (from Equation 3.1) is selected, a minimum controller sampling frequency of 250 Hz is obtained. To utilise the full bandwidth of the sensor, the sampling frequency can be made equal to the control step frequency. Here the problem is finding an actuator that is capable of such speeds. Many rotary wing aircraft, such as classical helicopters, ducted-fans (Oh et al., 2005), hovering fixed wings (Green and Oh, 2008) etc., run into this problem because they are using standard servos for actuation. Servos have an upper bandwidth limitation of approximately 50 Hz (Michiel et al., 1994), which is defined by the Pulse-Width Modulated (PWM) signal used to set its position. On such systems, a more complex controller, typically non-linear in design, may be necessary to achieve platform stabilisation. These types of controllers generally require an accurate model of the systems dynamics to perform well. On the other hand, if the problem of actuator bandwidth is solved, it is possible to increase the speed of the control system, reduce the complexity of the controller and eliminate the need for a complex dynamic model. The development of high-speed ( $\geq 500$  Hz) brushless motor controllers has led to the emergence of multi-rotor aircraft, such as quad-rotors (Gurdan et al., 2007), hex-rotors and oct-rotors (Salazar et al., 2009) that use simple stability controllers (e.g. Proportional-Integral-Derivative) and minimal moving parts. This active stabilisation allows the platform to have a highly adaptable controllability. Therefore, a quad-rotor utilising simple high-speed stability controllers would make a robust and adaptable, low-maintenance hovering platform ideal for indoor operation.

In order to achieve fully autonomous operation, the hovering platform also requires additional sensors for altitude control, platform drift compensation and obstacle avoidance. One of the simplest methods that can enable all of these capabilities simultaneously, is by implementing a controller strategy that utilises the spatial distance information between the robot and the surrounding obstacles. This spatial information can be used to minimise the velocity of the platform with respect to the obstacles (anti-drift), and push the platform away from an obstacle if its too close (obstacle avoidance). Laser range finders can provide

fast (10 Hz) and accurate ( $\pm 30$  mm) distance information to surrounding obstacles, however they are computationally expensive, costly ( $\$ > 2000$  USD<sup>3</sup>) and heavy ( $\geq 160$  g<sup>4</sup>), taking up most of the payload available on a small hovering platform. Alternatively, there are other sensors available that are lighter and can provide distance information at a much lower cost. For example, ultrasonic distance sensors (MaxSonar-EZ4<sup>5</sup> \$28 USD) utilising time-of-flight measurements, or infrared distance sensors (GP2Y3A003K0F<sup>6</sup> \$37 USD) utilising triangulation techniques. However, these sensors provide a lower quality measurement than a laser range finder and they only operate in one direction, usually with a wide beam-width ( $5^\circ$  to  $60^\circ$ ). Therefore, a symmetrical hovering platform, such as a quad-rotor, which can fly in any direction, requires multiple sensors or mechanically rotating sensors (see chapter A, appendix A.2.2) to cover the critical sensing directions.

## 3.2 Materials and methods

This section introduces the embedded electronics and sensing, of the robustness optimised hovering platform developed in chapter 2. A simple sensing and control strategy is then proposed for achieving autonomous obstacle avoidance and platform anti-drift capabilities.

### 3.2.1 Embedded electronics

The on-board embedded electronics includes a high-speed brushless motor controller, flight computer with attitude sensors and wireless communications.

The high-speed brushless motor control board, shown in figure 3.1, incorporates four motor channels, each with an 8-bit ATMEL micro-controller and a three phase MOSFET driver. The schematics and PCB have been custom designed in-house, however the source code has been provided by the Mikrokopter project<sup>7</sup>. The feedback for the motor speed control is provided by low-pass fil-

---

<sup>3</sup><http://www.acroname.com> (accessed Feb. 2011)

<sup>4</sup><http://www.hokuyo-aut.jp> (accessed Feb. 2011)

<sup>5</sup><http://www.maxbotix.com> (accessed Feb. 2011)

<sup>6</sup><http://sharp-world.com/products/device/lineup> (accessed Feb. 2011)

<sup>7</sup><http://www.mikrokopter.com> (accessed Feb. 2011)



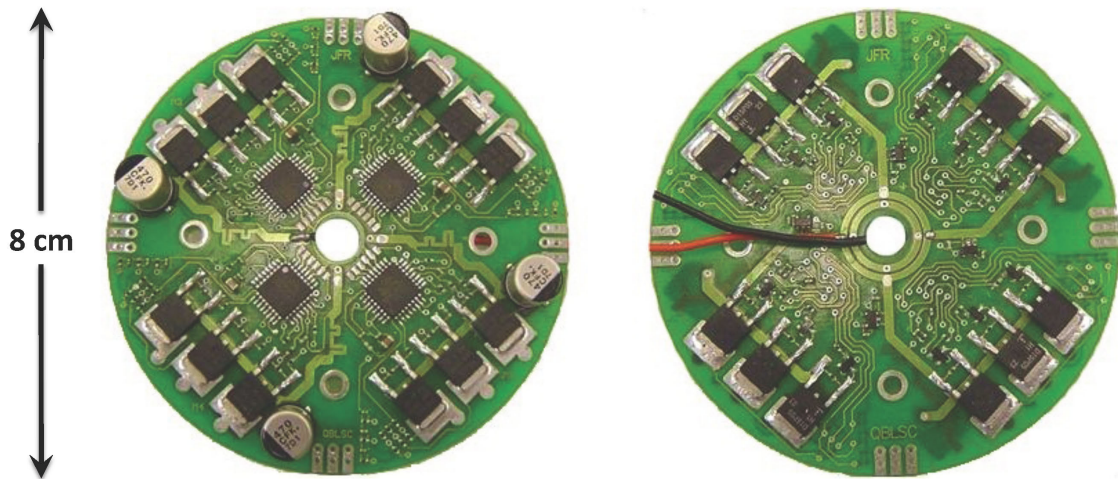


Figure 3.1: High-speed brushless motor control board. *Left: Top-view, Right: Bottom-view*

tering the induced electromotive force, produced when the motor is running. The motor speed is adjusted by controlling the duty-cycle of a 16 kHz PWM, which drives the MOSFETs. The speeds of each motor can be updated at a rate of 500 Hz, which allows for a high update-rate of the entire stability control system, from sensor to actuator. The four channel high-speed motor controller communicates with the flight controller via an  $I^2C$  connection.

The flight control board, shown in figure 3.2, incorporates a micro-controller for stability control (8-bit ATMEL 16-MIPS) and another micro-controller for autonomous control (16-bit dsPIC 40-MIPS). This minimises the risk of affecting the stability and manual controls, when implementing new higher-level control strategies. The board houses three gyroscopes, a 3-axis accelerometer, a pressure sensor and a 2-axis magnetometer. However, the later two sensors are not active in the following experiments.

A radio control receiver is connected through a Pulse-Position Modulation (PPM) input to allow for manual flight control and switching between the autonomous and manual modes. The board has extended connectivity for adding additional sensors and/or controllers via two serial interfaces and four analog channels. In the following experiments one serial interface is connected to an Xbee wireless link for data analysis, the other is connected to an ultrasonic sensor for altitude sensing, and the analog channels are connected to four infrared sensors for obstacle sensing. Additionally, the board has 1 MB of memory (EEPROM) for storing experimental and/or configuration data.

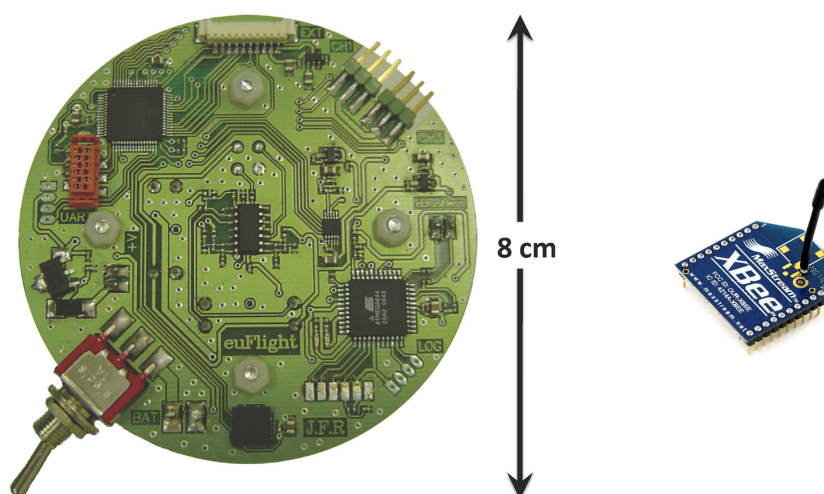


Figure 3.2: *Left*: Flight control board. *Right*: Xbee wireless module

Now that the embedded electronics and inertial sensing has been presented, the details of the attitude sensing can be introduced.

### 3.2.2 Attitude sensing

The quad-rotor is a highly non-linear and intrinsically unstable platform, which requires stability controllers to dampen its fast dynamics. Let us consider the earth fixed-frame  $E$  and the hovering platform body fixed-frame  $B$ , as shown in figure 3.3. Using Euler angles parameterization, the platform's orientation in space is given by a rotation  $R$  from  $B$  to  $E$ , where  $R \in SO3$  is the rotation matrix.

In order to stabilise the platform dynamics, inertial sensors have been added to estimate the Euler angles of the platform. There are several methods that can be used to estimate the attitude, including various implementations of Kalman or Complementary filters. Kalman filters require complex processing and can be difficult to apply robustly to applications with low-quality sensors (Mahony et al., 2005). Alternatively, Complementary filters are robust and simple to implement, and can be easily tuned (Mahony et al., 2005). Therefore, a Complementary filter has been chosen due to its simplicity, which has been inspired by the early work from the Mikrokopter project<sup>8</sup>. These methods are designed to combine the measurements from the embedded accelerometers and gyroscopes to obtain the best estimation.

<sup>8</sup><http://www.mikrokopter.com> (accessed Feb. 2011)

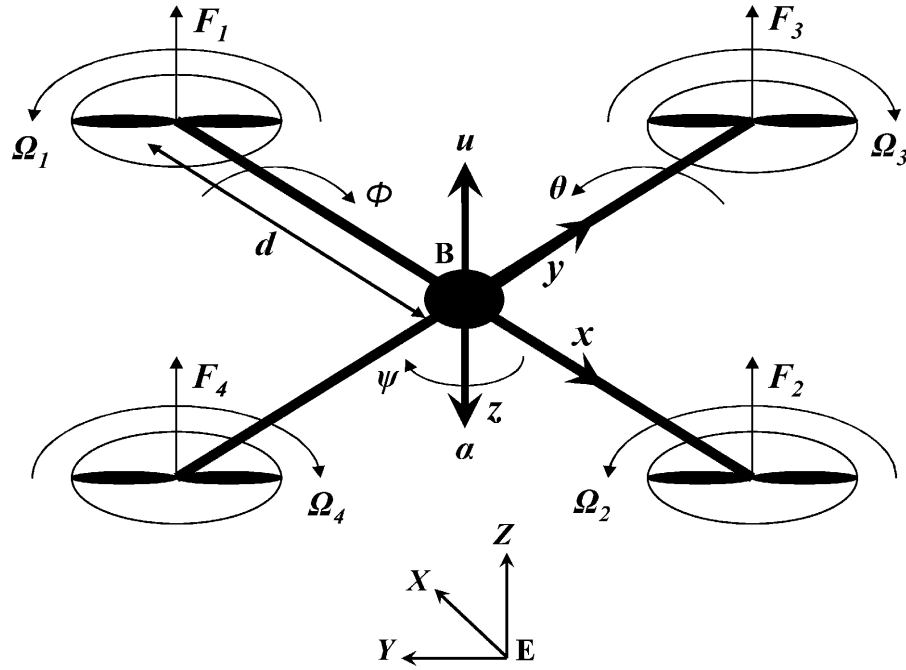


Figure 3.3: Quad-rotor hovering platform coordinate system

Accelerometers can be used to detect the inclination angle with respect to the gravitational acceleration of the earth (z-axis). This inclination angle is only accurate if the platform has no additional 3-D acceleration, which is only the case when the flying robot is statically hovering. The accelerometer response ( $Acc_{sense}$ ) can be modelled by:

$$Acc_{sense} = L(s)sense + \mu_{sense}$$

where  $sense$  is the ideal sensor response,  $L(s)$  is a low-pass filter associated with the sensor characteristics, and  $\mu_{sense}$  represents the noise (Mahony et al., 2005). Therefore, to remove as much as possible the acceleration that is imposed by the motion of the platform, the sensor output must be low-pass filtered. This method assumes that the long term average acceleration of the platform is mostly representing the vertical gravitational acceleration, which is only valid for small attitude angles. Such a method is sufficient for slow indoor translation and hovering.

In contrast, gyroscopes can be used to detect the angular rates of the platform's rotational motion. The gyroscopes response ( $Gyro_{sense}$ ) can be modelled by:

$$Gyro_{sense} = sense + \mu_{sense} + b(t)$$

where *sense* is the ideal sensor response,  $\mu_{sense}$  represents the noise and  $b(t)$  is the low-frequency bias (Mahony et al., 2005). Therefore, to remove as much as possible the angular rate that is imposed by the low-frequency bias, the sensor output must be high-pass filtered.

A Complementary filter can be used to obtain the estimated attitude angles, where the low-bandwidth response of the accelerometer ( $Acc_{x,y}$ ) can be combined with the high-bandwidth response of the gyroscope ( $Gyro_{\theta,\phi}$ ). The estimated roll ( $\phi$ ) and pitch ( $\theta$ ) attitude angles can then be defined as:

$$\theta = F_1(s)Acc_x + F_2(s)\frac{Gyro_\theta}{s}, \quad \phi = F_1(s)Acc_y + F_2(s)\frac{Gyro_\phi}{s}$$

where  $F_1$  is a low-pass filter and  $F_2$  is a high-pass filter. Note that the measurement ( $Gyro_{\theta,\phi}$ ) is first integrated to convert the gyroscopes angular rate to an angle (Mahony et al., 2005). For this transfer function to be complementary,  $F_1(s)$  and  $F_2(s)$  must be equal to one when combined. Depending on the hardware implementation, the sensor values will need to be scaled before they are combined. On a hovering platform most of the time the z-axis is aligned with gravity, this means that the 3-axis accelerometers hold little or no information about the yaw angle. However, due to this fact, the inherent stability of the yaw is naturally dampened. Thus, the yaw angular rate can simply be integrated and high-pass filtered to obtain the yaw angle ( $\psi$ ).

Now that the attitude sensing has been presented, the additional sensing required for autonomous flight can be introduced.

### 3.2.3 Autonomous flight sensing

In order to achieve autonomous indoor flight, it is necessary to stabilise the hovering platform drift, in the  $x$ ,  $y$ , and  $z$  axis. For this purpose, five additional distance measuring sensors have been added to the platform, having a total weight of only 45 g and cost of  $\approx 170$  USD. This is desirable as it is more than 3 times lighter and 10 times cheaper than a laser scanner, and minimises the computational requirements.

Obstacles are detected (in  $x$  and  $y$ ) using four infrared distance sensors (GP2Y3A003K0F<sup>9</sup>), shown in figure 3.4 *left-top*, which are facing the four perpendicular directions of the hovering platform ( $+x$ ,  $-x$ ,  $+y$  and  $-y$ ). The infrared

<sup>9</sup><http://sharp-world.com/products/device/lineup> (accessed Feb. 2011)

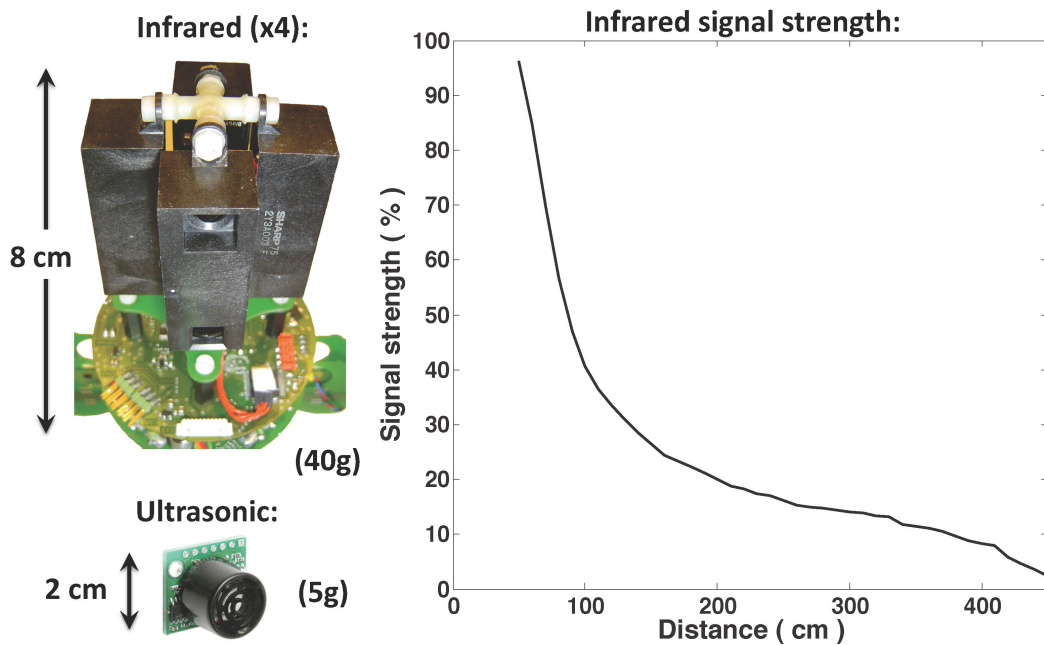


Figure 3.4: *Left-top*: Four infrared sensors mounted on top of the hovering platform, used for obstacle detection. *Left-bottom*: Ultrasonic sensor used for altitude sensing. *Right*: Signal strength response of the infrared distance sensor.

sensors have five selectable emitters that adjust the sensing direction, from  $5^\circ$  to  $25^\circ$ . They also have a Position Sensitive Detector (PSD) that can triangulate the distance measurement from 40 cm up to a range of approximately 3.5 m, however beyond 2 m the signal slope flattens out and the signal to noise ratio decreases. This distance measurement is represented as an analog voltage, which is updated at a rate of 60 Hz and sampled by the flight controller at 500 Hz. To determine the transfer function of the infrared sensors, they have been characterised over a range from 0 m to 4.5 m in 10 cm steps, shown in figure 3.4 *right*. These sensors can provide a reference for manoeuvring the hovering platform in a two-dimensional space and allow for obstacle detection of large objects.

The altitude ( $z$ ) is measured using an ultrasonic distance sensor (MaxSonar-EZ4<sup>10</sup>), shown in figure 3.4 *left-bottom*. This sensor has a range from 15 cm to 647 cm, with a resolution of 2.5 cm. The sensor includes an on-board microcontroller that calculates the distance using time of flight and sends the measurements through a serial connection to the flight controller at 20 Hz. Both the infrared and ultrasonic sensors are active sensors, which are not affected

<sup>10</sup><http://www.maxbotix.com> (accessed Feb. 2011)

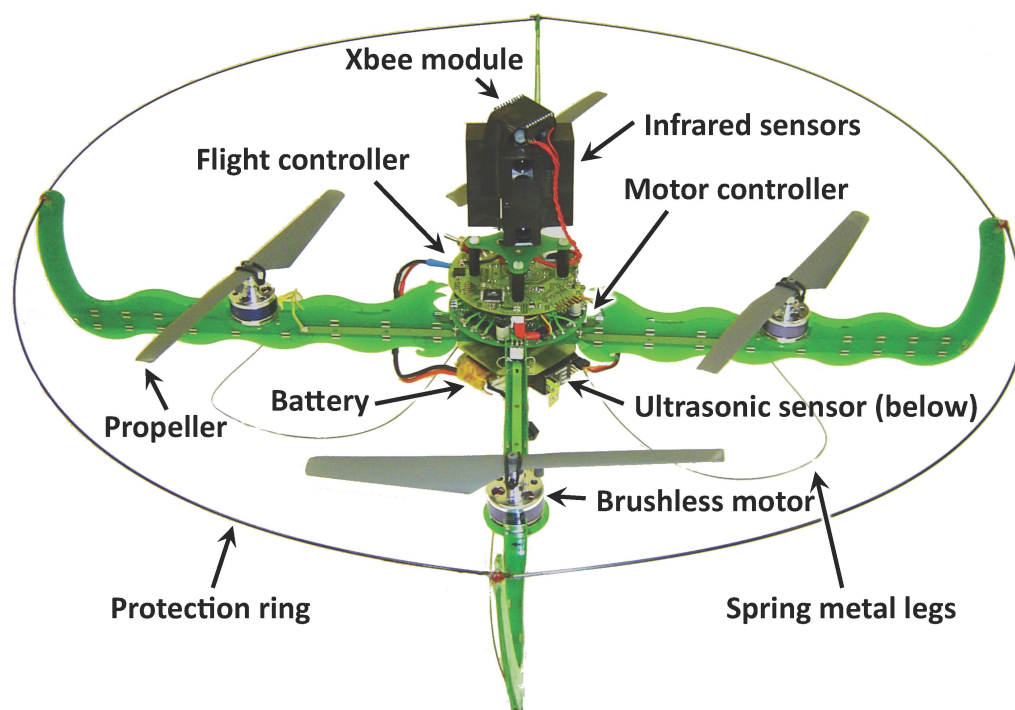


Figure 3.5: Hovering platform fitted with embedded control boards and sensors

by illumination, thus they will work in the dark or in poor lighting conditions. The robustness optimised hovering platform, from chapter 2, fitted with the embedded control boards and sensors required for autonomous flight is shown in figure 3.5.

Now that all the sensors required for autonomous indoor flight have been defined, a simple control strategy can be derived.

### 3.2.4 Control strategy

Autonomous indoor flight is implemented using a two-level cascaded control algorithm. The inside cascade is designed to stabilise the hovering platform, using the inertial sensing.

The amount of differential force required to stabilise the hovering platform depends on the distance ( $d$ ), shown in figure 3.3, between the centre of the hovering platform (pivot-point) and the motors. This can be expressed by the mechanical lever equation (Tipler and Mosca, 2004):

$$M = Fd$$

where  $F$  is the force produced by the motor ( $F_{1:4}$ ),  $d$  is the perpendicular distance between the force and the pivot-point, and  $M$  is the turning force known as the moment or torque. Therefore, the further the motors are placed away from the centre of the hovering platform, the less force is required for the same stabilisation moment.

The motor mixer, designed to command the four motor speeds, can be defined as:

$$\begin{aligned} u1 &= u \theta + u \psi + u z \\ u2 &= -u \theta + u \psi + u z \\ u3 &= -u \phi - u \psi + u z \\ u4 &= u \phi - u \psi + u z \end{aligned} \quad (3.1)$$

where  $u_{1:4}$  are the control inputs corresponding to the motor forces  $F_{1:4}$ . The attitude estimation of the pitch ( $\theta$ ), roll ( $\phi$ ) and yaw ( $\psi$ ) are used to stabilise the hovering platform. The yaw ( $\psi$ ) controller balances the four torques ( $\Omega_{1:4}$ ) produced by the rotational component of the motors.

Attitude control is implemented using three independent PID controllers augmented with feedback on acceleration, whose control law can be defined as:

$$\begin{aligned} u \theta &= k_{dd}(\ddot{\theta}_{ref} - \ddot{\theta}) + k_d(\dot{\theta}_{ref} - \dot{\theta}) + k_p(\theta_{ref} - \theta) + k_i \int_0^t (\theta_{ref} - \theta) dt \\ u \phi &= k_{dd}(\ddot{\phi}_{ref} - \ddot{\phi}) + k_d(\dot{\phi}_{ref} - \dot{\phi}) + k_p(\phi_{ref} - \phi) + k_i \int_0^t (\phi_{ref} - \phi) dt \\ u \psi &= k_{dd}(\ddot{\psi}_{ref} - \ddot{\psi}) + k_d(\dot{\psi}_{ref} - \dot{\psi}) + k_p(\psi_{ref} - \psi) + k_i \int_0^t (\psi_{ref} - \psi) dt \end{aligned} \quad (3.2)$$

where  $k_{dd}$ ,  $k_d$ ,  $k_p$  and  $k_i$  are the double derivative (angular acceleration), derivative, proportional, and integral control gains respectively.  $\theta_{ref}$ ,  $\phi_{ref}$ ,  $\psi_{ref}$  are the commanded reference angles.

The outer cascade is used to perform altitude control and obstacle avoidance. The altitude controller balances the downward force produced by gravity ( $mg$ ) with the collective vertical control force ( $u$ ) of the four motor forces ( $F_{1:4}$ ). Altitude control is implemented using a PID controller augmented with feedback on acceleration and linearization to compensate for the force of gravity when rolling and pitching, whose control law can be defined as:

$$u z = \frac{1}{\cos\theta \cos\phi} (k_{dd}(\ddot{z}_{ref} - \ddot{z}) + k_d(\dot{z}_{ref} - \dot{z}) + k_p(z_{ref} - z) + k_i(i_a)) \quad (3.3)$$



where  $z_{ref}$  is the commanded reference altitude and  $i_a$  is the altitude accumulator. The altitude accumulator counts up whenever the hovering platform is below the desired altitude and down otherwise, thus maintaining a mean value for the total thrust required to hover. The rate of ascent or decent is adjusted by the time constant between increments or decrements, respectively.

The obstacle avoidance uses a simple distance balancing control strategy:

$$\begin{aligned} x_{coll} &= d_{front} - d_{back} \\ y_{coll} &= d_{left} - d_{right} \end{aligned} \quad (3.4)$$

where  $d_{front}$ ,  $d_{back}$ ,  $d_{left}$  and  $d_{right}$  correspond to the infrared distances in those directions. The goal of the controller is to repel the hovering platform away from small distances on any of the four sides. Thus, preventing the hovering platform from colliding with the walls or other large obstacles. The obstacle avoidance is implemented using a PD controller, whose output controls the pitch and roll commands:

$$\begin{aligned} \theta_{ref} &= k_d \dot{x}_{coll} + k_p x_{coll} \\ \phi_{ref} &= k_d \dot{y}_{coll} + k_p y_{coll} \\ \psi_{ref} &= 0 \end{aligned} \quad (3.5)$$

Thus, providing a repulsion force away from any obstacle in 2-D, which naturally pushes the hovering platform to the middle of the room, thus also performing anti-drift compensation.

Now that the autonomous sensing and control strategy has been determined, the experiments towards achieving autonomous indoor flight can begin.

### 3.3 Results

The goal of these experiments is to demonstrate that the simple sensing and control strategy, presented in the last section, can provide anti-drift control and allow the robot to avoid collisions with surrounding obstacles, including the floor. This must be achieved without any human intervention or external aids. The following section first describes the experiment room. Three experiments are then presented that show the progression towards achieving anti-drift control and obstacle avoidance behaviours on the hovering platform.



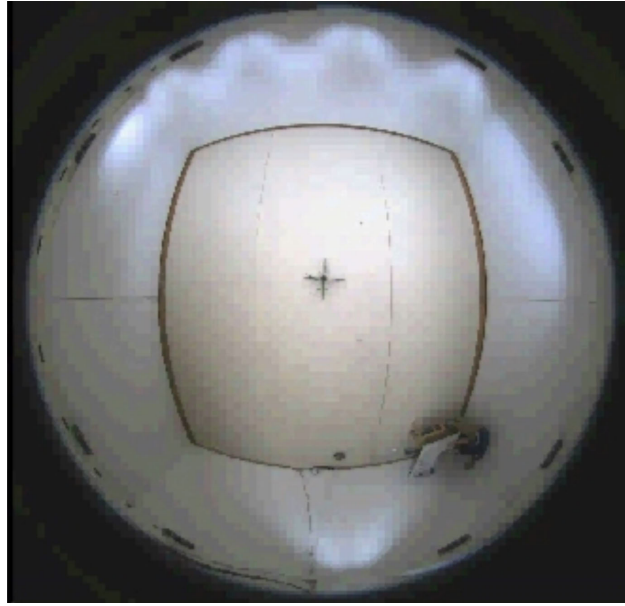


Figure 3.6: View of experiment room through the  $180^\circ$  field-of-view downward pointing dome camera, hovering platform visible in the center

### 3.3.1 Experiment room

The room where the experiments were conducted, shown in figure 3.6, is 6 m wide, 7 m long and 3 m high. A dome camera has been installed on the roof to track the platforms trajectory. This camera has a  $180^\circ$  field-of-view and is capable of seeing anywhere in the room below. To allow the platform to be seen clearly, the floor of the room was covered with white vinyl and all mobile obstacles in the room were removed. A desk was left in one of the corners to place a laptop computer, the computer is used to record the data from the camera and to allow quick re-programming of the control gains.

When experiments are conducted a safety pilot sits along the centre of the bottom wall, the pilot has the ability to activate and deactivate the system to start/stop an experiment, or in the case of a failure control the platform manually. The trajectory of the platform is extracted using a background subtraction algorithm from the pre-recorded video. The initial position of the platform for each experiment is in the centre of the room. Note that the  $180^\circ$  field-of-view from the camera is highly distorted. Because the platform flies close to the camera the perceived position of the platform is worse than it actually is in reality. Due to this, the following plots will include a dotted box defining the limits where the platform would collide with the wall at the hover height altitude.

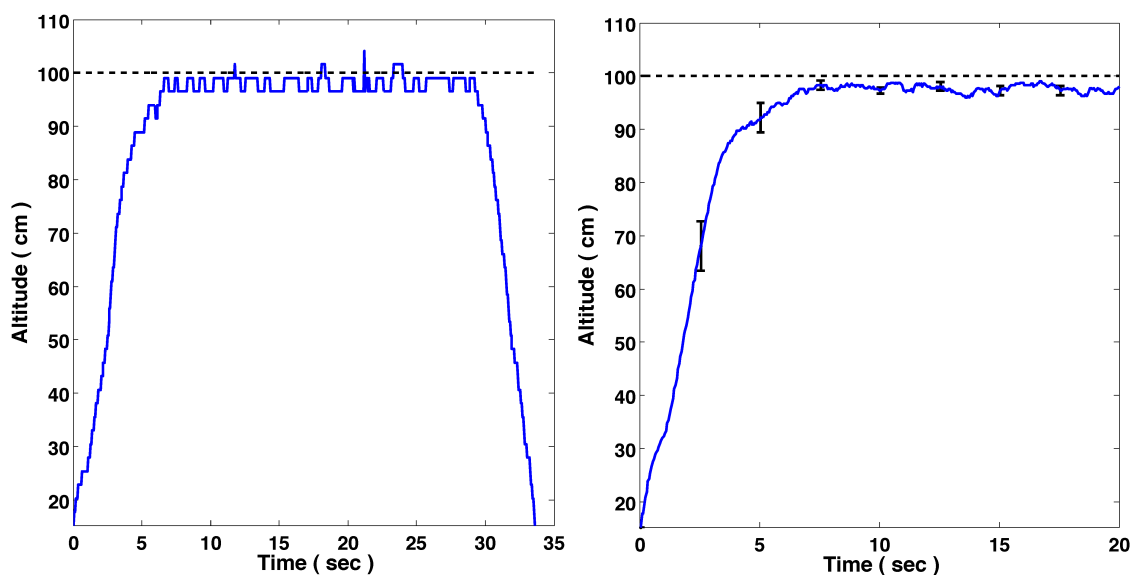


Figure 3.7: *Left:* Altitude response during a single run - take-off, hover and landing. *Right:* Mean altitude response of ten independent runs - take-off and hover.

### 3.3.2 Altitude control

The first experiment was designed to observe the altitude control capability. The aim was to achieve automatic take-off, altitude control and automatic landing with the pitch and roll controlled manually.

Altitude control is achieved by means of a PID controller using the downward pointing ultrasonic sensor. To enable automatic take-off the accumulator of the controller is slowly increased until the height is equal to one meter, this is done at a rate of approximately 15 cm per second. Similarly, automatic landing is achieved by slowly decreasing the height accumulator until the platform is on the ground. The altitude sensor data, shown in figure 3.7 *left*, was logged during an autonomous take-off, hover and landing sequence. The platform takes-off slowly then proceeds to a stable hover at the height of one meter. After 30 seconds the system comes down slowly and lands (see video<sup>11</sup>).

The altitude sensor data, shown in figure 3.7 *right*, has been logged for ten independent flights to show the systems repeatability and robustness. The mean altitude during stable hover was 97.4 cm, with a standard deviation of 3.05 cm. The sensor resolution is 2.5 cm therefore the deviation is well within two mea-

<sup>11</sup>Video: <http://jfroberts.com/phd> (quadrotor\_autonomous\_altitude.mp4)

surement steps. The 2.6 cm offset is approximately equal to the sensor resolution. This suggests that the gravity component acting on the platform tends to push the altitude to the lower bound of the two sensor increments, about the 100 cm height.

### 3.3.3 Obstacle avoidance

The second experiment was designed to observe the hands-off capability by implementing the four infrared distance sensors. The aim was to use both altitude control and infrared obstacle avoidance to achieve a fully autonomous flight.

Obstacle avoidance is achieved by using two PD controllers and a distance balancing algorithm for roll and pitch control. In this experiment the control gains are set to  $k_p = 5$  and  $k_d = 200$ . This algorithm simply calculates the difference in distance between the two opposing walls. The difference is fed into the controller, which then alters the attitude angle of the platform to turn away from the wall. The range of the infrared sensors has been limited to 1.5 meters by adding input limits on the ADC values within the acquisition code. The initial position of the platform, shown in figure 3.8, is in the centre of the room. At this position, due to the limits placed on the sensor range, the walls cannot be detected. The platform takes-off and flies in a random direction depending on its initial attitude. As it approaches the first wall the controllers act to prevent a collision and the platform flies off in another direction. This simple control approach allows the platform to fly safely avoiding the walls for as long as the battery permits (see video<sup>12</sup>).

### 3.3.4 Anti-drift control

The third experiment was designed to observe the hands-off capability by implementing the infrared distance sensor anti-drift control. The aim was to achieve both altitude control and anti-drift control to have a fully autonomous stable hover in the centre of the room.

By keeping the same control strategy as the previous experiment, reducing the controller gains and not limiting the range of the infrared sensors, an anti-drifting behaviour emerges. In this experiment the control gains are set to  $k_p =$

---

<sup>12</sup>Video: <http://jfroberts.com/phd> (quadrotor\_obstacle\_avoidance.mp4)

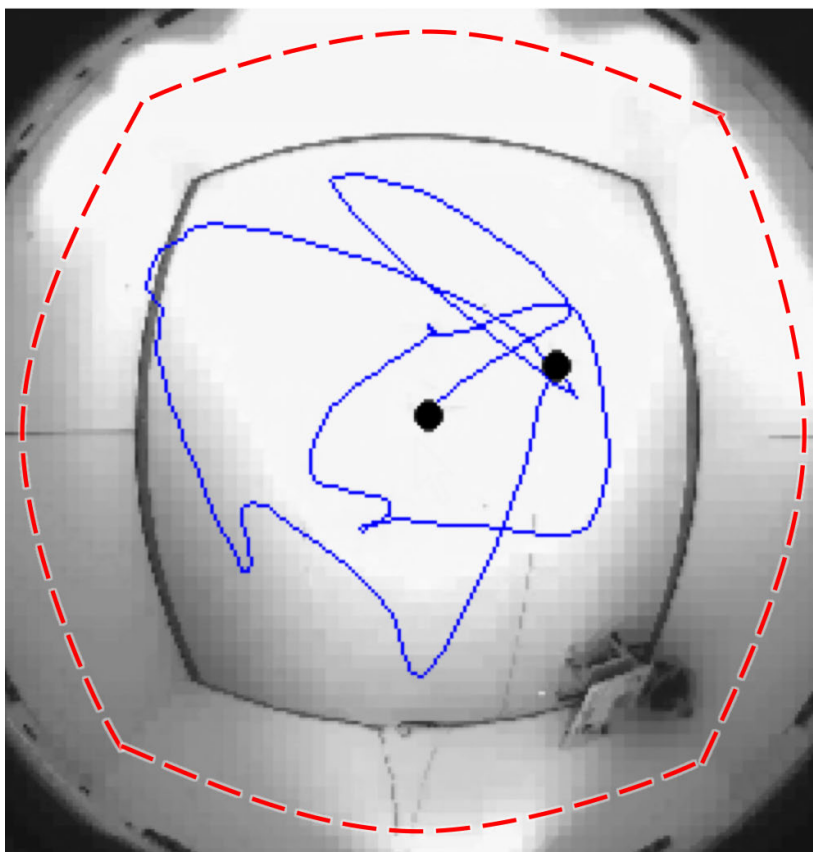


Figure 3.8: Obstacle avoidance trajectory plot. The dotted box defines the limits where the platform would collide with the wall at the hover height. The black circles represent the starting and ending positions

2.2 and  $k_d = 100$ . The initial position of the platform, shown in figure 3.9, is in the centre of the room. In the middle of the room the sensors can just detect the four walls, however any reading below two meters has little effect due to the flatness of the sensor response. The walls are between 3 m and 9.2 m away depending on the rotational orientation of the platform, so there is a 2 m x 3 m rectangular boundary in the centre where the sensors cannot accurately detect the position of the platform. The drift during position hold is due to this uncertainty. When the platform takes off, it instantly begins to correct for drift and keep the platform in the centre of the room (see video<sup>13</sup>). This simple control approach allows the platform to hold its position safely close to the centre of the room for as long as the battery permits.

<sup>13</sup>Video: <http://jfroberts.com/phd> (quadrotor\_antidrift.mp4)

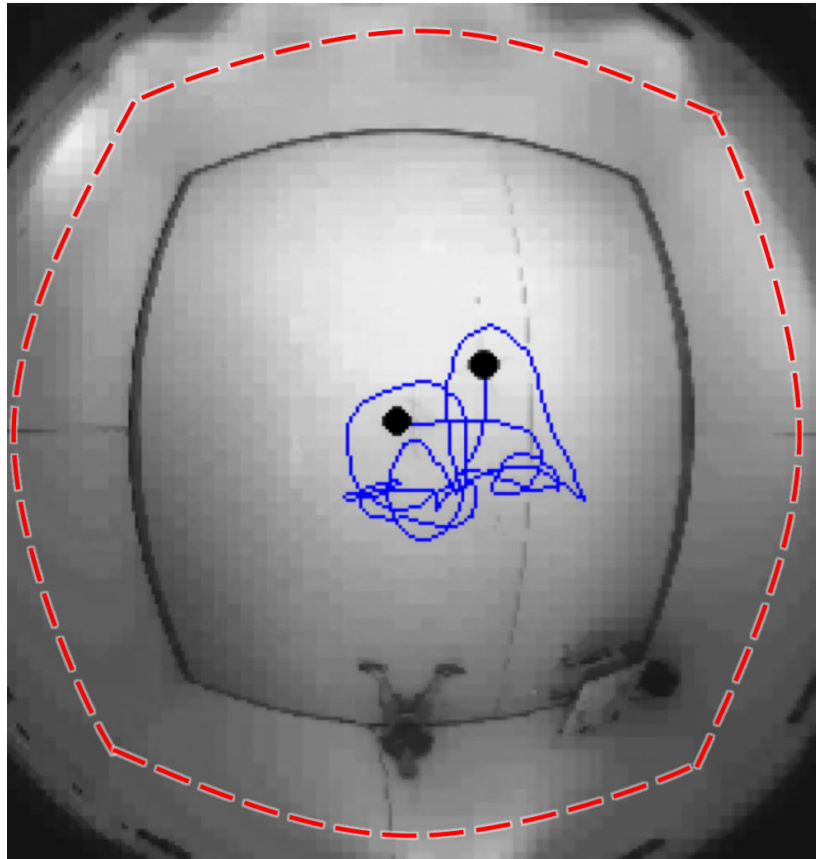


Figure 3.9: Anti-drift trajectory plot. The dotted box defines the limits where the platform would collide with the wall at the hover height. The black circles represent the starting and ending positions

These experiments were carried out several times with the same control strategy and the platform demonstrated good robustness. As most rooms within houses or offices are less than 6 m in dimensions this sensing and control strategy is considered adequate for highly dynamic indoor hovering platforms.

It is interesting to observe the change in behaviour of the flight while making small adjustments to the control gains. The obstacle avoidance behaviour could be viewed as a slightly unstable version of the anti-drift behaviour. This kind of purely reactive control can provide fully autonomous indoor flight. Additionally, using this control strategy 2-D position control may be possible, as long as the desired location is within the range of the infrared sensors. However, it is not possible to tell the hovering platform to fly along a set of waypoints and land at a desired location. In order to achieve such a behaviour a more complex level of sensing and control strategies are required.

### 3.4 Conclusion

In the journey towards the collective operation of indoor flying robots, it is necessary to first develop a control strategy for achieving stable hovering and obstacle avoidance capabilities. None of the existing commercially available platforms offer a solution providing autonomous indoor flight with an obstacle avoidance capability. This chapter develops a simple attitude estimation and control technique for stabilising a hovering platform using embedded inertial sensing. A simple sensing and control strategy is proposed for achieving obstacle avoidance and anti-drift control, which has been implemented on the robustness optimised hovering platform, from chapter 2. The approach is computationally simple, unlike laser scanner approaches, and will work in the dark or poor lighting conditions, unlike vision or optic-flow approaches. The results show that the simple sensing and control strategy can enable anti-drift control and obstacle avoidance behaviours on an indoor highly dynamic, hovering platform. The hovering platform is capable of automatic take-off, constant altitude control, obstacle avoidance, anti-drift control and automatic landing. This level of autonomous control alone is not enough to enable exploratory goal-directed flight. However, the flying robot that is presented in this chapter was one of the first indoor hovering platforms (Roberts et al., 2007) that could achieve such a capability without using any external aids.

---

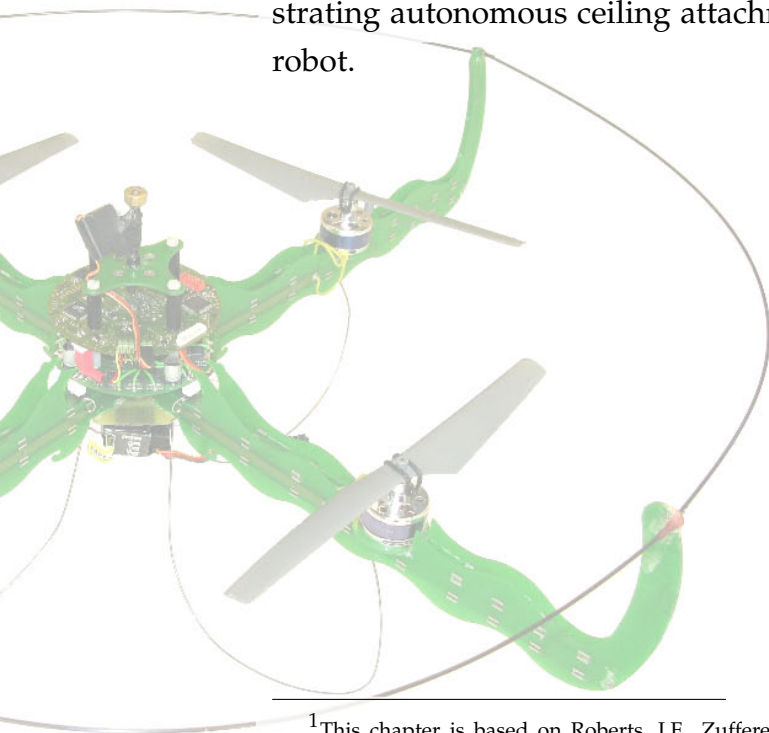
# 4

---

## Energy management

---

THE limitations in endurance, payload, sensing and processing capabilities of an indoor hovering platform, is directly related to the amount of energy that is available. For the collective operation of indoor flying robots to work in reality, this energy needs to be managed efficiently and conserved in a way that allows a swarm of robots to be useful, extending beyond the individual 10-20 min flight time. This chapter<sup>1</sup> tackles the energy problem of indoor flying robots. To aid in energy management, a generalised energy model is developed, allowing for the accurate estimation of the flight endurance and perching time of hovering platforms. In order to conserve energy, a method that allows a hovering platform to attach to, and detach from ferrous ceilings, while maintaining a birds-eye-view of the environment is developed. The chapter ends by demonstrating autonomous ceiling attachment and detachment on an indoor hovering robot.



---

<sup>1</sup>This chapter is based on Roberts, J.F., Zufferey, J.-C. and Floreano, D. (2008). Energy Management for Indoor Hovering Robots. *IEEE/RSJ International Conference on Intelligent Robots and Systems (IROS'2008)*.

## 4.1 Introduction

This chapter aims to mitigate the energetic cost of flying, in order to improve mission endurance and therefore the practicality of a swarm of indoor flying robots. Consider a swarm of flying robots being deployed one by one to search an indoor environment. It takes some time to deploy numerous flying robots. As each individual has a flight time of only 10-20 min, due to the limitations in battery technology, it is important to come up with alternative methods to extend mission endurance, otherwise the practicality of the swarm is highly limited.

There are various ways of prolonging the mission endurance of a flying robot, such as increasing battery specific energy density, improving thrust efficiency, harvesting energy from external sources, or designing behaviours that reduce the flight time and prolong mission time.

Increasing battery specific energy density is a slow moving process (Crompton, 2000). Since the first rechargeable Lead-Acid battery was invented in 1859 by Gaston Planté, it has taken 137 years to get to the latest Lithium Ion Polymer (LIPO/PLiON) battery, which was released in 1996. There are three important aspects that make a battery useful for flying robots. First, the battery must have a high specific energy density, in order to minimise the battery weight and allow for longer flight times. Second, the battery must be rechargeable (a secondary cell) to limit the cost of continuous use and provide a renewable operation. Third, the battery must be relatively safe to prevent danger to the user or the environment. The ideal battery would be able to provide an infinite amount of power, for an infinite amount of time and weigh nothing. However, in reality current battery technologies are limited in all of these respects (see figure 4.1).

In the field of indoor flying robots, the most common, currently used battery technology is the LIPO battery. This is mainly because it has the highest specific energy density among other batteries that are easily available in stores, including Lead-acid, Ni-Cd, NiMH and Li-Ion technologies. LIPO technology has a specific energy density ranging from 100 to 200 W.h/kg (Tarascon and Armand, 2001), which relates to a typical indoor flight endurance of 20 min (see section 1.2.1). There is a new battery technology, named Lithium Sulfur (LI-S), currently being developed that is expected soon to be released in the commercial market. LI-S technology has a specific energy density of 350 W.h/kg<sup>2</sup>, which is

---

<sup>2</sup><http://sionpower.com/technology.html> (accessed Feb. 2011)



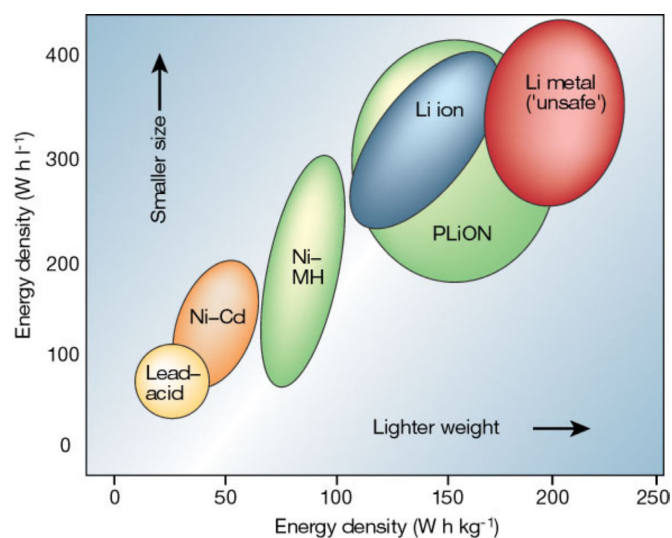


Figure 4.1: Comparison of the different battery technologies in terms of volumetric and gravimetric energy density (Tarascon and Armand, 2001)

nearly twice that of the LIPO technology. By simply replacing the LIPO batteries with LI-S batteries, an indoor flight endurance of 40 min could be attainable. As new technologies are developed the specific energy density of batteries will slowly increase, which will in turn provide a longer possible flight endurance for indoor flying robots. However, to obtain useful flight times extended over several hours, the battery technology needs to improve by a factor of five to ten times. Such a degree of improvement is not foreseen in the near future.

Another way to increase the endurance of a hovering platform would be to improve the propeller-motor thrust efficiency. However, as shown in chapter 2 there is a trade-off between the flight endurance, payload and robustness of an indoor hovering platform. In order to increase the endurance, through improving thrust efficiency, a larger platform would be required, which is not practical for indoor flying robots due to the indoor size constraints.

Additionally, harvesting energy from external sources could potentially allow for extended endurance. Thomas and collaborators have investigated several energy scavenging techniques including Photonic (solar), kinetic-flow (wind), thermal, electromagnetic, and autophagous structure - power concepts that allow for energy generation through self-consumption of system structure, for small unmanned systems (Thomas et al., 2006). However, for most of these techniques the amount of energy that can be collected indoors is minimal and the additional weight required is not practical for small flying robots.

Therefore, as the energy on a flying robot is a limited and valuable resource, it should be managed efficiently. In the context of a single flying robot, a mathematical model can be developed to predict the energy consumption of a hovering platform, allowing for the energy to be managed efficiently by high-level controllers. In order to develop an energy model, the power consumption of the hovering platform and embedded electronics needs to be determined. Information about the battery storage can easily be gathered, as most battery manufacturers provide the voltage, capacity (Ah) and mass of the battery. However, the power consumption of a hovering platform depends on many variables, including motor-propeller efficiency, platform weight and avionics power consumption, which have a high-level of interaction.

In the context of collective operation, a behavioural strategy can be developed to optimise the global mission endurance, allowing for efficient deployment of several flying robots. The types of indoor tasks that these robots will be used for are often tasks that require sensor analysis over an extended period of time, for example mobile sensor networks (Ogren et al., 2004) or surveillance and monitoring (Min et al., 2009), thus if the robot is hovering in a static position while performing the task then the valuable and limited energy resource is not efficiently managed. A perching mechanism can be utilised to extend the mission endurance of an indoor flying robot. Perching, whether on the floor or attached to the ceiling, can be considered as any state where the flying robot is not utilising its propulsion system. Perching mechanisms can provide a stable base for on-board systems, such as vision and infrared sensing. The limited available energy and payload of an indoor flying robot reduces the possibilities for on-board processing power. Thus, it can take some time to visually scan a room for a pre-defined target, while processing the images. However, perching presents an opportunity to attach to the ceiling and conserve energy, while providing a birds-eye-view of the environment and more processing time. It is challenging to find universal attachment technologies that will work on a broad range of surfaces. Research in this field is relatively new, therefore none of the existing technologies can provide a robust solution of attaching to non-ferrous ceilings (see section 1.2.2). However, in order to explore the ceiling attachment concept, techniques using magnets can be implemented. Once a suitable attachment technology is developed, the knowledge gained from the proof of concept, including control strategies and related problems, can speed up the realisation process.

A combination of energy management and perching methods would be useful to help mitigate the energetic cost of flying. In the context of collective operation, energy management can have a large impact on the usefulness of a swarm of flying robots. In the next section, a generalised energy model for hovering platforms is developed, which allows for the accurate prediction of flight and perching endurance. Additionally, a method of autonomously attaching to, and detaching from ferrous ceilings is developed, in order to conserve energy.

## 4.2 Materials and methods

This section first introduces a generalised energy model that can be used to estimate the flight endurance of any hovering platform. The endurance model is then extended to incorporate a perching time, allowing for any combination of flight and perching times to be predicted. Finally, the hovering platform and ceiling attachment mechanism is presented, in preparation for the experiments.

### 4.2.1 Flight endurance model

A model has been developed that incorporates all aspects relating to the conservation of energy of the hovering platform. The model provides the flight endurance ( $t_e$ ) estimation, for a specific battery and payload requirement, which can also be used for online estimation of the remaining flight time.

The energy of any mobile system can be defined by the amount of energy going into the system (energy storage) and the amount of energy going out of the system (work being done). The energy storage on the hovering platform is defined by the battery capacity ( $c_b$ ), represented as watt-hours (W.h), which gives an indication of the amount of power that can be delivered over a period of time. The work being done is related to the power required to lift the total take-off weight ( $m_t$ ) of the platform, and the total idle-state power consumption ( $p_i$ ) to operate the on-board electronics and sensors.

As the weight of the platform increases the amount of power required to lift it also increases (see figure 4.5). Additionally, if more payload mass ( $m_p$ ) is added, the weight of the platform further increases. If the payload consumes power ( $p_p$ ), for example a sensor using up energy, the power required by the platform will further increase. It would be beneficial to be able to model all of

these parameters so that the flight endurance can be predicted. Essentially, this is exactly what the energy model does using two main assumptions. The model assumes that when the platform is flying the collective thrust is equal to its own weight. The model also assumes that the fluctuations in the stability control response average to a constant value and are equal to the static thrust (thrust while not moving) test case.

The flight endurance model is defined as follows. First, the total take-off weight ( $m_t$ ) is obtained by summing the individual component masses of the structure ( $m_s$ ), battery ( $m_b$ ) and payload ( $m_p$ ):

$$m_t = m_s + m_b + m_p$$

Similarly, the total idle-state power consumption ( $p_i$ ) is a summation of the avionics power ( $p_a$ ) and payload power ( $p_p$ ) consumption:

$$p_i = p_a + p_p$$

The battery capacity ( $c_b$ ) can be defined by its specific energy density ( $e_d$ ) in W.h/kg and relative mass ( $m_b$ ):

$$c_b = e_d m_b$$

The estimated flight endurance ( $t_e$ ) can then be expressed as:

$$t_e = \frac{c_b}{p_m + p_i}$$

where  $p_m$  is the motor power required to lift the total take-off weight ( $m_t$ ) of the platform. The power of a single motor ( $p_{sm}$ ) is taken from the thrust curve (figure 4.5) at the point where the thrust equals the total take-off weight ( $m_t$ ), divided by the number of motors ( $n_m$ ). Therefore:

$$p_m = p_{sm} n_m$$

There is one major limitation, with respect to the battery voltage, that needs to be taken into account. As the battery voltage reduces during the flight, shown in figure 4.2), there is also a relative reduction in the maximum available thrust. Therefore, it is necessary to take a measurement of the motor thrust limit ( $m_l$ ), when the battery is at its minimum voltage. This thrust measurement allows for the maximum payload mass limit ( $m_x$ ) to be determined:

$$m_x = m_l - m_t$$

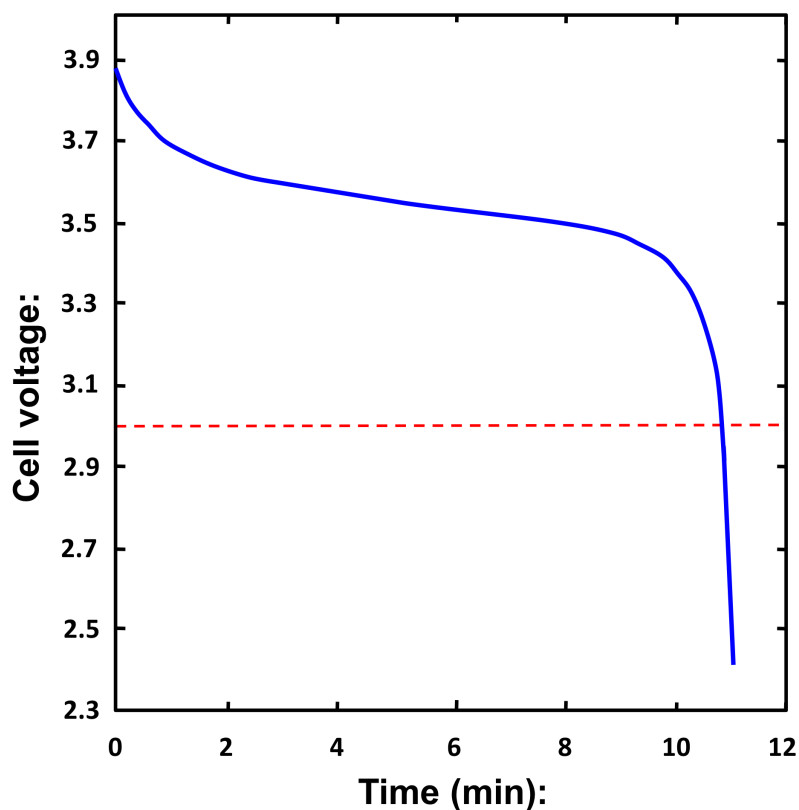


Figure 4.2: Discharge curve of a single cell LIPO battery. The dotted line represents the critical cell voltage.

The estimation model incorporates variations in payload mass, payload power consumption and idle state power consumption. With this method the performance of future battery technologies can also be estimated, based on the specific energy density of the current technology. The endurance model can be applied to various different hovering platforms by manipulating the motor power input parameter, without having to know anything about the discharge characteristics of the battery (see figure 4.2). This is possible as the amount of energy inside a battery is a finite number, the model simply uses this finite value in the prediction. At this stage the proposed model does not yet include battery degradation over the life cycle of the battery. Further studies on this topic would be required to determine where a significant effect on the estimated flight endurance starts to occur.

Now that the flight endurance model has been defined, the model can be extended to the perching case.

### 4.2.2 Perching endurance model

Perching should be taken in its general meaning of static attachment with the environment, which could be a simple landing or attaching to the ceiling. This kind of capability can extend the mission endurance from minutes to hours. However, in the case of ceiling attachment, it is important to leave some reserved energy for the platform to be able to detach from the ceiling, fly back and land safely. The platform continues to consume power while perching, at a rate determined by the idle-state power consumption. The model can be extended to estimate the remaining operation time of the system while perching. It can also be adjusted to estimate the reserved energy to determine the flight endurance after perching for a given time.

The estimated perching endurance ( $t_p$ ) can be calculated without the influence of the motor power consumption:

$$t_p = \frac{c_b}{p_i}$$

In order to easily transfer the energy between flying and perching endurance, the energy can be represented as a reserved energy ratio ( $r_e$ ), relating to the original estimated flight endurance ( $t_e$ ) and the elapsed flight time ( $t_f$ ):

$$r_e = \frac{t_e - t_f}{t_e}$$

This allows the reserved endurance to be calculated at the exact moment the platform attaches to the ceiling. The reserved endurance energy ratio ( $r_e$ ) can then be used to take into account the time that the platform is attached to the ceiling. The post perching reserved endurance energy ratio ( $r_{ep}$ ), which is the reserved endurance energy ratio ( $r_e$ ) after an elapsed attachment time ( $t_a$ ), can then be defined as:

$$r_{ep} = r_e - \frac{t_e t_a}{t_p}$$

The reserved endurance ( $t_r$ ), which takes into account the elapsed flight time ( $t_f$ ) and the elapsed attachment time ( $t_a$ ), can then be calculated:

$$t_r = \frac{c_b r_{ep}}{p_m + p_i}$$

Representing the energy as an endurance ratio, makes for a highly flexible model that allows for any combination of flight and perching times to be predicted.

Now that the model has been extended to perching, the hovering platform can be presented, in preparation for the experiments.

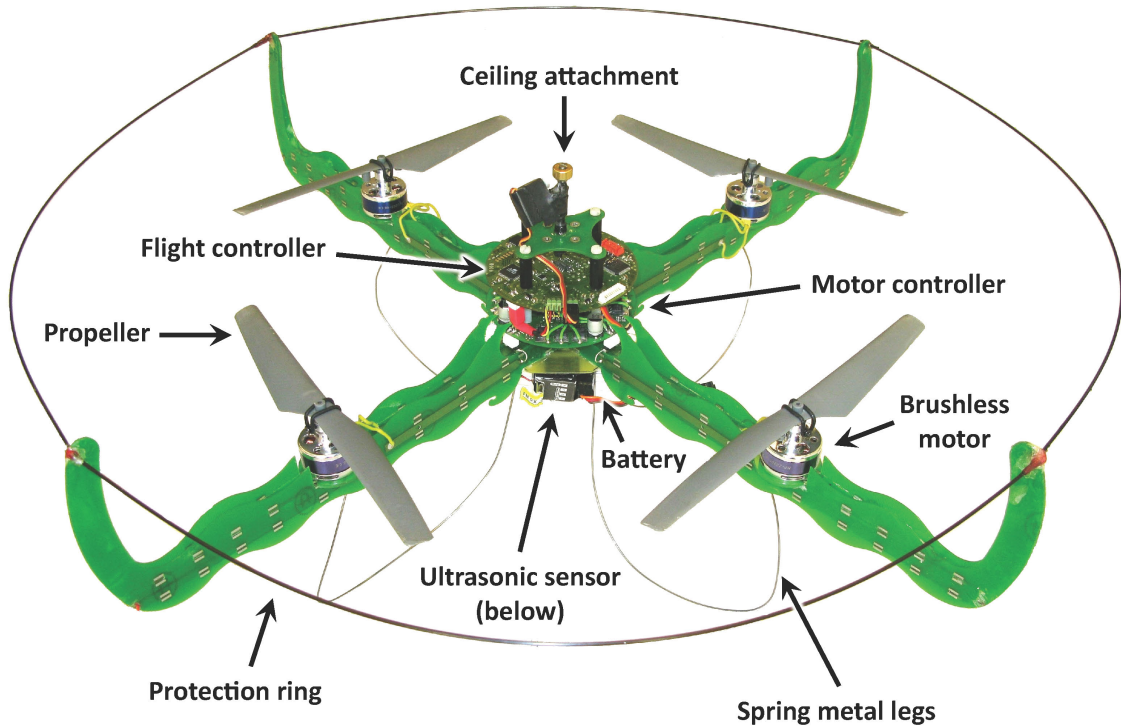


Figure 4.3: Quad-rotor fitted with the propulsion system, control boards, sensors and ceiling attachment device

### 4.2.3 Hovering platform preparation

The robustness optimised hovering platform, from chapter 3, is a useful test platform for implementing the endurance and perching estimation model.

In order to achieve autonomous ceiling attachment the platform, shown in figure 4.3, has been fitted with a simple ceiling attachment mechanism. Autonomous altitude control is implemented using the same simple sensing and control strategy presented in chapter 3. For easy experimentation the commands for the pitch, roll and yaw are given by a safety pilot. Additionally, the platform has an automatic landing feature, which is triggered when the flight computer detects that the battery level is at the minimum battery voltage. This feature is used to prevent damage to the battery, increase the flight safety for the pilot and the platform, and allows for accurate timing of the endurance during experiments. The voltage for battery cut-off is set at 3.0 V per cell, which is recommended by the battery manufacturer. Therefore, if the 3-cell Lithium Polymer (LIPO) battery voltage goes below 9.0 V, the platforms thrust is slowly decremented for a safe automatic landing.

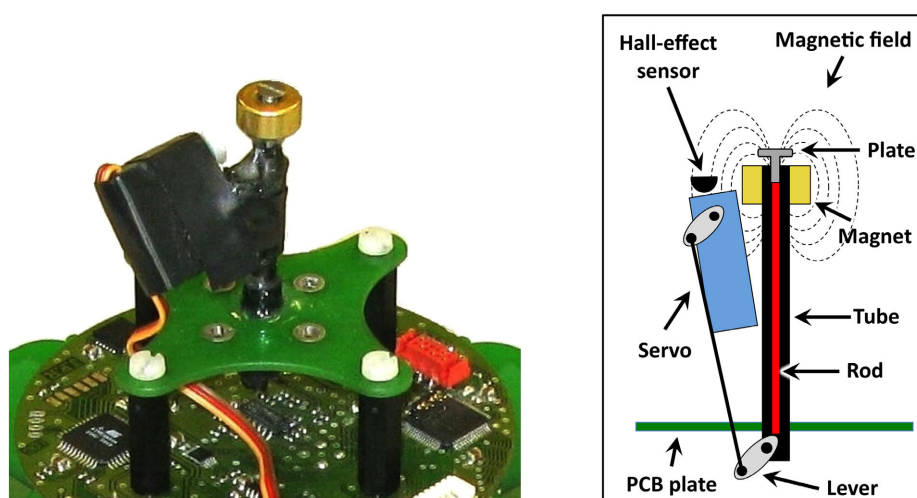


Figure 4.4: *Left*: Ceiling attachment mechanism. *Right*: Functional diagram.

In order to attach to the ceiling a proof of concept device has been developed utilising magnets (see video<sup>3</sup>). By using a magnetic system, the task of attaching to the ceiling is greatly simplified. In the future it may be possible to use more universal attachment technologies, such as dry adhesives (Unver et al., 2006; Murphy et al., 2006; Kim et al., 2007; Autumn et al., 2006), to attach to non-ferrous ceilings. However, the main goal of this research is to explore the concept of ceiling attachment and not to develop new attachment technologies.

A small (2.5 g) gold plated, toroidal neodymium magnet is used to attach to ferrous ceilings, which has a total attractive force of 2.2 kg (21.5 N). The ceiling attachment device, shown in figure A.4, is located centrally at the top of the platform. A passive system like this allows the platform to remain attached to the ceiling, while consuming minimal energy. A small servo motor, controlled by the flight computer, is used to detach from the ceiling. The servo converts the electrical energy into mechanical motion that is used to drive a lever. The mechanical lever pushes a carbon fibre rod up through the centre of the toroid. At the end of the rod there is a small metal plate which is used to push against the ceiling. As the plate extends, the gap between the top of the magnet and the ceiling increases, until the attractive force of the magnet is too weak to keep the platform attached. The hovering platform then detaches and can continue flying. To detect when a ferrous ceiling is present, a hall-effect sensor has been placed perpendicular to the toroidal magnet. The hall-effect sensor can detect

<sup>3</sup>Video: <http://jfroberts.com/phd> (quadrotor\_ceiling\_attachment.mp4)



small changes in the magnetic field, when the sensor comes near a ferrous object. This can be used as an indication of when the ceiling attachment device has a connection. At the building where these tests were conducted most of the ceilings are metallic. This system is by no means solving the problem of ceiling attachment, however it does provide the practicality for proving the concept.

Now that the energy model and the test hovering platform are ready for operation, the practical implementation and validation experiments can begin.

## 4.3 Results

This section first characterises the static thrust of the propulsion system, showing the relationship between power consumption and thrust generation. The estimation model is then used to find the best battery for the hovering platform, by performing an optimal search from a list of available batteries. Finally, two experiments are presented in order to observe the accuracy of the flight and perching endurance estimation, with multiple autonomous attachments and detachments. During these experiments the payload mass, payload power consumption and time spent attached to the ceiling is varied.

### 4.3.1 Static thrust characterisation

In order to estimate the flight endurance it is necessary to first characterise the propeller and motor setup. In this case, a custom test-rig to measure the thrust and power consumption of the motor-propeller system was developed. This simple test-rig consists of an aluminium motor mount, motor speed controller, current and voltage meters and weight balance. The motor is fixed to the motor-mount, which is then attached to the weight balance. By attaching the test-rig directly to the weight balance the thrust can be directly read from the meter (after zeroing the setup mass). A high current DC power supply can be used to regulate the input power and simplify the testing. The current and voltage meters are used to determine the power consumption. Samples of the current and voltage are then taken at regular thrust increments depending on the desired resolution. The propeller should be inverted, so that the airflow is facing upwards, to prevent any ground effect errors caused by the propellers downwash.

In order to determine the thrust curve, shown in figure 4.5, the above proce-

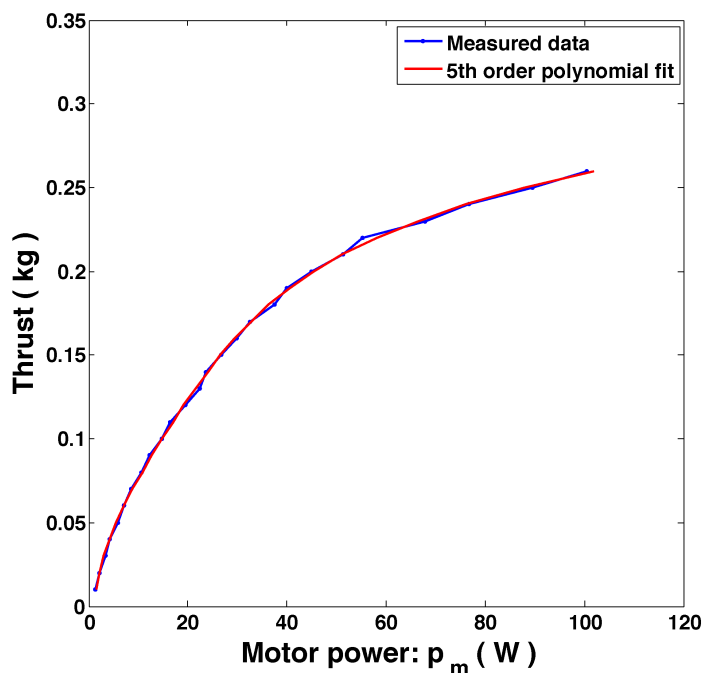


Figure 4.5: Thrust curve of the motor-propeller system showing the power required for a certain hover thrust (taken at a nominal voltage of 12.5 V)

ture has been used to characterise the quad-rotor motor-propeller system. Samples of the current and voltage were taken at thrust increments of ten-grams. A thrust model has been created by fitting the characterisation data to a fifth order polynomial. For the quad-rotor platform,  $n_m$  is equal to four, thus the single motor power ( $p_{sm}$ ) is taken from the thrust curve at the point where the thrust is equal to a quarter of the total take-off weight.

Now that the propeller and motor has been characterised, the energy model can be used to find an optimal battery for the hovering platform.

### 4.3.2 Battery selection optimisation

In order to maximise the flight endurance of the platform the optimum battery should be found. The energy model can be used to find the optimum battery weight for a given platform, based on the platforms specific thrust, power and weight properties.

Plotting the estimated flight endurance, using equation 4.2.1, versus the battery mass, shown in figure 4.6, indicates that there is an optimal point where the flight endurance is maximised. This point can be referred to as the “Ideal

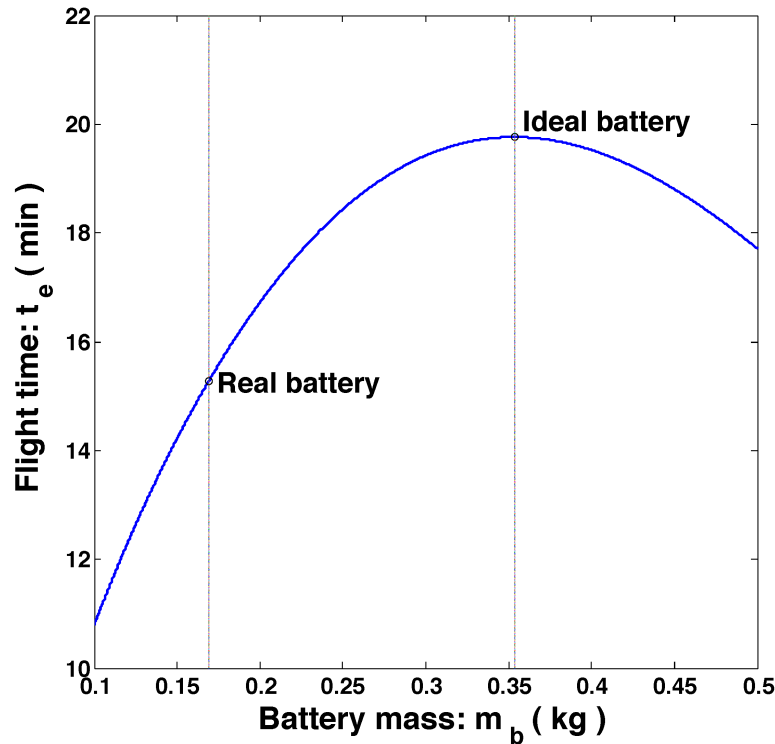


Figure 4.6: Flight time versus battery mass, showing the optimum battery mass for the quad-rotor without additional payload ( $m_s=0.431$  kg,  $m_p=0$  kg,  $p_a=2.44$  W,  $p_p=0$  W,  $e_d=164$  W.h/kg)

battery” optimum, as it shows the extended endurance as if the battery voltage was kept constant until all of its energy is depleted. However, in reality the voltage of a battery (see figure 4.2) reduces slowly as the energy is depleted. This lower voltage causes a reduction in the maximum available thrust. Therefore, to obtain the realistic optimum, the maximum payload limit ( $m_x$ ) taken at the minimum battery voltage should be applied. This limit, shown in figure 4.6, is used to determine the “Real battery” optimum. The output of the optimisation function shows that the optimal ideal battery mass and the optimal realistic battery mass is  $m_b=0.353$  kg and  $m_b=0.169$  kg, respectively. This relates to a predicted endurance of  $t_e=19.76$  min, and  $t_e=15.28$  min, respectively.

It is possible to use this optimisation method to automatically select the best battery from a list of battery packs available in shops. This is done by first creating a list of the battery specifications, which must include the specific energy density and the battery mass as given by the manufacture. The optimisation method above is then performed on each of the batteries in the list. After doing

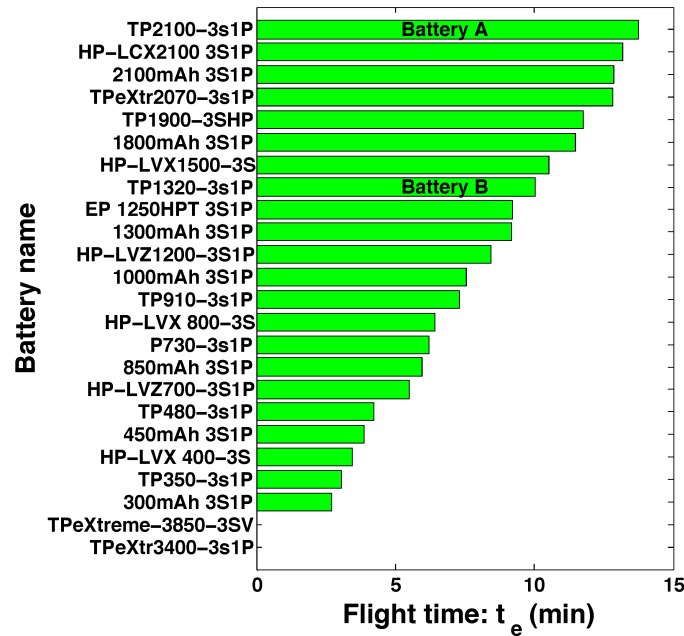


Figure 4.7: List of battery packs sorted by flight endurance. Battery-A = TP-2100-3S1P, Battery-B = TP-1320-3S1P ( $m_s=0.431$  kg,  $m_p=0$  kg,  $p_a=2.44$  W,  $p_p=0$  W)

this for every battery, the list can then be sorted in order of flight endurance, where the battery with the highest endurance is the optimal battery for the system. For the hovering platform, a list has been created from 24 different 3-cell battery packs that are available online. The sorted list, shown in figure 4.7, indicates that the optimal battery is the “TP-2100-3S1P”, which is defined as “Battery-A”. Any battery that does not meet the payload limit has its respective endurance set to zero.

Now that the optimal battery has been determined for the hovering platform, the endurance testing can begin.

### 4.3.3 Endurance test

The first experiment is designed to observe the accuracy of the estimations, for variations in payload mass and payload power consumption, with two different battery sizes.

The platform was flown under manual control and a stop watch was used to time the flight endurance. Battery-A ( $m_b=0.144$  kg,  $e_d=164$  W.h/kg) was chosen because it is the optimal battery for the system without payload, and Battery-B ( $m_b=0.085$  kg,  $e_d=172$  W.h/kg) was chosen because it lies in the middle range

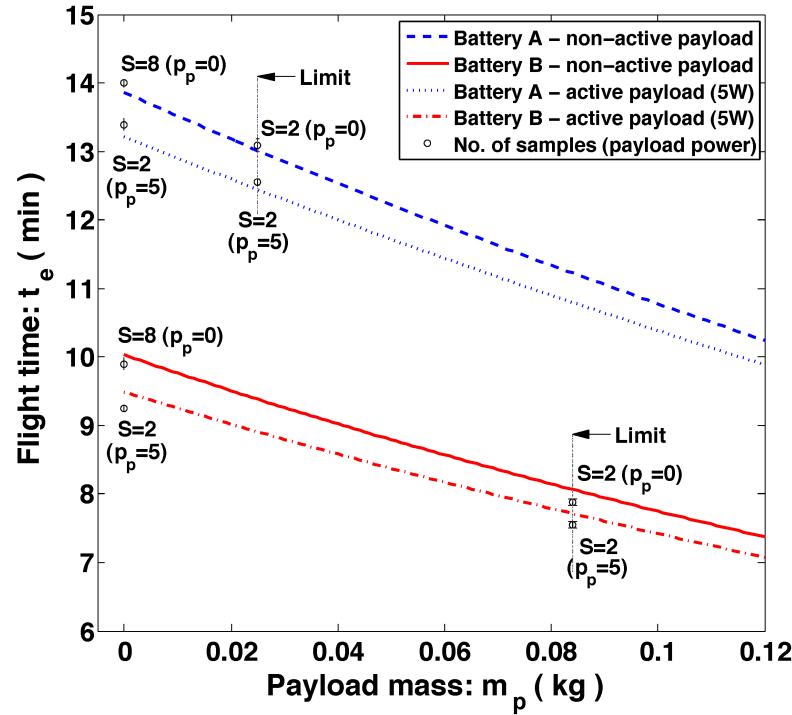


Figure 4.8: Estimated and measured endurance for variable payloads and active payload power consumptions. Error bars have been plotted on each sample point marked by a circle ( $m_s=0.431$  kg,  $p_a=2.44$  W. Battery-A:  $m_b=0.144$  kg,  $e_d=172$  W.h/kg. Battery-B:  $m_b=0.085$  kg,  $e_d=164$  W.h/kg).

(see figure 4.7). The estimated flight endurance, shown in figure 4.8, over the full range of payloads has been plotted for both batteries, each with and without an active payload of 5 W. The top pair of lines and the bottom pair of lines represent the estimated flight endurance of Battery-A and Battery-B, respectively. The higher line and the lower line of each pair represents the non-active and active payloads, respectively. In order to see the realistic range of the endurance estimations, the maximum payload limits ( $m_x$ ), have been indicated. Samples have been taken at the minimum and maximum payload points, with and without the active payload. For the no-payload test cases, a set of eight flight time samples were taken for the two different battery sizes. However, due to the large amount of time required to do the extra 48 test flights, only two samples have been taken for the other test cases. We assume that these two samples are a reasonable representation of the actual measured endurance. We also assume that if the minimum and maximum payload limits are reasonable, then any measurement between these points are also realistic representations.

For both battery sizes, shown in figure 4.8, the estimated flight endurance is very accurate, where the samples have a maximum mean error of only 2.52%. These results suggest that the power model for flight endurance estimation, for both payload mass and payload power consumption, is realistic and that the assumptions are reasonable.

Now that the flight endurance estimation has been validated, the testing can be extended to incorporate perching.

#### 4.3.4 Ceiling attachment test

The second experiment was designed to test the perching endurance estimation and to observe the accuracy of the estimations, for a mission with multiple autonomous ceiling attachments and detachments.

The altitude log for a single autonomous ceiling attachment and detachment cycle, is shown in figure 4.9. The quad-rotor performs an automatic take-off and hovers at the pre-defined altitude of 1 m. A command is wirelessly sent to the quad-rotor to initiate a ceiling attachment. The altitude then slowly increments until the quad-rotor is attached to the ceiling at 2.5 m. The hall-effect sensor is used to determine if the quad-rotor has a good connection and then the motors are powered down. After some time, the detach command is sent to the quad-rotor causing it to reactivate the motors, detach from the ceiling and return to the pre-defined hovering altitude. The quad-rotor then performs an automatic landing on the ground.

An additional experiment was conducted to test a realistic mission cycle with multiple ceiling attachments and detachments. The quad-rotor was commanded to fly through several cycles of hovering, attaching to the ceiling, powering off the motors and waiting, re-activating the motors and detaching from the ceiling. The hovering time and perching time have been defined as 2 min and 30 min, respectively. This cycle was repeated three times, giving a total elapsed flying time ( $t_f$ ) of 6 min and a total elapsed perching time ( $t_a$ ) of 90 min. The flight time from the last detachment, until the battery was depleted was then recorded.

The endurance models, for both the hovering and the perching cases, have been used to estimate the total mission endurance of 103 min ( $m_s=0.431$  kg,  $p_a=2.44$  W,  $m_b=0.144$  kg,  $e_d=164$  W.h/kg). The measured mission endurance was recorded for two different test cases. The estimated mission endurance, shown in Table 4.1, is very accurate, giving a mean error of only 0.97%. These results

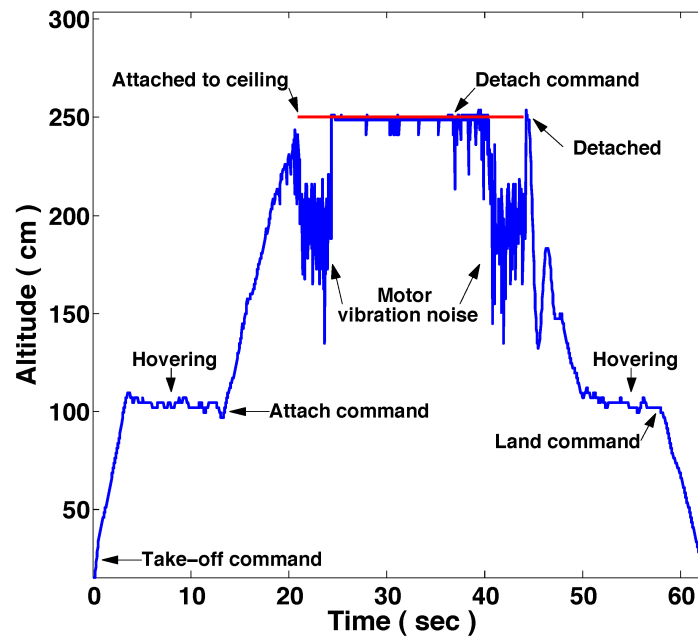


Figure 4.9: Altitude log during a single autonomous ceiling attachment and detachment cycle

Table 4.1: Mission endurance estimation for two test cases, each including three cycles of hovering and perching

Case	Battery	Estimated (min)	Measured (min)	Remaining endurance error (%)	Overall error (%)
Test 1	Battery-A	103.3	102.1	16.4	1.16
Test 2	Battery-A	103.3	102.5	10.9	0.77

suggest that the power model for ceiling endurance estimation is realistic and that the assumptions are reasonable.

It would be possible to implement the endurance estimation model on the actual platform to give the platform an “awareness” of its own available energy. A small battery monitoring circuit could be permanently fitted to each battery, running the proposed model as an online estimation algorithm. Information about the platform could be communicated to the device in order to accurately determine the platforms flight time. An algorithm could then be used to adjust the estimation for battery degradation based on the error between the estimated and actual measured flight endurance.

This information can be used by higher-level control strategies for optimising the limited energy resource. Additionally, it might be interesting to incorporate an automatic recharging system, where the platform can dock to a ceiling based recharging station for fully autonomous operation over long endurance indoor missions. However, for such a system to be viable, some form of relative positioning sensing would be required, to guide the platform to the docking station.

## 4.4 Conclusion

For the collective operation of indoor flying robots to work in reality, the limited energy on a hovering platform needs to be managed efficiently and conserved in a way that allows a swarm of robots to be useful, extending beyond the individual 10-20 min flight time. To aid in energy management, a generalised energy model has been developed, allowing for the accurate estimation of the flight endurance and perching time of hovering platforms. The energy model can be used to optimise the battery selection process of a hovering platform, to obtain the highest possible endurance. In order to conserve energy, a method has been developed that allows a hovering platform to attach to, and detach from ferrous ceilings, while maintaining a birds-eye-view of the environment. The concept of ceiling attachment has been successfully demonstrated, by flying through several cycles of hovering, attaching to the ceiling, powering off the motors and waiting, re-activating the motors and detaching from the ceiling. The interesting point of this study was not the ceiling attachment mechanism itself, as the proposed mechanism only works on ferrous ceilings, it was about proving the concept of achieving such a capability on an indoor flying robot and being able to perform this in an autonomous manner. The experimental results show that it is possible to predict mission endurance, including several cycles of flying and perching, with an average overall mission endurance error of 0.97%. This is the only model known that is able to predict any combination of flying endurance and perching times. By applying energy management techniques, through use of energy modelling and behaviours that reduce the flight time, the energetic cost of flying can be mitigated and the mission endurance can be extended. This is especially useful for collective operation, as efficient deployment strategies could optimise the task allocation and implementation of individual robots within the swarm.



---

# 5

## 3-D relative positioning

---

**I**N order to enable the collective operation of indoor flying robots, spatial-coordination between individual robots is essential. However, there is a lack of on-board sensing technologies available that can enable spatial-coordination in real-world environments. No existing sensors, commercially available or in research can provide embedded 3-D relative positioning for indoor hovering platforms. This chapter<sup>1 2</sup> introduces a practical on-board sensing method for achieving spatial-coordination between multiple robots in three dimensions. First, the underlying functioning principle of the 3-D relative positioning sensor is explained. The details of the sensor are then discussed, including the communication algorithm, the infrared transmission and reception process. The physical constraints and possible layouts of the sensor are then described, showing how it can be constructed for a flying robot. Extensive characterisation is then performed on the sensor to determine its range, bearing and elevation performance. The chapter ends by comparing the developed 3-D relative positioning sensor with the best three 2-D relative positioning sensors found in the literature.



---

<sup>1</sup>This chapter is based on Roberts, J.F., Stirling, T.S., Zufferey, J.-C. and Floreano, D. (2012). 3-D Relative Positioning Sensor for Indoor Collective Flying Robots. *Autonomous Robots (in preparation)*.

<sup>2</sup>Additionally, the chapter builds upon Roberts, J.F., Stirling, T.S., Zufferey, J.-C. and Floreano, D. (2009). 2.5D Infrared Range and Bearing System for Collective Robotics. *IEEE/RSJ International Conference on Intelligent Robots and Systems (IROS'2009)*.

## 5.1 Introduction

This chapter introduces a sensor designed to enable spatial-coordination and collective operation between multiple flying robots, in real-world environments.

Relative positioning sensors constitute the holy grail of collective robotics. They allow multiple robots to cooperate and work together in a team to achieve a common goal. Relative positioning sensors use simple, local sensing and communication in the form of distances and angles between neighbouring robots. This simple local sensing and communication minimises the embedded computational requirements, as the relative position information is directly attained.

To the best of our knowledge, the only on-board relative positioning system for an indoor flying robot is presented by Welsby and Melhuish (2001); Melhuish and Welsby (2002) for use on a swarm of lighter than air vehicles. In their work, a long range (20 m) infrared relative positioning sensor is used to achieve a simple gradient ascent behaviour towards an emitting beacon. However, due to the small payload available on a lighter than air vehicle and its very slow dynamics, their sensor was reduced to only  $180^\circ$  sensing. All of these existing relative positioning sensors (see section 1.2.4) give only planar 2-D information. This 2-D information is useful for robots operating on the ground and for flying robots with slow dynamics that stay at the same height and do not tilt their body as they fly. However, for flying robots that have fast dynamics (e.g. helicopters and quad-rotors), fast and high accuracy sensing is required. During flight, these platforms can tilt as they translate and the difference in altitude can vary by several meters. Therefore, to achieve robust sensing for highly dynamic flying robots it is necessary to have a 3-D sensor coverage.

By having at least one flying robot stationary, used as a static reference point, several flying robots can use relative positioning information to achieve position control, mitigate platform-drift, enable goal-directed flight and achieve collective operation. Such an approach could be used in most situations, as it does not rely on feature extraction in the surrounding environment like SLAM based (laser scanner and vision) approaches and is computationally simple. The performance of existing relative positioning sensors (see section 1.2.4) suggest that infrared could provide fast update rates and a long range, however this has not yet been achieved. Additionally, there are no existing sensors, commercially available or in research that can provide on-board 3-D relative positioning.

The aim of this chapter is to design an infrared 3-D relative positioning sensor that is capable of sensing the range, bearing and elevation between indoor flying robots, which can also provide proximity sensing in a 3-D space. Such a sensor can potentially enable goal-directed flight and collective operation between multiple flying robots, within real-world environments. The developed approach should allow for easily adaptation, to suit other robots and applications, depending on a specific sensing requirement.

## 5.2 Materials and methods

This section introduces the underlying functioning principle of the 3-D relative positioning sensor, to explain how it operates. The details of the sensor are then discussed, including the communication algorithm, the infrared transmission and the reception process. Finally, the physical constraints and possible layouts of the sensor are described, showing how it can be constructed for a flying robot.

### 5.2.1 Functioning principle

To explain the functioning principle of the 3-D relative positioning sensor, two sensors can be represented as spheres, where one is transmitting and the other is receiving infrared signals. In this example the emitting and receiving functionalities are represented separately, however during normal operation each sensor will implement both functions. The receiving sensor must be able to detect the relative range, bearing and elevation of the transmitting sensor within a localised 3-D space. An example diagram showing the 3-D geometry can be seen in figure 5.1. The transmitting sensor emits infrared equally in every direction. As the infrared signal propagates through the air the signal is attenuated, thus the received signal strength is proportional to the inverse square of the range ( $r$ ) between the sensors (Naboulsi et al., 2005). The signal strength ( $s$ ) from each photodiode can be linearised and converted into a range using a linear interpolator and a look-up table. The receiving sensor detects this emitted signal on multiple photodiodes and can triangulate the bearing and elevation angles towards the transmitting sensor.

In order to calculate the relative range, bearing and elevation to the transmitting sensor, a variation of the 2-D (range and bearing) sensor algorithm as

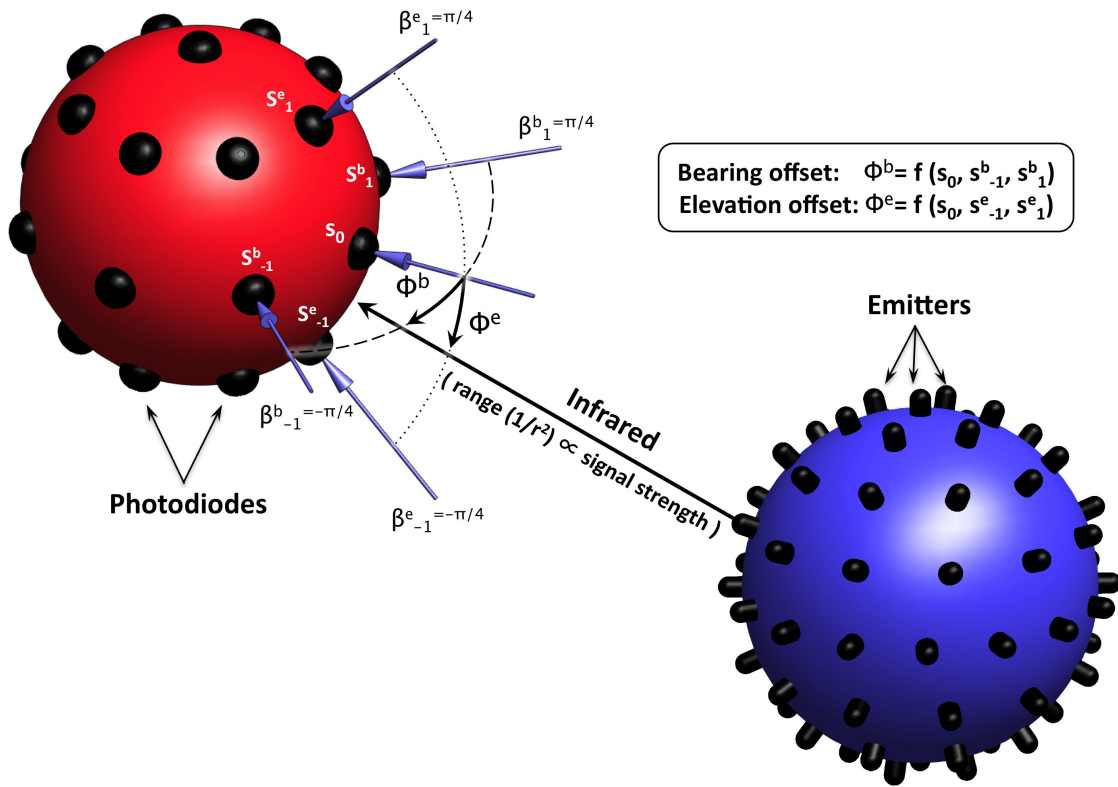


Figure 5.1: Example diagram showing the idealised 3-D geometry of one sensor receiving (*left*) and another transmitting sensor (*right*), where both are represented as spheres. The received signal strength ( $s$ ) is proportional to the inverse square of the sphere-to-sphere range ( $r$ ). The sensor with the strongest signal strength is defined as  $s_0$  and the angular spacing ( $\beta$ ) of the sensors is  $\frac{\pi}{4}$ . The bearing and elevation offset angles can be triangulated using the three sensor values ( $s_{-1,0,1}$ ) along the corresponding plane. In this example the emitting and receiving functionalities are represented separately, however during normal operation each sensor will implement both functions.

described by Pugh et al. (2009) is employed, which has been extended to 3-D. This algorithm assumes that both the bearing ( $\theta^b$ ) and elevation ( $\theta^e$ ) angles are calculated using only planar spaced photodiodes that are angled equally about the corresponding axis. The geometry of the photodiodes and their angular sensitivity determines the way in which the bearing and elevation angles are calculated. The angular sensitivity of the photodiodes that has been used, is closely

modelled by the square-root of the cosine function<sup>3</sup> using the angle of incidence ( $\theta$ ) to the transmitter. Therefore, if  $r$  is the range term of the photodiode when directly facing the transmitter, the value of the linearised signal strength ( $s'$ ) with respect to the angle of incidence to the transmitter can be approximated by:

$$s' = s\sqrt{\cos(\theta)}, \quad \text{with} \quad s = \frac{1}{r}$$

During a transmission approximately half of the photodiodes around the sphere will detect a signal. Thus, the “area of interest” can be defined as a set of  $m$  sensors with the highest received signals, where  $m$  is no greater than half of the number of sensors around the sphere. The photodiode closest to the centre of this area, i.e. with the strongest linearised signal strength, is defined as  $s_0$ . The horizontal planar sensors corresponding to the bearing have a clockwise or counter-clockwise angle from the centre of the receiving area, whereas the vertical planar sensors corresponding to the elevation have a higher or lower angle than the centre of the receiving area. Let the sensors that have a higher or counter-clockwise angle be defined as  $s_1, \dots, s_{\frac{m}{2}}$ , and the sensors that have a lower or clockwise angle be defined as  $s_{-1}, \dots, s_{-\frac{m}{2}}$ . The sensor values, for the corresponding horizontal or vertical plane, can then be defined as:

$$s'_i = s\sqrt{\cos(\theta + \beta_i)}, \quad \text{with} \quad \beta_i = -\beta_{-i}$$

where  $\beta_i$  is the angular offset of sensor  $i$  from the centre of the area. By rearranging the equation to incorporate the signal values from multiple photodiodes, it can be derived that:

$$\begin{aligned} s'^2_{-i} + s'^2_i &= s^2 \cos(\theta - \beta_i) + s^2 \cos(\theta + \beta_i) \\ &= 2s^2 \cos(\theta) \cos(\beta_i) \\ s'^2_{-i} - s'^2_i &= s^2 \cos(\theta - \beta_i) - s^2 \cos(\theta + \beta_i) \\ &= 2s^2 \sin(\theta) \sin(\beta_i) \end{aligned}$$

In order to find the angle of the incoming signal, these sensor values need to be combined:

$$a = \frac{\sum_{i=1}^n s'^2_i + s'^2_{-i}}{\sum_{i=1}^n 2 \cos(\beta_i)} = s^2 \cos(\theta), \quad c = \frac{\sum_{i=1}^n s'^2_i - s'^2_{-i}}{\sum_{i=1}^n 2 \sin(\beta_i)} = s^2 \sin(\theta)$$

<sup>3</sup><http://www.vishay.com> (BPV22NE, accessed Feb. 2011)

The bearing and elevation angular offsets ( $\phi^{b,e}$ ) from the centre of the segment can then be calculated using the sensor values from their corresponding planes. The linearised signal strength ( $s^{b,e}$ ) for the co-planar ranges can also be corrected by exploiting the trigonometric identity,  $A = A\cos^2(x) + A\sin^2(x)$ :

$$\phi^{b,e} = \arctan\frac{c}{a}, \quad s^{b,e} = (a^2 + c^2)^{\frac{1}{4}}$$

The linearised signal strength ( $s^{b,e}$ ) must then be corrected depending on the angular offsets ( $\phi^{b,e}$ ) from the opposite plane. Thus, the sphere-to-sphere range ( $r$ ) can be defined as:

$$r = \frac{2}{s^b \sqrt{\cos(\phi^e)} + s^e \sqrt{\cos(\phi^b)}}$$

The bearing ( $\theta^b$ ) and elevation ( $\theta^e$ ) angles of the transmitting sensor are then determined by the offset angles ( $\phi^{b,e}$ ) and the photodiode geometric spacing ( $\beta_i$ ), with respect to the corresponding plane:

$$\theta^{b,e} = \phi^{b,e} + \beta_i$$

This method explains how the relative range, bearing and elevation to a transmitting robot can be estimated using multiple signals from a known geometric sensor spacing. As the algorithm calculations are relatively simple, the processing can be implemented easily on a micro-controller.

## 5.2.2 Coordination among multiple sensors

Since the goal is to use this sensor for collective operation, signal interference from multiple infrared transmissions must be prevented, thus only one sensor at a time can be transmitting within the local transmission range of the sensor. For dynamic scalability, communication algorithms such as Carrier Sense Multiple Access (CSMA) can be implemented (Pugh et al., 2009). Such algorithms provide a maximum robot density in a given area, which is dependant on the operational update-rate. This link between robot density and operational update-rate is the key limitation of any sensor designed for collective operation. Therefore, increasing the update-rate of the sensor allows for an improved robot density. As the development of scalable communication algorithms is a solved problem, the focus here is on developing higher operational update-rates. Thus,

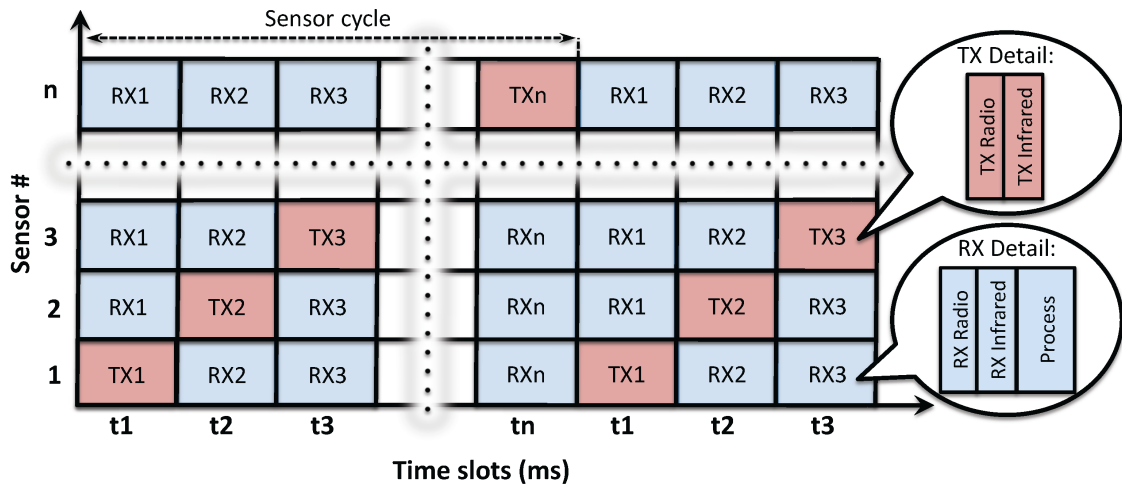


Figure 5.2: Sensor timing diagram. Each sensor takes a turn in transmitting (TX) while the others receive (RX) and calculate the range, bearing and elevation measurements.

a simple turn-taking algorithm is employed, where each sensor takes a turn to transmit while the others listen (see figure 5.2). This is done by creating time slots, where each time slot is allocated a number that repeats every sensor cycle. Each sensor communicates with the others to coordinate the transmission sequence and allow for synchronisation.

Existing range and bearing sensors (McLurkin and Smith, 2004; Pugh et al., 2009; Melhuish and Welsby, 2002; Kelly and Keating, 1996) encode the communication data directly into the infrared signal. However, as the data encoding takes an extended time, this slows down the sensor cycle and increases the complexity of both the transmitter and receiver electronics. To mitigate these problems the data communication is separated from the infrared signal and a simple radio transceiver is used to send the communication data. Doing this allows for a faster infrared signal sampling, thus reducing the sensor cycle time and effectively increasing the update-rate of the sensor by a factor of four when compared to the fastest existing 2-D sensor (Pugh et al., 2009).

When a sensor is activated, the sensor will begin by listening on the radio for another sensor. If no other sensor is detected within 10 sensing cycles, which is long enough to assume that there are no other sensors active, it will start transmitting in the first time slot. The time slot spacing can be adapted to suit the application, where  $t$  in ms, is the minimum time required to receive the radio

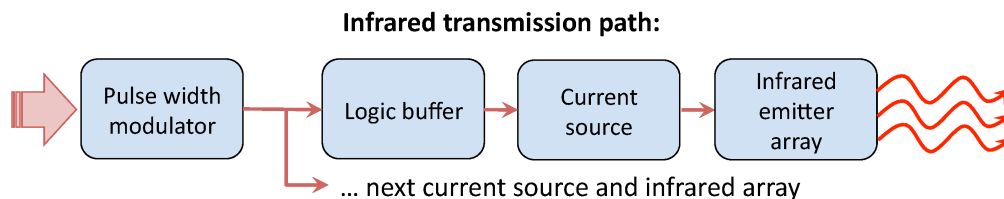


Figure 5.3: Transmission block diagram showing the infrared transmission path of the emitter arrays

communications, sample the infrared signal and process it to obtain a relative position measurement. Therefore, there are  $n$  time slots of  $t$  available, where  $n$  is equal to the maximum number of robots in the swarm, giving a sensor update rate of  $\frac{1}{tn}$  kHz. If another sensor is then activated, it will start to listen and within 2 sensor cycles it should detect the first sensor. After the second sensor detects the first it will then begin to transmit in the next available time slot, in this case time slot 2. This is true for additional sensors, up until the last empty time slot ( $n$ ) in the sensor cycle is filled. The number of time slots can be dynamically adapted to accommodate any number of sensors. The only limit here is that the update rate is reduced by adding more time slots. However, as the update-rate of the sensor is very fast (1 kHz), the developed simple turn taking algorithm can provide enough speed (10 Hz per robot) for a swarm of up to 100 flying robots.

### 5.2.3 Infrared transmission

In order to obtain the best range, bearing and elevation measurements, it is necessary to evenly emit infrared light in all directions, the more evenly the light is spread, the less the error will be if the sensor is rotated during operation. The number of emitters required for full spherical coverage depends on the emitter beam-width, where the angle of half intensity defines the geometric emitter spacing. However, there is a compromise between the number of emitters and the maximum range of the sensor. If you compare two infrared emitters with the same radiation power, the emitter with the smallest beam-width will have the highest light concentration, thus a further range. Therefore, to improve the maximum range of the sensor it is beneficial to use a high number of emitters with a small beam-width and a high power rating.

A block diagram of the infrared transmission path is shown in figure 5.3. A



constant current source is required to keep the radiated power at a constant level. This current source needs to be pulsed at a defined carrier frequency, which is activated on demand during a communication time slot. The carrier frequency allows the received signal to be bandpass filtered to reject other frequencies that are emitting on the same wavelength. To reduce the number of driver components, arrays of emitters can be used, where one transistor current source can drive several serially connected emitters. Each current source is controlled by a logic buffer to prevent overloading the micro-controller's Pulse Width Modulator (PWM) output pin. The array dimensions are determined by the voltage drop across the emitters and the maximum voltage that is available to the sensor. During a communication time slot the micro-controller will enable its PWM and drive the emitters at the defined carrier frequency with a constant radiated power.

#### 5.2.4 Infrared reception

An important part of the sensor operation is the infrared reception, as the performance of the sensor depends on the quality of the received signal strength. The infrared signal strength is proportional to the inverse square of the range (Naboulsi et al., 2005), meaning that it is difficult to obtain a high dynamic range over a long distance. A standard method to measure the signal strength, is to use a Radio Frequency (RF) chip equipped with a Received Signal Strength Indicator (RSSI) pin that outputs an analogue voltage corresponding to the strength of the received signal (McLurkin and Smith, 2004; Pugh et al., 2009; Melhuish and Welsby, 2002; Kelly and Keating, 1996). These chips are designed for audio radios, so they operate in the MHz band. This is a problem as it requires complex RF circuitry that can cause interference in other nearby electronics. The RSSI is normally used only to indicate when a radio channel is tuned correctly, thus the signal tends to have a relatively small non-linear dynamic range. This non-linear response prevents simply amplifying the signal in order to extend the range of the sensor. Using a high gain amplifier would cause the signal to be saturated at short ranges. The communication data is frequency modulated and transmitted over the audio channel of the radio, thus the communication bandwidth is limited to approximately 20 kbps, which is the maximum bandwidth typically used by an audio signal. To overcome these problems, a new technique is proposed involving cascaded filtering, which improves the dynamic range of

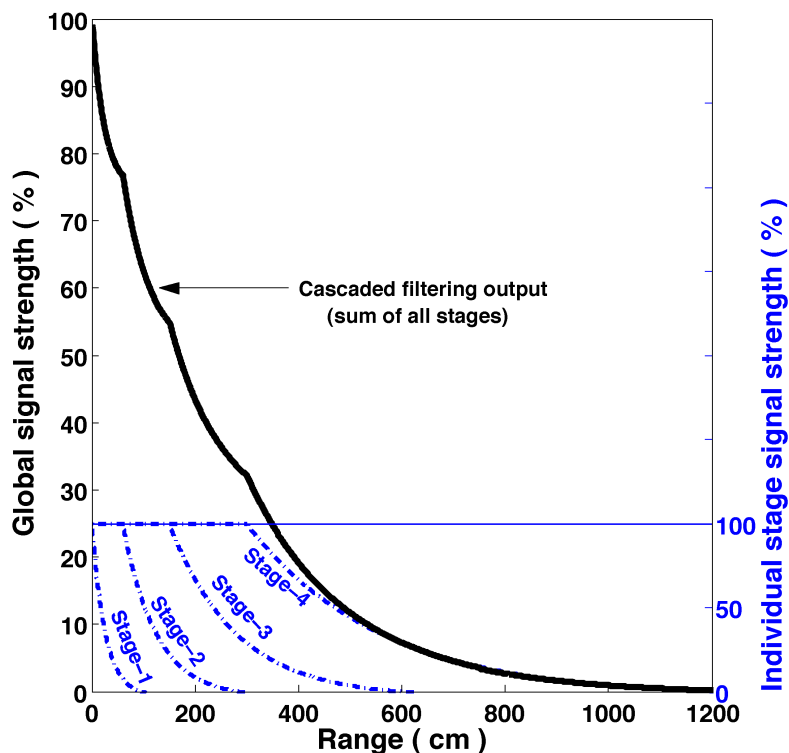


Figure 5.4: Theoretical signal strength of the cascaded filtering output (solid line) with respect to the range. The four individual stage outputs of the cascaded filter before they are added together are shown as dashed-dotted lines where each represents 25 % of the total global signal.

the signal by segmenting the range space into smaller complementary regions, where each region is covered by a specific amplifier stage (see figure 5.4). By doing this, the signal becomes more linear, the signal-to-noise ratio of the sensor is improved and the resolution is expanded.

A block diagram of the infrared reception path is shown in figure 5.5. The photodiode converts the infrared light into small electrical currents that are then pre-amplified. To improve the sensor's immunity against large changes in ambient light and allow the sensor to also function outdoors, the signal is AC coupled directly at the photodiode. This prevents the ambient DC bias voltage from prematurely saturating the pre-amplifier (see section 5.3.3). This small modulated signal is fed into a four stage cascaded amplifier. The gain of each amplifier is precisely tuned to cover a specific range segment. By using multiple amplifier stages the non-linear response of the photodiode is effectively stretched out by zooming in on small sections of the original signal. On each stage of the

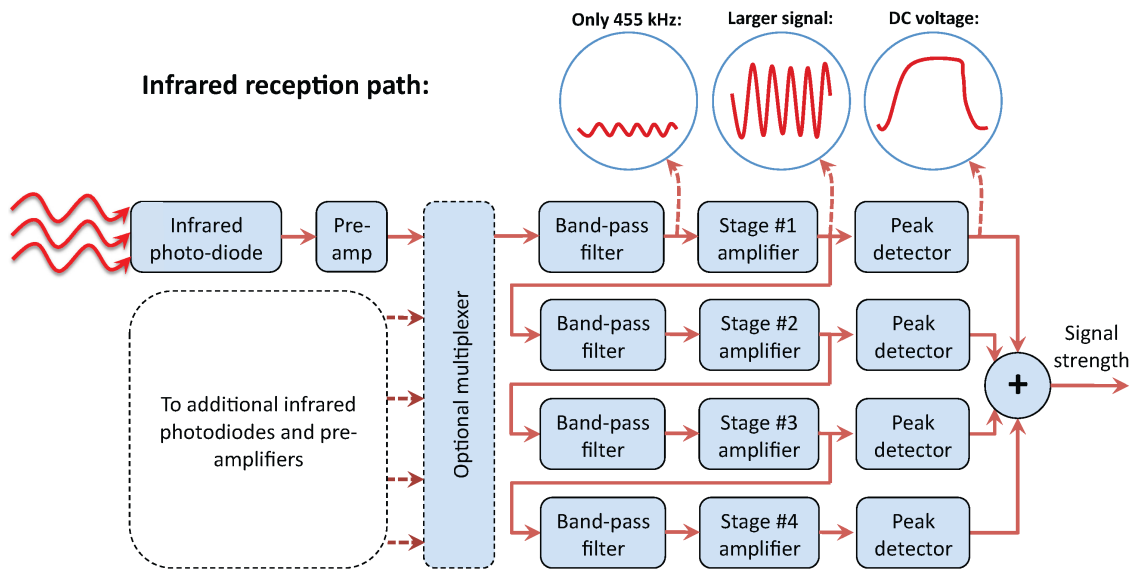


Figure 5.5: Reception block diagram showing the infrared reception path of the cascaded filtering method

cascade there is a highly selective ( $\pm 3$  kHz) bandpass filter tuned to detect the carrier frequency (455 kHz) of the transmitter. This carrier frequency has been chosen as it is the high-speed standard for infrared modules and it is easy to obtain small and cheap bandpass filters at this frequency. Half-wave rectifiers (Lander, 1993) are then used as peak detectors to convert these four signals into DC voltages. These four DC voltages, corresponding to complementary regions of the range space, are then sampled by an analogue-to-digital converter (10-bit provided by the micro-controller) and are added together to obtain the received signal strength. A look-up table is created by collecting the signal strength measurements at different known distances. A linear interpolator is then used to convert the signal strength into a range estimation.

### 5.2.5 Physical constraints and possible layouts

The physical implementation of the sensor can be varied depending on the particular robot that it is being used on. It is possible to design a sensor tailored to the robot's speed requirement, for example a mechanically stabilised coaxial helicopter requires a slower sensor speed than a quad-rotor due to the different system dynamics (Chen and McKerrow, 2007). The size of the sensor can be defined as a function of the operating speed and the individual components

required for range sensing. The time delay ( $\tau$ ) of the cascaded filter response limits the maximum operating speed to  $\frac{1}{\tau}$ . To achieve this maximum speed, it is necessary to have a cascaded filter for every photodiode. Alternatively, for a reduced size it is also possible to multiplex a single cascaded filter to many photodiodes, in this case the speed ( $f_r$ ) is determined by dividing the cascaded filter speed by the number of photodiodes that have been multiplexed. Assuming that a cascaded filter having a time delay of approximately 1 ms is used, the maximum operating speed would be 1 kHz. The approximate size and weight of the individual parts needed for operation, can be defined experimentally based on the required surface mount components: the size of a single photodiode and pre-amplifier is 1 cm<sup>2</sup> (0.4 g), a cascaded filter and peak detector is 4 cm<sup>2</sup> (4 g), a single emitter circuit is 0.5 cm<sup>2</sup> (0.15 g), a multiplexer is 2 cm<sup>2</sup> (0.5 g), a processor is 4 cm<sup>2</sup> (1 g) and an RF transceiver is 4 cm<sup>2</sup> (1 g). Using these values, it is possible to create a model to predict the size ( $A_s$  in cm<sup>2</sup>) and weight ( $m_s$  in grams) of the sensor based on its operating speed:

$$A_s = n_d + 4n_c + \frac{n_e}{2} + 2n_m + 4n_p + 4$$

$$m_s = 0.4n_d + 4n_c + 0.15n_e + \frac{n_m}{2} + n_p + 1$$

where  $n_d$  is the number of photodiodes,  $n_c$  is the number of cascaded filters,  $n_e$  is the number of emitters,  $n_m$  is the number of multiplexers and  $n_p$  is the number of processors used. To have a consistent operating speed for all photodiodes, there are only certain combinations of photodiodes and cascaded filters that make sense, as each photodiode and cascaded filter combination must obey  $f_r \propto \frac{n_c}{n_p}$ ,  $\forall. n_c \leq n_p$ .

Two examples that use this model to show a possible 2-D and 3-D sensor layout are discussed here. For a 2-D sensor, with 8 photodiodes and 16 emitters having a planar 360° sensor coverage, a single cascaded filter could be used to keep the size small. This would give an operating speed of  $f_r = \frac{1}{8}$  kHz, or 125 Hz. The size and weight of the sensor would be approximately 30 cm<sup>2</sup> or a circle with a 6 cm diameter and 12.1 g, respectively. For a 3-D sensor, with 26 photodiodes and 74 transmitters (as shown in figure 5.1) having a full spherical sensor coverage, a cascaded filter for every photodiode could be used to achieve the maximum operating speed ( $f_r = 1$  kHz). The size and weight of the sensor would be approximately 175 cm<sup>2</sup> or a circle with a 15 cm diameter and 127.5 g, respectively. To reduce the maximum dimensions of the sensor it is possible

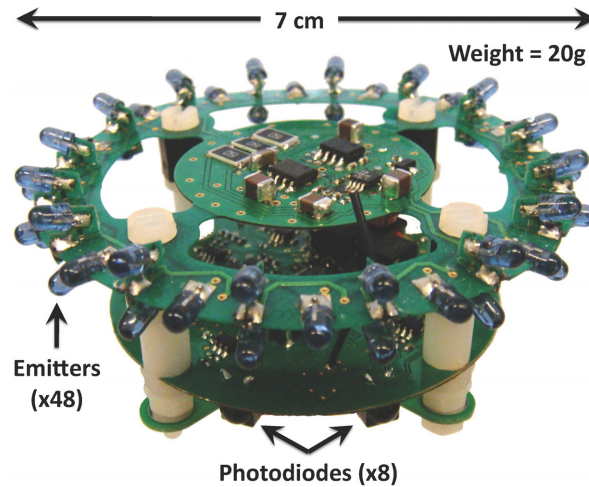


Figure 5.6: 2.5-D relative positioning sensor (2-D planar reception with 3-D transmission for a robustness to tilting)

to stack several circuit boards on top of one another. An example of this is presented in (Roberts et al., 2009), which is a 2.5-D sensor (2-D planar reception with 3-D transmission for a robustness to tilting) with a 7 cm diameter weighing 20 g, shown in figure 5.6. This sensor model can be used as a guide, showing that a 2-D or 3-D sensor can be customised for different physical implementations.

## 5.2.6 Integration on a flying robot

In order to achieve unobstructed 3-D sensing on a hovering platform, such as a quad-rotor, the physical construction of the sensor must be considered. The minimum size of a 3-D sensor using the proposed technique has been determined, in section 5.2.5, as a 15 cm circle with a weight of 127.5 g. However, for all of the hovering platforms, shown in section 1.2.1, it is important not to disrupt the airflow of the propellers. Disturbing or blocking the airflow will affect the flight characteristics and reduce the efficiency. Thus, this presents a challenging practical implementation problem. One solution is to increase the size of the platform so that there is enough space in the centre for the sensor. However, to achieve unobstructed sensing the sensor would have to be split in two, to cover the top and bottom hemispheres. This implementation is not practical if additional mechanics or sensors need to be added to either the top or bottom of the platform, such as a ceiling attachment mechanism or an omni-directional camera, respectively. Additionally, this goes against the philosophy of keeping the

platform size as small as possible. One solution that is suitable for unobstructed spherical sensing, is to create a circular sensing ring around the perimeter of the platforms structure. Such a solution, if designed well, could also be used to protect the propellers. By placing the sensor electronics around the perimeter, the sensor geometry is like a compressed sphere, where the sensor angles are kept the same as in the normal spherical geometry. This physical implementation of 3-D relative positioning sensor has been constructed, as shown in figure 5.7.

The sensor ring must be robust to small collisions and easy to replace, suggesting that a modular design would be suitable. Thus, the sensor was designed in modular sections, where eight sensor sections combine to create one complete ring. For mechanical support two sections are placed in a sandwich configuration, where each sensor section is identical and is designed to plug into a second inverted sensor section, which then covers  $1/4^{th}$  of the sphere. As the sensors are placed around the circular perimeter of the flying robot, additional sensors are required to prevent sensing occlusion caused by the robots structure. On each sensor section there are 4 transmitting and 2 receiving arrays, whose size is defined by the angle of half intensity of the emitters and angular sensitivity of the photodiodes, respectively. These arrays provide a  $1/8^{th}$  ( $90^\circ$  wedge) coverage of the sphere. The holders of the transmitter and receiver arrays are 3-D printed in ABS plastic (see the close up in figure 5.7). The transmitter holders each support 5 infrared emitters (Vishay TSAL4400) that are spaced at  $22.5^\circ$  angles from  $0^\circ$  along the circular perimeter, to  $90^\circ$  either upward or downward facing. The receiver holders each support three infrared photodiodes (Vishay BPV22NF) spaced at  $0^\circ$  along the circular perimeter,  $45^\circ$  and  $90^\circ$  either upward or downward facing. These additional sensors are highly redundant and cause some non-homogeneity (i.e. a stronger intensity cone of  $22.5^\circ$  upward and downward facing), however they are necessary for this particular arrangement in order to prevent sensing occlusion and allow for a modular sensor design. The additional upward and downward facing emitters and photodiodes also provide an improved altitude proximity sensing of the floor and the ceiling (see section 5.3.4). Therefore, the sensor ring has a total of 48 photodiodes (16 receiver arrays) and 160 emitters (32 transmitter arrays). To obtain the best signal-to-noise ratio from the sensors, sampling and linearisation of the four cascaded outputs is done by a micro-controller placed directly on each section. The results are then sent to a main micro-controller for processing.

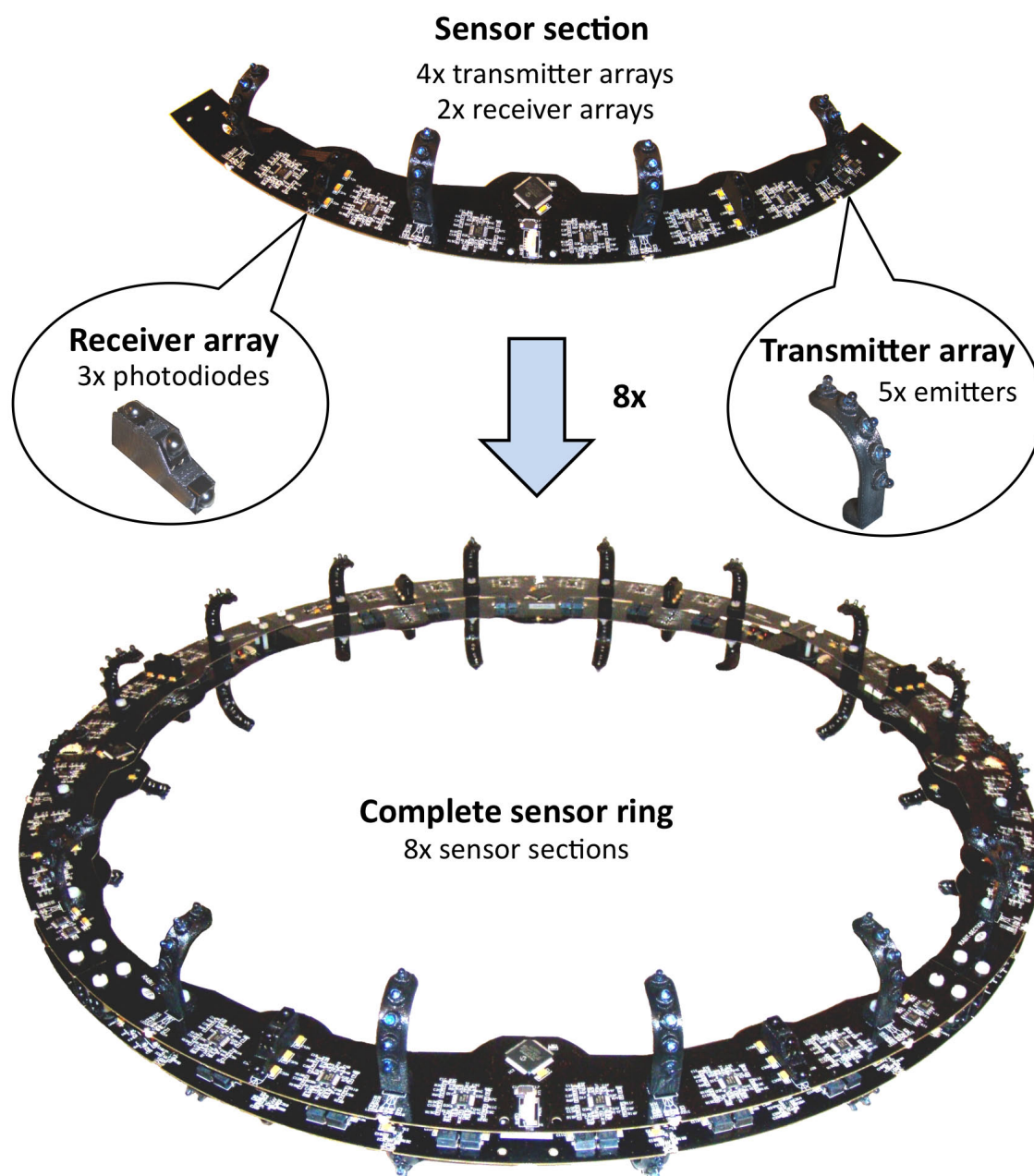


Figure 5.7: *Left*: Close-up of a transmitter array (*top*) and receiver array (*bottom*). *Middle-left*: A single sensor section with two receiver arrays and four transmitter arrays. *Right*: A complete sensor ring showing eight sensor sections connected together

Using the physical sensor model in section 5.2.5, the physical attributes of the sensor electronics can be predicted. The sensor should operate at the 1 kHz speed, therefore each photodiode must have a dedicated cascaded filter. The size of the sensor would be approximately  $360\text{ cm}^2$  (245.2 g) or a circle with a 22 cm diameter. This translates into a two layer sensor ring with approximately 48 cm internal diameter and 50 cm outer diameter, which would leave only 1 cm width per side for the electronics. However, this is not practical as the smallest possible width is 2.5 cm, which is defined by the cascaded filter. Also, a ring with these dimensions is too fragile to be mechanically self-supporting. Therefore, the chosen average width is approximately 3.5 cm, which adds an extra 19 g of mechanical weight for supporting each section, giving a completed ring weight of approximately 400 g, which now includes rotor protection. The ring can be made larger or smaller depending on the size of the hovering platform. The ring can connect at each end of the sections to the structure of a flying robot using light-weight nylon nuts and bolts. The sensor sections all connect to a communications hub and then to the main micro-controller, using light-weight flex cables. The thin printed circuit boards in the sandwich configuration creates a uni-directional flexible structure that protects the propellers from walls or other large obstacles, but allows for vertical flexing to protect the sensors in the case of a small collision.

As the sensor is used on a flying robot the power consumption is important. The average power consumption of the finished sensor while operating at full speed is 10 watts. Comparing this to the power required to hover, it accounts for only a small percentage (<10%) of the total power.

### 5.3 Results

This section explains how the 3-D relative positioning sensor was calibrated in order to analyse its resolution and signal noise. The sensor performance is then shown by characterising the 3-D relative positioning error for the range, bearing and elevation angles. The light immunity and proximity sensing was also tested to observe the sensor's ability to be used for obstacle avoidance and within environments with large changes in ambient lighting, respectively. Finally, a comparison is performed between the developed 3-D relative positioning sensor and the three best performing 2-D relative positioning sensors in the literature.



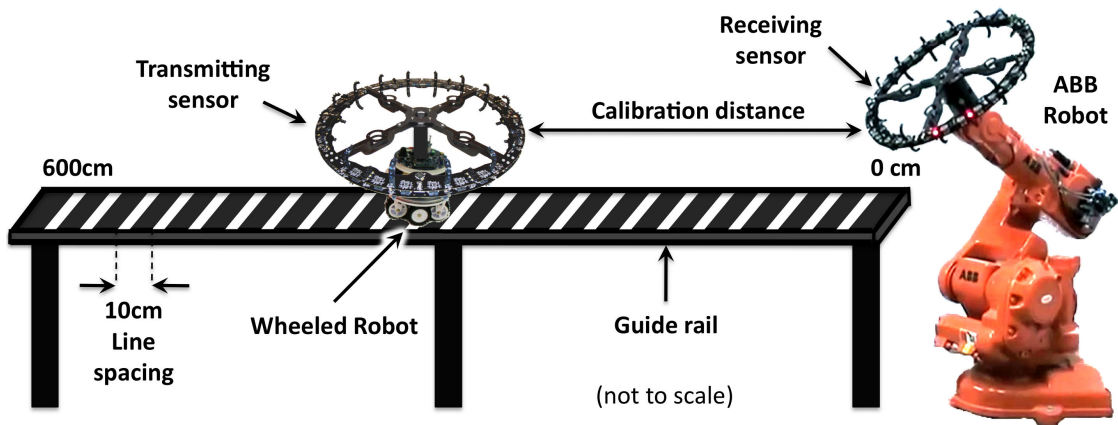


Figure 5.8: Calibration setup showing the transmitting sensor (*left*) and the receiving sensor (*right*). The ABB robot aligns each photodiode of the receiving sensor with the centre of the transmitting sensor, taking 25 samples at each step. After the data is collected the Wheeled robot moves the transmitting sensor along the guide rail to the next 10 cm position.

### 5.3.1 Resolution and noise

In order to analyse the sensor's resolution and signal noise, each photodiode of the sensor has been calibrated. For this experiment, one sensor was used as a transmitter, and another was used as a receiver. To automate the tests, the receiving sensor was attached to an IRB-140 ABB robotic arm and the transmitting sensor was attached to a wheeled robot (Bonani et al., 2010) (see figure 5.8). Calibration was performed with help from several partners, see chapter i. A computer was used to remotely control the 6-axis of the ABB robot and to set the distance of the wheeled robot along a guide rail. The 600 cm long, suspended, black guide rail was marked every 10 cm with white lines so that the position could be detected by the wheeled robot's ground sensors. This allowed the transmitting sensor to be automatically displaced from the receiving sensor at 10 cm increments from 0 cm to 600 cm. At each position, the ABB robot aligned each of the 48 photodiodes of the receiving sensor with the centre of the transmitting sensor and 25 consecutive samples of the signal strength were recorded at a rate of 10 Hz (see video<sup>4</sup>).

To determine the resolution of the sensor, the gradient of the signal strength

<sup>4</sup>Video: <http://jfroberts.com/phd> (sensor\_calibration.mp4)

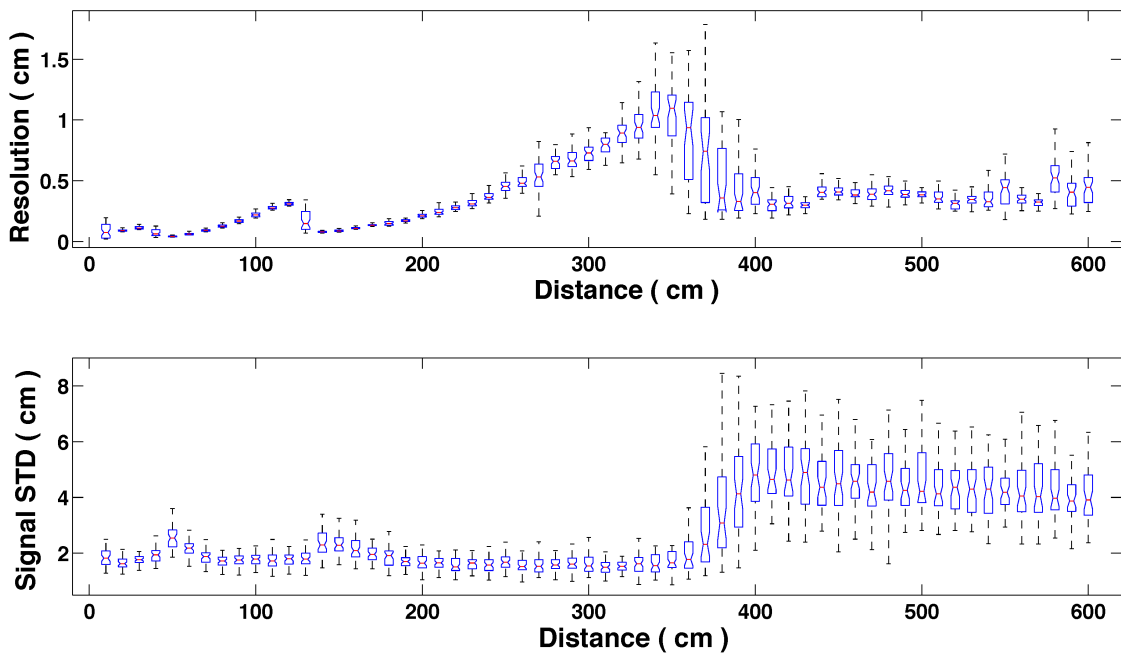


Figure 5.9: Resolution (*top*) and signal standard deviation (*bottom*) characteristics of the infrared photodiodes over the calibrated range, each item of the box-plot shows the variance across the sensors 48 photodiodes

was calculated at each tested distance by taking the difference in signal strength between two adjacent test distances and dividing by the 10 cm displacement. Figure 5.9 *top*, shows the resolution of the relative positioning sensor, each item of the box-plot shows the variance across the 48 photodiodes. The mean RMS resolution is 0.4 cm at distances up to 600 cm and 0.14 cm at distances below 200 cm. The max RMS resolution is 1.1 cm at distances up to 600 cm and 0.3 cm at distances below 200 cm. The changes in the resolution over the distances show the ripples caused by the slope of the outputs of the cascaded filtering technique.

To calculate the noise in the signal strength, the signal standard deviation was calculated from the 25 samples for each photo-diode at each test distance. Figure 5.9 *bottom*, shows the signal strength standard deviation of the relative positioning sensor, each item of the box-plot shows the variance across the 48 photodiodes. The mean RMS signal standard deviation is 3.2 cm at distances up to 600 cm and 1.95 cm at distances below 200 cm. The max RMS signal standard deviation is 6.66 cm at distances up to 600 cm and 2.6 cm at distances below 200 cm. The signal standard deviation is very low until the fourth stage of the cascade begins at around 350 cm. The gain of the fourth stage introduces a

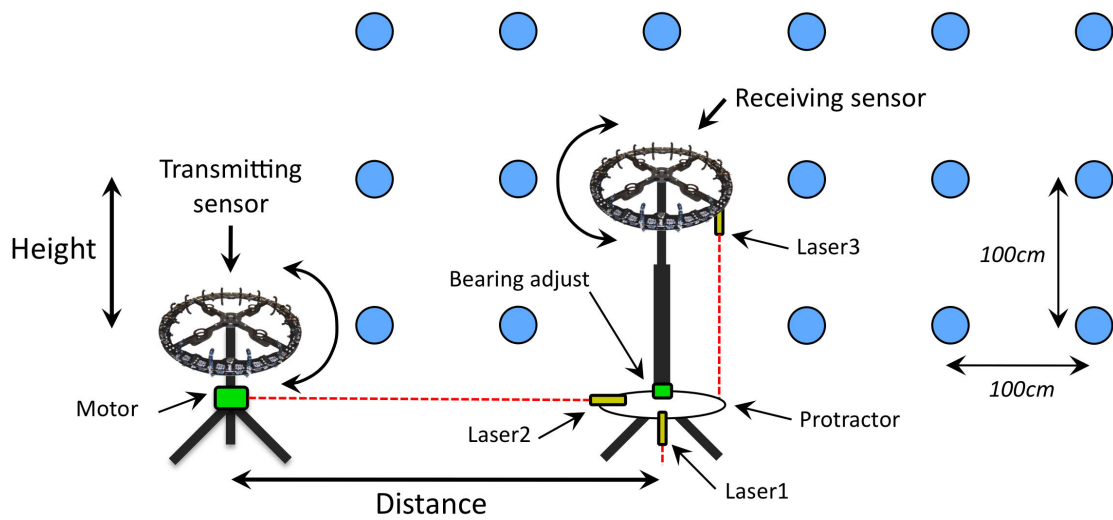


Figure 5.10: Characterisation setup showing the transmitting sensor (*left*) with respect to the receiving sensor (*right*), along a six by three two dimensional vertical grid with a 100 cm spacing. Three laser pointers, providing a straight edge, helped with the alignment of the distance (*Laser-1*) and angles (*Laser-2,3*) between the two sensors

higher signal strength/distance slope, thus an improved resolution. This indicates that there is a trade-off between resolution and signal noise. These results also suggest that the sensor performance extends further than this 600 cm calibration range.

These measurements were used to calibrate each sensor by creating a look-up table for the range estimation. This high resolution and low noise performance is directly related to the cascaded filtering technique, presented in section 5.2.4. Such a performance over a long range would not be possible using the existing signal strength measurement techniques that are shown in Table 1.2, chapter 1.

### 5.3.2 Relative positioning error

In order to analyse the sensor's 3-D relative positioning performance, two relative positioning sensors were used to measure the error in the calculated range, bearing and elevation measurements. For this experiment, one sensor was used as a transmitter, and the other was used as a receiver. The transmitting sensor was kept at a fixed height and position during the experiment. The receiving sensor was manually placed along a two dimensional vertical grid, shown in

figure 5.10. The 100 cm spaced grid consists of six defined distances (100 cm to 600 cm), by three defined heights (0 cm to 200 cm) from the transmitter. Three laser pointers, providing a straight edge, helped with the alignment of the distance (*Laser-1*) and angles (*Laser-2,3*) between the two sensors. For each position the distance is set using *Laser-1*, then the reference bearing is set using *Laser-2*. The receiving sensor height is then adjusted using an extendable mast, which is mounted on a mechanical bearing allowing the receiving sensor to rotate. A large protractor was fixed to the base of the mast and a laser fixed to the receiving sensor (*Laser-3*) is then used to determine the bearing angle. The six defined distances were chosen so that the results would span across the full calibration range of the sensors. The three defined heights were chosen based on the assumption of a standard office room ceiling height being 2.5 m. Thus, the height between the transmitting and receiving sensors can never be larger than 2 m, due to the height of the flying robots (see chapter 6, section 6.4.1). This vertical grid represents the normal operating space for indoor flying robots.

The symmetry in the photodiode spacing every  $45^\circ$  around the perimeter of the sensor, allows for a reduction in the bearing tests. Therefore, at each of the measurement positions the receiving sensor was rotated and tested at 6 different bearing orientations from  $0^\circ$  to  $50^\circ$  thus, covering all of the critical bearing angles. For each tested position 50 samples of the received range, bearing and elevation were recorded. During all tests the bearing orientation of the transmitting sensor was continuously rotated backwards and forwards by  $90^\circ$  using a servo motor. This was to incorporate any transmission errors that are related to non-uniform emissions patterns within the results. During a single measurement of 50 samples, the transmitting sensor would make approximately 5 rotations of  $90^\circ$  (see video<sup>5</sup>).

### Range performance

The range response, shown in figure 5.11, has been measured over the 600 cm calibration range of the sensor, at a fixed bearing ( $0^\circ$ ) and elevation ( $0^\circ$ ). Error bars show the standard deviation of all measurements and include errors from the rotating transmitter. The range response is very linear and has a small standard deviation across all ranges.

---

<sup>5</sup>Video: <http://jfroberts.com/phd> (sensor\_characterisation.mp4)

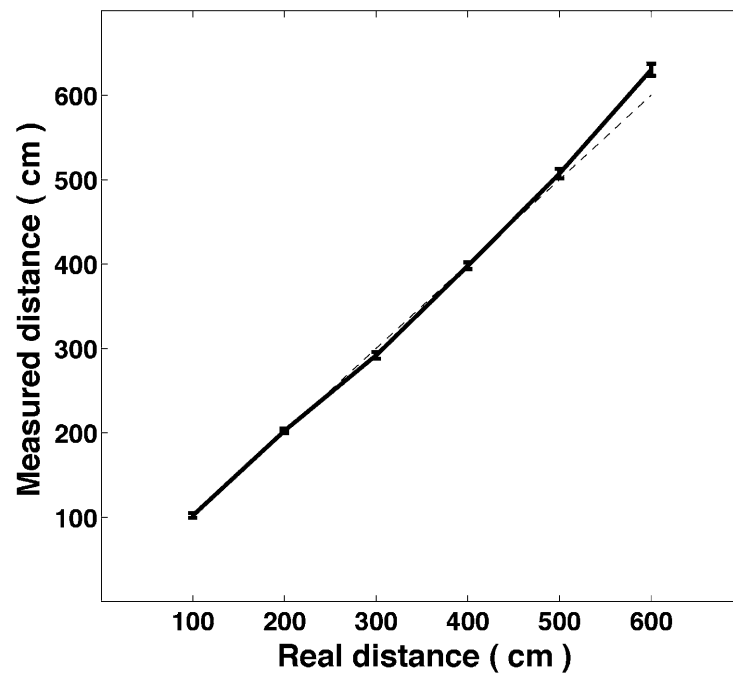


Figure 5.11: Range measurements over the 600 cm calibration range of the sensor at a fixed bearing ( $0^\circ$ ) and elevation ( $0^\circ$ ). Error bars show the standard deviation

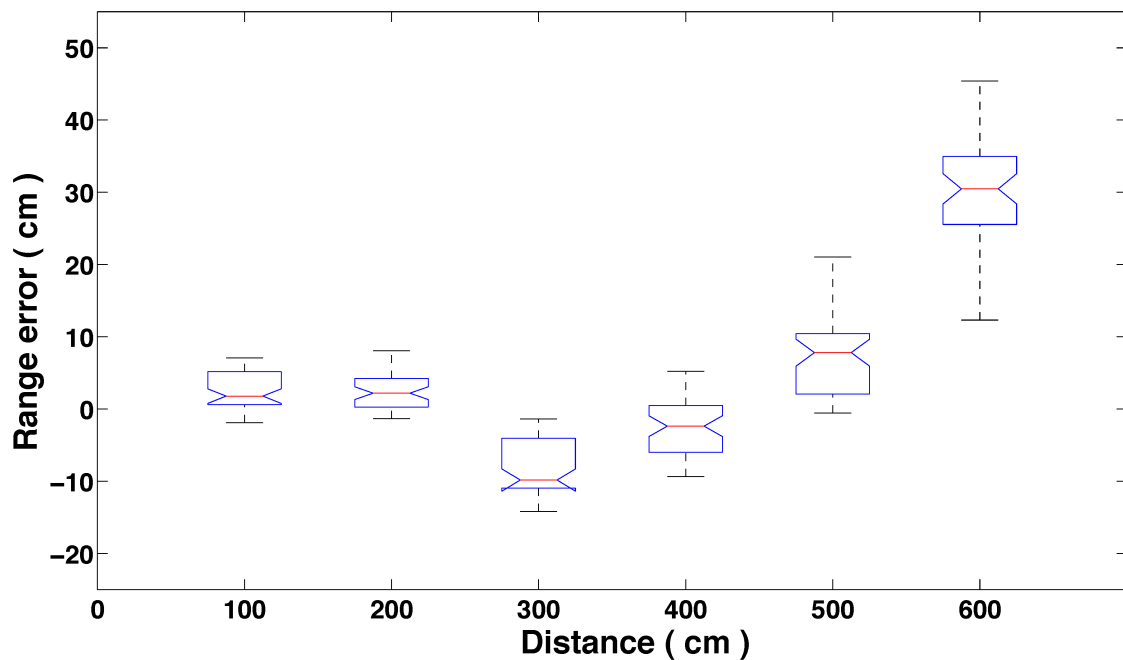


Figure 5.12: Box-plot of the range error over the distance, indicating the variance across the samples at a fixed bearing ( $0^\circ$ ) and elevation ( $0^\circ$ )

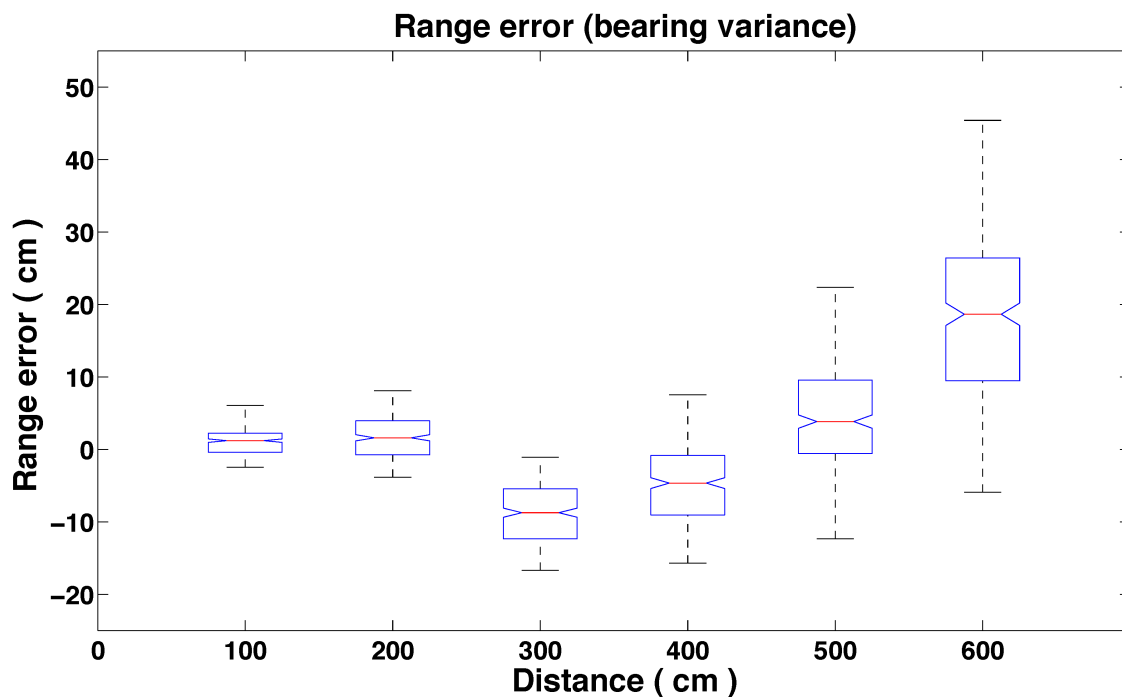


Figure 5.13: Box-plot of the range error over the distance, indicating the variance across all tested bearings at a fixed elevation ( $0^\circ$ )

The range error has been analysed across all samples, all the tested bearings and all the tested elevations. The box-plot of the range error over the distance, in figure 5.12, shows the variance across the samples at a fixed bearing ( $0^\circ$ ) and fixed elevation ( $0^\circ$ ). Analysing the range error shows that the average absolute and relative error was always below 5.02% (30.13 cm, measured at 600 cm). The maximum absolute and relative error was always below 7.57% (45.40 cm, measured at 600 cm). This test case can then be used to determine if changes in the bearing and elevation causes observable differences in the range error.

The box-plot of the range error over the distance, shown in figure 5.13, indicates the variance across all tested bearings at a fixed elevation ( $0^\circ$ ). Analysing the range error shows that the average absolute and relative error was always below 3.06% (18.39 cm, measured at 600 cm). The maximum absolute and relative error was always below 7.57% (45.40 cm, measured at 600 cm). Comparing this with the test case shows that the range error introduced by changes in the bearing is small.

The box-plot of the range error over the distance, shown in figure 5.14, indicates the variance across all tested elevations at a fixed bearing ( $0^\circ$ ). The elevation

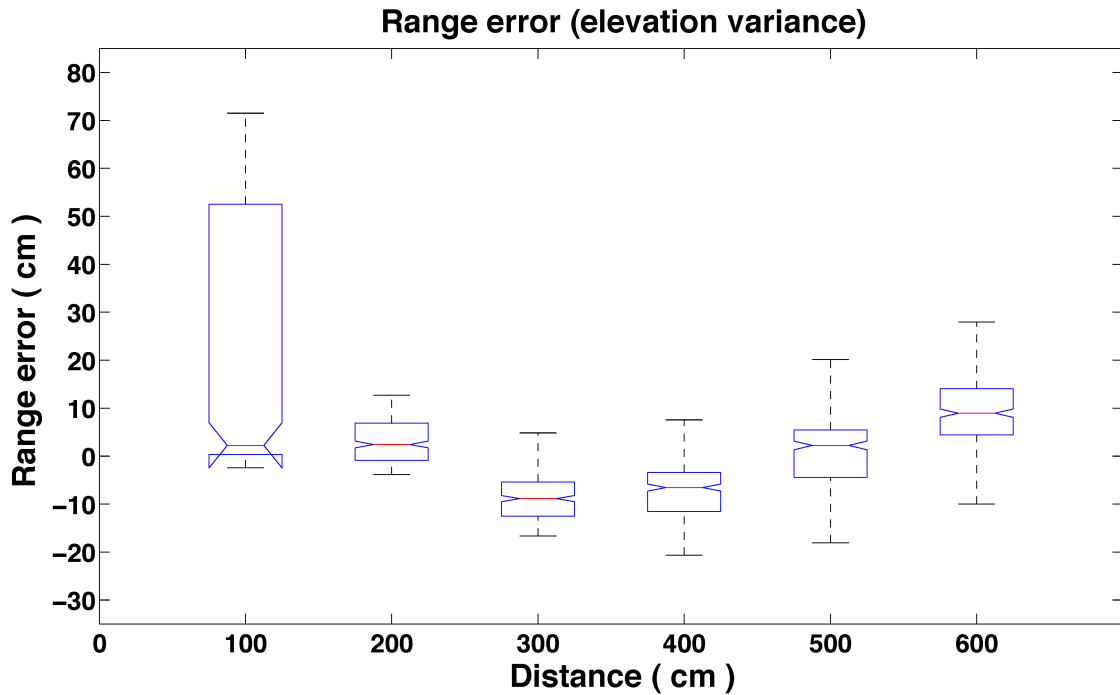


Figure 5.14: Box-plot of the range error over the distance, indicating the variance across all tested elevations (see Table 5.1) at a fixed bearing ( $0^\circ$ )

angle, for the vertical testing grid, is dependant on the height and the distance between the sensors. Therefore, all combinations of the ranges and heights allows for 13 different elevation angles, shown in Table 5.1. These elevation angles range from  $0^\circ$  to  $76^\circ$  and have been calculated from the geometry between the sensor rings. Analysing the range error shows that the error values are quite high for the 100 cm distance (max error of 71.50 cm), however they quickly improve at 200 cm and slowly increase as expected towards the 600 cm distance. The large error at 100 cm indicates that the sensor has a problem with elevation angles above  $53.1^\circ$ . Analysing the range error at elevations of  $53.1^\circ$  or less, shows that the average absolute error was always below 7.99 cm (1.33%, measured at 600 cm) and the average relative error was always below 2.71% (5.43 cm, measured at 200 cm). The maximum absolute error was always below 35.70 cm (7.14%, measured at 500 cm) and the maximum relative error was always below 13.01% (26.02 cm, measured at 200 cm). Comparing this with the test case shows that the range error introduced by changes in the elevation is minimal for elevation angles that are  $53.1^\circ$  or less. However, the range error is large for elevation angles  $> 53.1^\circ$ , which is assumed to be due to the compressed sphere geometry

Table 5.1: Elevation angles calculated from the geometry between the sensors

Heights:	Distances:					
	100 cm	200 cm	300 cm	400 cm	500 cm	600 cm
200 cm	76.0°	53.1°	38.7°	29.7°	24.0°	20.0°
100 cm	63.4°	33.7°	21.8°	15.9°	12.5°	10.3°
0 cm	0°	0°	0°	0°	0°	0°

of the sensor ring and its non-homogeneous transmission pattern.

The calibration guide rail length (Figure 5.8) was limited to the size of the experiment room, thus limiting the calibration range to 600 cm. However, the sensor is capable of operating at much further distances. This has been achieved by analysing the trend of the signal strength curve and extending the look-up table manually. The range was measured at a fixed elevation ( $0^\circ$ ) and a bearing of  $22.5^\circ$ , which is the angle of minimum sensitivity between two infrared photodiodes and represents the worst-case bearing orientation. To determine the reliable operating range of the sensor, the receiver was tested above the calibration range at distances of 700 cm, 900 cm, 1100 cm, and again at 1200 cm. The maximum reliable operating range was found to be 1200 cm, as shown in figure 5.15. As the sensor was not calibrated for ranges over 600 cm, the error is not an accurate indication of the maximum performance. However, even without calibration the range error, shown in figure 5.16, is small. Analysing the range error shows that the average absolute and relative error was always below 9.11% (109.37 cm, measured at 1200 cm). The maximum absolute and relative error was always below 15.27% (183.23 cm, measured at 1200 cm). A summary of the range errors can be seen in Table 5.2.

### Bearing performance

The bearing response, shown in figure 5.17, has been measured across the 6 tested bearings ( $0$  to  $50^\circ$ ) of the sensor, at a fixed distance (300 cm, middle data set) and elevation ( $0^\circ$ ). Error bars show the standard deviation of all measurements and include errors from the rotating transmitter. The bearing response is very linear and has a small standard deviation across all tested bearings.

The bearing error has been analysed across all samples, all the tested distances and all the tested elevations. The box-plot of the bearing error across the



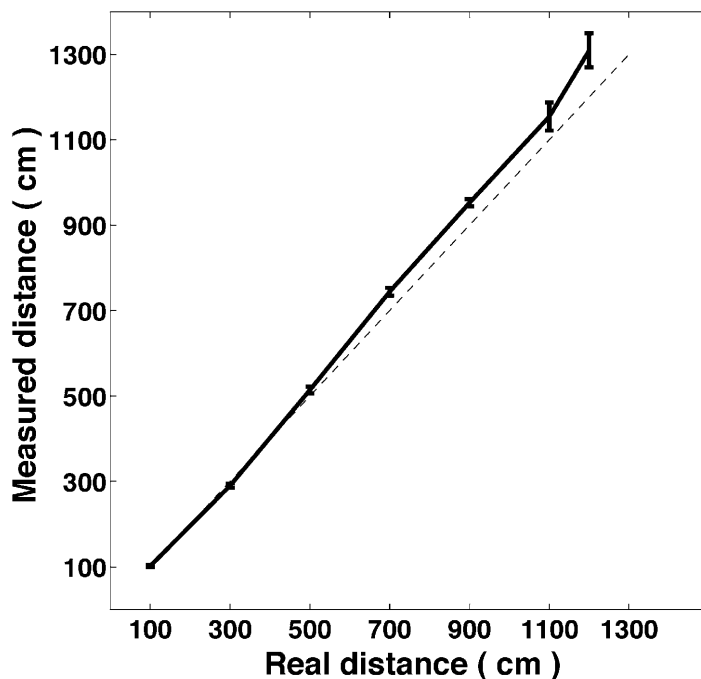


Figure 5.15: Extended range measurements for the full range of the sensor at a fixed bearing ( $22.5^\circ$ ) and elevation ( $0^\circ$ ). Error bars show the standard deviation. The signal skew above 600 cm is because the sensor has not been calibrated at these ranges, due to the limited size of the calibration room

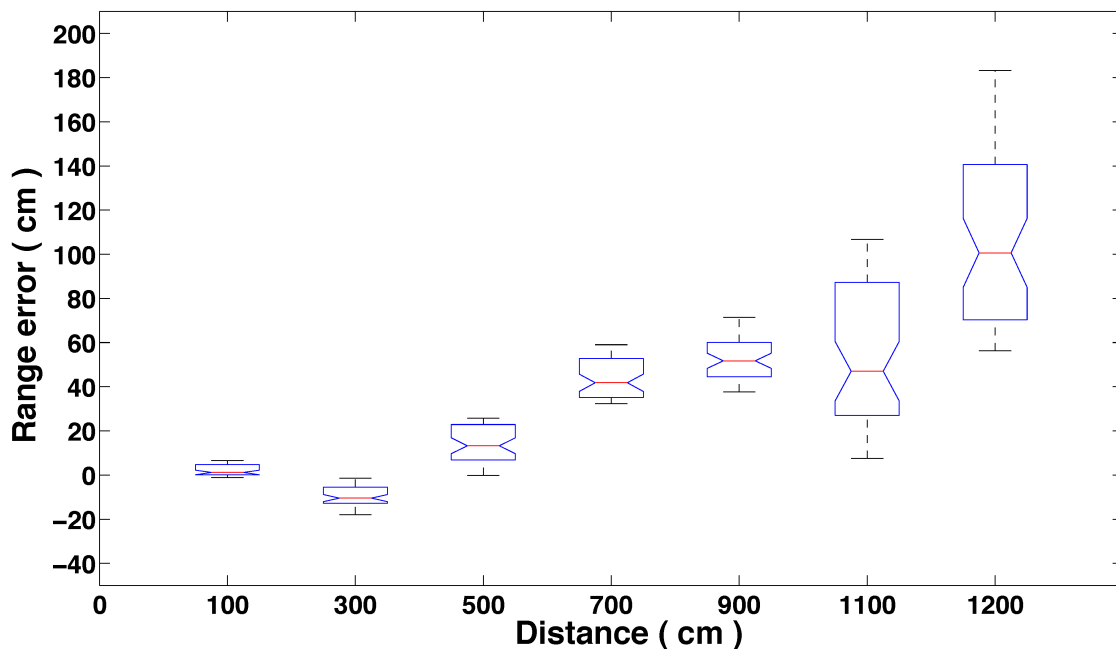


Figure 5.16: Box-plot of the extended range error over the distance, indicating the variance across the samples at a fixed bearing ( $22.5^\circ$ ) and elevation ( $0^\circ$ )

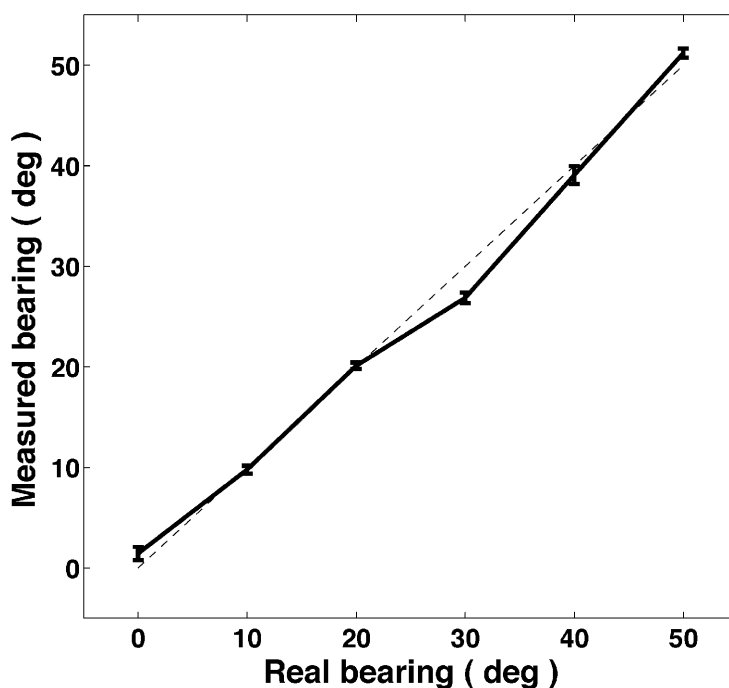


Figure 5.17: Bearing measurements across the 6 tested bearings of the sensor, at a fixed distance (300 cm) and elevation ( $0^\circ$ ). Error bars show the standard deviation

6 tested bearings, shown in figure 5.18, indicates the variance across the samples at a fixed distance (300 cm, middle data set) and fixed elevation ( $0^\circ$ ). Analysing the bearing error shows that the average error was always below  $3.13^\circ$  (0.87%, measured at  $30^\circ$ ). The maximum error was always below  $4.40^\circ$  (1.22%, measured at  $30^\circ$ ). The observable skew of the bearing at  $30^\circ$  with a small distribution, relates to either the error in the model used to represent the sensitivity response of the photodiode, or the human error introduced in the testing alignment. This test case can then be used to determine if changes in the distance and elevation causes observable differences in the bearing error.

The box-plot of the bearing error, in figure 5.19, shows the variance across all tested bearings at a fixed elevation ( $0^\circ$ ) with respect to distance. Analysing the bearing error shows that the distribution of the values are quite high for the 100 cm distance (max error of  $10.79^\circ$ ), however it quickly improves at 200 cm and is significantly equal towards the 600 cm distance. Taking a closer look at the sensor geometry gives some insight on why this is the case. The bearing estimation is calculated using a model of the photodiodes, which is related to

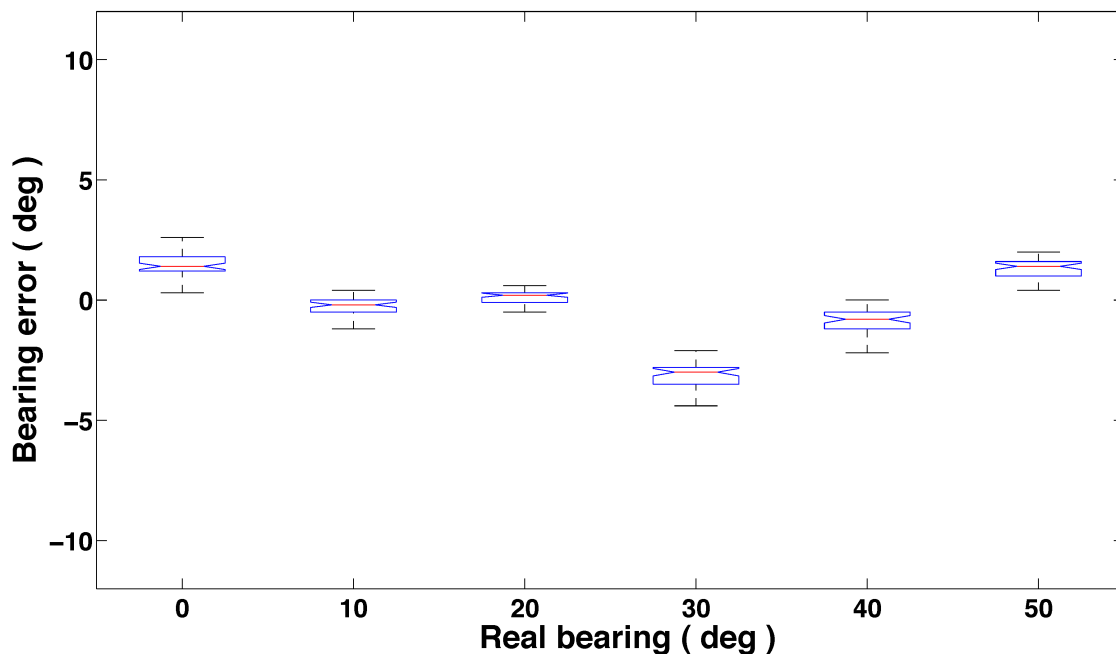


Figure 5.18: Box-plot of the bearing error across the 6 tested bearings, indicating the variance across the samples at a fixed distance (300 cm, middle data set) and elevation ( $0^\circ$ )

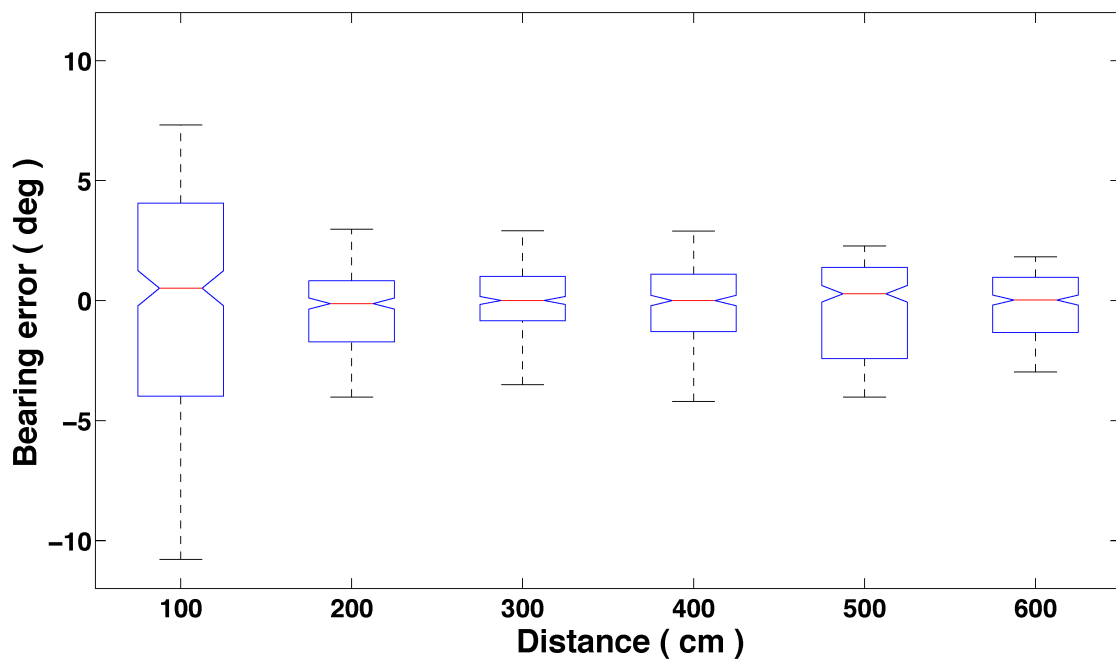


Figure 5.19: Box-plot of the bearing error with respect to the distance, indicating the variance across the 6 tested bearings at a fixed elevation ( $0^\circ$ )

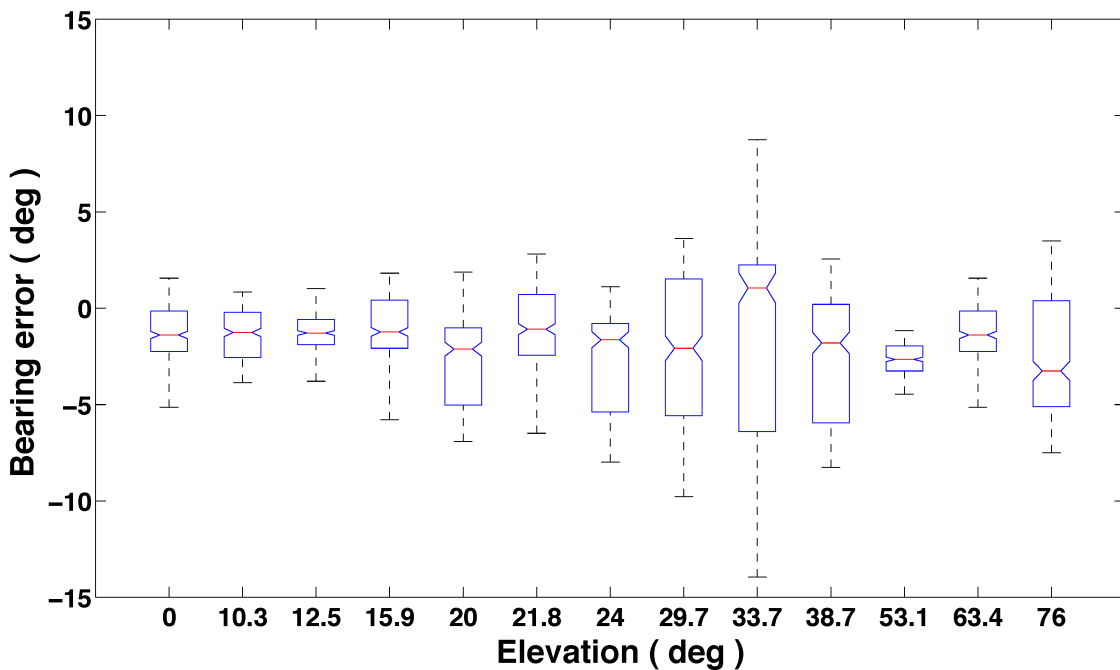


Figure 5.20: Box-plot of the bearing error with respect to the elevation angle, indicating the variance across the 6 tested bearings

their sensitivity response. For this model to hold true, the angle cannot go beyond  $60^\circ$ . The distance where the angles overlap, when placed on a 50 cm sensor ring, determines the minimum distance between the sensors, where the model is accurate. Calculating this distance shows that angles do not overlap until 191.5 cm between the centre of each sensor, which explains why the bearing error is low from a 200 cm distance and above. To generalise, a larger sensor diameter introduces bearing errors at lower distances and is dependant on the model of the photodiodes. Note that this is not the case for the elevation as the vertical photodiodes are close together. Analysing the bearing error above the 100 cm distance shows that the average error was always below  $0.25^\circ$  (0.07%). The maximum error was always below  $4.40^\circ$  (1.22%, measured at 300 cm). Comparing this with the test case shows that the bearing error introduced by changes in the distance above the 100 cm distance is small.

The box-plot of the bearing error, shown in figure 5.20, indicates the variance across all tested bearings with respect to the elevation angle. Analysing the bearing error shows that the average error was always below  $2.64^\circ$  (0.73%, measured at  $76^\circ$  elevation). The maximum error was always below  $13.95^\circ$  (3.87%, measured at  $33.7^\circ$  elevation). Analysing the bearing error shows that the distribution of

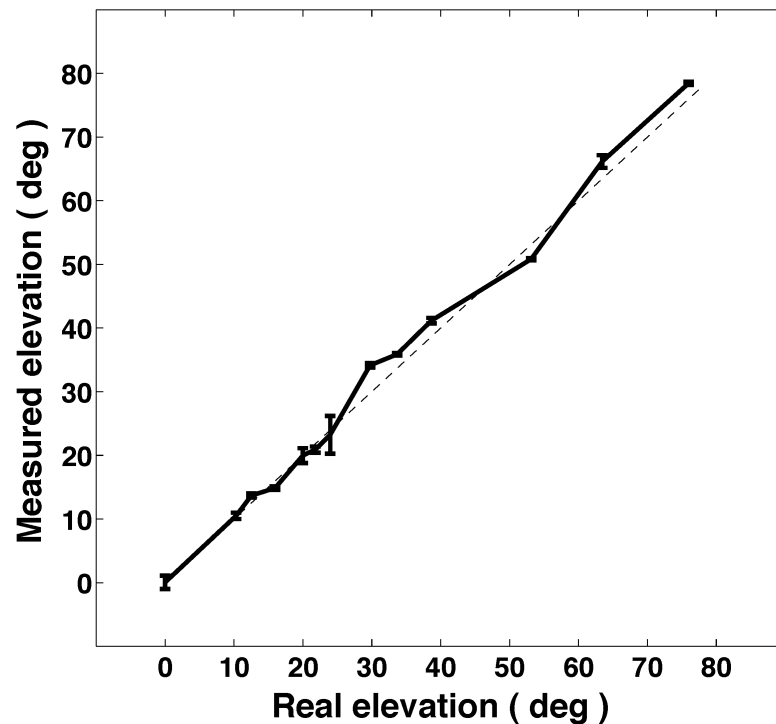


Figure 5.21: Elevation measurements across the 13 tested elevation angles of the sensor (see Table 5.1). Error bars show the standard deviation. The measurements are not evenly distributed due to the vertical grid geometry

the values are quite high for the  $33.7^\circ$  elevation (max error of  $13.95^\circ$ ), however the values of the other elevations are similar to the previous distance variation test. As the vertical photodiodes are close together the sensor ring geometry should not be the source of this error. Comparing this observation to the test case further suggests that the model of the photodiodes is not accurate around the  $30^\circ$  bearing or elevation angles. A summary of the bearing errors can be seen in Table 5.2.

### Elevation performance

The elevation response, shown in figure 5.21, has been measured across the 13 tested elevation angles of the sensor (see Table 5.1). The elevation measurements are not evenly distributed due to the vertical grid geometry. Error bars show the standard deviation of all measurements and include errors from the rotating transmitter. The elevation response is very linear and has a small standard deviation across all tested elevations.

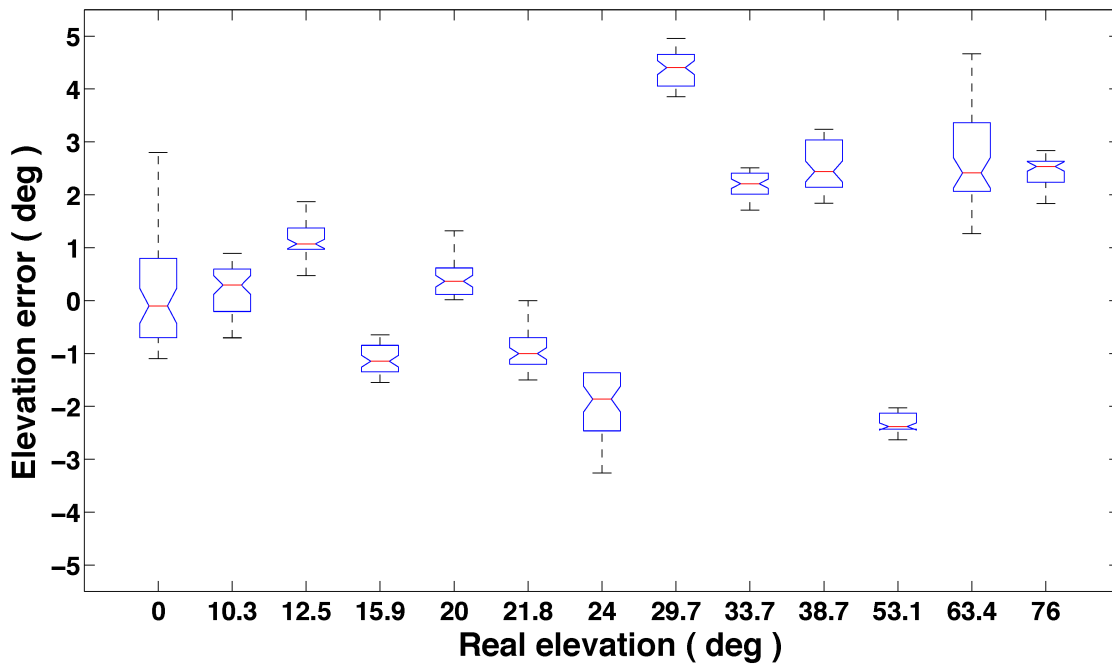


Figure 5.22: Box-plot of the elevation error across the 13 tested elevation angles of the sensor, indicating the variance across the samples, which are spread over all distances and heights

The elevation error has been analysed across all samples, all the tested distances and all the tested bearings. The box-plot of the elevation error across the 13 tested elevation angles, shown in figure 5.22, indicates the variance across the samples spread over all distances and heights. Analysing the elevation error shows that the average error was always below  $4.40^\circ$  (1.22%, measured at  $29.7^\circ$ ). The maximum error was always below  $5.14^\circ$  (1.43%, measured at  $33.7^\circ$ ). Even though the measurements are scattered due to the varying distances and heights, the error values are similar to the bearing errors. This test case can then be used to determine if changes in the distance and bearing causes observable differences in the elevation error.

The box-plot of the elevation error, shown in figure 5.23, indicates the variance across all tested elevation angles at a fixed bearing ( $0^\circ$ ), with respect to distance. Analysing the elevation error shows that the average error was always below  $2.81^\circ$  (0.78%, measured at 600 cm). The maximum error was always below  $9.40^\circ$  (2.61%, measured at 600 cm). Comparing this with the test case shows that the mean elevation error introduced by changes in the distance is minimal. However, the maximum elevation error does vary at different ranges. Naturally

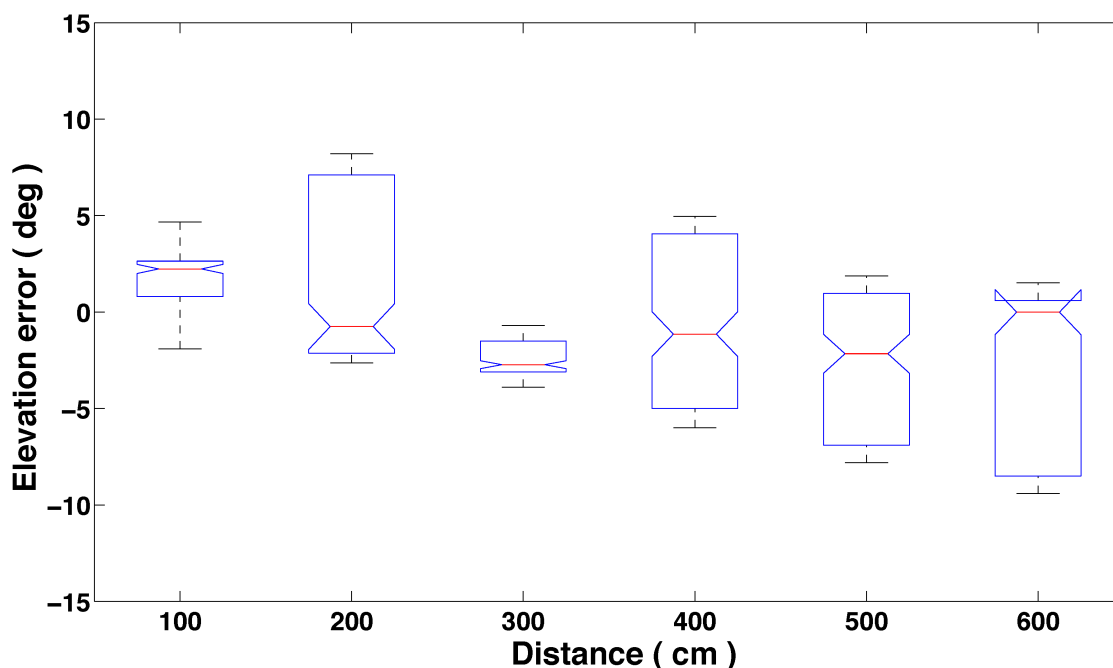


Figure 5.23: Box-plot of the elevation error with respect to the distance, indicating the variance across the elevation angles for each tested distance with a fixed bearing ( $0^\circ$ )

the error should increase with distance, however the error at the 200 cm and 400 cm distances does not follow this trend. Looking closer at the geometry it is evident that these distances include an elevation of  $33.70^\circ$  and  $29.7^\circ$ , respectively. Thus, it is known from the previous results that the photodiode model is not accurate at the  $30^\circ$  angle, which explains the phenomenon.

The box-plot of the elevation error, shown in figure 5.24, indicates the variance across all tested elevations with respect to the 6 tested bearing angles. Analysing the elevation error shows that the average error was always below  $2.74^\circ$  (0.76%, measured at  $40^\circ$  bearing). The maximum error was always below  $5.74^\circ$  (1.59%, measured at  $40^\circ$  bearing). Comparing this with the test case shows that the elevation error introduced by changes in the bearing is small. A summary of the elevation errors can be seen in Table 5.2.

The effect of the elevation angle on the sensor with respect to height and distance displacement, is similar to the effect of attitude tilting during flight translation. Operation indoors requires slow translational speeds therefore, the tilting angle is expected to be low ( $<10^\circ$ ). However, when the sensors have a height difference, as shown in Table 5.1, this elevation angle can quickly in-

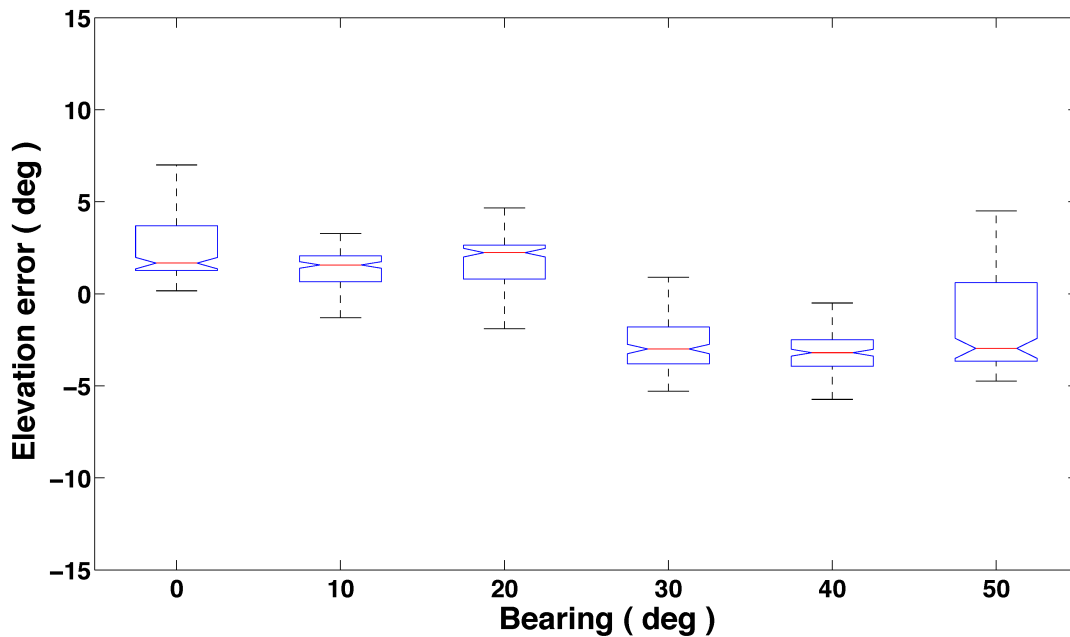


Figure 5.24: Box-plot of the elevation error with respect to the bearing angle, indicating the variance across the 13 tested elevation angles

crease. Thus, the elevation perceived by the sensor during flight is a function of height, distance and tilt, where the elevation angle with respect to the height and distance geometry is added to the tilting angle during translation.

The elevation error is good ( $<9.40^\circ$ ) over all the tested elevation angles up to  $76^\circ$ . Therefore, the large range error for elevation angles above  $53.1^\circ$  is fully observable, which means that the error could be corrected. Additionally, all errors could further be reduced if the model of the photodiode was improved. Despite this the errors are generally good and can provide accurate positioning sensing for collective flying robots.

### 5.3.3 Light immunity

In order to test the sensor's immunity against large ambient light changes, several measurements were recorded in a room with high-powered controllable lighting. The position between the transmitting sensor and the receiving sensor was fixed at 600 cm. Using a light meter, measurements were taken at 0, 500, and 10,000 lux, which is equivalent to a dark room, office room, and an overcast day outdoors, respectively. For all of these light levels less than 1% relative error was observed, therefore the sensor is robust to large ambient light changes.



Table 5.2: Summary of the specifications for the 3-D relative positioning sensor

<b>Operating constraints:</b>			
<b>Range:</b>	10 cm to 12 m		
<b>Bearing:</b>	0° to 360°		
<b>Elevation:</b>	0° to $\pm 76^\circ$		
<b>Speed:</b>	1 kHz	(÷ by # of robots)	
<b>Size:</b>	22 cm diameter	(single board solution),	43/50 cm ring diameter (modular solution)
<b>Weight:</b>	245.2 g	(single board solution),	400 g (modular solution)
<b>Power:</b>	10 W	(at full speed)	
	<b>Average:</b>	<b>Worst case:</b>	<b>Comment:</b>
<b>Resolution:</b>	0.40 cm (0.14 cm)	1.1 cm (0.3 cm)	RMS $\leq 6$ m ( $\leq 2$ m)
<b>Noise:</b>	3.20 cm (1.95 cm)	6.6 cm (2.6 cm)	RMS $\leq 6$ m ( $\leq 2$ m)
<b>Range error:</b>	<5.02 %	<7.57 %	$\leq 6$ m (across all bearings and 0° elevation)
	<5.02 %	<13.01 %	$\leq 6$ m (across all bearings and elevations up to 53.1°)
	<9.11 %	<15.27 %	$\leq 12$ m (fixed bearing and 0° elevation)
<b>Bearing error:</b>	<3.13°	<10.79°	$\leq 6$ m (across all ranges and 0° elevation)
	<3.13°	<13.95°	$\leq 6$ m (across all ranges and elevations up to 53.1°)
<b>Elevation error:</b>	<4.40°	<9.40°	$\leq 6$ m (across all ranges, bearings for elevations up to 76°)

### 5.3.4 Proximity sensing

The sensor is also capable of detecting obstacles using the 3-D proximity sensing. This is achieved by listening to the reflected signal during a transmission. The angular resolution of the 3-D proximity sensing is defined by the number of photodiodes. The current sensor has 48 detectable sectors around the robot. The most useful sectors are the eight that are spaced around the  $0^\circ$  perimeter of the robot, these can be used for obstacle avoidance and navigation. Also, the eight that are facing  $90^\circ$  up and the eight that are facing  $90^\circ$  down can be used for altitude sensing with reference to the floor and ceiling. The proximity sensing has been tested on a white, glossy wall and a brown, dull wall. Signal strength measurements were taken at intervals of 10 cm, from 10 to 300 cm. The response, shown in figure 5.25, of the white, glossy wall is stronger than the response of the brown, dull wall, where the maximum detectable range is 300 cm and 200 cm, respectively. This suggests that the proximity sensing can be used for obstacle detection, but care must be taken in different environments.

### 5.3.5 Sensor limitations

The standard deviation for the range, bearing and elevation errors is very small and shows a good signal-to-noise ratio. However, there are small skews in the sensor's accuracy, the reason for this is likely due to environmental reflections. The reflectivity of the surrounding environment can change the intensity of the received signal strength, thus skewing the perceived measurements between robots. The sensor has been calibrated in a large open room, so when used in a smaller indoor environment the accuracy can be skewed. The extent of the skewing depends on the reflectivity of the surrounding objects. The reflectivity is affected by the contrast and texture of the surrounding materials. For example, a lighter wall tends to have a higher reflectivity than a darker wall. However, it is possible for a darker wall with a glossy finish to have higher reflectivity than a darker wall with a dull finish. In order to improve the accuracy of the sensor it may be possible to reduce the skew caused by reflection by taking into account the information observed about the surrounding environment from the proximity sensing, however this must be further investigated.

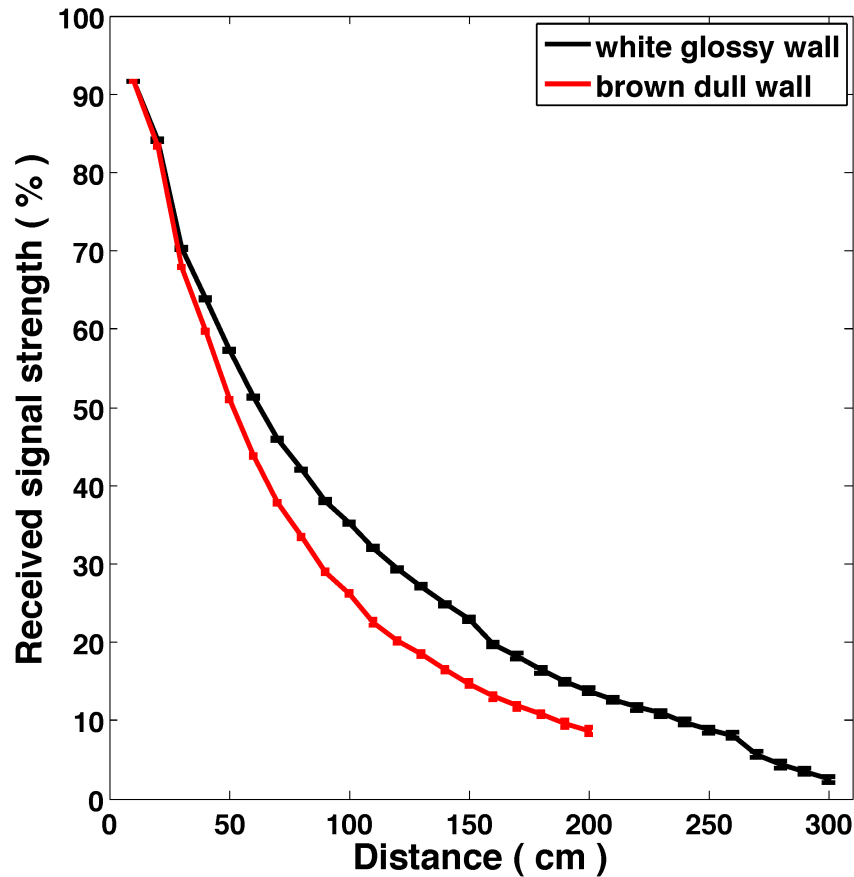


Figure 5.25: Proximity sensing showing the range as a function of the reflected signal strength from a single sensing sector, for a white, glossy wall and a brown, dull wall

### 5.3.6 Comparison with other relative sensors

The above-presented sensor is the only existing embedded 3-D relative positioning sensor. However, its 2-D features can be compared against the three best performing 2-D relative positioning sensors (with a full 360° coverage) from research that are shown in Table 1.2, chapter 1, (note that there are currently no stand alone commercially available relative positioning sensors).

Taking a closer look at the performance of the three sensors from the state of the art, shown in Table 5.3, indicates that none are the best across all categories. The infrared based 2-D relative positioning sensor by Kemppainen et al. (2006), uses a variable gain amplifier with a mirror to achieve the longest operating range (10 m) and a rotating receiver to achieve the best bearing accuracy (max error of 5.0 deg at 3 m). However, the rotating receiver causes it to have

the slowest update-rate (0.5 Hz for 10 robots) among the three sensors. The ultrasonic based 2-D relative positioning sensor by Rivard et al. (2008), uses Time Of Flight (TOF) sensing to achieve the best range accuracy (max error of 5 cm at 6 m). However, as ultrasonics is sound based it has an update-rate limited by the propagation of the sound waves (1.33 Hz for 10 robots). The infrared based 2-D relative positioning sensor by Pugh et al. (2009), uses high-frequency modulation (10 MHz) to achieve the fastest operating update-rate (25 Hz for 10 robots) among the three sensors. However, the RSSI chip ranging technique causes it to have the shortest range (3.3 m) among the three sensors.

The developed 3-D relative positioning sensor when compared against these three state of the art sensors, shows that it performs very well in all categories. Note that it is difficult to find comparative data that is sufficient for a true comparison as most papers have not characterised the performance of their sensors in detail. The 3-D infrared relative positioning sensor has been compared against the infrared based 2-D relative positioning sensor by Kemppainen et al. (2006). The developed sensor is 200 times faster, has a maximum range that is 1.2 times longer, with an accuracy performance that is 1.2 times and 1.2 times better for range and bearing respectively (comparison at 3 m range due to limited available data). The 3-D infrared relative positioning sensor has been compared against the ultrasonic based 2-D relative positioning sensor by Rivard et al. (2008). The developed sensor is 75 times faster, has a maximum range that is 1.8 times longer, with an accuracy performance that is 9 times worse and 3.3 times better for range and bearing respectively (comparison at 6 m range). The 3-D infrared relative positioning sensor has been compared against the infrared based 2-D relative positioning sensor by Pugh et al. (2009). The developed sensor is 4 times faster, has a maximum range that is 3.6 times longer, with an accuracy performance that is 2.5 times and 3.5 times better for range and bearing respectively (comparison at 3 m range).

The ultrasonic 2-D sensor by Rivard et al. (2008), due to the high accuracy of TOF, has the best range error performance. However, the developed 3-D sensor performs better in every other category and has a better range error than the other infrared based sensors. Additionally, the developed sensor is the only sensor capable of providing proximity sensing and 3-D relative positioning information.

Table 5.3: State of the art comparison between top three relative positioning sensors and the developed 3-D sensor. Cells marked in **bold** indicate the best performing in that category

Author Reference	Ranging Method	Range Error: (max)		Bearing Error: (max)		Update-rate (10 robots)	Operating Range
		3 m	6 m	3 m	6 m		
Kemppainen et al. (2006) †	IR, variable gain	16.9 cm	X	5.0°	X	0.5 Hz	10 m
Rivard et al. (2008) *	Ultrasound, TOF	<b>3.0 cm</b>	<b>5.0 cm</b>	9.0°	10.0°	1.33 Hz	6.7 m
Pugh et al. (2009) Δ	IR, RSSI RF chip	35 cm	n/a	15.1°	n/a	25 Hz	3.3 m
Developed 3-D sensor ⊗	IR, cascaded filtering	14.2 cm	45.4 cm	<b>4.3°</b>	<b>3.0°</b>	<b>100 Hz</b>	<b>12 m</b>

†: Data taken from Table 2 - STD + mean error (transmission spread by mirror)

\*: Data taken from Figure 6 (transmission spread by reflector)

Δ: Data taken from Table 1 and Figure 8 (including error from rotating transmitter)

⊗: Data taken from figure 5.12 and figure 5.19 (including error from rotating transmitter)

## 5.4 Conclusion

In order to enable the collective operation of indoor flying robots, spatial coordination between individual robots is essential. However, there is a lack of on-board sensing technologies available that can enable spatial-coordination in real-world environments. No existing sensors, commercially available or in research can provide embedded 3-D relative positioning for indoor hovering platforms.

This chapter presents a practical on-board sensing method for achieving spatial-coordination between multiple robots in three dimensions. The developed infrared 3-D relative positioning sensor is capable of sensing the range, bearing and elevation between indoor flying robots and can provide proximity sensing in a 3-D space. A newly developed ranging technique allows for an improved sensing performance, including long range (12 m), high speed (1 kHz per robot) and high resolution (better than 1.1 cm up to 6 m). The developed approach allows for easily adaptation, to suit other robots and applications, depending on a specific sensing speed and coverage requirement.

Comparing the 3-D relative positioning sensor with other 2-D relative positioning sensors, shows that the developed sensor performs better in every category, all except the range error. The ultrasonic based 2-D relative positioning sensor by Rivard et al. (2008), uses TOF sensing to achieve the best range accuracy (max error of 5 cm). However, as ultrasonics is sound based it has an update-rate limited by the propagation and reflection waiting time of the sound waves (1.33 Hz for 10 robots). The developed 3-D relative positioning sensor operates at an update-rate that is 75 times faster than this. Additionally, the developed sensor is the only sensor capable of providing proximity sensing and 3-D relative positioning information. The main challenge was in the development of the new high performance ranging technique and being able to achieve unobstructed sensing without affecting the practicality of a flying robot. The developed sensor is the only embedded 3-D relative positioning sensor available that has the ability to enable inter-robot spatial-coordination in three dimensions, which is necessary for achieving goal-directed flight on highly dynamic flying robots. This approach does not require computationally expensive algorithms, external sensors or modification of the environment, and is largely independent on varying environmental illumination.

---

# 6

---

## Validation

---

Now that all the pieces are in place, it is time to validate that the developed coaxial counter-rotating propulsion system (chapter 2) together with the 3-D relative positioning sensor (chapter 5), is capable of enabling the collective operation of indoor flying robots. This chapter introduces an efficient swarm search scenario, based on the Swarmanoid<sup>1</sup> project application, which has been the driving motivation for this research. An autonomous flight control strategy that builds upon the control strategy, from chapter 3, is then presented. The dimensioning strategy, from chapter 2, is then used to design a high-payload capable and robust hovering platform suitable for this application. The developed hovering platform is fitted with the 3-D relative positioning sensor, from chapter 5. A performance comparison between the developed platform and commercially available platforms is then shown. The chapter ends by demonstrating that the developed platform with the 3-D relative positioning sensor, is capable of goal-directed autonomous indoor flight and collective deployment of highly dynamic flying robots.

---

<sup>1</sup><http://www.swarmanoid.org> (accessed Feb. 2011)

## 6.1 Introduction

This chapter brings together the proposed methodologies and developed technology, to enable the collective operation of indoor flying robots. In order to do this, a new platform, named the Eye-bot, has been developed that is highly suitable for collective operation. But first the underlying motivation will be presented regarding the Eye-bots design requirements.

Eye-bots are autonomous flying robots with powerful sensing and communication abilities for search, monitoring and pathfinding within built environments. Eye-bots operate together in a swarm, to efficiently explore built environments, locate predefined targets, and guide other robots or humans. Eye-bots are part of the Swarmanoid<sup>2</sup>, a European research project aimed at developing a heterogeneous swarm of wheeled<sup>3</sup>, climbing<sup>4</sup>, and flying robots that can carry out tasks normally assigned to humanoid robots (figure 6.1). Eye-bots serve the role of the eyes within the Swarmanoid and guide other robots that have simpler sensing abilities. Eye-bots can also be deployed on their own within built environments to locate humans who may need help, suspicious objects, or traces of dangerous chemicals. Their programmability, combined with swarm intelligence behaviours, makes them rapidly adaptable to several types of situations that may pose a danger for humans.

An energy efficient swarm search algorithm, developed in simulation by Stirling et al. (2010), uses flying robots to search a building for a pre-defined target. The algorithm solely relies on local sensing and local communication from a relative positioning sensor. The flying robots operate in two modes: a static beacon or a flying explorer (see video<sup>5</sup>). In the beginning, the swarm is located in a cluster. One at a time, flying explorers are deployed within the environment, shown in figure 6.2. When the explorers reach the edge of the sensing range they attach to the ceiling and become a beacon. Each robot extends the reach of the last, thus building a chain that can be used to guide other robots or people, to accomplish the searching task. While attached they use an omni-directional camera with a birds-eye-view, to search the room below for a pre-defined target.

---

<sup>2</sup><http://www.swarmanoid.org> (accessed Feb. 2011)

<sup>3</sup><http://mobots.epfl.ch/marxbot.html> (accessed Feb. 2011)

<sup>4</sup><http://mobots.epfl.ch/handbot.html> (accessed Feb. 2011)

<sup>5</sup>Video: <http://jfroberts.com/phd> (energy\_efficient\_swarm\_search.mp4)



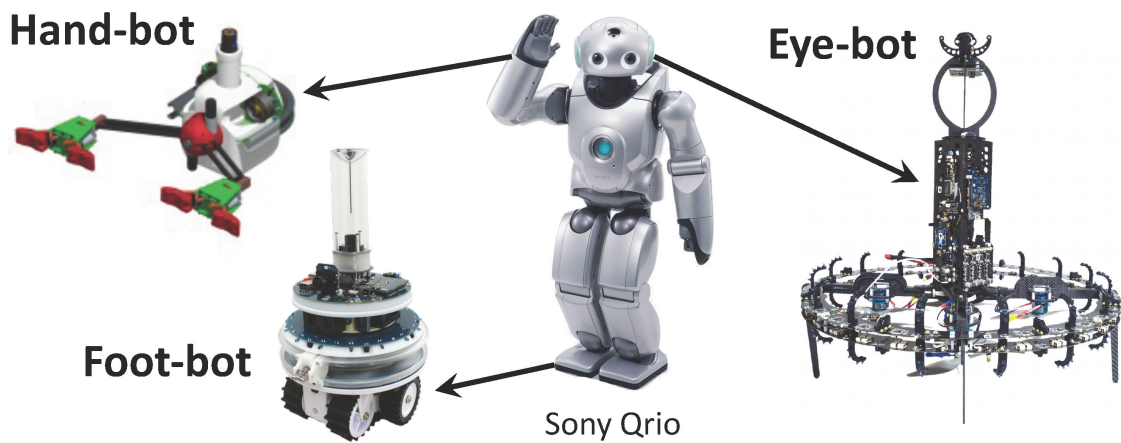


Figure 6.1: "From Humanoid to Swarmanoid", a heterogeneous robotic swarm made up of several Foot-bots (*wheeled*), Hand-bots (*climbing*) and Eye-bots (*flying*)

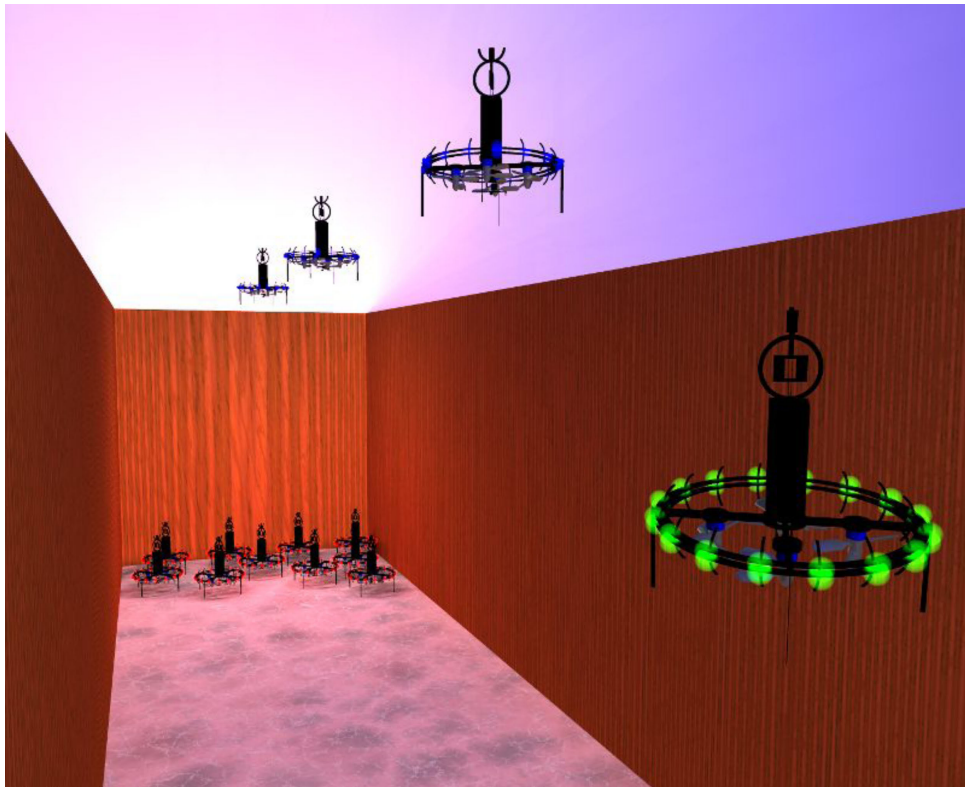


Figure 6.2: Simulation of search algorithm, showing Eye-bots building a chain

In the case of the Swarmanoid scenario, this target is a book on a shelf, which needs to be retrieved and brought back to the start of the chain. The Foot-bots and Hand-bots are design to perform the retrieval task and are guided by the Eye-bots attached overhead.

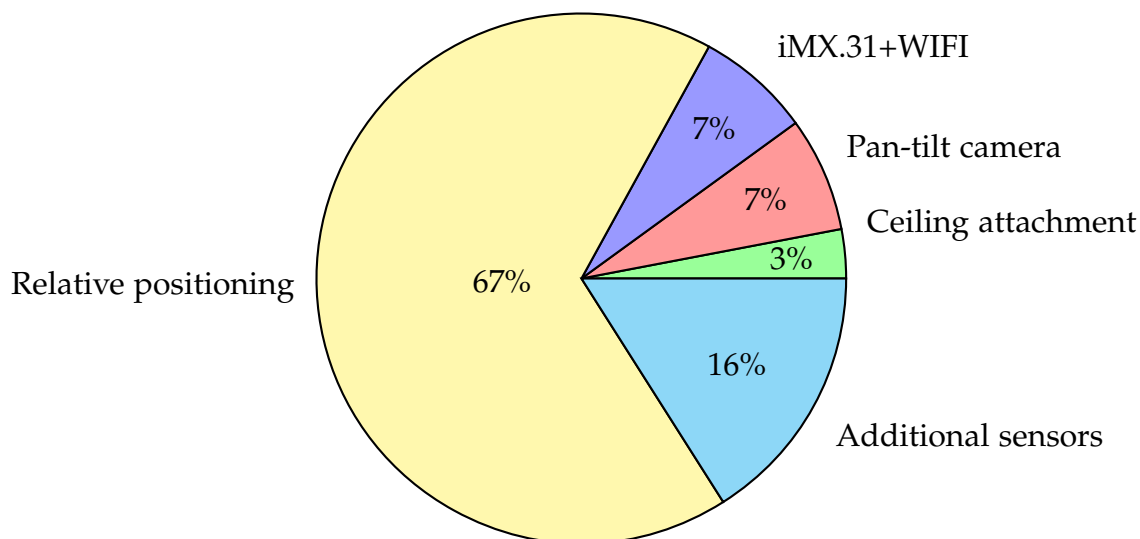


Chart 6.1: Weight distribution of the Eye-bots payload requirement

In order to accomplish such a challenging task, the Eye-bot must be able to carry the required sensing and processing capability suitable for collective operation. Thus, the Eye-bots payload includes a ceiling attachment mechanism (20 g), omni-directional camera (40 g), embedded iMX.31 computer with WIFI (40 g), 3-D relative positioning sensor from chapter 5 (400 g), and some additional optional sensors useful for autonomous flight (100 g). A detailed explanation of each of these is provided in appendix A.2. Thus, the total payload requirement for the Eye-bot is 600 g. The payload weight distribution, shown in chart 6.1, indicates that a substantial part of the payload (67% = 400 g) is allocated for relative positioning sensing. This 400 g payload alone, is higher than any commercial platform, suitable for indoor operation, is capable of carrying (see table 1.1). Therefore, to enable collective operation on an indoor hovering platform, it is necessary to use a high-payload capable coaxial counter-rotating propulsion system, such as the design implemented in chapter 2, section 2.3.6.

Now that the Eye-bots application and payload requirement has been defined, the dimensioning strategy, from chapter 2, is used to design a high-payload capable and robust hovering platform suitable for the Eye-bot application.

## 6.2 Optimising for high-payload and robustness

In order to design the Eye-bot platform, the payload optimised hovering platform from chapter 2, section 2.3.3 has been used as a reference design. The reference design used coaxial motors with counter-rotating thin-electric propellers, which have been chosen due to their high-payload capability. The payload requirement of the platform has already been defined, in section 6.1, as 600 g. In order to increase the robustness of the platform, some additional structural weight will be required. The ceiling attachment mechanism and the relative positioning sensor will also require additional structural support. Due to this extra weight, a reasonable flight endurance of 10 min has been chosen.

The dimensioning method, presented in chapter 2, section 2.2.1, can now be used to determine the recommended physical attributes of the hovering platform. The platform weight can be estimated based on the 600 g payload requirement and a 30% payload loading, giving an estimated platform weight of 2000 g. This is a 20% lower payload loading than the reference design, which has been chosen so that more structural weight can be allocated. As the platform will be optimised for a high-payload and robustness, a medium 22% battery loading has been chosen, which is the same as the reference design.

For this specific flight endurance and payload requirement, a realistic range of propeller-motor efficiencies, shown in figure 6.3 *left*, corresponding to various platform sizes has been determined. This is based on the chosen 600 g payload and a FM of 0.39 for the coaxial counter-rotating thin-electric propellers. Additionally, a realistic range of battery weights, shown in figure 2.10 *right*, corresponding to various platform sizes has been determined.

Based on the desired 22% battery loading, an estimated platform size of 50 cm in diameter with a propeller diameter of 18 cm, would be suitable for a high-payload hovering platform. In order to implement this in reality, a coaxial motor that is capable of producing at least 500 g of thrust with a propeller-motor efficiency equal to  $\approx 4.3$  g/W is required. The dimensioning method also indicates that the goal structure weight should be approximately 952 g and the goal battery weight should be approximately 449 g, to achieve the desired 10 min flight endurance. The hovering platform weight distribution, shown in chart 6.2, indicates that the most weight has been allocated to the structure, for supporting the unique payload and added robustness requirements.

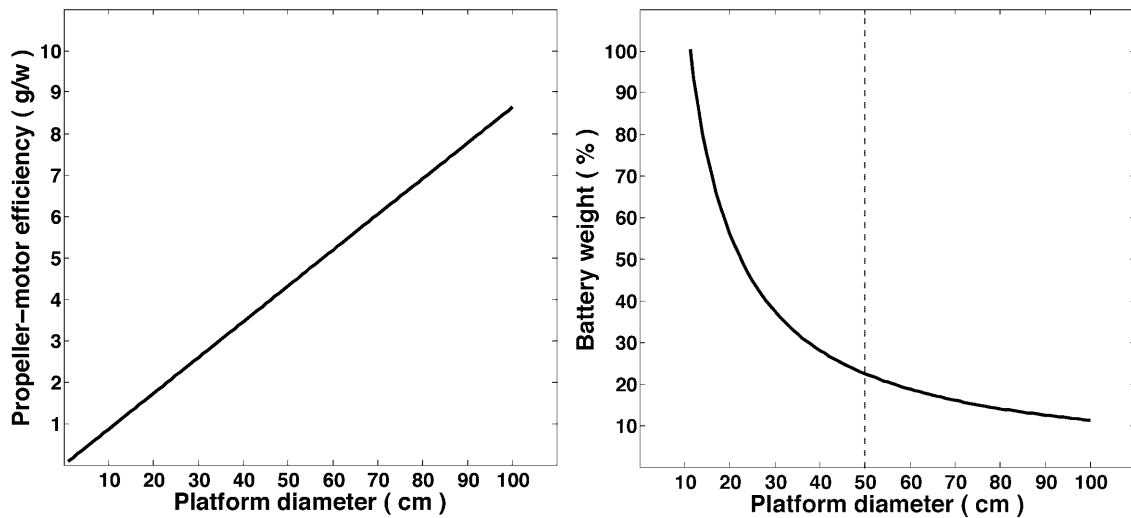


Figure 6.3: Eye-bot design. *Left*: Estimated propeller-motor efficiency with respect to the platform diameter. *Right*: Estimated battery weight with respect to the platform diameter. The dotted line indicates the recommended platform size, which is selected using the desired battery loading ( $m_p = 600$  g,  $FM = 0.39$  (coaxial thin-electric propellers),  $L_p = 30\%$ ,  $L_b = 22\%$ )

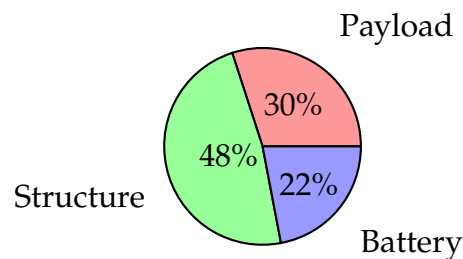


Chart 6.2: Weight distribution of the Eye-bot hovering platform

Now that the Eye-bot design goal has been defined, an autonomous flight control strategy can be developed that builds upon the autonomous indoor flight work from chapter 3.

### 6.3 Flight control strategy

In order to achieve autonomous goal-directed flight and collective deployment, a 3-D waypoint controller has been developed that uses only the information from the 3-D relative positioning sensor and inertial sensing.

Let us consider the earth fixed-frame  $E$  and the hovering platform body fixed-frame  $B$ , as shown in figure 6.4. Using Euler angles parameterization, the platforms orientation in space is given by a rotation  $R$  from  $B$  to  $E$ , where  $R \in SO3$  is the rotation matrix. Let us also consider that a 3-D relative positioning sensor has been installed on the hovering platform and another at the earths origin. The relative range ( $r$ ), bearing ( $\theta^b$ ) and elevation ( $\theta^e$ ) from the 3-D relative positioning sensor are spherical coordinates, which first need to be translated onto the cartesian coordinate framework of the hovering platform as follows:

$$\begin{aligned} x &= r \sin \theta^e \cos \theta^b \\ y &= r \sin \theta^e \sin \theta^b \\ z &= r \cos \theta^e \end{aligned} \quad (6.1)$$

This is because the control inputs to the hovering platform are pitch, roll and altitude commands corresponding to a translation in the  $x$ ,  $y$  and  $z$  axis, respectively. The yaw command defines the reference frame of  $R$ , which cannot be obtained through the standard range, bearing and elevation information. The yaw reference must be obtained through the inverse bearing ( $\theta^{ib}$ ), which is the bearing of the hovering platform as perceived by the earths origin. This inverse bearing is wirelessly communicated between relative positioning sensors over the internal RF communication channel.

The attitude estimation of the pitch ( $\theta$ ), roll ( $\phi$ ) and yaw ( $\psi$ ) are obtained using the same method as derived in chapter 3. However, the motor mixer now commands eight motor speeds instead of four, which can be defined as:

$$\begin{aligned} u1 &= u \theta - u \psi + u z & u5 &= u \theta + u \psi + u z \\ u2 &= -u \theta - u \psi + u z & u6 &= -u \theta + u \psi + u z \\ u3 &= -u \phi - u \psi + u z & u7 &= -u \phi + u \psi + u z \\ u4 &= u \phi - u \psi + u z & u8 &= u \phi + u \psi + u z \end{aligned} \quad (6.2)$$

where  $u1:8$  are the control inputs corresponding to the motor forces  $F_{1:8}$ . The yaw controller balances the eight torques ( $\Omega_{1:8}$ ) produced by the rotational component of the motors. Attitude control, inspired by Huang et al. (2009), is implemented using three independent PID controllers augmented with feedback on

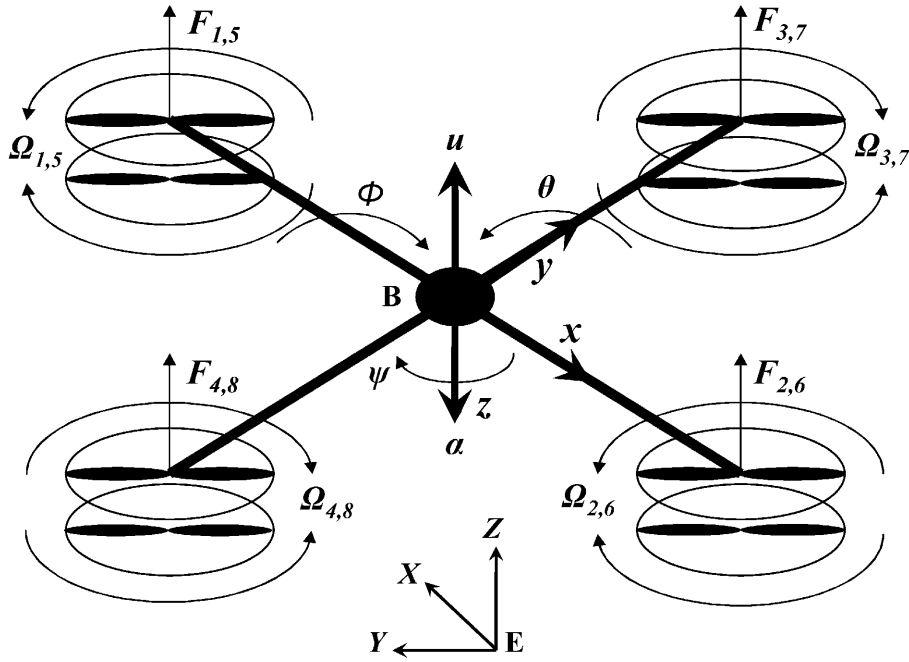


Figure 6.4: Eight propeller, hovering platform coordinate system

acceleration, whose control law can be defined as:

$$\begin{aligned}
 u \theta &= k_{dd}(\ddot{\theta}_{ref} - \ddot{\theta}) + k_d(\dot{\theta}_{ref} - \dot{\theta}) + k_p(\theta_{ref} - \theta) + k_i \int_0^t (\theta_{ref} - \theta) dt \quad (6.3) \\
 u \phi &= k_{dd}(\ddot{\phi}_{ref} - \ddot{\phi}) + k_d(\dot{\phi}_{ref} - \dot{\phi}) + k_p(\phi_{ref} - \phi) + k_i \int_0^t (\phi_{ref} - \phi) dt \\
 u \psi &= k_{dd}(\ddot{\psi}_{ref} - \ddot{\psi}) + k_d(\dot{\psi}_{ref} - \dot{\psi}) + k_p(\psi_{ref} - \psi) + k_i \int_0^t (\psi_{ref} - \psi) dt
 \end{aligned}$$

where  $k_{dd}$ ,  $k_d$ ,  $k_p$  and  $k_i$  are the double derivative (angular acceleration), derivative, proportional, and integral control gains respectively.  $\theta_{ref}$ ,  $\phi_{ref}$ ,  $\psi_{ref}$  are the commanded reference angles.

Altitude control is also implemented using a PID controller augmented with feedback on acceleration and linearization to compensate for the force of gravity when rolling and pitching, whose control law can be defined as:

$$u z = \frac{1}{\cos\theta \cos\phi} (k_{dd}(\ddot{z}_{ref} - \ddot{z}) + k_d(\dot{z}_{ref} - \dot{z}) + k_p(z_{ref} - z) + k_i(i_a)) \quad (6.4)$$

where  $z_{ref}$  is the commanded reference altitude and  $i_a$  is the altitude accumulator. The altitude accumulator counts up whenever the hovering platform is below the desired altitude and down otherwise, thus maintaining a mean value for the total thrust required to hover.

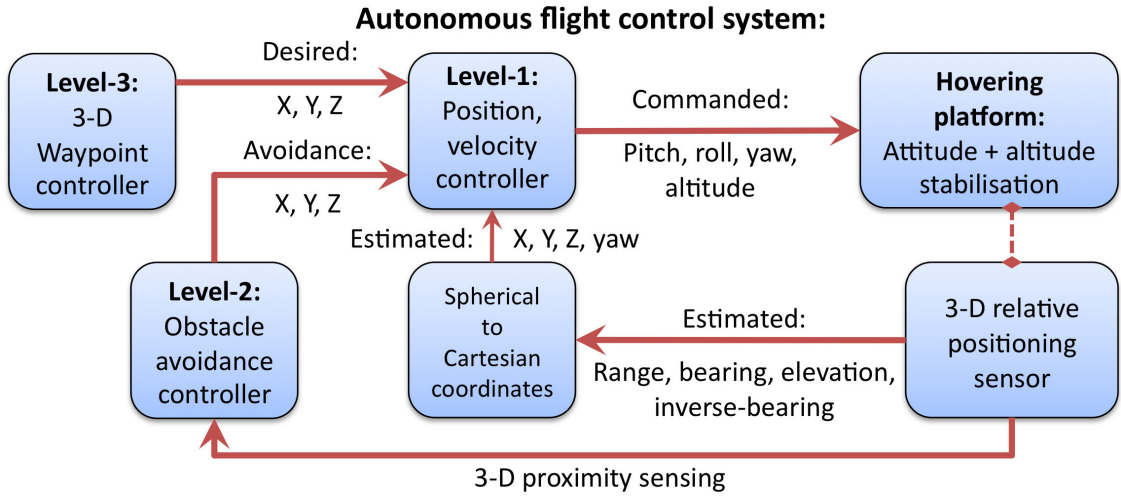


Figure 6.5: Functional diagram of the autonomous flight control system

The autonomous flight control algorithm, shown in figure 6.5, has three different levels of control: a position and velocity controller, an obstacle avoidance controller and a 3-D waypoint controller.

The first level is a position and velocity controller, which allows the hovering platform to fly to a desired location, while keeping a safe and controllable translational speed. The  $x$  and  $y$  positions are dependant on the rotation of  $R$ , which is defined by the difference between the bearing and the inverse bearing, thus the yaw reference can be defined as:

$$\psi_{ref} = \pi - \theta^{ib} + \theta^b \quad (6.5)$$

where the yaw angle of the hovering platform will always point the same heading as the sensor at the earths origin. Therefore, if  $x_{ref}$  and  $y_{ref}$  are the desired position coordinates, then the error can be defined as:

$$\begin{aligned} e_x &= x - y_{ref} \sin \psi_{ref} + x_{ref} \cos \psi_{ref} \\ e_y &= y + y_{ref} \cos \psi_{ref} - x_{ref} \sin \psi_{ref} \end{aligned} \quad (6.6)$$

where,  $\psi_{ref}$  is used to de-rotate the  $x$  and  $y$  position error.

A cascaded controller is implemented for position and velocity control, which is inspired by the controller presented in Gurdan et al. (2007). For the speed of the hovering platform to be determined, first the actual position is filtered to obtain a moving reference point:

$$\begin{aligned} \dot{x}_f &= F_{x1}(s)\dot{x} \\ \dot{y}_f &= F_{y1}(s)\dot{y} \end{aligned} \quad (6.7)$$

where  $F_{x1}$  and  $F_{y1}$  are low-pass filters affecting platform velocity. The outer part of the cascade is a PD controller, whose output is the desired speed for traveling to the desired position:

$$\begin{aligned} v x_{ref} &= k_d \dot{x}_f + k_p e_x \\ v y_{ref} &= k_d \dot{y}_f + k_p e_y \end{aligned} \quad (6.8)$$

The inner part of the cascade is a horizontal speed controller that uses the speed and acceleration as inputs, whose output is the command angle for traveling to the desired position:

$$\begin{aligned} \theta_{ref} &= k_{dd} F_{x2}(s) \ddot{x}_f + k_d (v x_{ref} - \dot{x}_f) \\ \phi_{ref} &= k_{dd} F_{y2}(s) \ddot{y}_f + k_d (v y_{ref} - \dot{y}_f) \end{aligned} \quad (6.9)$$

where  $F_{x2}$  and  $F_{y2}$  are low-pass filters affecting platform acceleration, and  $u \theta$  and  $u \phi$  need to be limited to a maximum angle, which corresponds to a maximum translation velocity, allowing for safe operation.

The second level is a 3-D obstacle avoidance controller that uses the 3-D proximity sensing (see chapter 5, section 5.3.4) to push the hovering platform away from the walls, the ceiling, the floor and other dangerous obstacles. The  $x$  and  $y$  obstacle detection is implemented using a vector field from the eight proximity sensing sectors, around the hovering platforms perimeter. The vector field is created based on the photodiode geometric spacing ( $\beta_i = \frac{\pi}{4}$ ):

$$\begin{aligned} x_{prox}(i) &= \cos\left(\frac{\pi i}{4} + \frac{\pi}{8}\right) \\ y_{prox}(i) &= \sin\left(\frac{\pi i}{4} + \frac{\pi}{8}\right) \end{aligned} \quad (6.10)$$

where  $i$  is the photodiode index around the perimeter and the second term is the sensor offset ( $\frac{\pi}{8}$ ). The normalised  $x$  and  $y$  collision avoidance vector is then defined as:

$$\begin{aligned} x_{coll} &= \sum_{i=1}^8 \left( \left(1 - \frac{d_{prox}(i)}{d_{max}}\right) x_{prox}(i) \right) \\ y_{coll} &= \sum_{i=1}^8 \left( \left(1 - \frac{d_{prox}(i)}{d_{max}}\right) y_{prox}(i) \right) \end{aligned} \quad (6.11)$$

where  $d_{prox}$  is the measured proximity distance and  $d_{max}$  is the maximum proximity distance. The  $z$  obstacle detection is implemented using the eight upward



facing ( $d_{prox-up}$ ) and eight downward facing ( $d_{prox-dwn}$ ), proximity sensing sectors:

$$z_{coll} = \frac{1}{8} \sum_{i=1}^8 \left( 1 - \frac{d_{prox-up}(i)}{d_{max}} \right) - \frac{1}{8} \sum_{i=1}^8 \left( 1 - \frac{d_{prox-dwn}(i)}{d_{max}} \right) \quad (6.12)$$

where  $d_{prox-up}$  and  $d_{prox-dwn}$  are normalised and averaged to combine all the sensors facing common directions.

The 3-D collision avoidance is implemented using a PD controller, whose output adjusts the pitch, roll and altitude commands:

$$\begin{aligned} \theta_{ref} &= \theta_{ref} - k_d \dot{x}_{coll} + k_p x_{coll} \\ \phi_{ref} &= \phi_{ref} - k_d \dot{y}_{coll} + k_p y_{coll} \\ z_{ref} &= z_{ref} - k_d \dot{z}_{coll} + k_p z_{coll} \end{aligned} \quad (6.13)$$

Thus, providing a repulsion force away from any obstacle in 3-D, which naturally pushes the hovering platform to the largest open space.

The third level is a 3-D waypoint controller that commands the hovering platform to fly along a pre-defined flight path. This is achieved using some basic control logic and a list representing the  $x$ ,  $y$  and  $z$  waypoints along the desired flight path. The waypoint list is defined by:

$$w_p(i) = \begin{pmatrix} x_{ref} \\ y_{ref} \\ z_{ref} \end{pmatrix} \quad (6.14)$$

where  $i$  is the waypoint index. In order to determine when the hovering platform has reached the desired position, the waypoint error can be determined:

$$e_w = \sqrt{(x_{ref} - x)^2 + (y_{ref} - y)^2} \quad (6.15)$$

where  $e_w$  combines both  $x$  and  $y$  position errors. The control logic determines when the waypoint index should be incremented:

$$i = \begin{cases} i + 1 & \text{if } e_w < w_t \\ i & \text{otherwise} \end{cases} \quad (6.16)$$

where  $w_t$  is a pre-defined waypoint threshold error, which depends on the desired position accuracy for the waypoint location. Therefore, when the desired

position is achieved within a certain acceptance error, the waypoint list is incremented and the hovering platform flies to the next waypoint.

Now that an autonomous flight control strategy has been defined, which is compatible with the relative positioning sensor and incorporates an eight propeller motor mixer, the dimensioning strategy from chapter 2 can be used to design a suitable hovering platform.

## 6.4 Results

In this section the constructed Eye-bot hovering platform, fitted with the 3-D relative positioning sensor from chapter 5, is presented. A performance comparison between the developed platform and commercially available platforms is then shown. The chapter ends by demonstrating that the developed platform, when fitted with the 3-D relative positioning sensor, is capable of goal-directed autonomous indoor flight and collective deployment.

### 6.4.1 Eye-bot hovering platform

The Eye-bot hovering platform, shown in figure 6.6, has been specifically designed for collective indoor operation and to meet the requirements of the Swarmoid project, by implementing the dimensioning design method.

The Eye-bot structure is fabricated from quasi-isotropic carbon fibre plate, which is designed for high-strength and light weight. The body is 54 cm tall with a base diameter of 50 cm. In order to attach to ferrous ceilings, a ceiling attachment and detachment mechanism is installed at the top of the body. This mechanism allows the Eye-bot to have an extended perching time up to 3 hours, while maintaining a bird's-eye view. At the base there are four Himax CR2805 coaxial brushless motors that are fitted with twin counter-rotating APC 7x5E/EP *inch* propellers. A detailed explanation of the structure is provided in appendix A.1.

The Eye-bot electronics consists of several distributed control boards and an embedded computer. The distributed control, includes an eight channel high-speed (500 Hz) brushless motor controller, flight controller, relative positioning controller and autonomous controller. The autonomous controller runs the flight control algorithm, presented in section 6.3. The relative positioning controller runs the 3-D sensing algorithm, presented in chapter 5, section 5.2.1, which pro-

Table 6.1: Comparison between the design and the real platform performance

	Diameter	Endurance	Motor-propeller Efficiency	Payload	Structure Weight	Battery Weight
<b>Design:</b>	50 cm	10 min	4.3 g/W	600 g	952 g	449 g
<b>Real:</b>	50 cm	9.9 min	4.4 g/W	600 g	897 g	451 g

(endurance with no payload = 17 min)

duces the range, bearing, elevation and proximity sensing information used by the autonomous controller. The flight controller is in charge of the attitude estimation and stability controllers, presented at the beginning of section 6.3. This flight controller outputs the eight motor speed commands used by the brushless motor controller. A detailed explanation of the custom designed control electronics is provided in appendix A.2.

The Freescale i.MX31, embedded computer (provided by Bonani et al. (2010) LSRO, EPFL) is used for machine vision processing and behavioural control algorithms. The Eye-bot is capable of seeing and pointing, anywhere in its lower hemisphere using its omni-directional, pan-tilt, high definition video camera and laser pointer, respectively. Note that the i.MX31 embedded computer and vision system are not used in the validation experiments presented in section 6.4. A detailed explanation of the embedded computer is provided in appendix A.2.

The thrust curve for the Eye-bot motor and propeller combination is shown in figure 6.7. At the hover point thrust, which is defined as 1/4 of the platform weight (488 g), the motor-propeller efficiency is determined. Notice that this point is in the upper thrust range, which is optimal for a high-payload capability.

Table 6.1 shows a comparison between the predicted dimensioning design and the real constructed, Eye-bot hovering platform. The structure weight is 55 g lighter, motor-propeller efficiency is 0.1 g/W better and the battery that was used is 2 g heavier. The lighter structure would suggest that the flight endurance would be underestimated, however the flight endurance is very close to the envisioned design. This is because the design strategy does not take into account the power consumption of the avionics. Using the endurance estimation model from chapter 4, section 4.2.1 indicates that the flight endurance is correct for the 20 W power consumption of the sensors and embedded processing. For a comparative measure the flight endurance without the 600 g payload was 17 min.

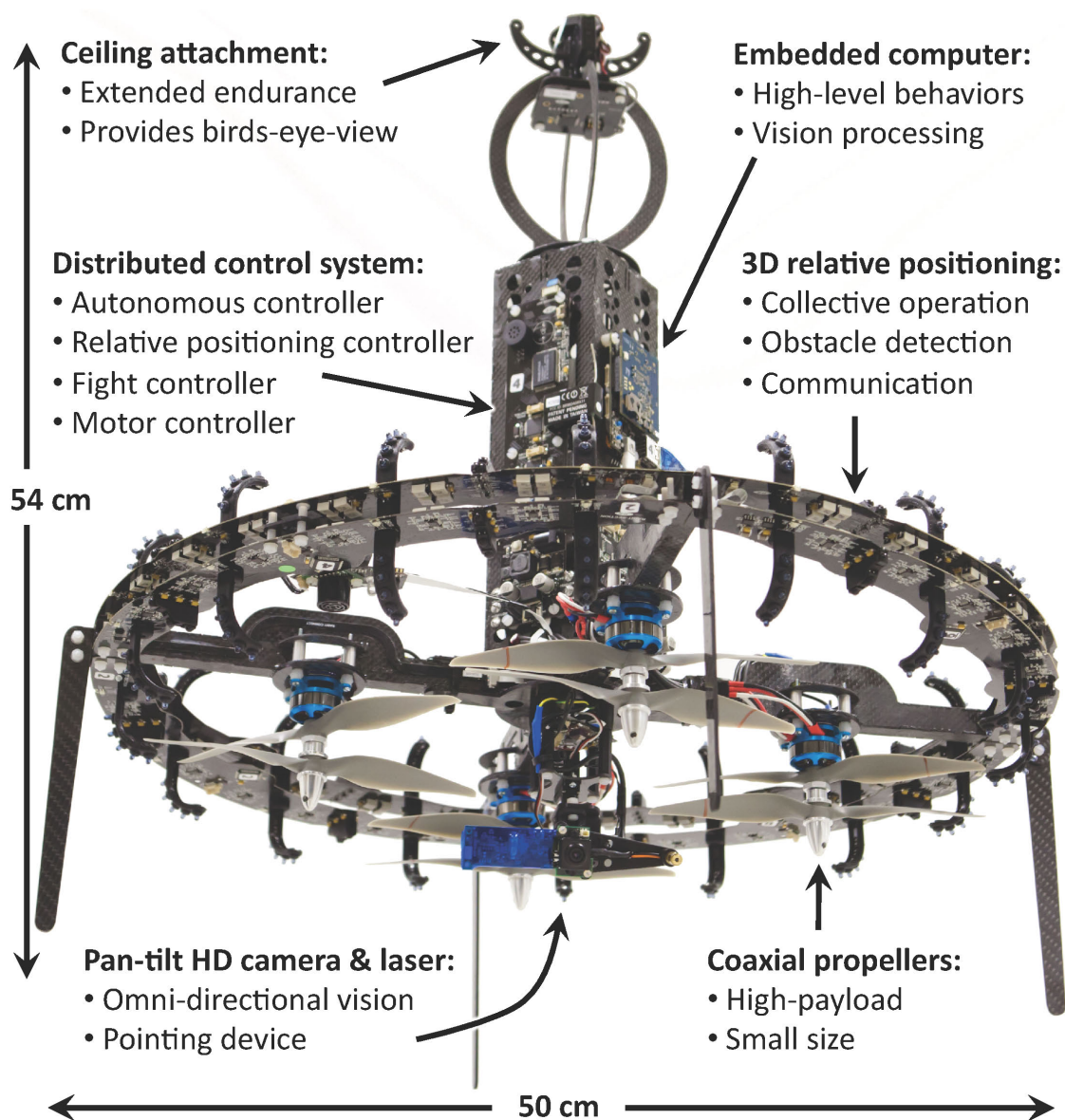


Figure 6.6: The Eye-bot - A flying robot custom designed for indoor collective operation, fitted with a 3-D relative positioning sensor (*base perimeter*) and ceiling attachment mechanism (*top*), having a diameter of 50 cm and a maximum take-off weight of 2 kg including a payload of 600 g

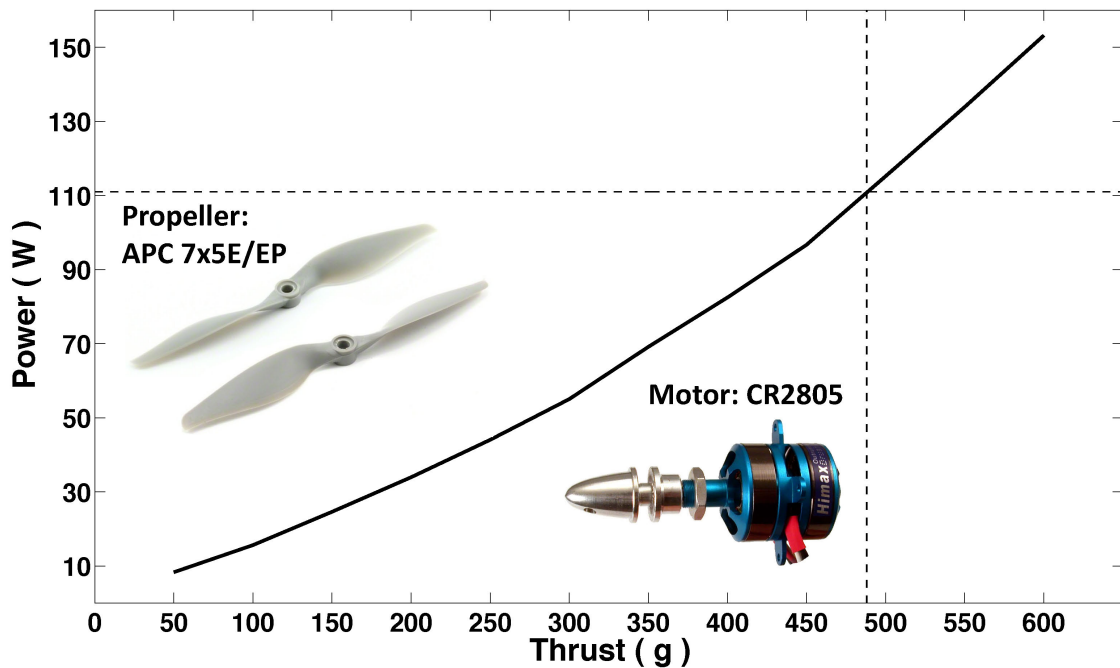


Figure 6.7: Thrust curve of the Himax CR2805 motor with twin APC 7x5 inch propellers. The dotted lines indicate the hover point thrust and power

## 6.4.2 Comparison against commercial platforms

The developed Eye-bot hovering platform can now be compared against the commercially available platforms that have been presented in chapter 1, table 1.1. A graphical comparison showing the maximum payload versus the diameter can be seen in figure 6.8. Similarly, a graphical comparison showing the maximum endurance versus the diameter can be seen in figure 6.9. The shaded gradient represents the increase in risk of a collision as the platform size approaches the 100 cm standard doorway limitation. For a fair comparison they have been compared in the maximum payload and maximum flight endurance conditions, with a constant battery size.

The Eye-bot, high-payload and robustness optimised hovering platform ("Eye-bot-RP"), does not perform better than the Payload optimised hovering platform ("Payload-RP") from chapter 2, section 2.3.7, due to the additional structural weight. However, it does stand out in comparison to the commercial platforms. The Eye-bot payload capability is 3 times higher than any other commercial platform of the same size, and 1.6 times higher than the "Pelican-RP", which is 1.6 times larger in diameter. The maximum flight endurance performance is similar

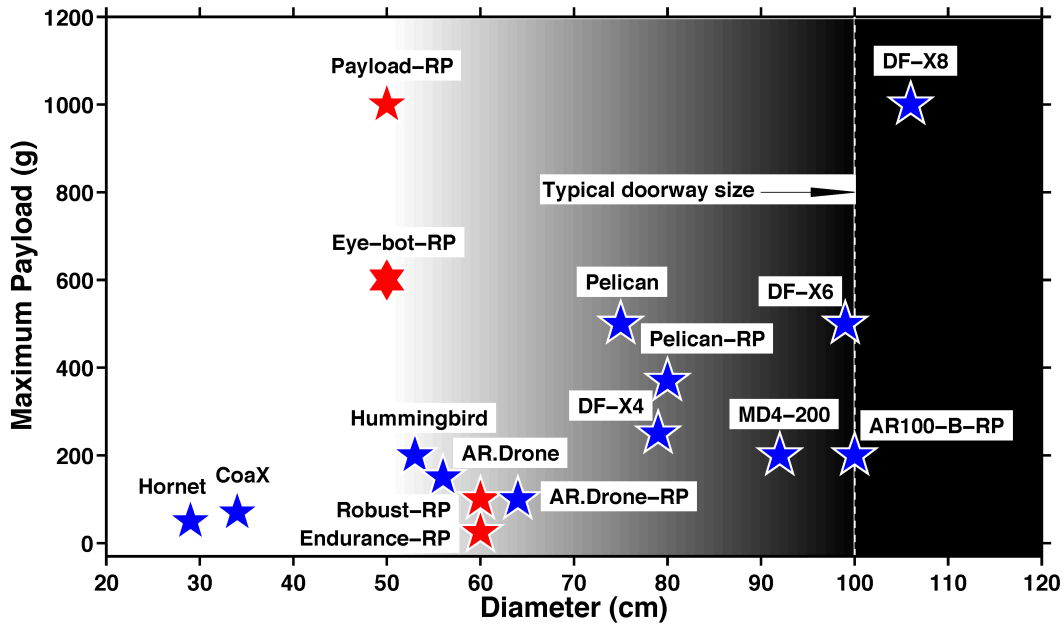


Figure 6.8: Payload versus diameter comparison against commercially available platforms (see chapter 1, table 1.1). The background shows a gradient of increasing risk of a collision as the platform size approaches the 100 cm doorway limitation. "-RP" indicates a platform with rotor protection

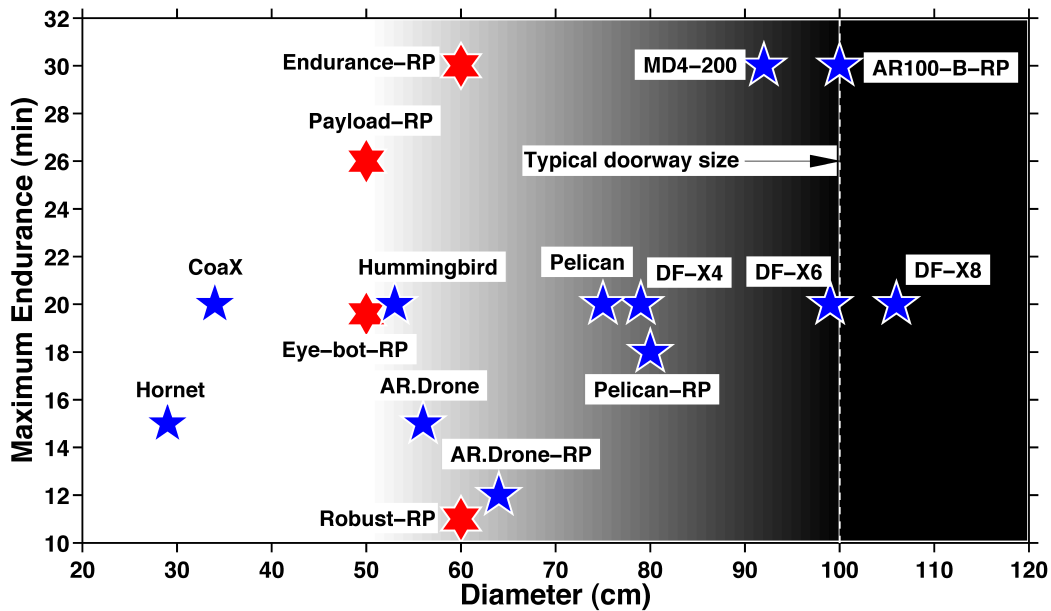


Figure 6.9: Endurance versus diameter comparison against commercially available platforms (see chapter 1, table 1.1). The background shows a gradient of increasing risk of a collision as the platform size approaches the 100 cm doorway limitation. "-RP" indicates a platform with rotor protection

to any other commercial platform suitable for indoor operation (below 80 cm). This platform is small (50 cm), has a high-payload capability (600 g) and high flight endurance (10-17 min). Therefore, it is highly suitable for carrying the required sensing and processing, in order to demonstrate goal-directed flight and collective deployment, in the following validation experiments.

### 6.4.3 Energy efficient swarm search implementation

In order to implement the energy efficient swarm searching algorithm, introduced in section 6.1, there are three incremental steps required; flight controller tuning, goal-directed flight and collective deployment. First, it is necessary to tune the autonomous flight controller parameters, in order to achieve basic autonomous flight behaviours including hovering on the spot, basic collision avoidance and simple waypoint "ping-pong" control, using a stationary Eye-bot as a fixed reference. In any of these experiments the reference Eye-bot could be attached to the ceiling, like in the simulation, or simply stationed on the ground. Goal-directed flight, specifically designed for the searching algorithm, can then be implemented and the performance of the system analysed. The fixed reference compensates for the platform drift and allows for the Eye-bot to fly to a desired location. However, using one reference Eye-bot alone does not allow for chain following, as required by the searching algorithm. Finally, collective deployment can then be implemented, which incorporates goal-directed flight and additionally allows the flying Eye-bot to continue along a chain of several stationary reference Eye-bots. To allow for seamless chain building, the flying robot must be able to dynamically switch between multiple reference robots while flying along the chain. This is a fundamental feature required to prove that the efficient swarm search algorithm would work in reality.

### 6.4.4 Flight controller tuning

The autonomous flight control algorithm parameters have been determined empirically and tuned experimentally to obtain the best performance. The position and velocity controllers were tuned first, the goal was to hover on the spot with the smallest amount of positioning error. During these tests a safety pilot was ready at all times to take control if there was a problem. Once the smallest positioning error was obtained, the collision avoidance controller was tuned. For

the hovering platforms protection, the weighting of the collision avoidance controller should be stronger than that of the waypoint controller, but not too strong or else the hovering platform will oscillate between closely spaced walls. Therefore, if the proximity sensors detect an obstacle, the collision avoidance will adapt the desired commands to push the hovering platform towards the largest open space. A test video has been documented to demonstrate the hovering and collision avoidance capabilities (see video<sup>6</sup>). After achieving a reasonable compromise between positioning error and collision avoidance, the waypoint controller was implemented. The velocity controller gains were tuned, which are responsible for controlling the transition speed between waypoints. The goal is to find a fast transition speed that does not overshoot the waypoint. A test video has been documented to demonstrate a simple two point "ping pong" waypoint control (see video<sup>7</sup>). Now that the flight control algorithm has been tuned, the autonomous goal directed flight experiment can be implemented.

### 6.4.5 Goal-directed flight

The aim of this experiment is to demonstrate the performance of the 3-D relative positioning sensor in closed-loop control and to enable autonomous goal-directed flight, specifically for the swarm searching algorithm. Two Eye-bots equipped with 3-D relative positioning sensors have been tested in a  $12 \times 3.4 \times 2.5$  m room (see figure 6.10). The first Eye-bot was used as a static reference and was pre-positioned on the floor at one end of the room near the door. The second Eye-bot was placed 150 cm in front of the first Eye-bot, on the floor and commanded to fly along a 3-D path and attach to the ceiling. The desired final location was a position which was 800 cm along the length of the room.

In this experiment, three waypoints are defined in the list before the flight, where the  $x$ ,  $y$  and  $z$  axis are aligned with the length, width and height of the room respectively (see figure 6.10). The reference Eye-bot is located at:

$$\text{Ref} = \begin{pmatrix} x = 0 \text{ cm} \\ y = 0 \text{ cm} \\ z = 0 \text{ cm} \end{pmatrix} \quad (6.17)$$

<sup>6</sup>Video: <http://jfroberts.com/phd> (eyebot\_hovering\_collision.mp4)

<sup>7</sup>Video: <http://jfroberts.com/phd> (eyebot\_ping\_pong.mp4)



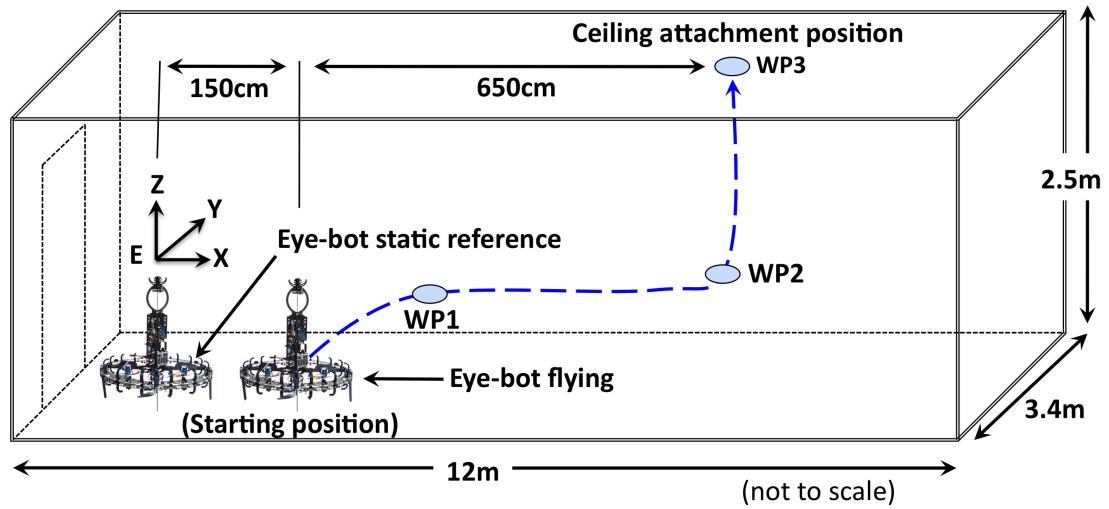


Figure 6.10: Goal-directed flight - Diagram of the experiment room showing the desired flight path of the flying Eye-bot with respect to the reference Eye-bot

For a safe take-off away from the reference Eye-bot, the first waypoint is defined in the direction of the flight path as:

$$w_p(1) = \begin{pmatrix} x_{ref} = 300 \text{ cm} \\ y_{ref} = 0 \text{ cm} \\ z_{ref} = 100 \text{ cm} \end{pmatrix} \quad (6.18)$$

A second waypoint is defined as:

$$w_p(2) = \begin{pmatrix} x_{ref} = 800 \text{ cm} \\ y_{ref} = 0 \text{ cm} \\ z_{ref} = 125 \text{ cm} \end{pmatrix} \quad (6.19)$$

where  $x$  and  $y$  is the final position, but at a height ( $z$ ) that is half way between the floor and the ceiling. For the final ceiling attachment position the last waypoint is defined as:

$$w_p(3) = \begin{pmatrix} x_{ref} = 800 \text{ cm} \\ y_{ref} = 0 \text{ cm} \\ z_{ref} = 300 \text{ cm} \end{pmatrix} \quad (6.20)$$

where  $z$  is a point slightly above the ceiling to make sure that the robot can attach to the ceiling safely.

The flight trajectory of the flying Eye-bot over 14 trials was measured in real-time using a Leica TS30 tracking system<sup>8</sup>. The tracking system has an expected

<sup>8</sup>[www.leica-geosystems.com](http://www.leica-geosystems.com) (accessed Feb. 2011)

measurement accuracy of better than  $\pm 1$  cm. Trajectory information for  $x$ ,  $y$  and  $z$  was recorded at a rate of 5 Hz. The flight path of all 14 trajectories for  $x$  versus  $z$  (*top*), and  $x$  versus  $y$  (*bottom*) is shown in figure 6.11. The flying Eye-bot takes off, flies along the desired flight path and then attaches to the ceiling at approximately 800 cm along the length of the room (see video<sup>9</sup>).

The locations of the final ceiling attachment positions are shown in figure 6.12. Analysing the ceiling attachment locations shows that the mean position was 827 cm for  $x$  and 0.41 cm for  $y$ . The relative distance between the reference Eye-bot and the flying Eye-bot was 800 cm. Therefore, the mean error for  $x$  and  $y$  was 2.78 % (23 cm) and 0.05 % (0.41 cm) respectively, the standard deviation for  $x$  and  $y$  was 2.66 % (22 cm) and 2.54 % (21 cm) respectively, and the maximum error for  $x$  and  $y$  was 6.53 % (54 cm) and 4.59 % (38 cm) respectively.

These results show that the error in the final position is larger for the length of the room ( $x$ ) than for the width of the room ( $y$ ). This is due to the flight path being along the  $x$ -axis. The inertia of the Eye-bot increases as it accelerates from waypoint 1 to waypoint 2. The flight controller must slow down this inertia as it gets closer to the final location, thus leading to a small overshoot of the final ceiling attachment position.

This experiment demonstrates the performance of the sensor in closed-loop control and validates that the sensor can be used to achieve goal-directed flight. Goal-directed flight has been achieved using only the information from the embedded relative positioning sensors. The next step is to achieve collective deployment to allow for seamless chain following.

#### 6.4.6 Collective deployment

The aim of this experiment is to demonstrate that the developed sensing and control strategy, can be used to deploy a swarm of flying robots for a searching task. Three Eye-bots equipped with 3-D relative positioning sensors have been tested in a  $12 \times 3.4 \times 2.5$  m room (see figure 6.13). The first Eye-bot was used as a static reference, with an earth fixed-frame of  $E(1)$ , and was pre-positioned on the floor at one end of the room near the door. The second Eye-bot was also used as a static reference, with an earth fixed-frame of  $E(2)$ , and was placed on the ceiling, 400 cm in front of the first Eye-bot. The third Eye-bot was placed

---

<sup>9</sup>Video: <http://jfroberts.com/phd> (eyebot\_tracking.mp4)

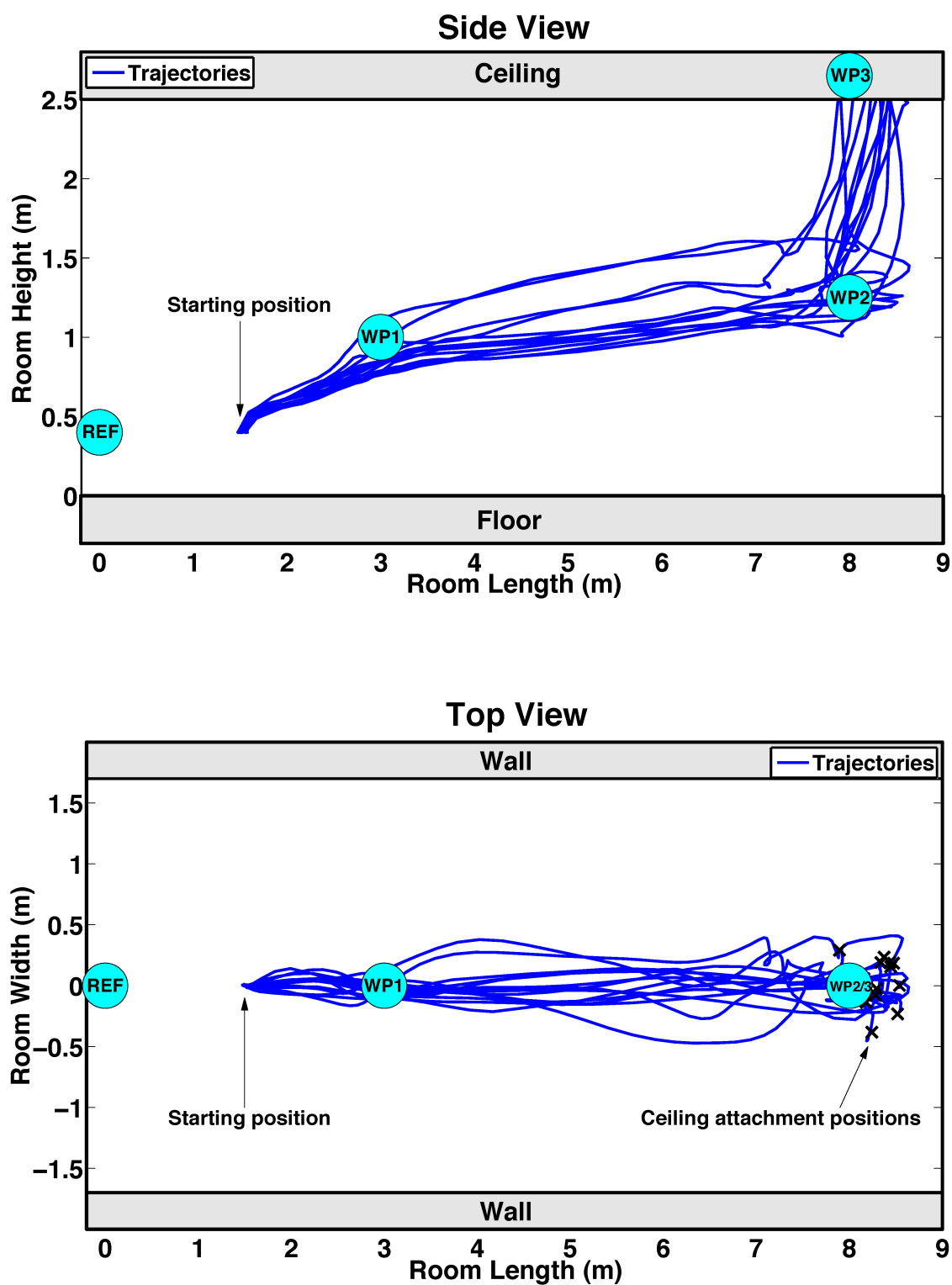


Figure 6.11: Goal-directed flight - The flight trajectory of the Eye-bot over 14 trials. *Top:* Trajectory plot of the room length ( $x$ ) versus the room height ( $z$ ). *Bottom:* Trajectory plot of the room length ( $x$ ) versus the room width ( $y$ )

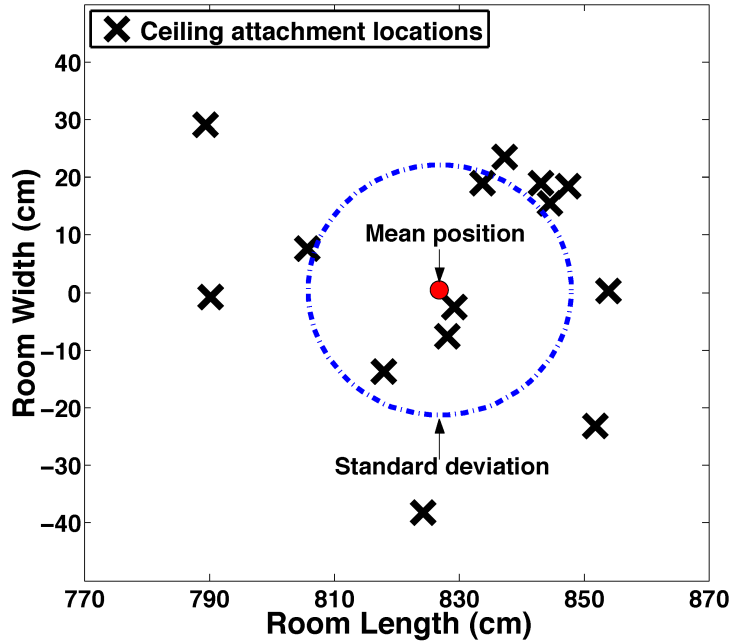


Figure 6.12: Goal-directed flight - The final ceiling attachment locations, room length ( $x$ ) versus the room width ( $y$ ), for all 14 flights. The mean position is 827 cm for  $x$  and 0.41 cm for  $y$ . The dash-dotted circle represents the standard deviation of the 14 positions

150 cm in front of the first Eye-bot, on the floor and commanded to fly along a 3-D path and attach to the ceiling. The desired final location was a position which was 900 cm along the length of the room.

In order to achieve seamless chain following, some additional control logic has been developed to handle the dynamic switching between multiple reference Eye-bots. The control logic determines when the earth fixed-frame  $E$  of the flying Eye-bot, should be changed to the next static reference Eye-bot:

$$E = \begin{cases} E(j) & \text{if } x > x(j) > 0 \text{ and, if } \theta^e(j) < \frac{\pi}{4} \\ E & \text{otherwise} \end{cases} \quad (6.21)$$

where  $j$  is the static Eye-bot reference index and  $x(j)$  is positive in the direction of the flight path. This means that when the flying Eye-bot is in front of a new reference Eye-bot, with a elevation angle that is less than  $45^\circ$ , the new reference will be used. Thus, the reference Eye-bot will always be behind the flying Eye-bot and the elevation angle is limited due to the inaccuracy of the range estimation above  $45^\circ$  (see chapter 5, section 5.3.2). Therefore, as the flying

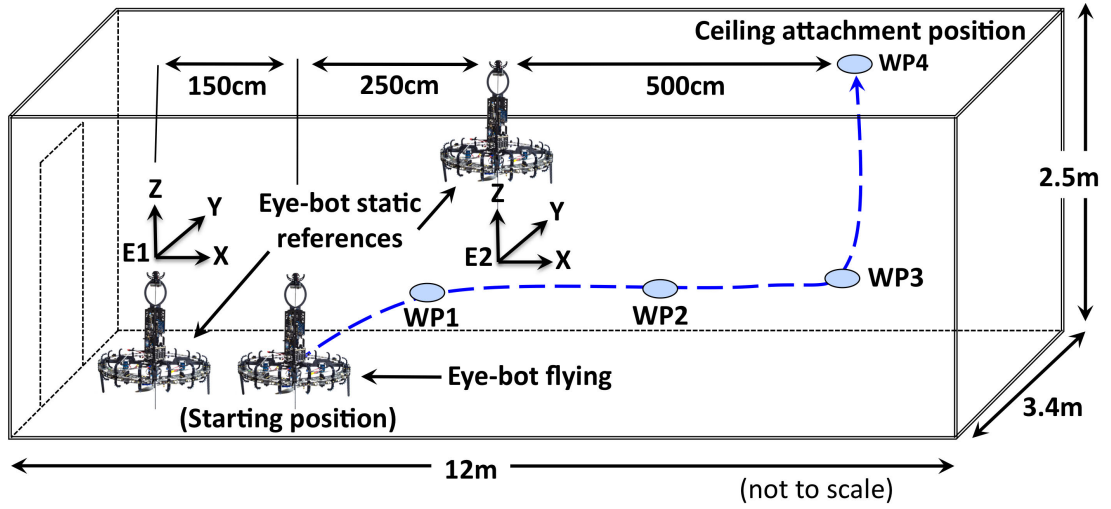


Figure 6.13: Collective deployment - Diagram of the experiment room showing the desired flight path of the flying Eye-bot with respect to the reference Eye-bots

Eye-bot travels along the chain past another Eye-bot, the control logic simply changes to the next reference Eye-bot and clears the old positioning variables.

In this experiment, four waypoints are defined in the list before the flight, where the  $x$ ,  $y$  and  $z$  axis are aligned with the length, width and height of the room respectively (see figure 6.13). The reference Eye-bots are located at:

$$\text{Ref1} = \begin{pmatrix} x = 0 \text{ cm} \\ y = 0 \text{ cm} \\ z = 0 \text{ cm} \end{pmatrix} \quad \text{Ref2} = \begin{pmatrix} x = 400 \text{ cm} \\ y = 0 \text{ cm} \\ z = 250 \text{ cm} \end{pmatrix} \quad (6.22)$$

The earth fixed-frame control logic of the flying Eye-bot automatically selects the first reference Eye-bot for waypoints 1 and 2, and second reference Eye-bot for waypoints 3 and 4. For a safe take-off away from the first reference Eye-bot, the first waypoint is defined in the direction of the flight path as:

$$w_p(1) = \begin{pmatrix} x_{ref} = 300 \text{ cm} \\ y_{ref} = 0 \text{ cm} \\ z_{ref} = 100 \text{ cm} \end{pmatrix} \quad (6.23)$$

A second waypoint is defined as:

$$w_p(2) = \begin{pmatrix} x_{ref} = 650 \text{ cm} \\ y_{ref} = 0 \text{ cm} \\ z_{ref} = 125 \text{ cm} \end{pmatrix} \quad (6.24)$$

where  $x$  and  $y$  is a position in front of the second reference Eye-bot, with an elevation that is less than  $45^\circ$ , and the height ( $z$ ) is half way between the floor and the ceiling. Thus, before this position is reached the reference Eye-bot will change, allowing for a smooth change over between references.

A third waypoint, using the second reference Eye-bot is defined as:

$$w_p(3) = \begin{pmatrix} x_{ref} = 500 \text{ cm} \\ y_{ref} = 0 \text{ cm} \\ z_{ref} = -125 \text{ cm} \end{pmatrix} \quad (6.25)$$

which is the final  $x$  and  $y$  position but at a height ( $z$ ) that is half way between the floor and the ceiling. Note that the  $x$ ,  $y$  and  $z$  are relative to the second reference Eye-bot. For the final ceiling attachment position the last waypoint is defined as:

$$w_p(4) = \begin{pmatrix} x_{ref} = 500 \text{ cm} \\ y_{ref} = 0 \text{ cm} \\ z_{ref} = 100 \text{ cm} \end{pmatrix} \quad (6.26)$$

where  $z$  is a point slightly above the ceiling to make sure that the robot can attach to the ceiling safely.

The flight path of all 15 trajectories for  $x$  versus  $z$  (*top*), and  $x$  versus  $y$  (*bottom*) is shown in figure 6.14. The flying Eye-bot takes off, flies along the desired flight path, swaps from the first reference Eye-bot to the second, and then attaches to the ceiling at approximately 900 cm along the length of the room. The locations of the final ceiling attachment positions are shown in figure 6.15. Analysing the ceiling attachment locations shows that the mean position was 907 cm for  $x$  and  $-1$  cm for  $y$ . The relative distance between the second reference Eye-bot and the flying Eye-bot was 500 cm. Therefore, the mean error for  $x$  and  $y$  was 1.4% (7 cm) and 0.2% (1 cm) respectively, the standard deviation for  $x$  and  $y$  was 5.3% (26.5 cm) and 2.92% (14.6 cm) respectively, and the maximum error for  $x$  and  $y$  was 9.48% (47.4 cm) and 4.69% (23.47 cm) respectively.

Similarly to the previous experiment, the results show that the error in the final position is larger for the length of the room ( $x$ ) than for the width of the room ( $y$ ). The mean error is smaller than in the previous experiment, which is due to the second reference Eye-bot being closer to the final ceiling attachment position. However, the maximum error is larger than in the previous experiment, which is not a problem as the error is still low. This is likely due to the abrupt change over of the reference Eye-bot. This experiment demonstrates that

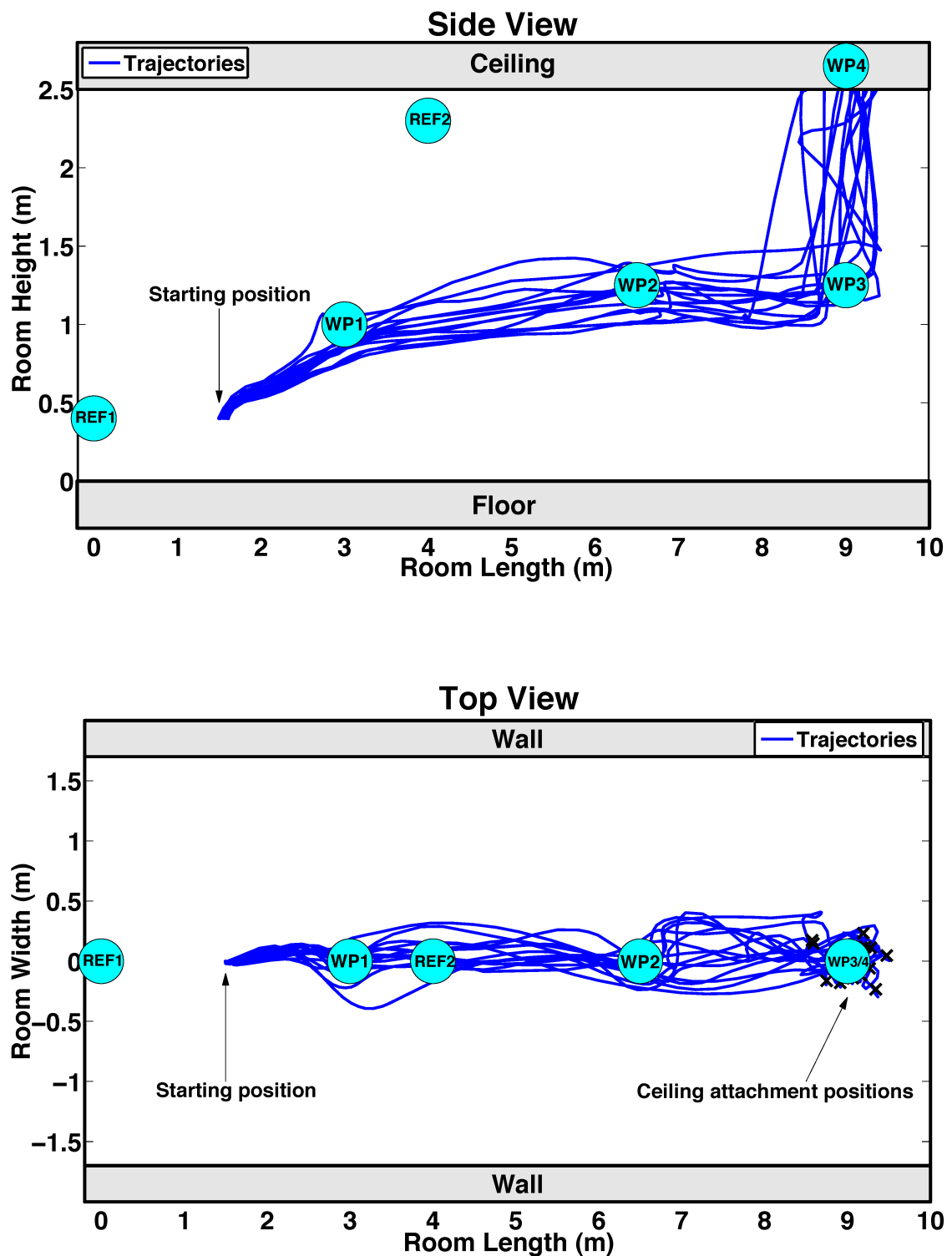


Figure 6.14: Collective deployment - The flight trajectory of the Eye-bot over 15 trials. *Top*: Trajectory plot of the room length ( $x$ ) versus the room height ( $z$ ). *Bottom*: Trajectory plot of the room length ( $x$ ) versus the room width ( $y$ )

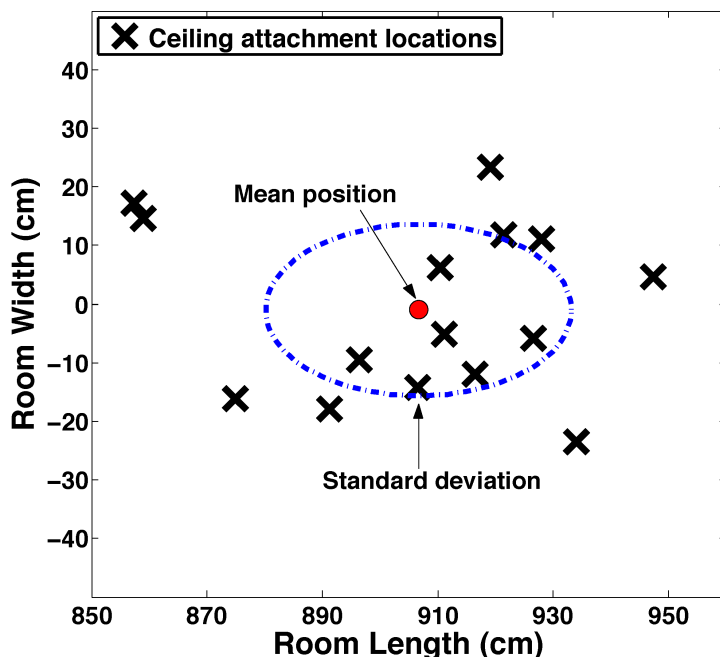


Figure 6.15: Collective deployment - The final ceiling attachment locations, room length ( $x$ ) versus the room width ( $y$ ), for all 15 flights. The mean position is 907 cm for  $x$  and  $-1$  cm for  $y$ . The dash-dotted circle represents the standard deviation of the 15 positions

proposed sensing and control approach can be used to build a chain of flying robots, for the realisation of multi-robot control algorithms for real-world applications. These examples show a simple flight trajectory, however more complex trajectories can be achieved by simply adding additional waypoints along the desired flight path. The only limitation is that the robots need to be within line-of-sight of one another in order for the sensors to work. For trajectories that travel beyond corners, a robot must be stationed directly on the corner to creating a link for the new flight direction. For two robots it is possible to take turns, one flies while the other is a reference, this is the minimum requirement for spatial-coordination. If there are several robots then swarming can be implemented, allowing for efficient indoor spatial-coordination (Stirling et al., 2010).

A Swarmanoid scenario video has been documented to demonstrate the chain building with more autonomous flying robots (see video<sup>10</sup>). This video shows the implementation of a swarm of flying robots for an indoor searching

<sup>10</sup>Video: <http://jfroberts.com/phd> (eyebot\_scenario.mp4)



scenario, where the robots are commanded to find a book on a shelf at the end of a long room. The autonomous flight in the video is 100% real, however the visual recognition of the book shelf has been done at a later time. The pan-tilt camera of the Eye-bot is used to visually identify the bookshelf with a computer vision algorithm developed by Manuele Brambilla from IRIDIA<sup>11</sup>.

## 6.5 Conclusion

The limited amount of payload available on commercial hovering platforms and the lack of embedded 3-D relative positioning sensing, has prevented collective swarms of indoor flying robots from becoming a reality. However, this chapter demonstrates that this has been overcome, using the methodologies and technologies presented in this thesis. The dimensioning strategy, from chapter 2, has been useful in developing the Eye-bot hovering platform. The Eye-bot has a payload capability that is 3 times higher than any other commercial platform of the same size, with a flight endurance performance that is similar to any other commercial platform suitable for indoor operation (below 80 cm). This platform is small (50 cm), has a high-payload capability (600 g) and high flight endurance (10-17 min). It has proven to be highly suitable for carrying the required sensing and processing, to enable the collective operation of indoor flying robots. A practical sensing and control methodology has been developed that can enable spatial-coordination between multiple robots in three dimensions, which provides hovering platform stabilisation, 3-D collision avoidance and 3-D way-point navigation, all from the same sensor. Goal-directed flight and collective deployment has been achieved using only the information from the 3-D relative positioning sensing. The developed coaxial counter-rotating propulsion system (chapter 2) together with the 3-D relative positioning sensor (chapter 5) and autonomous flight control strategy, is capable of enabling the collective operation of highly dynamic indoor flying robots. 3-D relative positioning is a practical alternative to external tracking sensors<sup>12</sup>, allowing for the realisation of multi-robot control algorithms in the real-world.

---

<sup>11</sup><http://iridia.ulb.ac.be> (accessed Feb 2011)

<sup>12</sup><http://www.vicon.com> (accessed Feb. 2011)



---

# 7

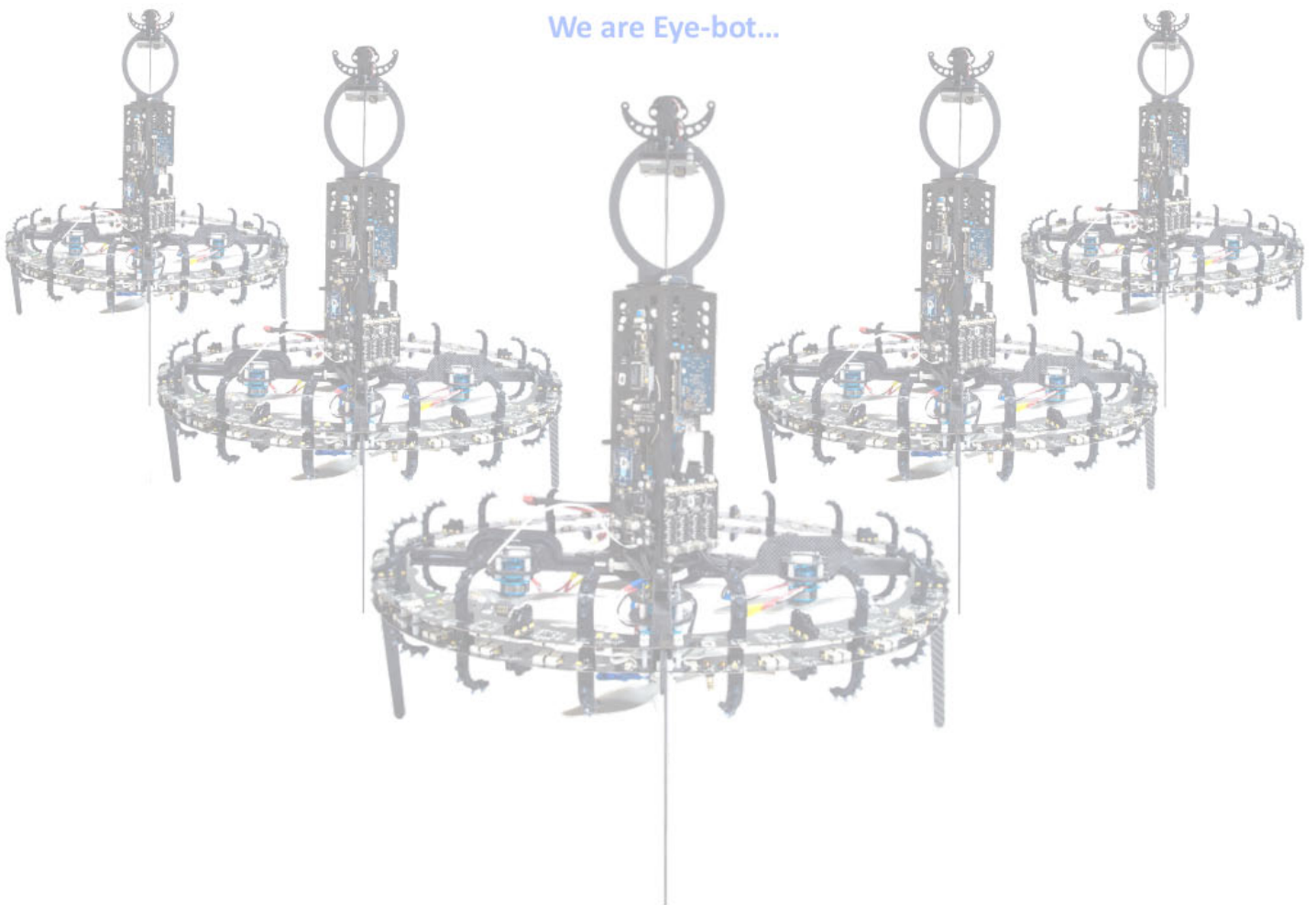
---

## Conclusion

---

**T**HIS closing chapter highlights the main accomplishments that have been presented in this thesis. The limitations of the proposed methodologies and the possibility for future work in this area, is further discussed. The chapter ends with an outlook on the applications that the technology within this thesis enables, beyond swarms of flying robots.

We are Eye-bot...



## 7.1 Motivation and challenges

Collective flying robots show great potential in many diverse indoor applications. Their added robustness, parallel operation and redundancy has clear advantages over a single flying robot. However, flying within cluttered and unprepared indoor environments, even for a single flying robot, is extremely challenging.

The main reason why collective flying robots have not yet been successful within indoor environments, is due to a combination of several challenges related to the size constraints placed on an indoor hovering platform, which directly limits the available energy, embedded sensing and processing capabilities of a flying robot. The energetic cost of flying, places limits on the flight endurance and practicality of a swarm of flying robots. The current spatial-coordination approaches implement methods that are either too computationally expensive, or impractical for real-world operation, within unknown and unprepared indoor environments.

The only practical demonstration of collective indoor flying robots, without using external aids, is the work by Melhuish and Welsby (2002) with a swarm of Lighter Than Air Vehicles (LTAV). In their work, they achieved a simple gradient ascent behaviour towards an emitting beacon using four LTAV. However, the limited payload (<43 g) of the LTAV prevents carrying useful sensing and processing hardware. Additionally, the low-force (4 g) propulsion system of a LTAV, reduces its speed and manoeuvrability, which prevents such a system from being useful in real-world scenarios.

The goal of this thesis was to develop a practical methodology for enabling energy efficient, autonomous indoor flying robots capable of inter-robot spatial-coordination for unprepared indoor environments, without using external aids. In order to push through this barrier and allow for real-world deployment of collective indoor flying robots, several practical methodologies have been proposed and demonstrated.

## 7.2 Accomplishments

- The amount of payload available for on-board sensing and processing within the indoor size constraints is highly limited. A generalised design strategy has been proposed to dimension a hovering platform for a specific flight endurance, payload capability and robustness criteria. The developed method can be used as a practical design tool for anyone working with hovering platforms. The dimensioning strategy has created an endurance optimised hovering platform that has a maximum flight endurance that is 1.5 times longer, when compared to any other commercial platform suitable for indoor operation ( $\leq 80$  cm). The dimensioning strategy has also created a payload optimised hovering platform, with a diameter that is only half the size of a typical doorway opening, that has a payload capability that is 5 times higher than any other platform the same size. Additionally, its maximum flight endurance is 1.3 times longer, when compared to any other commercial platform suitable for indoor operation ( $\leq 80$  cm). The developed coaxial counter-rotating propulsion system, together with the dimensioning strategy, has produced an efficient hovering platform design, which is highly suitable for carrying the necessary sensing and processing required to enable the collective operation of indoor flying robots.
- None of the existing commercially available platforms offer a solution providing autonomous indoor flight with an obstacle avoidance capability. A simple sensing and control strategy is proposed for enabling anti-drift control and obstacle avoidance behaviours on an indoor highly dynamic, hovering platform. The strategy allows the hovering platform to achieve automatic take-off, constant altitude control, obstacle avoidance, anti-drift control and automatic landing. The approach is computationally simple, unlike laser scanner approaches, and will work in the dark or poor lighting conditions, unlike vision or optic-flow approaches. The flying robot that is presented in chapter 3 was one of the first indoor hovering platforms, together with Bouabdallah and Siegwart (2007), that could achieve such a capability without using any external aids.

- The energetic cost of flying places strong limitations on the practicality of a swarm of flying robots. A generalised energy model has been developed, allowing for the accurate estimation of the flight endurance and perching time of hovering platforms. The energy model can be used to optimise the battery selection process of a hovering platform, to obtain the highest possible endurance. The experimental results show that it is possible to predict mission endurance, including several cycles of flying and perching, with an average overall mission endurance error of 0.97%. This is the only model known that is able to predict any combination of flying endurance and perching times.
- Additionally, a method of attaching to the ceiling has been presented that can be used to improve the practicality of a swarm of indoor flying robots. This unique method allows the hovering robot to conserve energy and have a stable birds-eye-view while performing static sensing tasks. The developed methodology is able to achieve autonomous ceiling attachment and detachment to ferrous ceilings. By applying energy management techniques, through use of energy modelling and behaviours that reduce the flight time, the energetic cost of flying can be mitigated and the mission endurance can be extended over several hours, which is especially useful for collective operation. The flying robot that is presented in chapter 4 is the first indoor hovering platform that could achieve such a capability.
- There is a lack of on-board sensing technologies available that can enable spatial-coordination and collective operation, within real-world environments. A new infrared ranging technique has been developed that is extremely versatile, as it can be used as a standalone point-to-point distance sensor, a 2-D range and bearing sensor, or extended to a 3-D range, bearing and elevation sensor that can also provide proximity sensing. The ranging technique allows for an improved sensing performance, including long range (12 m), high speed (1 kHz / # robots) and high resolution (better than 1.1 cm up to 6 m). A practical on-board sensing method has been developed that can provide spatial-coordination between multiple robots in three dimensions. The developed approach allows for easily adaptation, to suit other robots and applications, depending on a specific sensing speed and coverage requirement. The developed sensor is the worlds first

embedded 3-D relative positioning sensor that has the ability to enable inter-robot spatial-coordination in three dimensions, which is necessary for achieving goal-directed flight on highly dynamic flying robots. This approach does not require computationally expensive algorithms, external sensors or modification of the environment, and is largely independent on varying environmental illumination. The developed sensor can potentially provide collective operation between 100 multiple flying robots (running at a 10 Hz operational speed). The sensor outperforms the best existing 2-D infrared range and bearing sensors (Pugh et al., 2009; Kemppainen et al., 2006). The range error is not as good as a time of flight based ultrasonic 2-D relative positioning sensor (Rivard et al., 2008), however it operates at a speed that is 75 times faster (see section 5.3.6). The sensor is currently the only on-board 3-D relative positioning sensor that exists and is the only relative positioning sensor also capable of providing 3-D proximity sensing.

- The limited amount of payload available on commercial hovering platforms and the lack of embedded 3-D relative positioning sensing, has prevented collective swarms of indoor flying robots from becoming a reality. A practical autonomous flight control methodology has been demonstrated that can provide hovering platform stabilisation, 3-D obstacle avoidance and 3-D waypoint navigation, all using the 3-D relative positioning sensor. Goal-directed flight and collective deployment has been achieved using only the information from the 3-D relative positioning sensing. The developed coaxial counter-rotating propulsion system (chapter 2) together with the 3-D relative positioning sensor (chapter 5) and autonomous flight control strategy, has enabled for the first time the collective operation of highly dynamic indoor flying robots.

### 7.3 Limitations and future work

The results from this research can be applied directly to real-world applications, as the proposed approaches are highly flexible and do not require external aids. However, there are some limitations to the proposed approaches, which would

benefit from additional research.

The first limitation is that the ceiling attachment mechanism, developed in chapter 4, can only be used to attach to ferrous ceilings. The development of a new attachment technology is outside the scope of this thesis, however this is a strong limitation in regard to general usability. Some possible attachment technologies have been briefly introduced in chapter 4, section 1.2.2. However, further study into alternative attachment technologies needs to be investigated before this part of the proposed methodology can be used in the real-world.

The second limitation is that the position accuracy of the proposed 3-D relative positioning sensor can be skewed by environmental reflections. Depending on the reflectivity of the surrounding features, this skew can be up to tens-of-centimetres in the presence of highly reflective surfaces, such as glass or marbled tiles. Generally, the skew is not a major problem for the autonomous control as it simply shifts the waypoint location, but it does make the higher level control more difficult if accurate flying to a specific location is desired. The skew can be corrected with a simple manual gain factor adjustment. However, this reflection limitation has been exploited by using the reflected signals to gather proximity sensing information about the surrounding environment. Further research is required to determine if the proximity sensing from the reflection can be used to automatically de-skew the the positioning error, thus minimising the problem.

The third limitation is the current size and weight of the modular designed 3-D relative positioning sensor. The sensor has been designed to give the best possible 3-D position and high speed performance, however this has come with a larger size and weight consequence. The sensors weight is comparable to that of a laser range finder (UTM-30LX<sup>1</sup>) as used by Achtelik et al. (2009). This size and weight has not been a problem for the proposed high-payload capable hovering platform, however it may prove difficult to place on-board smaller commercially available hovering platforms. If we recall from chapter 5, section 5.2.5, the physical constraints are proportional to the sensors speed, where a higher speed equates to a larger sensor with more cascaded filters. This means that it is possible to drastically reduce the size of the sensor by multiplexing, at the cost of a lower speed. However, if the centre frequency of the cascaded filter can be increased the speed consequence can be mitigated. Further research is required

---

<sup>1</sup><http://www.hokuyo-aut.jp> (accessed Feb. 2011)



to find suitable bandpass filters that can work at higher frequencies.

The validation results have shown that 3-D relative positioning sensing alone can be used to achieve all the requirements for goal-directed flight. However, it would be beneficial to use multi-modal sensing techniques to further increase reliability. For example, platform drift compensation is one of the critical requirements for autonomous operation. Demonstrated by the AR-Drone<sup>2</sup> commercial hovering platform, optic-flow is useful for compensating platform drift, however it cannot be used for collective operation as it does not hold any inter-robot information. By utilising an optic-flow sensor, like the ones incorporated on the top and bottom of the Eye-bot, the platform drift can be taken care of. As both of the sensors provide platform drift compensation, the reliability of the anti-drift control could be improved. Additionally, as the platform drift problem is no longer solely handled by the relative positioning sensor, the speed of the relative positioning sensing could be reduced, meaning that more robots could be added to the swarm, which could further improve the scalability of the system.

Currently a simple turn-taking algorithm is utilised to coordinate the 3-D relative positioning sensors. For dynamic scalability, communication algorithms such as Carrier Sense Multiple Access (CSMA) can be easily implemented (Pugh et al., 2009). As the development of scalable communication algorithms is a solved problem, the focus in this thesis was on developing higher sensor operational speeds. Additionally, as the speed of the sensor is very fast (1 kHz), the developed simple turn taking algorithm can provide enough speed (10 Hz per robot) for a swarm of up to 100 flying robots.

## 7.4 Future applications

This thesis has presented several practical methodologies designed to enable energy-efficient, autonomous indoor flying robots capable of inter-robot spatial-coordination. The most fruitful development and contribution of this work is the 3-D relative positioning sensor, which has proven to be suitable for achieving goal-directed flight and collective deployment, on highly-dynamic flying robots. The proposed methodology is a practical solution, allowing for the realisation of multi-robot control algorithms for flying robots. It is a useful alternative to

---

<sup>2</sup><http://ardrone.parrot.com> (accessed Feb. 2011)

external tracking sensors<sup>3</sup>, which are commonly used in the field due to the non-existence of embedded 3-D positioning sensors. This thesis has only touched the surface of the possible capabilities of the proposed technology. In the future it would be possible to increase the number of robots and test other more complex control algorithms to further push the boundaries of autonomous indoor flying robots for real-world applications.

This technology can enable swarming algorithms to be ported from simulation to real flying robots for practical validation, in both indoor and outdoor scenarios. Such algorithms range from simple inter-robot collision avoidance behaviours (Hoffmann and Tomlin, 2008) to more complex behaviours such as flocking (Pilz et al., 2009) or mobile sensor networks (Ogren et al., 2004).

But what future applications can this sensing technology be applied to? The sensing technology presented in this thesis provides a simple six value output in the form of range, bearing, elevation and  $x$ ,  $y$  and  $z$  proximity information, thus it can be applied to many applications using simple control strategies. There are several immediate applications within the field of flying robotics that could be implemented, including search and rescue, the gaming industry and aerial photography.

**Search and Rescue:** As expressed in the introduction the main application envisioned for this research is to use swarms of flying robots to aid in disaster situations. The technology presented in this thesis has shown direct implementation in the presented swarm search video. The interest in using such a system for real disaster situations, like the recent disasters in Japan (March 11, 2011), is high due to the potential benefits. Benefits include high searching efficiency by the rapid deployment of large numbers of flying robots and being able to do this from a safe distance. It is envisioned that in the next couple of decades, robotics technology will rise to a level that is robust enough for real search and rescue deployment. This thesis has shown a large step towards achieving such a vision.

**Gaming:** Reducing the size of the 3-D sensor and combining it with the flying AR.Drone gaming system by Parrot<sup>4</sup>, could open up new real-world gaming

---

<sup>3</sup><http://www.vicon.com> (accessed Feb. 2011)

<sup>4</sup><http://ardrone.parrot.com> (accessed Feb. 2011)

opportunities. For example, it would be possible to command a team of autonomous flying robots from an iPhone/iPad. Two teams could battle against each other, remotely deploying their flying drones to fight on their behalf towards a glorious victory. This would enable a gaming environment that is more like the "idealised" computer simulated gaming, which would further integrate the virtual and real-world, thus increasing the excitement and thrill factor.

**Photography:** The 3-D sensor could be made into a small mobile sensing ball, which could then be used as a reference focal point for a flying platform equipped with a SLR camera. Pictures and video could then be taken from any angle or distance up to 12 m from the focal point. The focal point could be automatically tracked simply by moving the sensing ball, thus creating highly mobile and automatic recording device. The focal point could be changed by passing the sensing ball to another person. Such a system would be very intuitive and easy to use. The technology could also be implemented in sports to track moving people from the air.

The developed sensing technology can also be applied to some interesting off-topic applications that are not directly related to flying robotics or collective operation. Such applications include golf, child care and helping the disabled.

**Golf:** One of the biggest hassles with the leisurely sport of golfing, is to have to carry around a bag of heavy golf sticks over hills and through gullies. The sensing technology proposed in this thesis could be used to automate golf caddies so that the golf sticks are always a few meters behind. By wearing a hat equipped with a small transmitting beacon, which could be enabled or disabled by pushing a button attached to the hat. The caddie would be able to follow autonomously while the players focus can be on sinking the next hole.

**Child care:** Caring for small kids can be very distracting, especially when they are beginning to walk. The sensing technology proposed in this thesis could be used to indicate when a small toddler is no longer in line-of-sight. By equipping the toddler with a small transmitting beacon and an alarm, the toddler would be able to roam free until they are too far away or in an area which is "out of bounds". The alarm would then activate to inform the caretaker of a potential risk, allowing for piece of mind and a more relaxed situation.

**Helping the disabled:** On a more serious note, the sensing technology could be used to help the visually impaired. A special pair of gloves equipped with the sensors could provide a new set of eyes. As the sensor outputs six simple values (range, bearing, elevation and  $x$ ,  $y$  and  $z$  proximity) the human machine interfacing would be within practical possibility. The sensor could provide navigational guidance and obstacle detection to help them find their way within unknown environments. Homes, shopping malls and toilet facilities equipped with some strategically located sensors could provide directional guidance information and allow the visually impaired to live a more independent lifestyle.

## 7.5 Outlook

This thesis demonstrates for the first time, the operation of highly dynamic indoor flying robots that can help each other to achieve autonomous goal-directed indoor flight and collective deployment. The dimensioning strategy for designing a hovering platform for a specific payload, flight endurance and robustness criteria, has provided a winning combination of motors, propellers and structural design, which outperforms any other hovering platform in its size class. The 3-D relative positioning methodology that has been presented, is a breakthrough in on-board sensing technologies for indoor flying robotics, which can be extended to a variety interesting future applications. The combination of high-efficiency contra-rotating propulsion and 3-D relative positioning with simple control strategies, is sufficient to enable fully autonomous and collective deployment of indoor flying robots. The capabilities that have been demonstrated include automatic take-off and landing, 3-D obstacle avoidance, 3-D goal directed indoor flight, automatic ceiling attachment and detachment and collective deployment of several flying robots. These capabilities are all direct outcomes from the developed on-board 3-D sensing technology. 3-D relative positioning is a practical alternative to external tracking sensors<sup>5</sup>, allowing for the realisation of multi-robot control algorithms in the real-world.

---

<sup>5</sup><http://www.vicon.com> (accessed Feb. 2011)

---

A

---

Appendix

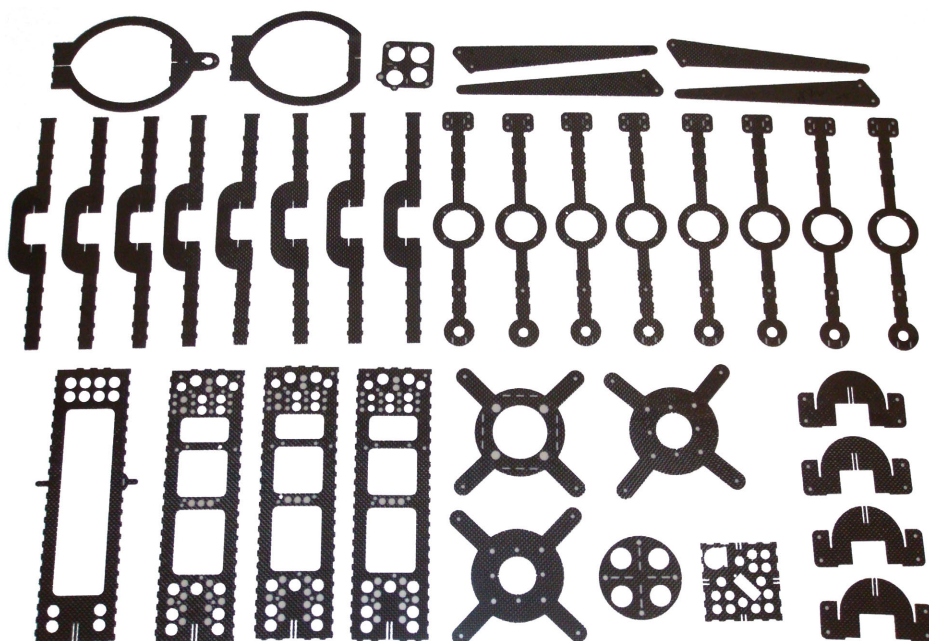


Figure A.1: Structural pieces cut from quasi-isotropic carbon fibre plate

## A.1 Eye-bot structure

The Eye-bot hovering platform has been designed using the dimensioning strategy from chapter 2. From the lessons learnt in chapter 2, section 2.1 about suitable materials for the platform structure, carbon fibre when compared to fibre-glass has a better strength-to-weight ratio. However, the uni-directional fibres of the carbon fibre square tubing, made it difficult to work with. To overcome this problem a new carbon fibre material, called quasi-isotropic plate<sup>1</sup>, has been used. The quasi-isotropic plate has carbon fibres which are aligned in the 0, 45 and 90 degree directions, thus it can be drilled and cut without risk of splitting. Quasi-isotropic carbon fibre plate is twice as strong in the torsion deflection than normal uni-directional carbon fibre. Therefore, sheets of quasi-isotropic carbon fibre plate have been used to build the platform structure.

The rapid prototyping technique, presented in chapter 2, section 2.3.4, has been used to fabricate the pieces of the structure. The pieces, shown in figure A.1, have been designed and cut using printed circuit board software and machines, respectively. The pieces fit together like a jigsaw-puzzle and are glued to create the 3-D parts of the structure.

<sup>1</sup><http://www.dragonplate.com/sections/technology.asp> (accessed Feb. 2011)

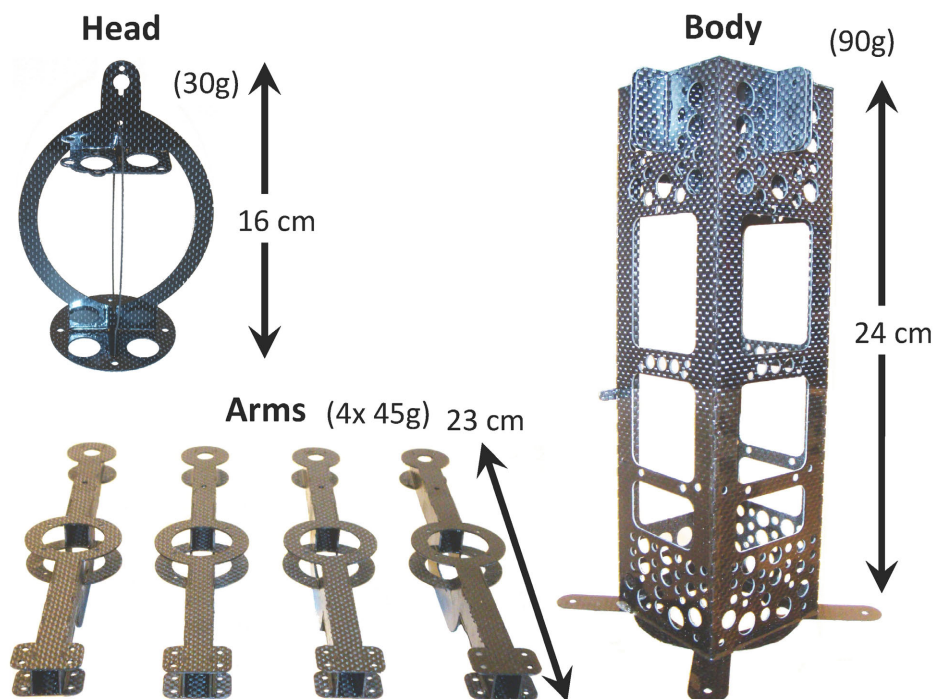


Figure A.2: Head (*left-top*), four motor arms (*left-bottom*) and main body (*right*) built from four, four and ten pieces of carbon fibre plate, respectively

The structure of the Eye-bot consist of a head, four arms, a body and four legs. The head, shown in figure A.2 *left-top*, is designed to hold the ceiling attachment mechanism and house the top sensors. The head, weighing 30 g, is constructed from four pieces of carbon plate. The heads egg shaped structure is designed to fit a distance scanner in its centre. The body, shown in figure A.2 *right*, is designed to house the avionics circuit boards and the battery. The body, weighing 90 g, is constructed from ten pieces of carbon plate. The circuit boards have been designed to fit exactly the holes on the body. The elongated rectangular shape allows a large battery to be installed inside the body. Additionally, this lowered distance from the ceiling, reduces infrared reflections from the relative positioning sensor and allows the sensor to operate through doorways. Similarly, this is also beneficial for the camera, which will attach to the bottom, allowing for more field-of-view.

The four arms, shown in figure A.2 *left-bottom*, are designed to hold the coaxial motors. Each arm, weighing 45 g, is constructed from four pieces of carbon plate. The arms extend out past the propellers, so that the legs can be attached. This gives the maximum base distance for the legs to provide the best stability



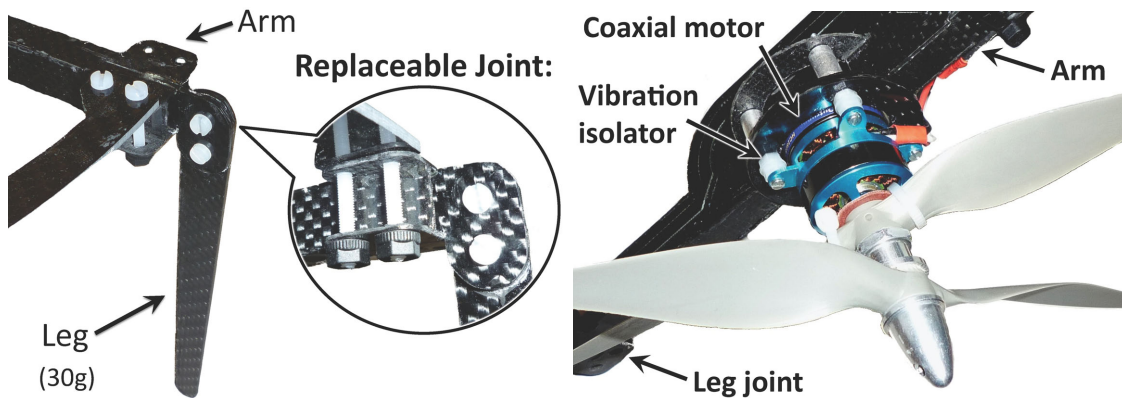


Figure A.3: *Left*: Carbon fibre leg and close-up of replaceable crash joint. *Right*: Arm fitted with coaxial motor and counter-rotating propellers

support. The legs, shown in figure A.3 *left*, are made from a single piece of carbon plate. They are attached to the end of the each arm using nylon nuts and bolts. The nylon bolts are designed to break in the case of a crash or heavy landing. These replaceable crash joints prevent the carbon pieces from breaking, help absorb the impact and allow for quick and easy repairs.

The Himax CR2805 coaxial motors, are fitted with APC 7x5 *inch* counter rotating thin-electric rigid propellers, shown in figure A.3 *right*. In order to reduce airflow disruption, the coaxial motors are attached to the bottom side of the arms. Plastic isolators are placed between the motor and the arm to reduce the motor vibrations from traveling to the inertial sensors.

The ceiling attachment mechanism, show in figure A.4, is located at the top of the Eye-bot head structure. The design is an improvement of the mechanical lever presented in chapter 4, section 4.2.3. It consists of a 10 g rare earth Neodymium magnet at the top, which is glued to a 3-D printed plastic cam. The magnet has a 7.7 kg holding force, which is strongest at the top (north pole). In order to reduce the force required to detach from a ferrous ceiling, the magnet can be removed by a levering mechanism. The cam is designed to minimise the levering force and allow the magnet to be remove easily by simply rotating the cam. This levering mechanism could be implemented with future alternative attachment techniques, such as dry-adhesives (see chapter 1, section 1.2.2). The 3-D printed plastic piece shaped like a "U", extends out to protect the cam against bumps during attachment. The top sensor board, presented later, screws directly onto the top head plate using nylon bolts.



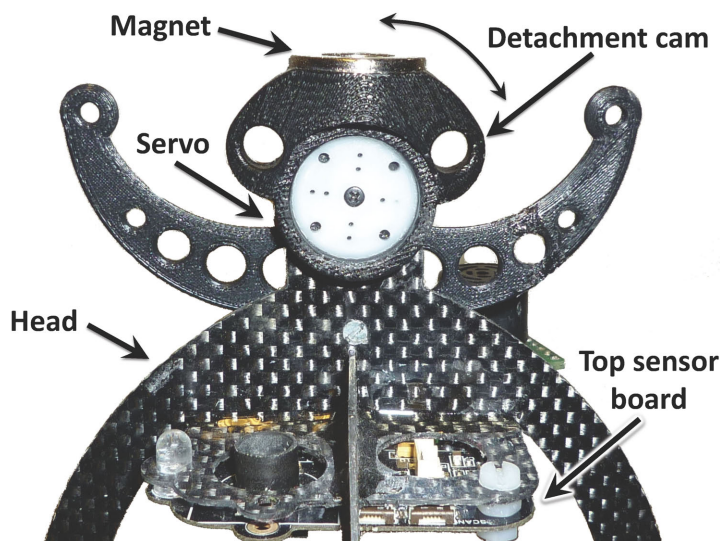


Figure A.4: Ceiling attachment and detachment mechanism, designed to attach to ferrous ceilings

## A.2 Eye-bot electronics

The Eye-bot platform, shown in figure A.5, consists of several custom designed distributed control boards and sensors, which can be split into four different categories, including the flight critical avionics, additional optional sensors, Swarmanoid specific electronics and relative positioning sensor support. The communication architecture between the distributed control boards is shown in figure A.6.

### A.2.1 Flight critical avionics

The flight critical avionics consist of anything necessary for the Eye-bot to fly, which includes the *Control*, *Flight* and two *Motor Controller* boards.

The main *Control* board, shown in figure A.7, has two embedded micro-controllers named *Master-Coms* and *Autonomous*. The *Master-Coms* 16 MIPS micro-controller is in charge of the power management, text-to-speech synthesiser, Xbee wireless interface and is the master of a communications bus linking all of the boards together. The Xbee allows for wireless remote operation from an interface on a computer. The *Autonomous* 40 MIPS micro-controller is designed to run the autonomous flight control algorithm (see section 6.3) and sends thrust, pitch, roll and yaw commands to the *Flight* board. It also connects to a radio

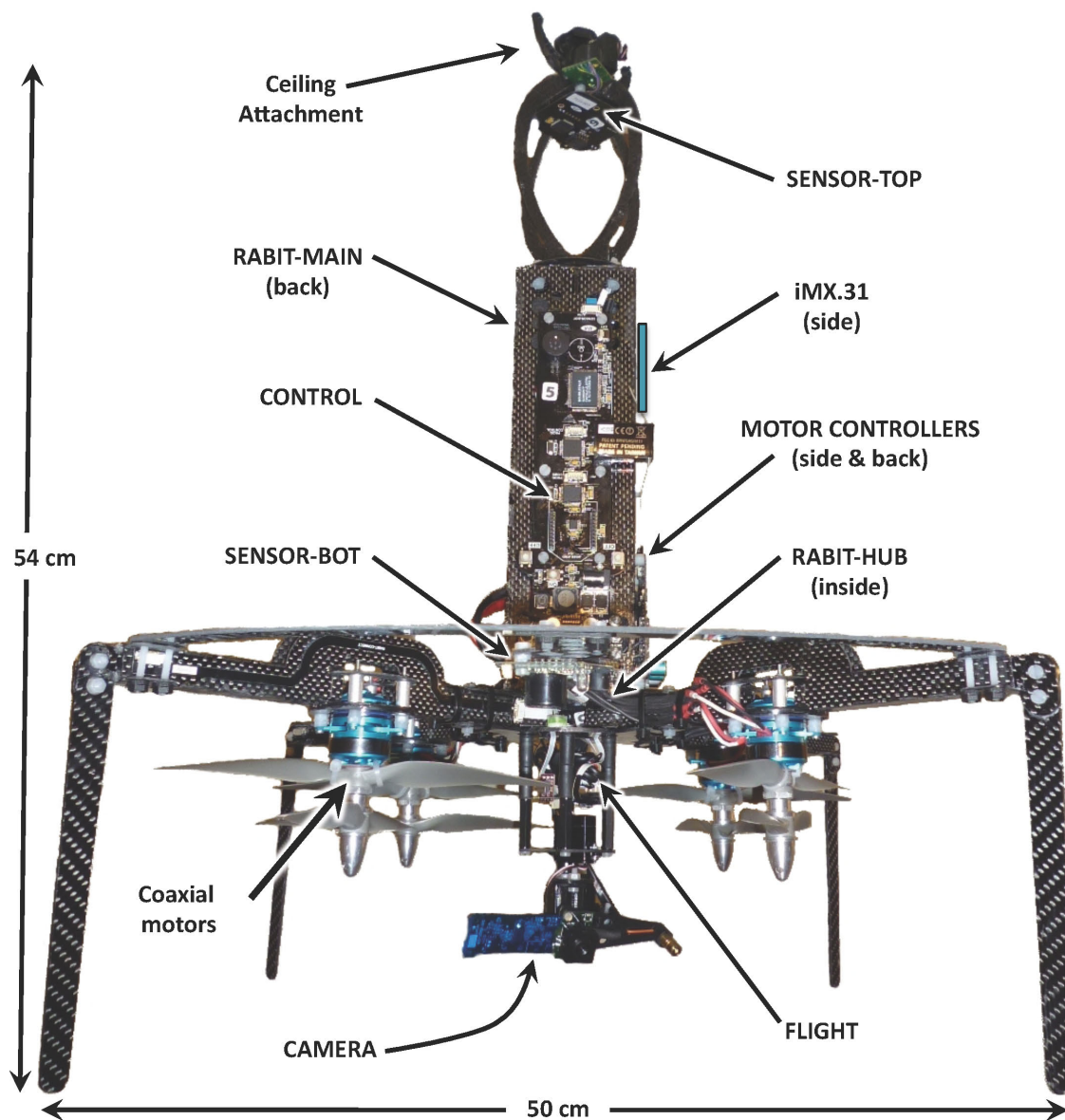


Figure A.5: Eye-bot fitted with coaxial motors, control boards and sensors

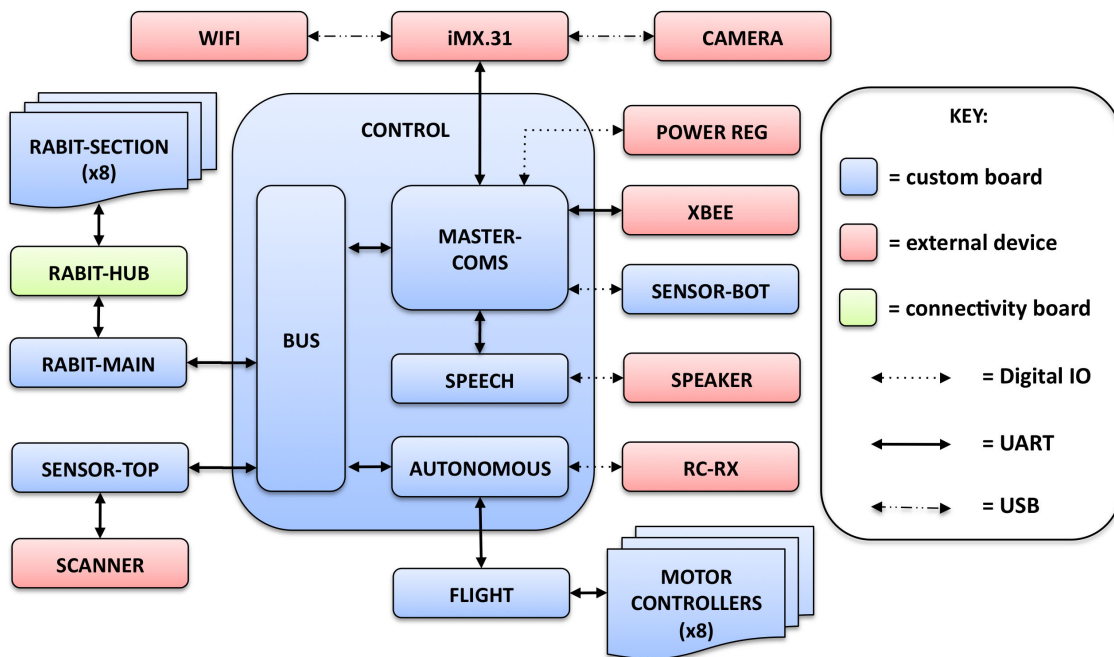


Figure A.6: Communications architecture

control receiver (*RC-RX*) to allow for a safety pilot and manual operation.

The *Flight* board, shown in figure A.8 left, has a 16 MIPS micro-controller that is in charge of stability control and the motor mixing. It incorporates a 3-axis accelerometer and 3-axis gyroscopes, for inertial estimation of the pitch, roll and yaw. The *Flight* board sends speed commands to the *Motor Controller* boards for platform stabilisation.

The *Motor Controller* boards, shown in figure A.8 right, are in charge of brushless motor speed control. Each board incorporates four motor channels, which includes a 8 MIPS micro-controller for speed control and a three phase high-current (12 A continuous) MOSFET driver.

### A.2.2 Additional optional sensors

The optional sensors include two sensor boards (*Sensor-Top*, *Sensor-Bot*) and a distance scanner (*Scanner*). These sensors are not required for autonomous flight, due to the high-performance of the 3-D relative positioning sensor, and its proximity sensing. However, they have been added for future experiments. Note that they are not used in the validation experiments presented in section 6.4.

The *Sensor-Top* and *Sensor-Bot* boards, shown in figure A.9, when fitted to

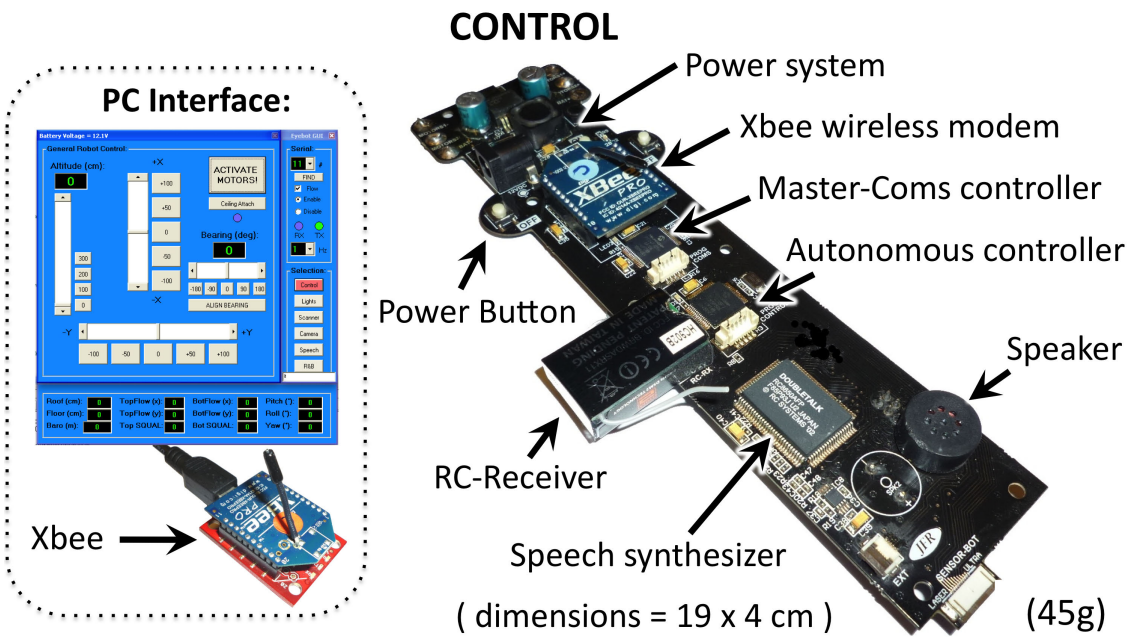


Figure A.7: Wireless computer interface (left) and main control board (right)

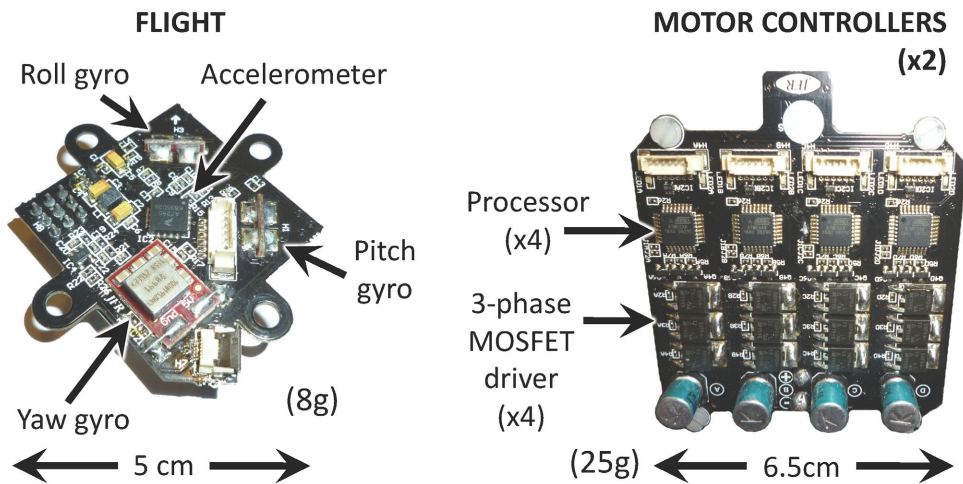


Figure A.8: Flight computer (left) and four channel, high-speed brushless motor controller (right)

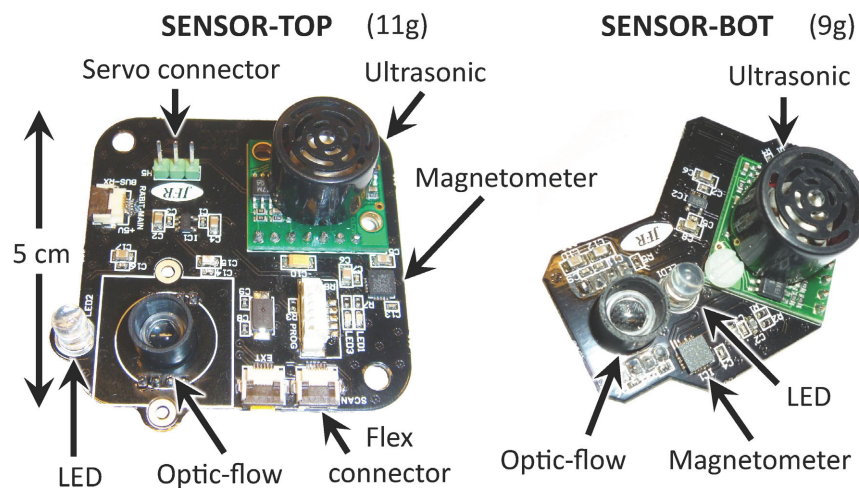


Figure A.9: Top sensor board (*left*) and bottom sensor board (*right*)

the robot are designed to point upwards and downwards, respectively. The top board fits into the head of the structure and the bottom board attaches to the underside of the 3-D relative positioning ring. Both boards have an optic-flow sensor (with LED illumination), ultrasonic sensor and 3-axis magnetometer. The optic-flow sensors can be used for detecting platform translational drift, the ultrasonic sensors can be used for detecting the differential altitude between the floor and the ceiling, and the magnetometers can be used as a digital compass. It was envisioned that differential magnetometer readings, between the top and bottom boards, could be used to detect the direction of a metallic structure for autonomous ceiling attachment, however this functionality has not yet been tested. Additionally, the top board has a servo connection and a serial connection, to control the ceiling attachment/detachment mechanism and connect a distance scanner, respectively.

The distance scanner (*Distance*), shown in figure A.10, only made it to the prototyping stage, however it was designed to fit into the centre of the structures head. A custom built rotating transformer (McLyman, 2004) with resonating coils is used to transfer power to the rotating sensors (see video<sup>2</sup>). The rotating transformer works in the same way as a regular transformer, however the primary and secondary coils are not fixed to each other. Due to the small gap between the coils, high-frequency ( $\approx 200$  kHz) alternating current is required to achieve high efficiencies ( $\approx 69\%$ ) at low power levels ( $\approx 1$  W). The ferrite core con-

<sup>2</sup>Video: <http://jfroberts.com/phd> (distance\_scanner.mp4)



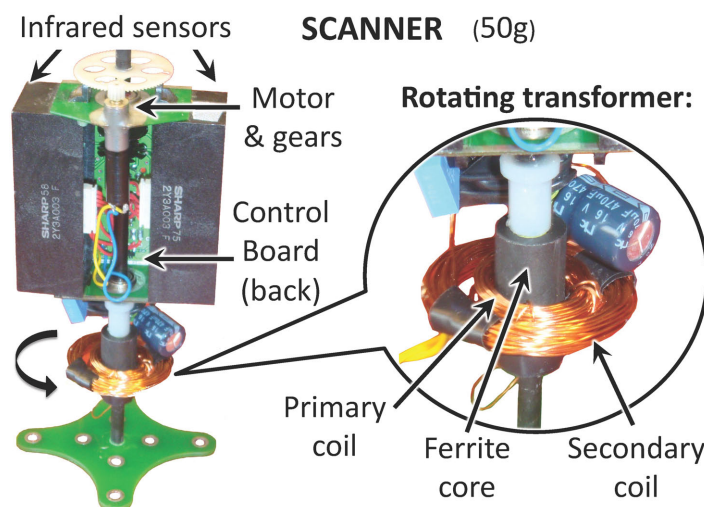


Figure A.10: Prototype distance scanner with rotating transformer

centrates the magnetic flux in the centre of the coils thus, improving efficiency.

### A.2.3 Swarmanoid specific electronics

The Swarmanoid specific electronics, include an embedded computer (*iMX.31*) and a pan-tilt camera (*Camera*). These electronics are for the visual recognition task of the Eye-bot, during the searching phase of the Swarmanoid project. Note that they are not used in the validation experiments presented in section 6.4.

The embedded computer (*iMX.31*), shown in figure A.11 *left*, is based on a Freescale i.MX31, vector floating point, ARM9/11 CPU, which can operate at speeds up to 532MHz. The core processing board, designed by LSRO<sup>3</sup> at EPFL, connects to a motherboard, designed by LIS<sup>4</sup> at EPFL, which provides the support power and peripheral connectivity. The motherboard has connectivity for a micro-SD card, micro-USB, standard USB and several other micro-controller compatible ports, including UART, SPI and GPIO. A dual band (2.4/5.8 GHz) WIFI dongle is connected to the standard USB port, the camera connects to the micro-USB port and communications with the main *Control* board is achieved through a UART connection.

The pan-tilt camera (*Camera*), shown in figure A.11 *right*, consists of a Webcam PRO-9000, laser pointer and two micro servos. In order to save weight the

<sup>3</sup><http://lsro.epfl.ch> (accessed April 2011)

<sup>4</sup><http://lis.epfl.ch> (accessed April 2011)

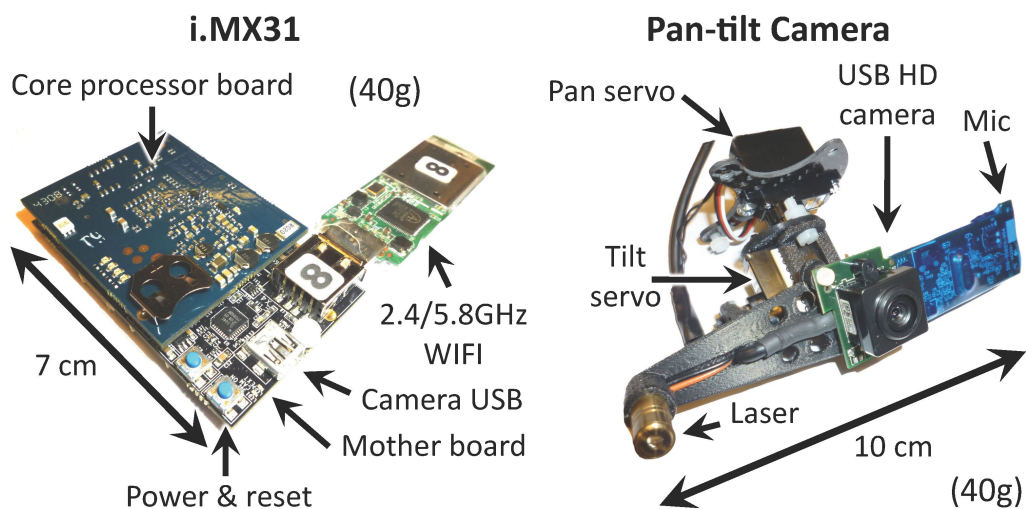


Figure A.11: i.MX31 embedded computer (*left*) and Pan-tilt video camera (*right*)

Webcam PRO-9000 has been stripped down and heat shrunk. The camera specifications include; high definition video, 2 MP pictures, autofocus and additional microphone. The laser pointer is used to indicate what the Eye-bots visual focus is. The laser has been offset from the camera (5 cm) so that a rough estimate of the distance to the target can be estimated using triangulation<sup>5</sup>.

#### A.2.4 Relative positioning sensor support

The relative positioning sensor support, includes the relative positioning sensors main processor (*Rabit-Main*) and communications hub (*Rabit-Hub*), which later connects to the 3-D relative positioning sensor ring from chapter 5.

The *Rabit-Main* board, shown in figure A.12 *left*, is designed to run the 3-D relative positioning algorithm, which calculates the range, bearing and elevation between robots and the 3-D proximity sensing. It has a 40 MIPS micro-controller coupled to a 2.4 GHz transceiver that is discussed in chapter 5, section 5.2.2. It connects to the eight *Rabit-Section* boards, presented in chapter 5, figure 5.7 via the *Rabit-Hub* board, shown in figure A.12 *right*. The *Rabit-Hub* board is simply a communications multiplexer that routes the 2.5 Mbps communications, to and from the eight *Rabit-Section* boards.

The developed 3-D relative positioning sensor, from chapter 5, can now be fitted in preparation for the validation experiments.

<sup>5</sup>[http://www.codeproject.com/KB/cs/range\\_finder.aspx](http://www.codeproject.com/KB/cs/range_finder.aspx) (accessed April 2011)

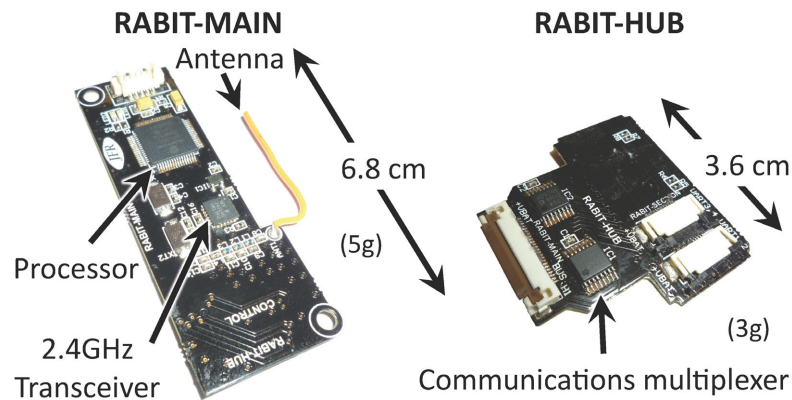


Figure A.12: Relative positioning processor (*left*) and communications hub (*right*)

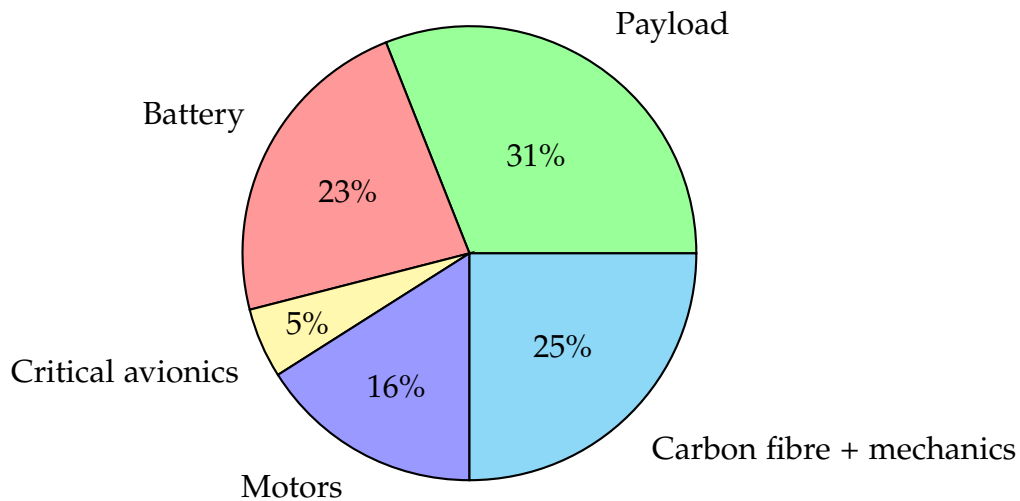


Chart A.1: Weight distribution of the completed Eye-bot

### A.2.5 Fitting the relative positioning sensor

Fitting the 3-D relative positioning sensor, from chapter 5, section 5.2.6, marks the completion of the Eye-bots hardware. The eight *Rabit-Section* boards that make up the 3-D relative positioning sensing ring, are attached to the arms using light-weight nylon nuts and bolts and connect electrically using light-weight flex cables. The completed Eye-bot hovering platform, ready for validation is shown in figure A.13. Chart A.1 shows the Eye-bots final weight distribution.



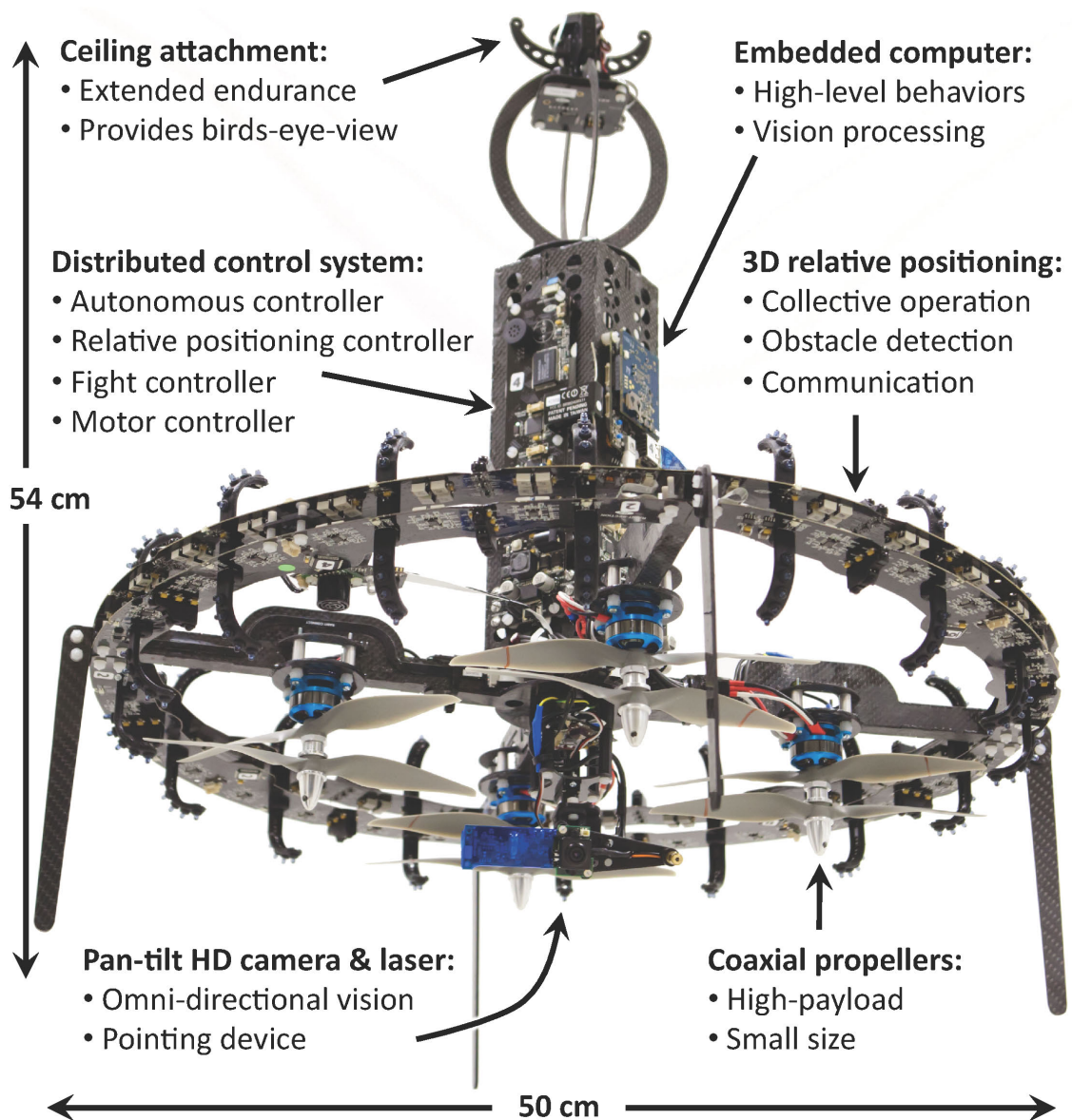


Figure A.13: The Eye-bot, a flying robot custom designed for indoor collective operation, fitted with a 3-D relative positioning sensor (*base perimeter*) and ceiling attachment mechanism (*top*), having a diameter of 50 cm and a maximum take-off weight of 2 kg including a payload of 600 g.



---

# Bibliography

---

- Achtelik, M., Bachrach, A., He, R., Prentice, S., and Roy, N. (2009). Stereo vision and laser odometry for autonomous helicopters in GPS-denied indoor environments. In *Proceedings of Unmanned Systems Technology XI (SPIE '09)*, volume 7332, pages 1901–1910, Orlando. The International Society for Optical Engineering.
- Altshuler, Y., Yanovsky, V., Wagner, I., and Bruckstein, A. (2008). Efficient cooperative search of smart targets using UAV swarms. *Robotica*, 26(4):551–557.
- Altug, E., Ostrowski, J., and Taylor, C. (2005). Control of a quadrotor helicopter using dual camera visual feedback. *The International Journal of Robotics Research*, 24(5):329–341.
- Amidi, O., Kanade, T., and Fujita, K. (1999). A visual odometer for autonomous helicopter flight. *Robotics and Autonomous Systems*, 28(2-3):185–193.
- Angeletti, G., Valente, J., Iocchi, L., and Nardi, D. (2008). Autonomous indoor hovering with a quadrotor. In *Proceedings of the International Conference on Simulation, Modelling and Programming for Autonomous Robots (SIMPAN '08)*, pages 472–481.
- Apostolyuk, V. (2006). Theory and design of micromechanical vibratory gyroscopes. In Leondes, C. T., editor, *MEMS/NEMS*, pages 173–195. Springer US.
- Autumn, K., Dittmore, A., Santos, D., Spenko, M., and Cutkosky, M. R. (2006). Frictional adhesion: a new angle on gecko attachment. *The Journal of Experimental Biology* 209, pages 3569–3579.

- Bachrach, A., He, R., and Roy, N. (2009). Autonomous flight in unstructured and unknown indoor environments. In *Proceedings of the 2009 European Micro Air Vehicle Conference and Flight Competition (EMAV '09)*.
- Beyeler, A., Zufferey, J.-C., and Floreano, D. (2009). Vision-based control of near-obstacle flight. *Autonomous Robots*, 27(3):201–219.
- Blösch, M., Weiss, S., Scaramuzza, D., and Siegwart, R. (2010). Vision based mav navigation in unknown and unstructured environments. In *Robotics and Automation (ICRA), 2010 IEEE International Conference on*, pages 21 –28.
- Bonani, M., Longchamp, V., Magnenat, S., Rétornaz, P., Burnier, D., Roulet, G., Vaussard, F., Bleuler, H., and Mondada, F. (2010). The MarXbot, a Miniature Mobile Robot Opening new Perspectives for the Collective-robotic Research. In *International Conference on Intelligent Robots and Systems (IROS), 2010 IEEE/RSJ*, pages 4187–4193. IEEE Press.
- Bouabdallah, S. and Siegwart, R. (2007). Full control of a quadrotor. In *Intelligent Robots and Systems, 2007. IROS 2007. IEEE/RSJ International Conference on*, pages 153 –158.
- Cavendish, M. (2008). *Inventors and Inventions*, volume 4. MTM Publishing, Marshall Cavendish Corporation.
- Chen, L. and McKerrow, P. (2007). Modelling the lama coaxial helicopter. In *Proceedings of the Australasian Conference on Robotics and Automation, Brisbane*.
- Coleman, C. P. (1997). A Survey of Theoretical and Experimental Coaxial Rotor Aerodynamic Research. Technical report, NASA Ames Research Center, Moffett Field, California.
- Courbon, J., Mezouar, Y., Guenard, N., and Martinet, P. (2009). Visual navigation of a quadrotor aerial vehicle. In *Proceedings of the 2009 international conference on Intelligent robots and systems (IROS '09)*, pages 5315–5320, Piscataway. IEEE Press.
- Crompton, T. (2000). *Battery reference book*. Newnes, a division of Reed Educational and Professional Publishing.

- 
- Dahmen, H., Millers, A., and Mallot, H. (2009). Insect inspired odometry by optic flow recorded with optical mouse chips. In Floreano, D., Zufferey, J., Srinivasan, M., and Ellington, C., editors, *Flying Insects and Robots*. Springer. in press.
- Eckert, J., German, R., and Dressler, F. (2011). An indoor localization framework for four-rotor flying robots using low-power sensor nodes. *Instrumentation and Measurement, IEEE Transactions on*, 60(2):336–344.
- Federal-Aviation-Administration (2007). *Rotorcraft Flying Handbook*. Skyhorse Publishing.
- Fowers, S. G., Lee, D.-J., Tippetts, B. J., Lillywhite, K. D., Dennis, A. W., and Archibald, J. K. (2007). Vision aided stabilization and the development of a quad-rotor micro UAV. In *Proceedings of the International Symposium on Computational Intelligence in Robotics and Automation*, pages 143–148, Piscataway. IEEE Press.
- Green, W. E. and Oh, P. (2008). Optic flow based collision avoidance on a hybrid MAV. In *IEEE Robotics and Automation Magazine*. in Press.
- Greer, D., McKerrow, P., and Abrantes, J. (2002). Robots in urban search and rescue operations. In *Proceedings of the Australasian Conference on Robotics and Automation*.
- Grzonka, S., Grisetti, G., and Burgard, W. (2009). Towards a navigation system for autonomous indoor flying. In *Proceedings of the International Conference on Robotics and Automation (ICRA '09)*, pages 2878–2883, Piscataway. IEEE Press.
- Guenard, N., Hamel, T., and Mahony, R. (2008). A practical visual servo control for a unmanned aerial vehicle. *IEEE Transactions on Robotics*, 24(2):331–341.
- Gurdan, D., Stumpf, J., Achtelik, M., Doth, K., Hirzinger, G., and Rus, D. (2007). Energy-efficient autonomous four-rotor flying robot controlled at 1 khz. In *Proceedings of the 2007 IEEE International Conference on Robotics and Automation*, pages 361–366.
- Hoffmann, G., Rajnarayan, D., Waslander, S., Dostal, D., Jang, J., and Tomlin, C. (2004). The stanford testbed of autonomous rotorcraft for multi agent con-

- trol (STARMAC). In *Proceedings of the 23rd Digital Avionics Systems Conference (DASC '04)*, volume 2, pages 1–10, Piscataway. IEEE Press.
- Hoffmann, G. M. and Tomlin, C. J. (2008). Decentralized cooperative collision avoidance for acceleration constrained vehicles. In *Proceedings of the 47th IEEE Conference on Decision and Control*, Cancun, Mexico.
- Holland, O., Woods, J., Nardi, R. D., and Clark, A. (2005). Beyond swarm intelligence: The ultraswarm. In *IEEE Swarm Intelligence Symposium*.
- Huang, H., Hoffmann, G., Waslander, S., and Tomlin, C. (2009). Aerodynamics and control of autonomous quadrotor helicopters in aggressive maneuvering. In *Robotics and Automation, 2009. ICRA '09. IEEE International Conference on*, pages 3277 –3282.
- Iida, F. (2003). Biologically inspired visual odometer for navigation of a flying robot. *Robotics and Autonomous Systems*, 44:201–208.
- Jeong, W. and Lee, K. M. (2005). Cv-slam: a new ceiling vision-based slam technique. In *Intelligent Robots and Systems, 2005. (IROS 2005). 2005 IEEE/RSJ International Conference on*, pages 3195 – 3200.
- Kelly, I. D. and Keating, D. D. A. (1996). Flocking by the fusion of sonar and active infrared sensors on physical autonomous mobile robots. In *In Proc. of the The Third Int. Conf. on Mechatronics and Machine Vision in Practice*, pages 1–4.
- Kelly, I. D. and Martinoli, A. (2004). A Scalable, On-Board Localisation and Communication System for Indoor Multi-Robot Experiments. *Sensor Review*, 24(2):167–180. Special issue on Sensor Simulation and Smart Sensors, C. Loughlin, editor.
- Kemppainen, A., Haverinen, J., and Roning, J. (2006). An infrared location system for relative pose estimation of robots. In *Symposium of Robot Design, Dynamics, and Control*, pages 379 – 386.
- Kim, S., Spenko, M., Trujillo, S., Heyneman, B., Mattoli, V., and Cutkosky, M. R. (2007). Whole body adhesion: hierarchical, directional and distributed control of adhesive forces for a climbing robot. In *IEEE International Conference on Robotics and Automation*.

- 
- Kirchner, N. and Furukawa, T. (2005). Abstract infrared localisation for indoor uavs. In *Proceedings of the International Conference on Sensing Technology*, pages 60–65.
- Kovac, M., Germann, J. M., Hürzeler, C., Siegwart, R., and Floreano, D. (2010). A Perching Mechanism for Micro Aerial Vehicles. *Journal of Micro-Nano Mechatronics*, 5(3-4):77–91.
- Kovacina, M. A., Palmer, D., Yang, G., and Vaidyanathan, R. (2002). Multi-agent control algorithms for chemical cloud detection and mapping using unmanned air vehicles. In *Proceedings of the International Conference on Intelligent Robots and Systems (IROS '02)*, volume 3, pages 2782–2788.
- Ladd, A. M., Bekris, K. E., Rudys, A., Kavraki, L. E., and Wallach, D. S. (2005). Robotics-based location sensing using wireless ethernet. *Wireless Networks*, 11(1-2):189–204.
- Lander, C.-W. (1993). *Power Electronics third edition*, chapter Rectifying Circuits. McGraw Hill.
- Lange, S., Sunderhauf, N., and Protzel, P. (2009). A vision based onboard approach for landing and position control of an autonomous multirotor uav in gps-denied environments. In *Advanced Robotics, 2009. ICAR 2009. International Conference on*, pages 1 –6.
- Leishman, J. G. (2006). Principles of helicopter aerodynamics. In *Cambridge Aerospace Series*. Cambridge University Press. in press.
- Leishman, J. G. and Ananthan, S. (2006). Aerodynamic optimization of a coaxial proprotor. *ANNUAL FORUM PROCEEDINGS- AMERICAN HELICOPTER SOCIETY*, 62:64–86.
- Levine, W. S. (1996). *Chapter 16: Sample-Rate Selection*, volume Series II, pages 313–321. CRC & IEEE Press.
- Liu, Z. and Moschetta, J.-M. (2009). Rotary vs. flapping-wing nano air vehicles: Comparing hovering power. In *European Micro Aerial Vehicle Conference and Flight Competition*.

- Lupashin, S., Schöllig, A., Sherback, M., and D'Andrea, R. (2010). A simple learning strategy for high-speed quadrocopter multi-flips. In *Proceedings of the International Conference on Robotics and Automation (ICRA '10)*, pages 642–648, Piscataway. IEEE Press.
- Lussier Desbiens, A. and Cutkosky, M. R. (2010). Landing and perching on vertical surfaces with microspines for small unmanned air vehicles. *J. Intell. Robotics Syst.*, 57:313–327.
- Mahony, R., Hamel, T., and Pflimlin, J.-M. (2005). Complementary filter design on the special orthogonal group  $so(3)$ . In *Decision and Control, 2005 and 2005 European Control Conference. CDC-ECC '05. 44th IEEE Conference on*, pages 1477 – 1484.
- Matsue, A., Hirose, W., Tokutake, A., Sundada, S., and Ohkura, A. (2005). Navigation of small and lightweight helicopter. *Trans. Japan Society Aeronautical and Space Sciences*, 48:177–179.
- McLurkin, J. and Smith, J. (2004). Distributed algorithms for dispersion in indoor environments using a swarm of autonomous mobile robots. In *7th International Symposium on Distributed Autonomous Robotic Systems*, Toulouse, France.
- McLyman, C. W. T. (2004). *Transformer and Inductor Design Handbook*. Marcel Dekker Inc.
- Melhuish, C. and Welsby, J. (2002). Gradient ascent with a group of minimalist real robots: Implementing secondary swarming. In *IEEE International Conference on Systems, Man and Cybernetics*, volume 2, pages 509–514.
- Michiel, J. M., Morris, J. C., and Nieuwstadt, M. V. (1994). Experimental platform for real-time control. In *In Proceedings of the ASEE Annual Conference*.
- Min, B. C., Cho, C. H., Choi, K. M., and Kim, D. H. (2009). Development of a micro quad-rotor uav for monitoring an indoor environment. In *FIRA RoboWorld Congress*, pages 262–271.
- Montesano, L., Montano, L., and Burgard, W. (2004). Relative localization for pairs of robots based on unidentifiable moving features. In *Intelligent Robots and Systems, 2004. (IROS 2004). Proceedings. 2004 IEEE/RSJ International Conference on*, volume 2, pages 1537–1543.



- 
- Murphy, M. P. and Sitti, M. (2009). Waalbot: agile climbing with synthetic fibrillar dry adhesives. In *Proceedings of the 2009 IEEE international conference on Robotics and Automation, ICRA'09*, pages 2637–2638, Piscataway, NJ, USA. IEEE Press.
- Murphy, M. P., Tso, W., Tanzini, M., and Sitti, M. (2006). Waalbot: An agile small-scale wall climbing robot utilizing pressure sensitive adhesives. In *IEEE/RSJ International Conference on Intelligent Robots and Systems*, pages 3411–3416.
- Naboulsi, A., Sizun, M., and H.D, F. (2005). Propagation of optical and infrared waves in the atmosphere. In *Proceedings of the Union Radio Scientifique Internationale*.
- Nakamura, T., Oohara, M., Ogasawara, T., and Ishiguro, H. (2003). Fast self-localization method for mobile robots using multiple omnidirectional vision sensors. *Mach. Vision Appl.*, 14(2):129–138.
- Nardi, R. D., Holland, O., Woods, J., and Clark, A. (2006). Swarmav: A swarm of miniature aerial vehicles. In *21st International UAV Systems Conference*, Bristol.
- Ogren, P., Fiorelli, E., and Leonard, N. (2004). Cooperative control of mobile sensor networks: adaptive gradient climbing in a distributed environment. *Automatic Control, IEEE Transactions on*, 49(8):1292 – 1302.
- Oh, P. Y., Joyce, M. J., and Gallagher, J. (2005). Designing an aerial robot for hover-and-stare surveillance. *International Conference on Advanced Robotics (ICAR)*, pages 303–308.
- Ohkura, A., Tokutake, A., and Sundada, S. (2005). Autonomous hovering of a small helicopter. *Trans. Japan Society Aeronautical and Space Sciences*, 53:376–378.
- Payton, D., Daily, M., Estowski, R., Howard, M., and Lee, C. (2001). Pheromone robotics. *Autonomous Robots*, 11(3):319–324.
- Pilz, U., Popov, A., and Werner, H. (2009). Robust controller design for formation flight of quad-rotor helicopters. In *Decision and Control, 2009 held jointly with the 2009 28th Chinese Control Conference. CDC/CCC 2009. Proceedings of the 48th IEEE Conference on*, pages 8322 –8327.

- Prahlad, H., Pelrine, R., Stanford, S., Marlow, J., and Kornbluh, R. (2008). Electro-adhesive robots - wall climbing robots enabled by a novel, robust, and electrically controllable adhesion technology. In *ICRA*, pages 3028–3033.
- Pugh, J. and Martinoli, A. (2006). Relative Localization and Communication Module for Small-Scale Multi-Robot Systems. In *IEEE International Conference on Robotics and Automation*, pages 188 – 193.
- Pugh, J., Raemy, X., Favre, C., Falconi, R., and Martinoli, A. (2009). A Fast On-Board Relative Positioning Module for Multi-Robot Systems. *IEEE/ASME Transactions on Mechatronics, Focused Section on Mechatronics in Multi Robot Systems*.
- Rivard, F., Bisson, J., Michaud, F., and Letourneau, D. (2008). Ultrasonic relative positioning for multi-robot systems. In *Robotics and Automation, 2008. ICRA 2008. IEEE International Conference on*, pages 323–328.
- Roberts, J., Stirling, T., Zufferey, J.-C., and Floreano, D. (2007). Quadrotor using minimal sensing for autonomous indoor flight. In *Proceedings of the 2007 European Micro Air Vehicle Conference and Flight Competition (EMAV '07)*.
- Roberts, J., Stirling, T., Zufferey, J.-C., and Floreano, D. (2009). 2.5D infrared range and bearing system for collective robotics. In *Proceedings of the International Conference on Intelligent Robots and Systems (IROS '09)*, pages 3659–3664, Piscataway. IEEE Press.
- Roberts, J., Zufferey, J.-C., and Floreano, D. (2008). Energy management for indoor hovering robots. In *Proceedings of the International Conference on Intelligent Robots and Systems (IROS '08)*, pages 1242–1247, Piscataway. IEEE Press.
- Rudol, P., Wzorek, M., Conte, G., and Doherty, P. (2008). Micro unmanned aerial vehicle visual servoing for cooperative indoor exploration. In *Proceedings of the Aerospace Conference*, pages 1–10, Piscataway. IEEE Press.
- Sahin, E. (2005). Swarm robotics: From sources of inspiration to domains of application. In *International Workshop on Swarm Robotics*, pages 10–20.
- Salazar, S., Romero, H., Lozano, R., and Castillo, P. (2009). Modeling and real-time stabilization of an aircraft having eight rotors. *Journal of Intelligent and Robotic Systems*, 57:455–470.

- 
- Shoval, S. and Borenstein, J. (2001). Measuring the relative position and orientation between two mobile robot with binaural sonar. In *ANS 9th International Topical Meeting on Robotics and Remote Systems*, Seattle, Washington.
- Sitti, M. and Fearing, R. S. (2003). Synthetic gecko foot-hair micro/nano-structures for future wall-climbing robots. In *ICRA*, pages 1164–1170.
- Soundararaj, S. P., Sujeeth, A. K., and Saxena, A. (2009). Autonomous indoor helicopter flight using a single onboard camera. In *Proceedings of the 2009 IEEE/RSJ international conference on Intelligent robots and systems, IROS'09*, pages 5307–5314, Piscataway, NJ, USA. IEEE Press.
- Spenko, M. J., Haynes, G. C., Saunders, J. A., Cutkosky, M. R., Rizzi, A. A., Full, R. J., and Koditschek, D. E. (2008). Biologically inspired climbing with a hexapedal robot. *J. Field Robot.*, 25:223–242.
- Stirling, T., Wischmann, S., and Floreano, D. (2010). Energy-efficient indoor search by swarms of simulated flying robots without global information. *Swarm Intelligence*, 4(2):117–143.
- Tarascon, J. M. and Armand, M. (2001). Issues and challenges facing rechargeable lithium batteries. *Nature*, 414(6861):359–367.
- Thomas, J. P., Qidwai, M. A., and Kellogg, J. C. (2006). Energy scavenging for small-scale unmanned systems. *Journal of Power Sources*, 159(2):1494 – 1509.
- Tipler, P. and Mosca, G. (2004). *Physics for Scientists and Engineers: Mechanics, oscillations and waves, thermodynamics*. Number pts. 1-13 in *Physics for Scientists and Engineers*. W.H. Freeman.
- Unver, O., Uneri, A., Aydemir, A., and Sitti, M. (2006). Geckobot: A gecko inspired climbing robot using elastomer adhesives. In *Proceedings of the IEEE International Conference on Robotics and Automation*, pages 2329–2335.
- Valenti, M., Bethke, B., How, J.-P., Farias, D.-P., and Vian, J. (2007). Embedding health management into mission tasking for UAV teams. In *American Control Conference*, pages 5777–5783, Piscataway. IEEE Press.
- Wataru, H., Akihiro, O., and Shigeru, S. (2003). A study of a coaxial helicopter(ii): Analysis on effects of a stabilizer bar on fuselage motion. *Proceedings of Aircraft Symposium*, 41(1):283–286.

- Welsby, J. and Melhuish, C. (2001). Autonomous minimalist following in three dimensions: A study with small-scale dirigibles. In *Proceedings of Towards Intelligent Mobile Robots*.
- Wilson, T. and Trickey, P. (1962). D.c. machine. with solid state commutation. In *AIEE*, pages 879–1962.
- Zufferey, J.-C., Hauert, S., Stirling, T., Leven, S., Roberts, J., and Floreano, D. (2011). *Handbook of Collective Robotics*, chapter Collective Aerial Systems. Pan-Stanford Publishing, Singapore.

---

# Curriculum Vitae

---

I was born on the 28th of October 1982 in Murwillumbah NSW, Australia, where I lived until the age of 18. In 2001, I began my Bachelor of Engineering in Micro Electronic Engineering majoring in Communication Systems at Griffith University Brisbane. I completed this in 2004 with honours. My graduation project, entitled "A Design for Air-Traffic Audio Control" was part of an Industrial Affiliates Program with Airservices Australia. My design now manages 11% of the worlds airspace and won the academic excellence award, best control system design award and best poster award. In 2004, I became Chief Engineer and co-founder of "Jimonics Engineering Solutions", specialising in custom designed electronics and mechanics for aerial robotic systems, including air-traffic audio control, data acquisition systems, experimental sensing and autonomous control systems. In 2005, I began my Masters of Engineering Research at the University of Sydney in the Aeronautical, Mechanical & Mechatronic Engineering department. I completed this in 2007. My graduation project, entitled "Design of an Autonomous Hovering Miniature Air Vehicle as a Flying Research Platform", sparked international interest in the field of Aerial Robotics. Since January 2008, I have been a Ph.D. candidate at the Ecole Polytechnique Fédérale de Lausanne, where I have been carrying out the research presented in this thesis under the supervision of Dr. Jean-Christophe Zufferey and Prof. Dario Floreano at the Laboratory of Intelligent Systems.

